Gulf General Atomic
Incorporated
P.O. Box 608, San Diego, California 92112

AEC RESEARCH AND
DEVELOPMENT REPORT

GA-9130

PUBLIC SERVICE COMPANY OF COLORADO
330-MW(E) HIGH-TEMPERATURE GAS-COOLED REACTOR
RESEARCH AND DEVELOPMENT PROGRAM

QUARTERLY PROGRESS REPORT
FOR THE PERIOD ENDING
DECEMBER 31, 1968

Prepared under
Contract AT(04-3)-633
for the
San Francisco Operations Office
U.S. Atomic Energy Commission

January 29, 1969

DISTRIBUTION OF THIS DOCUMENT IS UNLIMITED

DISCLAIMER

QUARTERLY REPORT SERIES

GA-6830-July, 1965, through September, 1965
GA-6950-October, 1965, through December, 1965
GA-7086-January, 1966, through March, 1966
GA-7314-April, 1966, through June, 1966
GA-7453-July, 1966, through September, 1966
GA-7634-October, 1966, through December, 1966
GA-7939-January, 1967, through March, 1967
GA-8038-April, 1967, through June, 1967
GA-8270-July, 1967, through September, 1967
GA-8420-October, 1967, through December, 1967
GA-8600-January, 1968, through March, 1968
GA-8725-April, 1968, through June, 1968
GA-8879-July, 1968, through September, 1968

INTRODUCTION

The objective of the research and development program work reported here is to develop and verify the information required to design, construct, operate, and maintain the Public Service Company of Colorado power plant as provided in U.S. Atomic Energy Commission Contract AT(04-3)-633.

Part I of this report includes the work described in Appendix B of the contract; this work consists largely of component development and testing, nuclear analysis, and fuel development and testing. Part II covers the work described in Appendix K of the contract on the fuel transfer machine, the series-steam-turbine-driven circulator, the control rod drives, the steam generator, and coated particles.

CONTENTS

PART I

AEC-SUPPORTED RESEARCH AND DEVELOPMENT PROGRAM FOR THE PUBLIC SERVICE COMPANY OF COLORADO HTGR

Task I

COMPONENT DEVELOPMENT

REACTOR VESSEL

The objective of this subtask is to develop information necessary to develop and specify the design of the Prestressed Concrete Reactor Vessel (PCRV) for the plant and to provide a technical basis for obtaining necessary approvals of regulatory bodies and insurance groups, by means of conceptual design, analyses, and testing of materials, scale models of the vessel, and full-scale parts of the vessel, such as tendons and penetrations, where necessary.

Model testing will include heating internally to produce appropriate temperature differences across the concrete, test to destruction, long-term tests, measurements of leakage through the concrete resulting from a simulated crack in the liner and tests to demonstrate the adequacy of the double closures on penetrations. Representatives of interested technical societies, regulatory bodies, and insurance groups will be informed of the progress of the programs and encouraged to witness key tests.

Prestressing System

The long-term prestressing relaxation test both at ambient and 120°F continued with relaxation data being taken once in two weeks. There is no significant change in relaxation losses either at 120°F or ambient temperature conditions from those reported in the previous quarterly report (GA-8879).

The long-term tendon anchor load test at 130°F has completed more than 4000 hr after the test beam was initially heated.

Concrete Properties

The Phase II creep and shrinkage specimens have attained the specified minimum load duration of six months. The concrete specimens will remain under load at the prescribed temperature levels for an indefinite additional time.

The program on preplaced aggregate concrete (PAC) at the University of California at Berkeley was completed. Table 1.1, an updated version of Table 1.1 given in an earlier quarterly report (GA-8725), includes strength results and other concrete test data at 180 days of age.

THERMAL BARRIER

The objective of this subtask is to establish the suitability and reliability and predict the maintainability of the thermal barrier materials

Table 1.1

SUMMARY OF PROPERTIES OF GROUTS AND OF 6- BY 12-IN. PAC SPECIMENS CONTAINING TYPE II, LOW-ALKALI, LOW-HEAT CEMENT

Properties	Mix 9:1:10	Mix 9:1:8
Intrusion Grouts		
W/(C + FA), by weight	0.47	0.44
Grout temp, °F	47	46
Flow factor, sec	21.8	21.1
Consistency factor, degrees	188	188
Extraction factor, min:sec	4:21	4:38
Unit weight of grout, lb/ft^3	129.7	128.8

Properties	Mix 9:1:10		Mix 9:1:8	
Test at ambient temperature	45°F	70°F	45°F	70°F
Expansion at 5 hr, %	7.6	11.7	8.6	12.5
Bleeding at 5 hr, %	0.8	0.8	0.6	0.5
Time of Set.(Vicat), hr:				
Initial	32½	16	32	17¼
Final	35	18	35¼	19
Preplaced Aggregate Concretes				
Type of curing at 70°F	Moist	Sealed	Moist	Sealed
Compressive strength, psi:				
7 days	2690	2470	2950	2950
28 days	5960	5610	6060	5560
90 days	7620	6760	7600	6890
180 days[a]	8560	7540	8800	7640
Tensile splitting strength, psi:				
28 days	611	611	631	607
90 days	689	633	688	704
180 days[a]	724	676	720	695

Mod. of Elast. E (10^6 psi), and Poisson's ratio μ:	E	μ	E	μ	E	μ	E	μ
7 days	3.1	0.18	3.1	0.19	3.2	0.20	3.2	0.20
28 days	4.1	0.21	4.1	0.21	4.1	0.20	4.1	0.22
90 days	4.7	0.20	4.4	0.21	4.7	0.20	4.4	0.21
180 days	5.1	0.21	4.9	0.21	5.0	0.20	4.8	0.21

Unit weight, lb/ft^3, (avg. up to 90 days)	Moist	Sealed	Moist	Sealed
	147.0	146.0	146.7	145.7

[a] Additional data.

and design for predicted operating conditions of the plant PCRV by means of analyses, conceptual designs, fabrication development, materials testing, thermal testing, and accelerated life testing where meaningful, on thermal barriers under simulated environmental conditions (in helium at temperatures up to or greater than those predicted in the reactor and, where analyses indicate necessary, at reactor pressure).

Attachment Fixtures for Class A Thermal Barrier

The Class A thermal barrier consists of a series of fibrous blankets compressed onto the inside surface of the prestressed concrete reactor vessel liner by 1/4-in. steel cover plates. On the majority of the reactor liner, including the vertical walls, a second series of blankets and a second cover plate are installed over the first to provide redundancy. The attachment fixture is so designed that the outer blanket layer may lose all resiliency, that is, it may creep under high-temperature conditions, without affecting the degree of compression of the inner layer. This is done by means of a spacer, as shown in the attachment fixture assembly in Fig. 1.1.

The fibrous blanket material is Kaowool (Ref. 1),* manufactured by Babcock and Wilcox, and the degree of compression was chosen for a balance between the decreasing gas flow permeation and the increasing loading on the cover plates and attachment fixtures with an increasing amount of compression. Figure 1.2 shows the pressure range that would be required to compress new Kaowool to the design compression figure of 70% of the nominal thickness.

This compression results in a loading on the weld stud and post in the attachment fixture which can have up to five components.

1. Tensile stress required to compress the fibrous material.
2. Bending moment due to the weight of the cover plate (vertical wall only).
3. Bending moment due to the frictional forces caused by expansion and contraction of the cover plates during reactor primary coolant temperature changes.
4. Torsional stress as unbalanced friction forces rotate the cover plate.
5. Tensile stress and bending moment caused by increased frictional forces following a PCRV liner movement behind one attachment fixture.

In addition, two other stresses must be taken into account, (1) thermal stress and (2) the tensile stress incurred during a decrease in primary coolant pressure, particularly as a result of the fast depressurization accident which has a pressure drop rate of 40 psi/sec. Three of these stresses, items 3, 4, and 5, could be applied cyclically with the reactor primary coolant temperature and required analysis using fatigue criteria.

---

*References will be found at the end of each task.

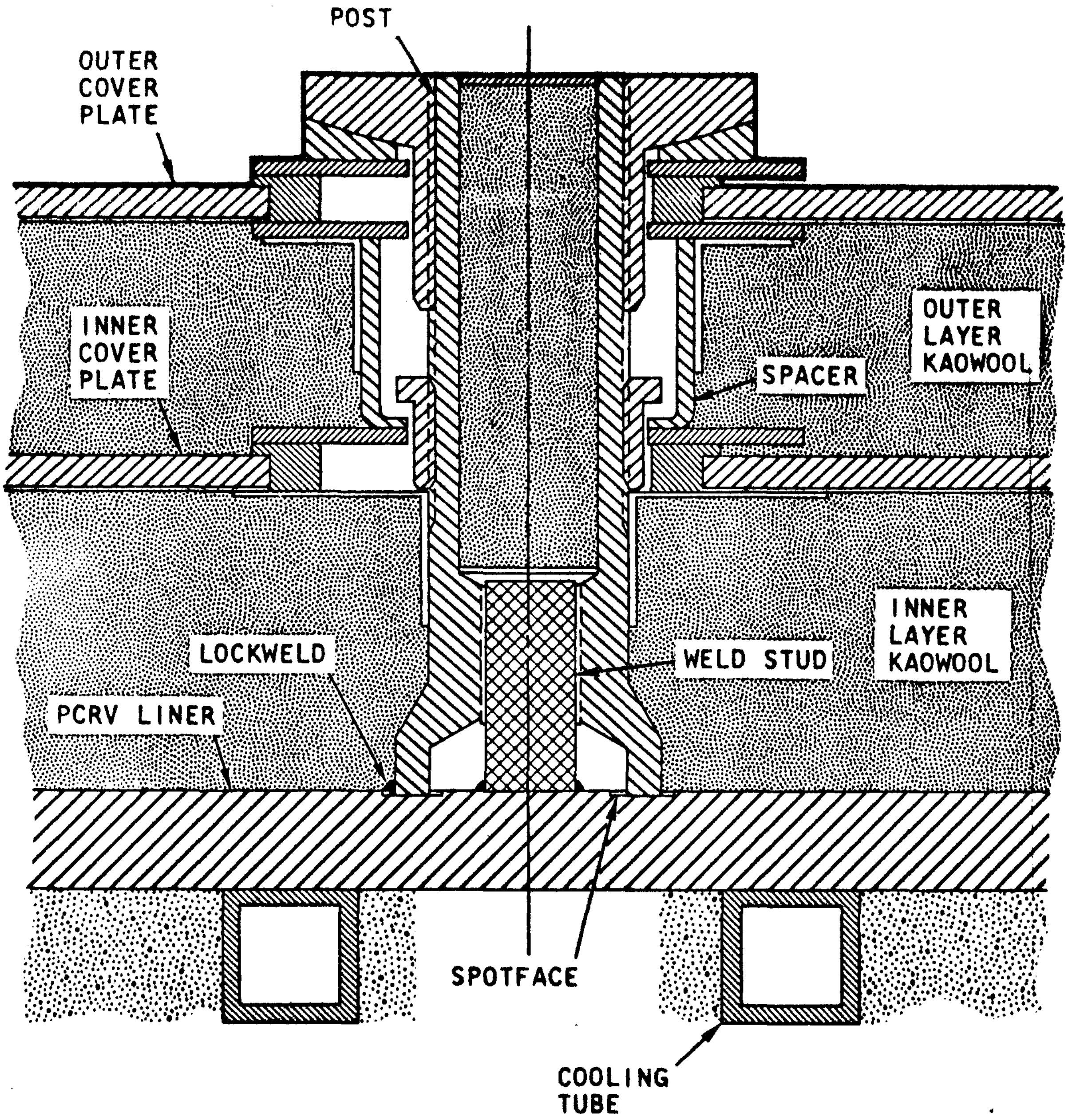

Fig. 1.1--Class A thermal barrier attachment fixture

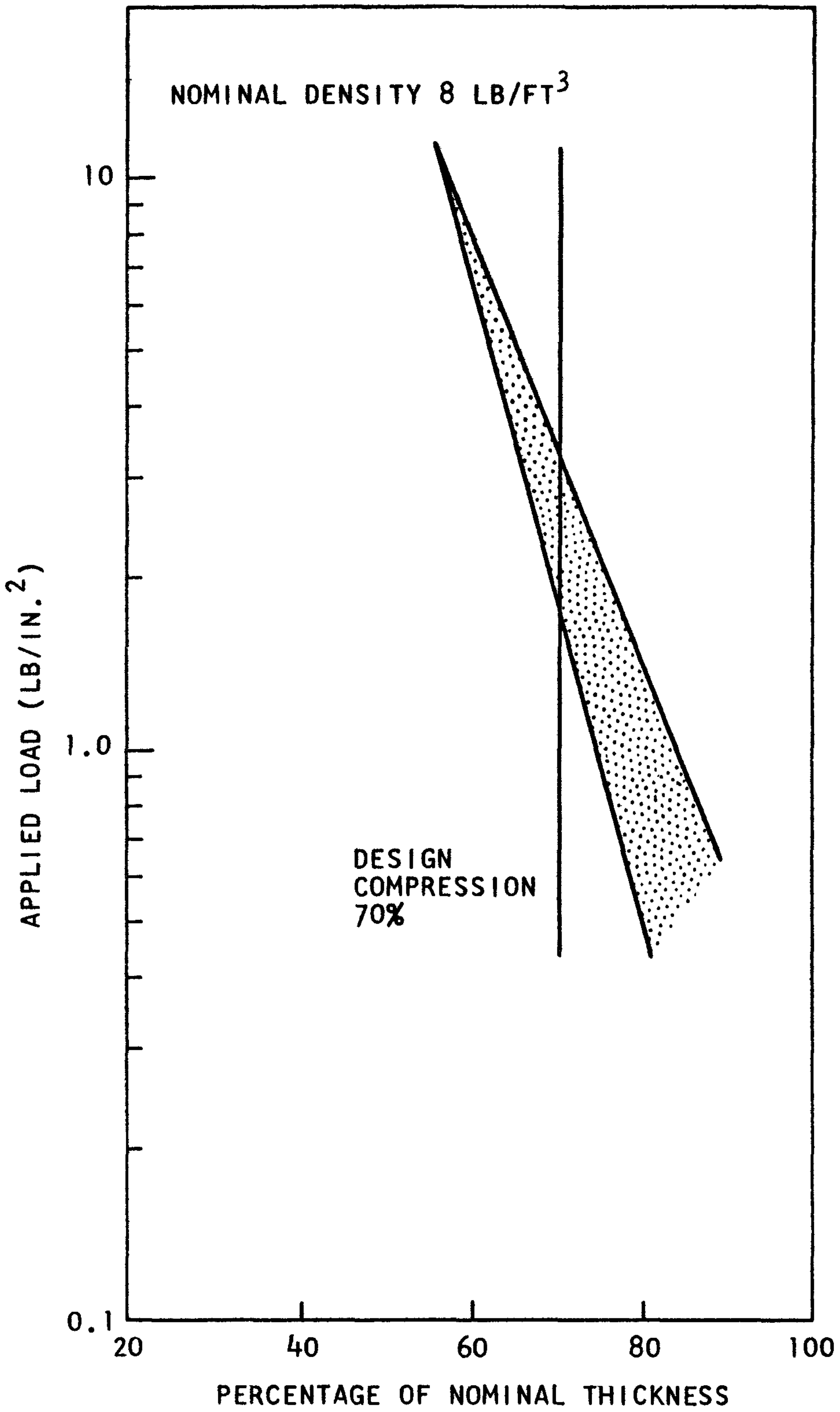

Fig. 1.2--Load/compression characteristics of new Kaowool

An analysis of these stresses was carried out, and it showed that the highest bending moment that the fixture must be designed to withstand is 6400 lb-in. and that the fatigue life of the fixture must be able to take this loading for 20,000 cycles, corresponding to the design number of temperature cycles of the primary coolant. The point of highest stress during the application of this bending moment is at the base of the weld stud.

Fatigue Test Program. Not only is the vertical liner wall the area in the reactor where the highest stresses are generated in the attachment fixture because of the additional effect of the weight of the plate, but it is also the area in which the quality of the stud weld is less reliable. This is due to the tendency of the molten metal to run vertically downwards during the weld cycle, producing an undercut on the top side of the weld. Because of this effect a 3/4-in.-diameter stud was the largest that could be used on the vertical wall. A fatigue test program was therefore set up to determine whether this was the optimum stud size from the point of view of fatigue and to develop a welding procedure that would give a satisfactory fatigue life under the predicted loading. It was also used to evaluate the effect on fatigue life of varying amounts of prestress in the stud and of the liner curvature of 186 in. radius.

The studs were tested by welding them, in the horizontal position, to a 4 by 4 by 3/4 in. thick plate fabricated of the same material as the PCRV liner (A537 Type B steel) and then subjecting this assembly in a 5000 lb reversible-load Budd fatigue test machine running at 1500 cpm. Figures 1.3, 1.4, and 1.5 show details of the specimen and test rig. All tests were run to failure or 5×10^5 cycles, except for some of the early ones that were run to 1×10^6 cycles. Loading on the stud was measured by a Narmco load cell, Model C-12-14, incorporating four Budd metal film strain gages. This load cell was fully calibrated.

Before the post was installed, the weld stud and plate were wire brushed and degreased, and the stud threads were lubricated with a coat of spray graphite.

The load-cell arrangement used to determine the relationship between stud prestesss and applied torque is shown in Fig. 1.6.

Results. Fatigue tests were carried out using two different stud diameters, 3/4 and 5/8 in. The tests (see Figs. 1.7 and 1.8) revealed that the 3/4-in.-diameter stud gave scattered results, several failures occuring after one or two cycles. However, the results with the 5/8-in.-diameter stud showed very good S/N fatigue characteristics, with the failures grouped in a small range of cycles for any given load.

Tests were carried out to determine the relationship between the torque applied to the post and the stress induced in the stud and to determine the effect of liner surface finish on this relationship (see Figs. 1.9 and 1.10). This information was then used to set up prestress levels in the tests on the fatigue life of the stud specimens.

The tests carried out on 3/4-in.- and 5/8-in.-diameter stud were with varying degress of prestress (Figs. 1.7 and 1.8), and it is apparent that there is a strong dependence of fatigue life on prestress in both cases.

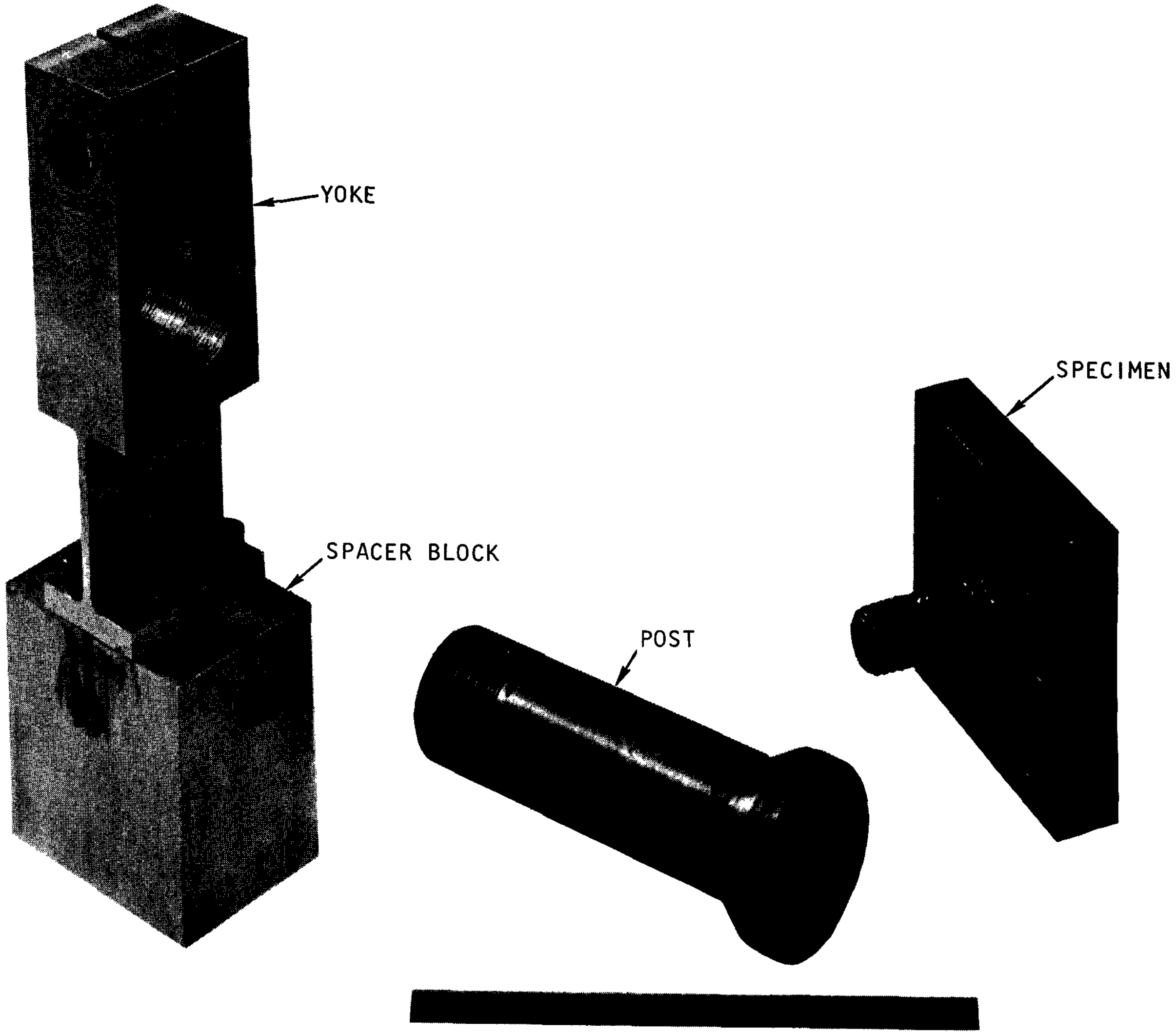

Fig. 1.3--Weld stud specimen

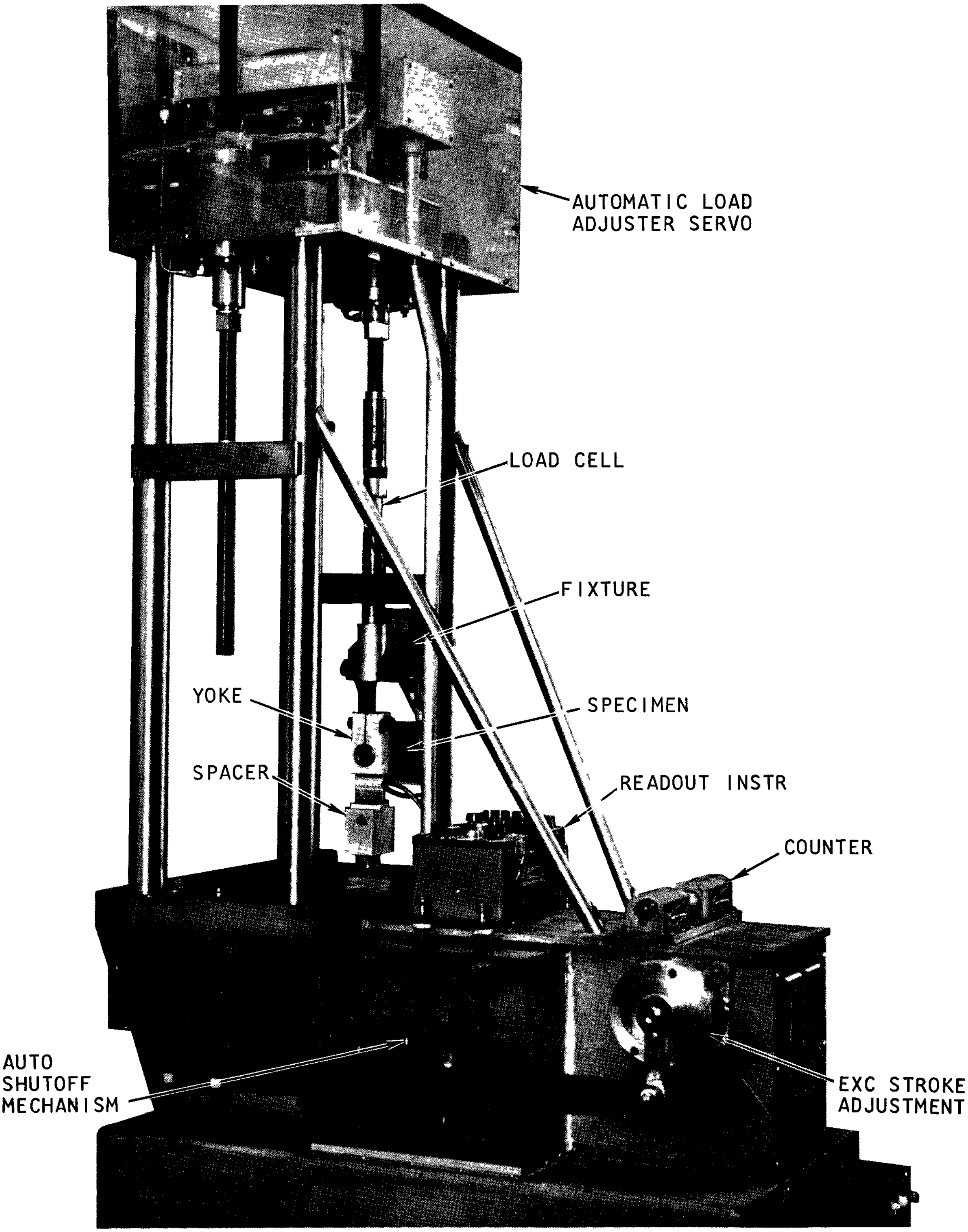

Fig. 1.4--Budd fatigue testing machine

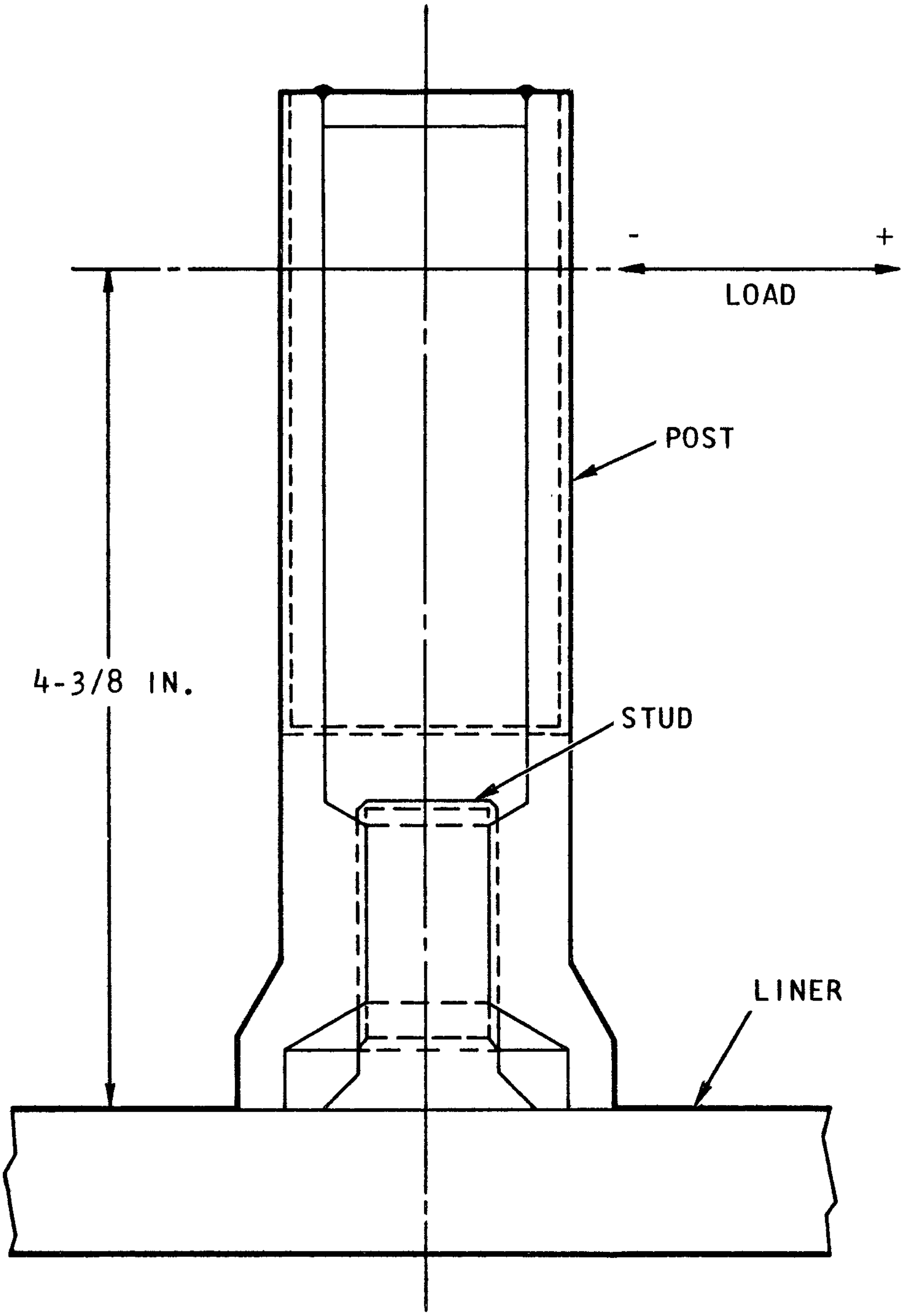

Fig. 1.5--Details of load application in fatigue test

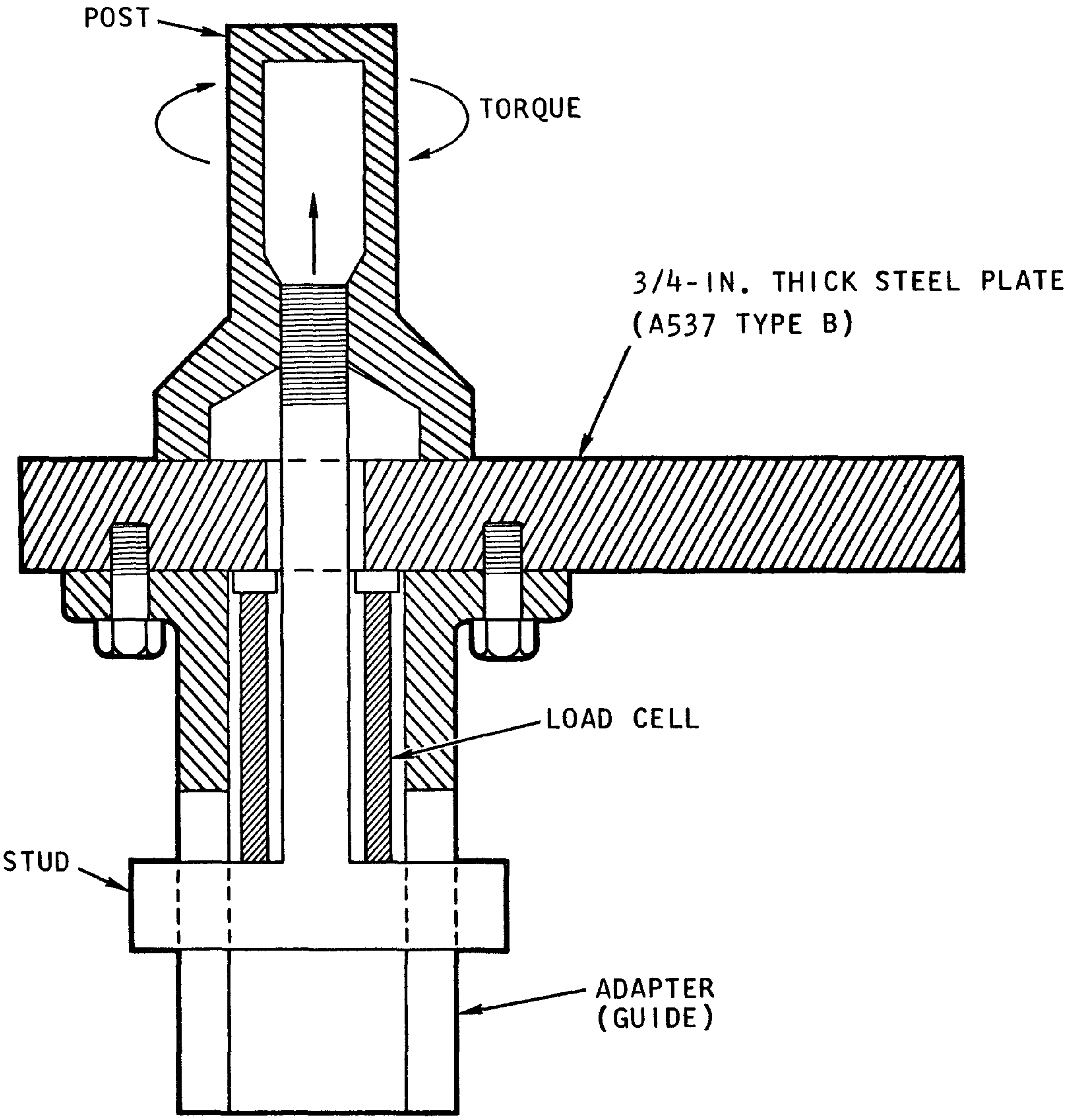

Fig. 1.6--Method used to determine the relationship between post applied torgue and stud tensile stress

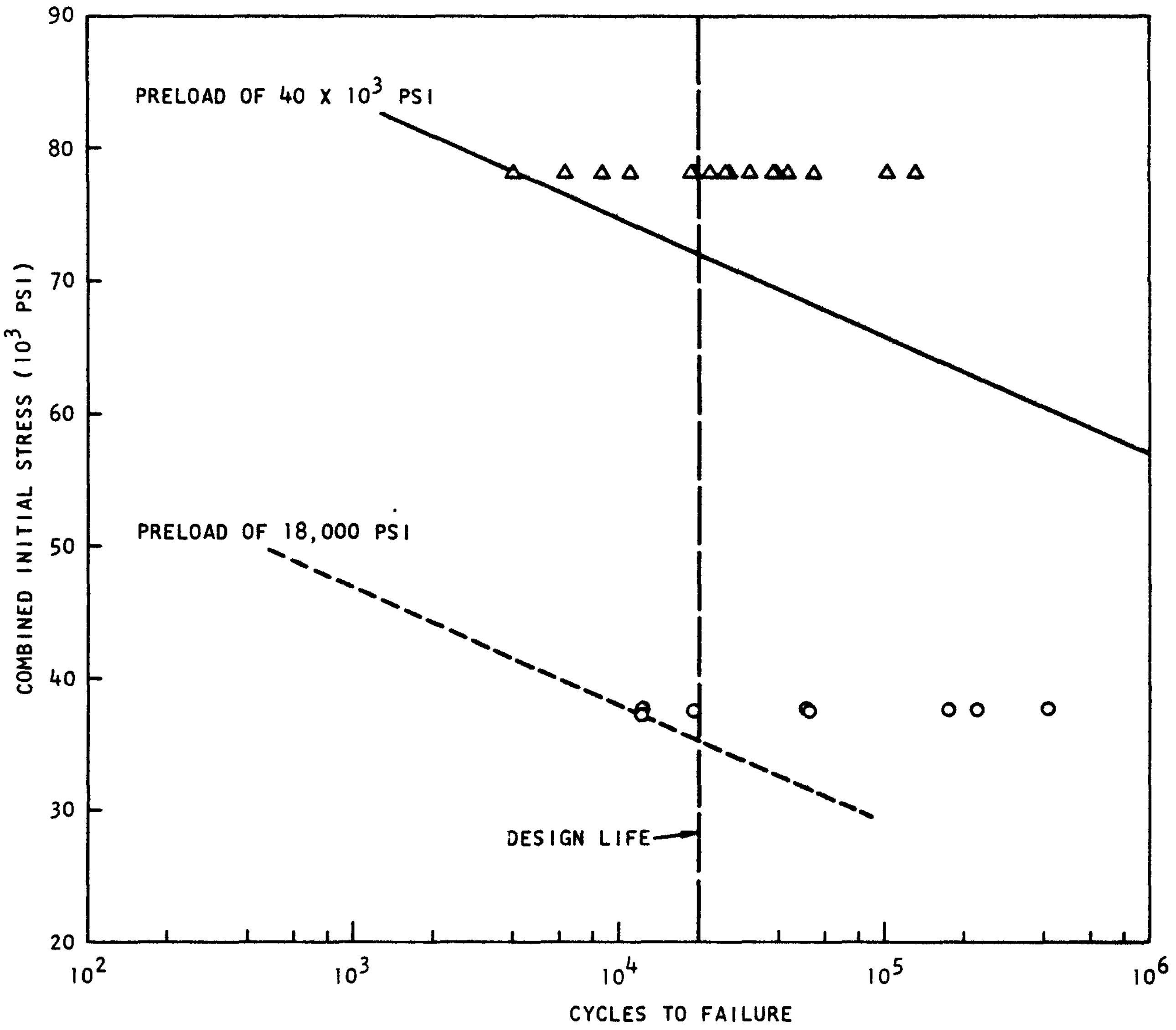

Fig. 1.7--Fatigue test data on 5/8-in.-diameter weld stud

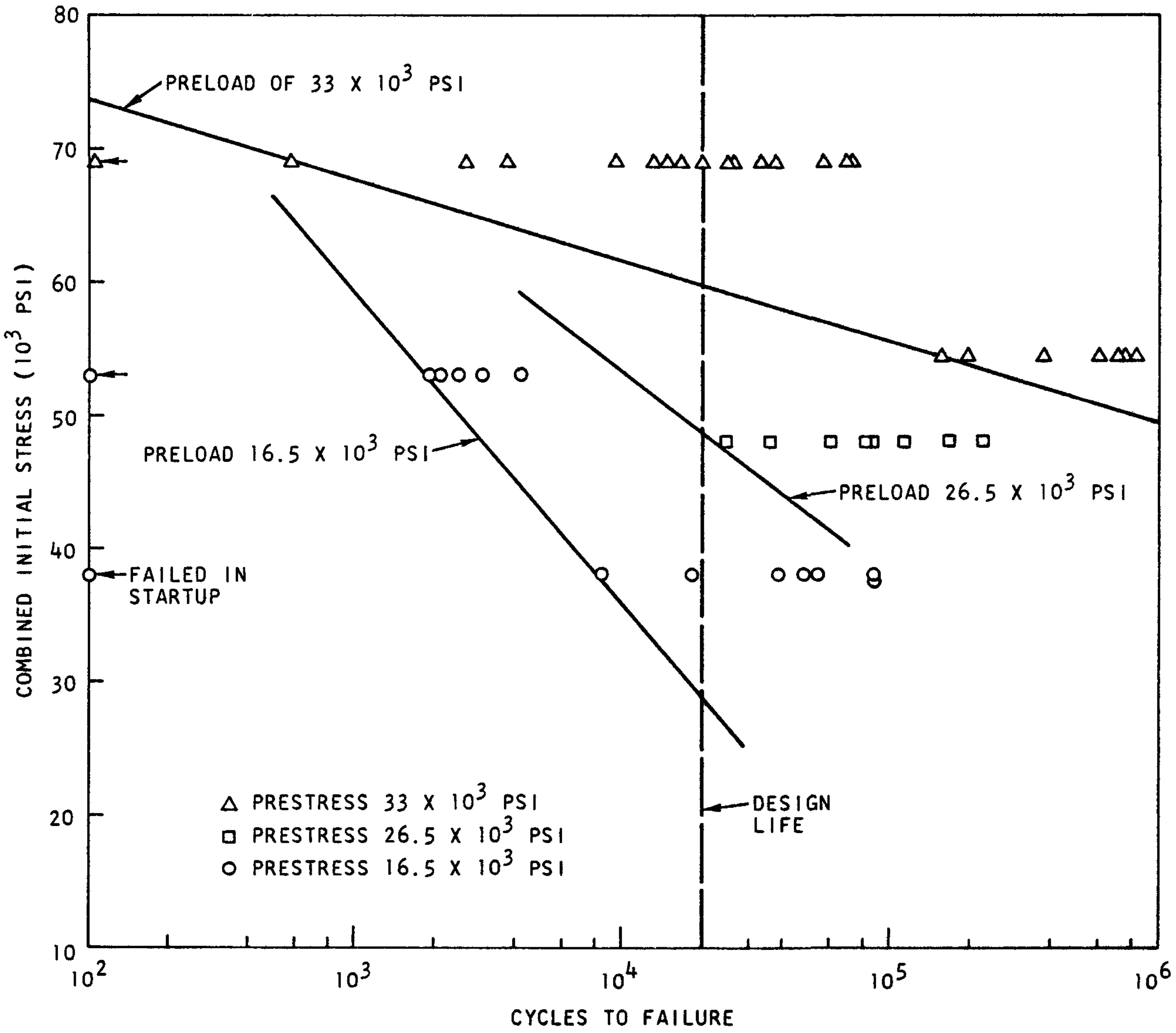

Fig. 1.8--Fatigue test data on 3/4-in.-diameter weld stud

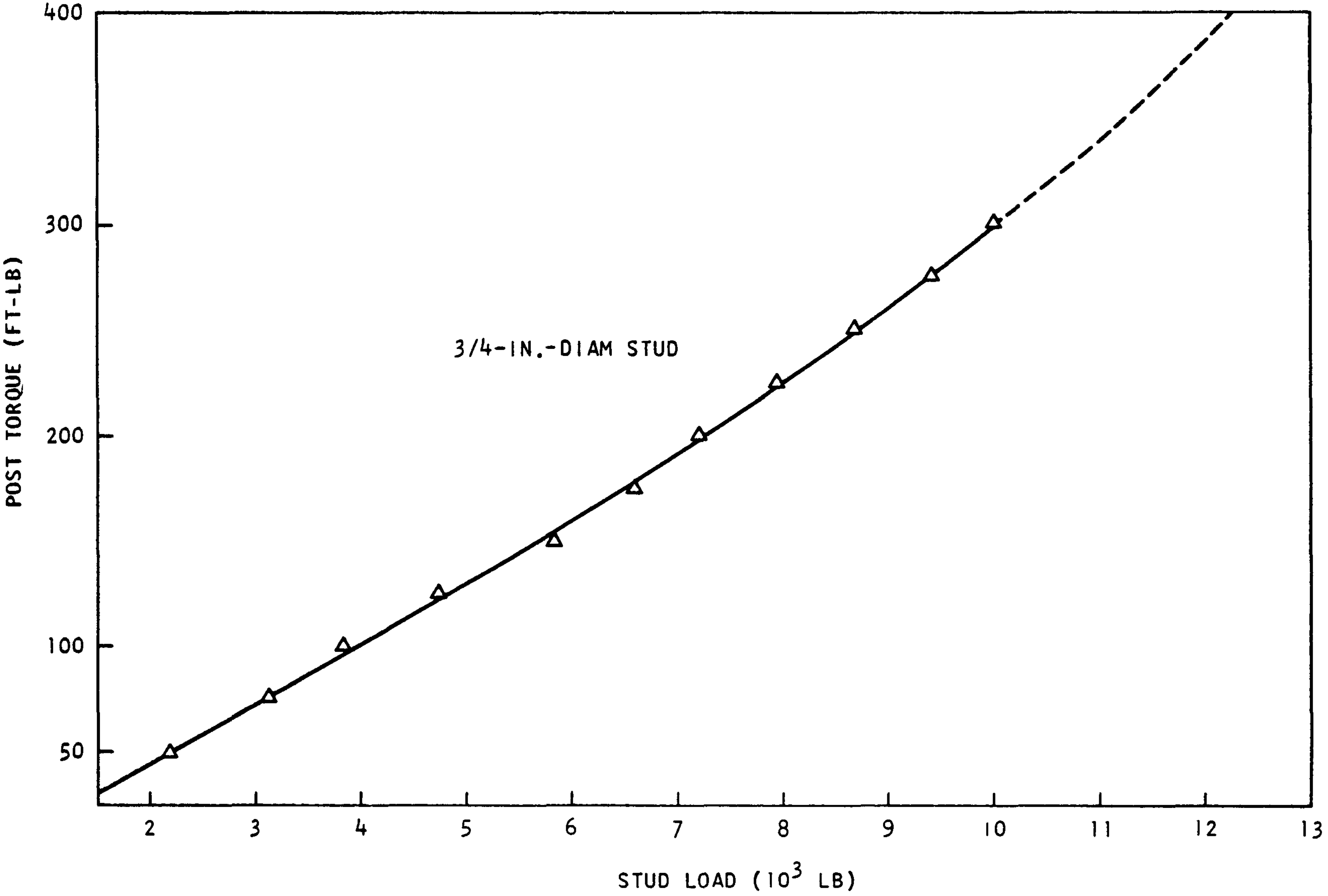

Fig. 1.9--Relationship between post applied torque and stud load, hot-rolled liner surface

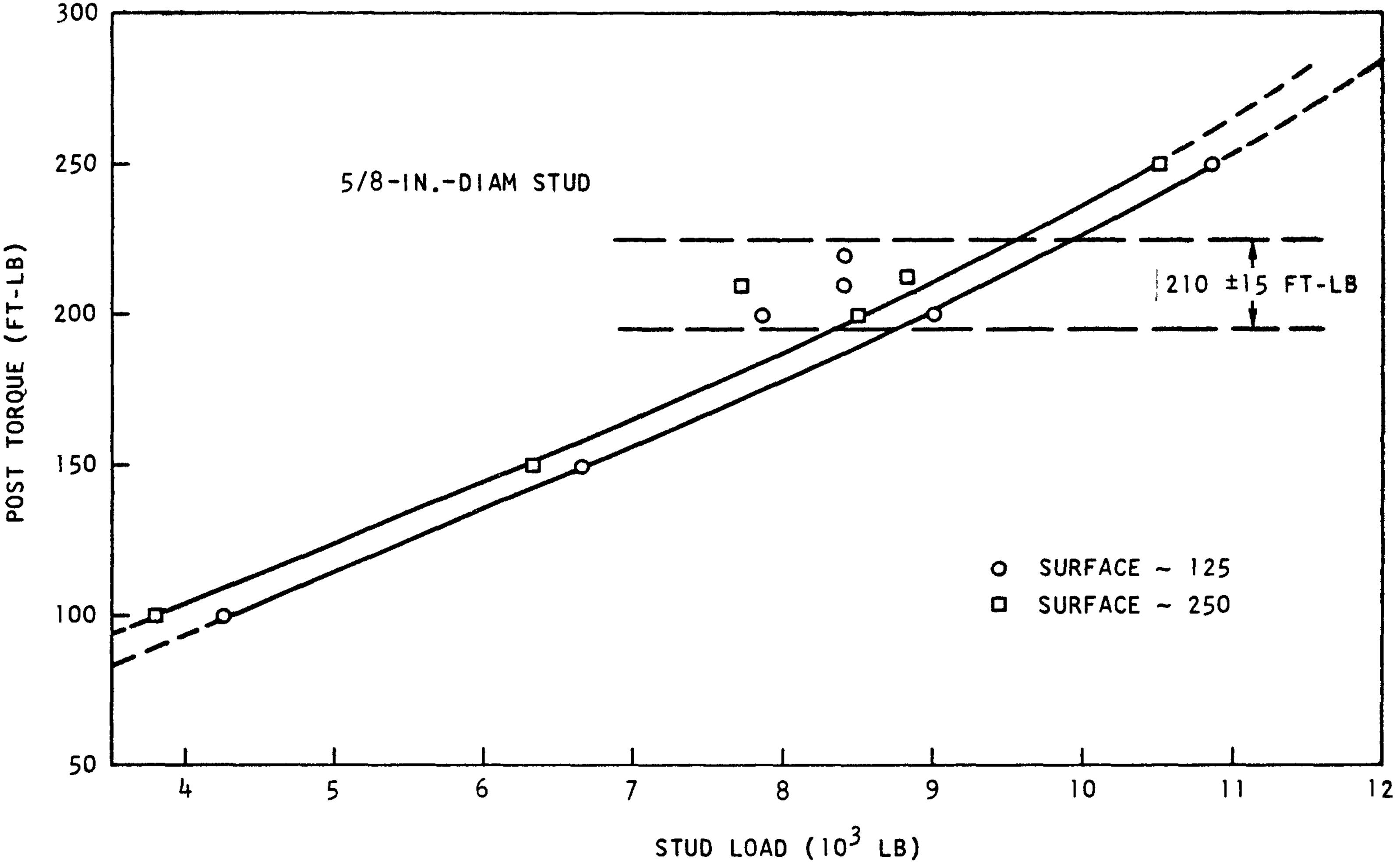

Fig. 1.10--Relationship between post applied torque and stud load, machined liner surface

A series of tests carried out on 3/4-in.-diameter stud, with the posts torqued down to 300 ft-lb on both a flat and a curved surface showed a sharp drop in the number of cycles to failure in the case of the curved surface (see Fig. 1.11).

The failure of all 3/4-in.-diameter studs occurred at the weld, as shown in Fig. 1.12, whereas the failure of all 5/8-in.-diameter studs occurred in the shank or in the thread.

Eight studs of each size were subjected to microscopic examination, and it was observed that the 5/8-in.-diameter studs were essentially free of voids, porosity, and inclusions but that in some cases the 3/4-in.-diameter studs had well-defined dendritic structures suggesting that the weld had cooled too fast and in one case had a large void and a slag pocket. Neither of these faults were easily detectable by the standard nondestructive testing procedures applicable to inspection of weld studs.

The posts used in the test rig were subjected to several separate stud fatigue tests, and some of them failed as shown in Fig. 1.13 at the wall thickness transition point (see Fig. 1.5). The lowest number of stress cycles achieved was 315 x 10^3 for a post on a 3/4-in.-diameter stud and 422 x 10^3 for a post on a 5/8-in.-diameter stud.

Conclusions. From the test results it can be concluded that a 3/4-in.-diameter stud cannot be welded on to a vertical surface so as to guarantee an acceptable fatigue life. However, a 5/8-in.-diameter stud can be welded sufficiently well for the fatigue life of the weld to be superior to that of the stud itself. It can also be seen that by increasing the degree of prestress, the stud is able to withstand a higher applied bending moment over the design life of 20,000 cycles.

With a 5/8-in.-diameter stud prestressed at 40 x 10^3 psi onto a flat surface, a load of ±1650 lb would be the lowest to cause failure after 20,000 cycles when applied on a moment arm of 4-3/8 in. (i.e., a moment of 7.2 x 10^3 lb-in.). The combined stress due to this moment and the prestress tensile load is 72 x 10^3 lb-in.^{2}, which indicates that the stud is yielding during the first few cycles and that the prestress is relieved to the point where the stud is then being cycled below its yield stress.

As previously stated, the maximum applied bending moment that the stud would be required to stand is 6.4 x 10^3 lb-in. over 20,000 cycles. This would result in a minimum life of 55,000 cycles based on the fatigue test results, and ignoring the following conservative assumptions already made in the analysis.

1. Lower creep rate of Kaowool than the tests indicate.
2. Higher coefficients of friction than the tests indicate.
3. The basic assumption that the condition giving highest stresses should be set up during the first few reactor temperature cycles and should in no way be relieved throughout the reactor life by further Kaowool creep or redistribution of friction loads.

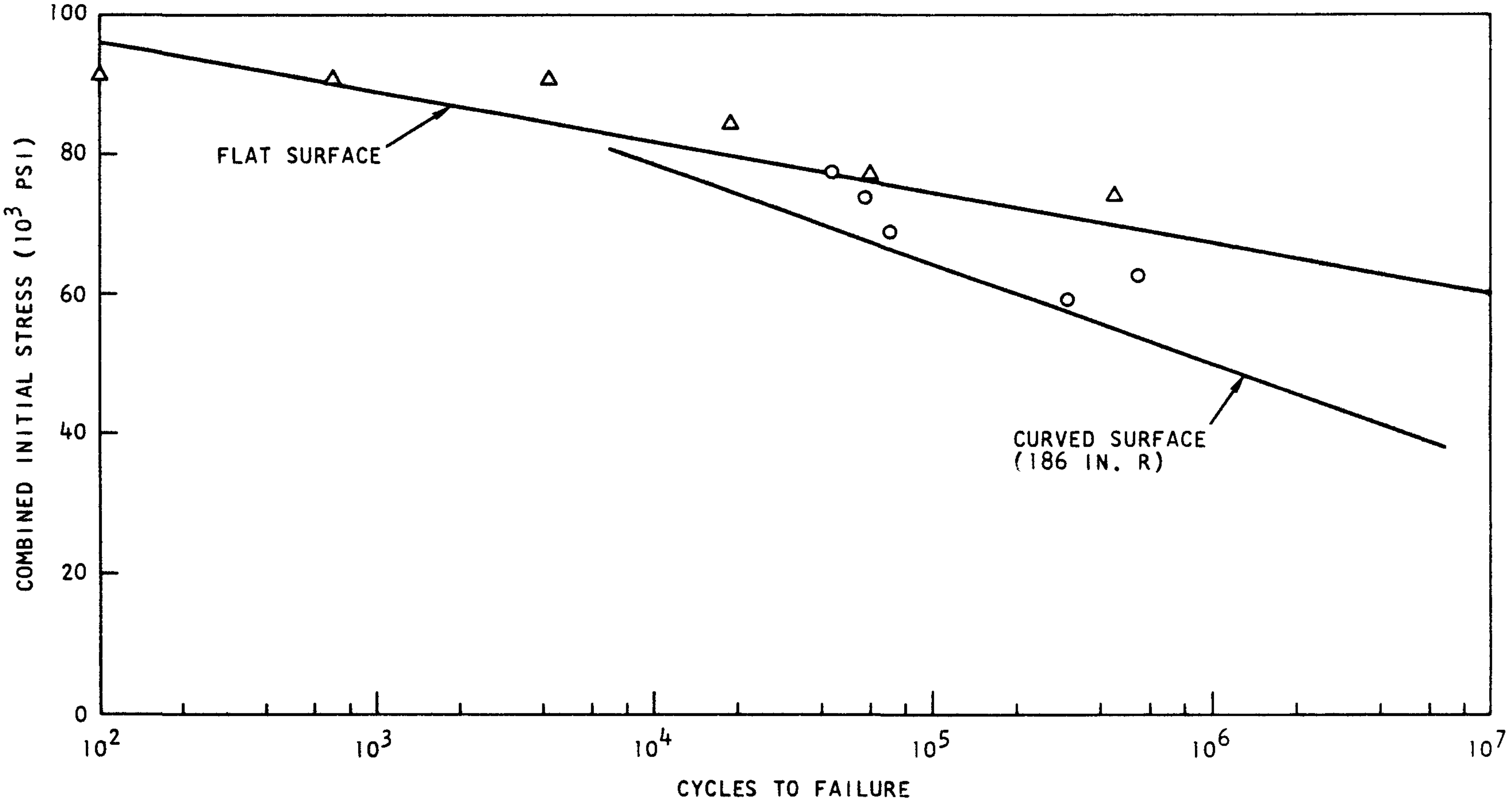

Fig. 1.11--Comparison of fatigue life against flat and curved liner surface

Fig. 1.12--Typical failure of 3/4-in.-diameter stud

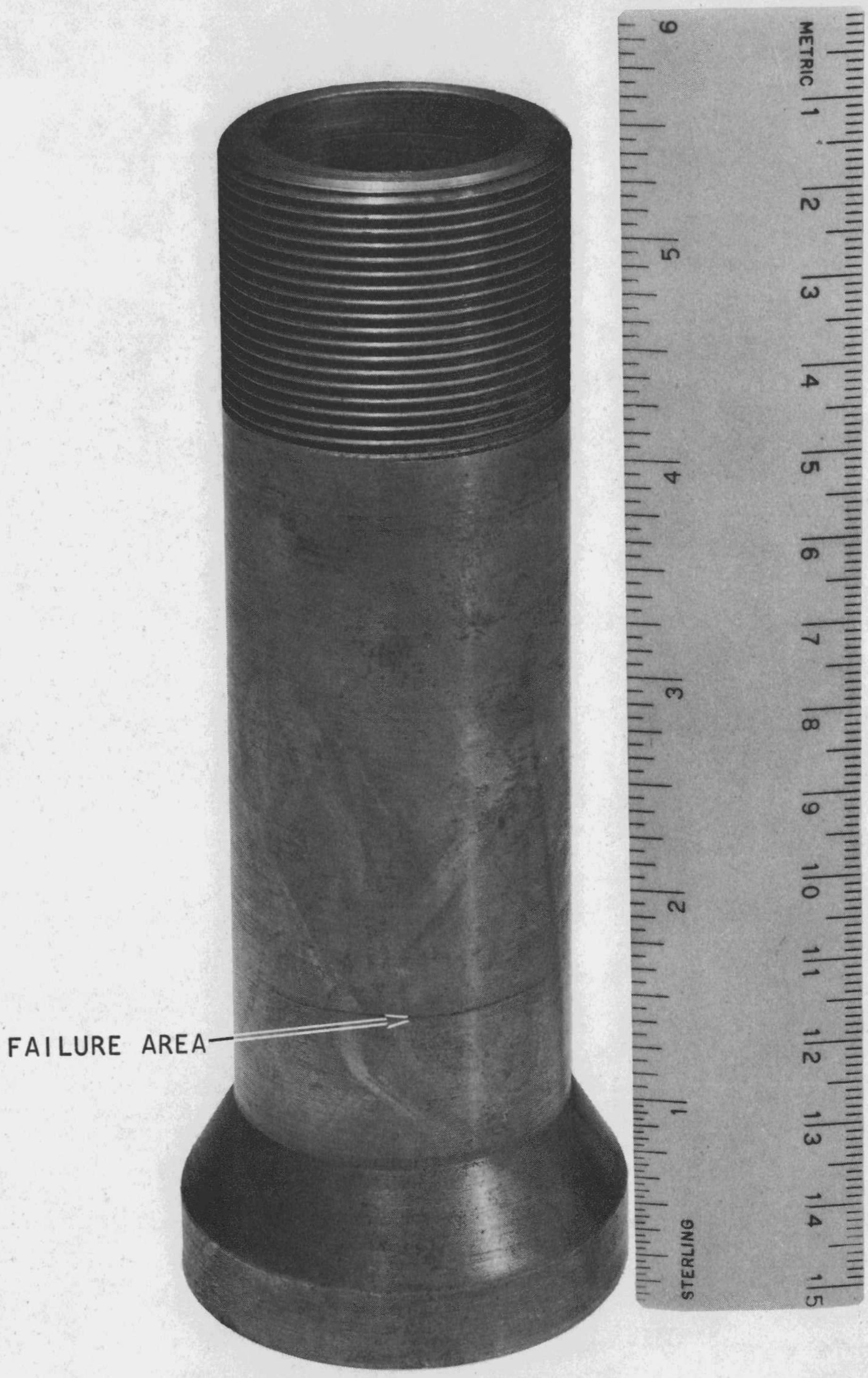

Fig. 1.13--Typical failure at wall thickness transition point (see Fig. 1.5)

The test program showed that the attachment fixture based on the post used in this test is satisfactory for the intended application. This post should be torqued onto a 5/8-in. weld stud to give a prestress of 40 x 10^3 psi, and the post should be seated onto a flat surface.

INSTRUMENTATION AND ELECTRICAL

The objective of this subtask is to develop sensors for measuring core outlet gas temperatures and moisture detectors and electrical penetrations, and to establish their operating characteristics, reliability, and maintainability in the plant by means of analysis and testing in helium, at temperature and, where analysis and/or preliminary tests indicate a necessity, at pressure and other environmental conditions.

Core Outlet Gas Thermometers

The thermal cycling of eight thermocouples between 1470° and 1650°F at the rate of 12°F/min was concluded. Two Chromel/Alumel thermocouples accumulated a total of 18,955 full cycles (temperature rise and drop). Three pairs of Geminol thermocouples accumulated 18,955, 6,582, and 3,234 full cycles. Calibration and metallurgical analysis of the test thermocouples was initiated.

AUXILIARY EQUIPMENT AND SPECIAL TOOLS

The objective of this subtask is to establish the suitability of the manipulators and tools, and the reactor viewing device for use in the plant by means of analysis and full-scale testing.

The heating test of the reactor viewing device was completed. The tests were performed on a Cohu Series 2500 miniature radiation resistant television camera that has a rated maximum continuous operating temperature of 131°F. The ambient temperature that the camera will be subjected to during use is 250°F, and as a result, cooling will be necessary. The camera will be cooled by means of a flow of helium originating outside of the reactor and flowing through a long, small-diameter flexible metal hose. Because of the limitations imposed by the length and size of the hose, the amount of cooling available is limited. The purpose of this test was to determine the camera's maximum operating temperature and the effect on camera performance of extended operation at this temperature.

The measure of the camera's performance in these tests was the visual quality of a standard test pattern transmitted by the camera to the monitor. The picture quality was determined by counting the lines of resolution and shades of gray distinguishable on the monitor in both the horizontal and vertical direction.

The tests were conducted with the camera mounted inside an autoclave, the test pattern being observed through a window in the wall of the autoclave. The camera was subjected to a nitrogen environment during the test to simulate the nitrogen environment within the camera's sealed housing during actual reactor viewing operations. The temperature of the camera was monitored by thermocouples mounted directly on the camera.

The test program was performed in two parts. The objective of the first part of the test was to determine the effect of temperature on picture quality. In the test, the temperature of the camera was raised in 10°F increments with the picture quality determined and recorded at each temperature increment. The results of this part of the test are shown plotted as a function of temperature in Figs. 1.14 and 1.15. Figures 1.16 through 1.22 are photographs of the monitor showing the gradual degradation of picture quality as the temperature increases.

The second part of the test was to determine the effect of extended operation at temperature. For this portion of the test the camera was maintained at a temperature of 200°F for a continuous period of 48 hr. During the 8-hr day shift, readings were taken at hourly intervals. No readings were taken in the intervals between the day shifts. The results of this part of the test are shown plotted as a function of time in Figs. 1.23 and 1.24.

As the temperature began to have a noticeably degrading effect on the picture, it was possible to partially restore the picture quality by adjusting the camera controls. This was done each time readings were made with a reading being taken both before and after the adjustment. The effects of these adjustments are indicated on Figs. 1.14 and 1.15 and on 1.23 and 1.24.

A study of Figs. 1.14 and 1.15 indicates that the first temperature effects occur at 140°F on the vertical resolution. A 152°F general picture deterioration becomes noticeable, and gradual deterioration of quality occurs from that point on. Up to a temperature of 200°F the deterioration of both the vertical and horizontal resolution can largely be restored by camera adjustment. The deterioration of discernible shades of gray can also be restored, but to a smaller degree. This results in a "washed out" picture as shown in Fig. 1.21. Beyond 200°F the resolution quality has deteriorated below the level at which the picture could serve a useful purpose.

The criteria for picture quality are that the resolution should be a minimum of 500 lines per inch in the vertical and 700 lines per inch in the horizontal, and the shades of gray discernible should be six in both the vertical and horizontal. Based on these criteria, a good picture can reliably be obtained with the camera operating in an environment of up to 170°F. Although the results plotted in Figs. 1.14 and 1.15 indicate that these criteria can be met at 200°F, the results obtained at 190°F would indicate that the picture quality is unreliable in this temperature range.

The results plotted in Figs. 1.23 and 1.24 indicate that at 200°F, the picture quality tends to deteriorate with time but that it can be restored by adjusting the camera controls. The net result over a 48-hr period is that continuous operation of the camera at 200°F over a 24-hr period has a negligible net effect on picture quality. At the end of the 48-hr test, when the temperature was restored to room conditions, the picture quality reverted to its initial quality, indicating that operation at temperature has no lasting effect on picture quality.

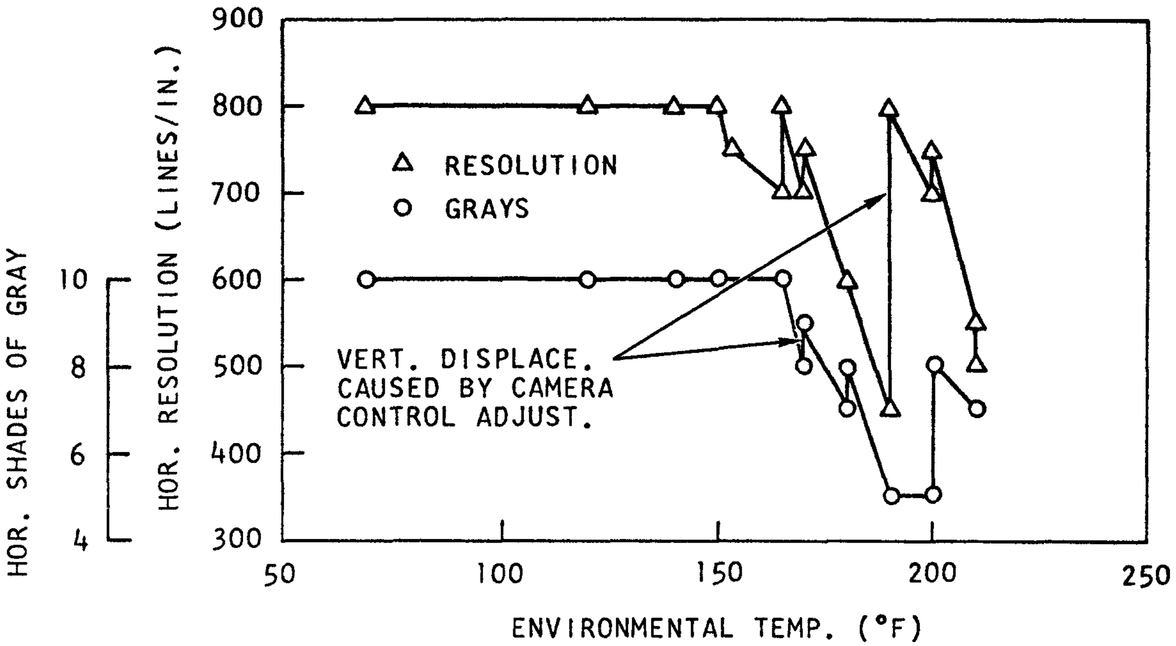

Fig. 1.14--Horizontal resolution and shades of gray versus environmental temperature

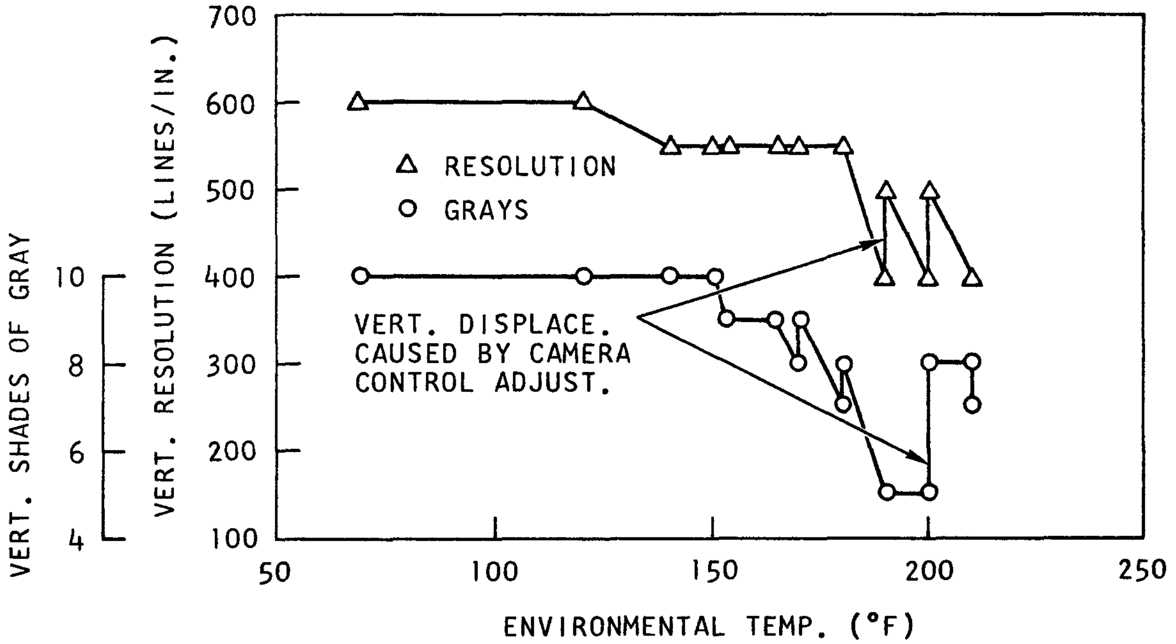

Fig. 1.15--Vertical resolution and vertical shades of gray versus environmental temperature

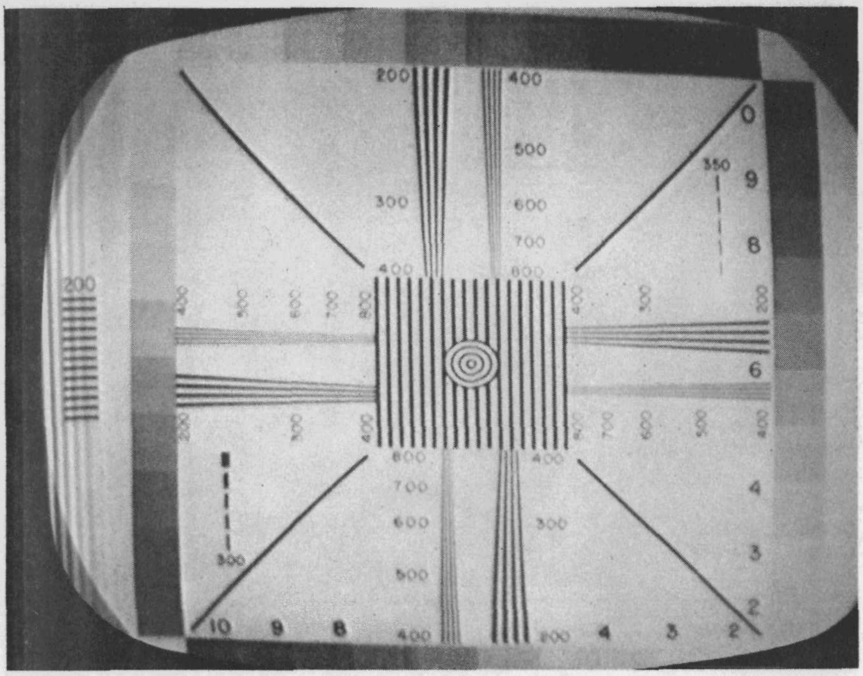

Fig. 1.16--Reference photo at 68°F; best obtainable picture at start of test

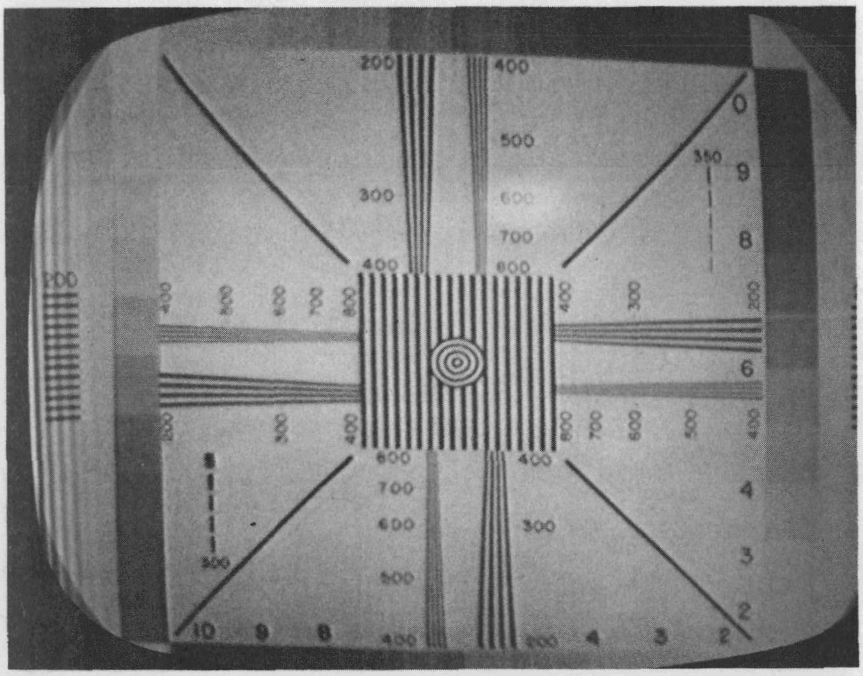

Fig. 1.17--Best picture obtainable at 120°F; no adjustment of controls required

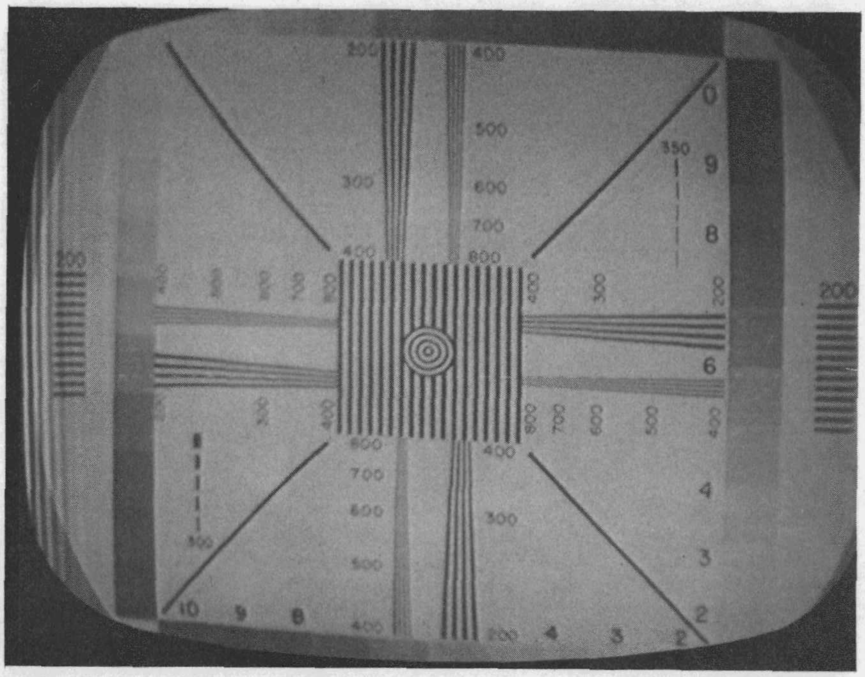

Fig. 1.18--Best picture obtainable at 165°F; sensitivity was decreased to restore resolution and grays

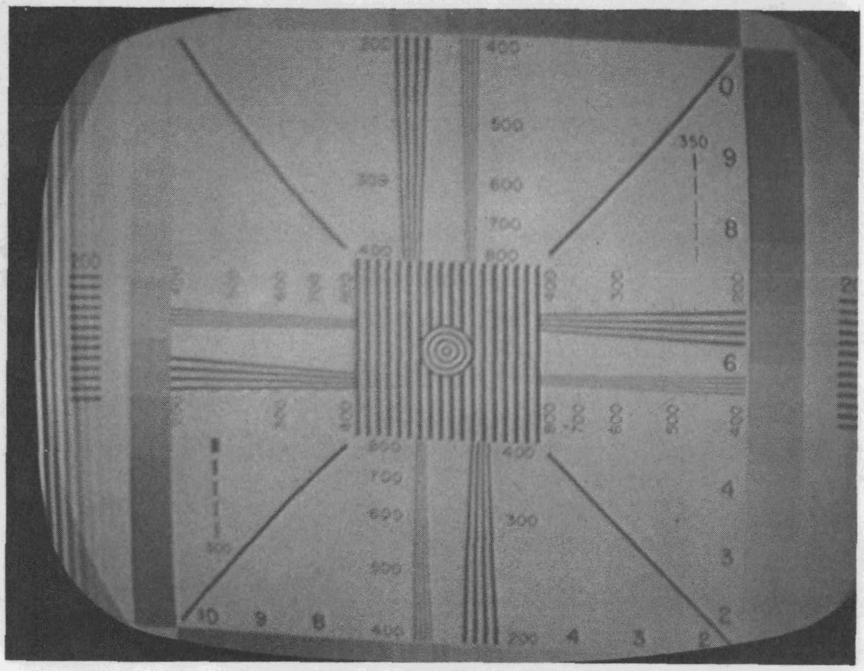

Fig. 1.19--Best picture obtainable at 170°F; sensitivity was reduced to improve resolution and grays

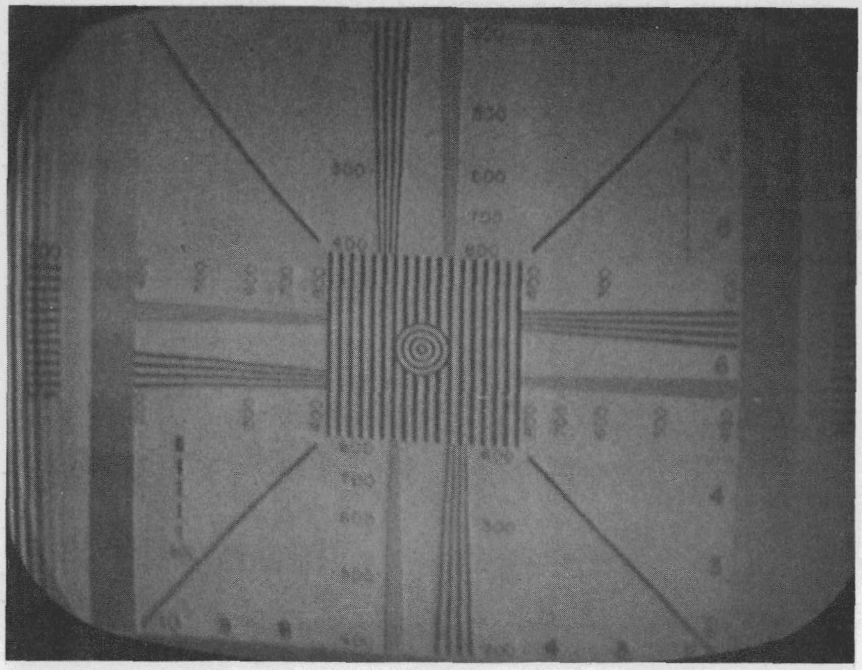

Fig. 1.20--Best picture obtainable at 190°F; sensitivity adjustment improved resolution but did not affect number of grays

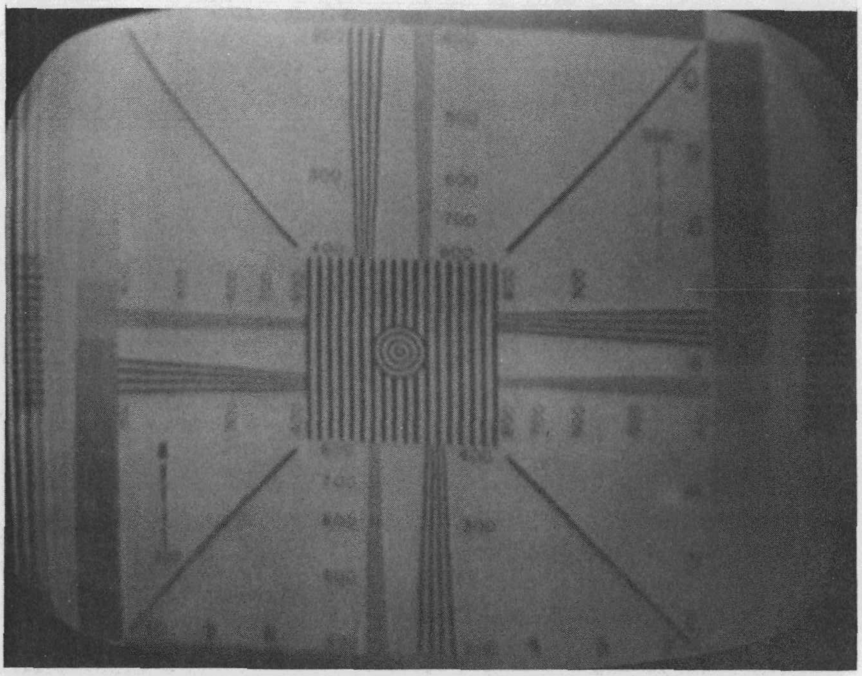

Fig. 1.21--Best picture obtainable at 200°F; gain was adjusted and effected a significant improvement. Note dark area beginning on right side of screen

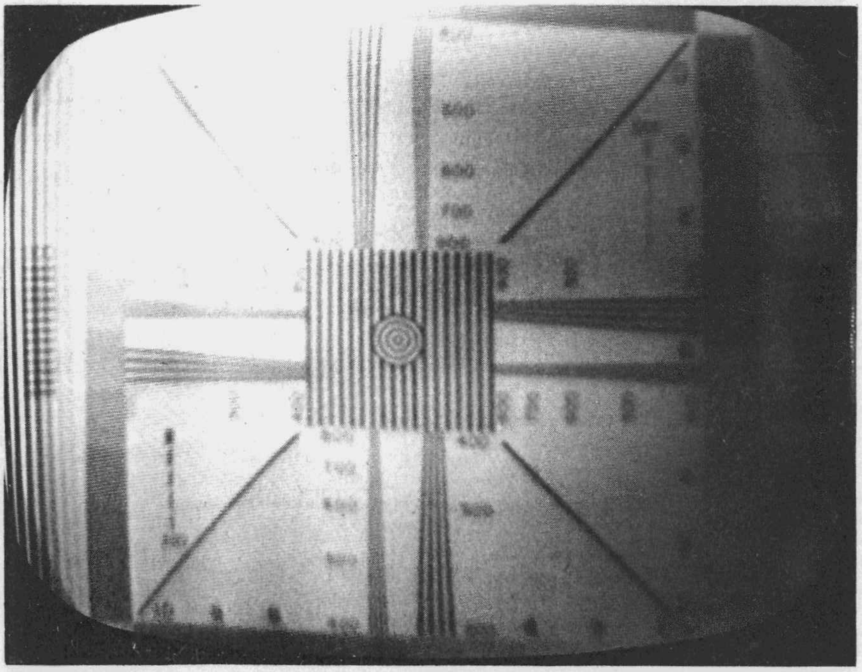

Fig. 1.22--Best obtainable picture at 210°F; adjustment to all controls caused loss of resolution. Note increased size of dark area at right

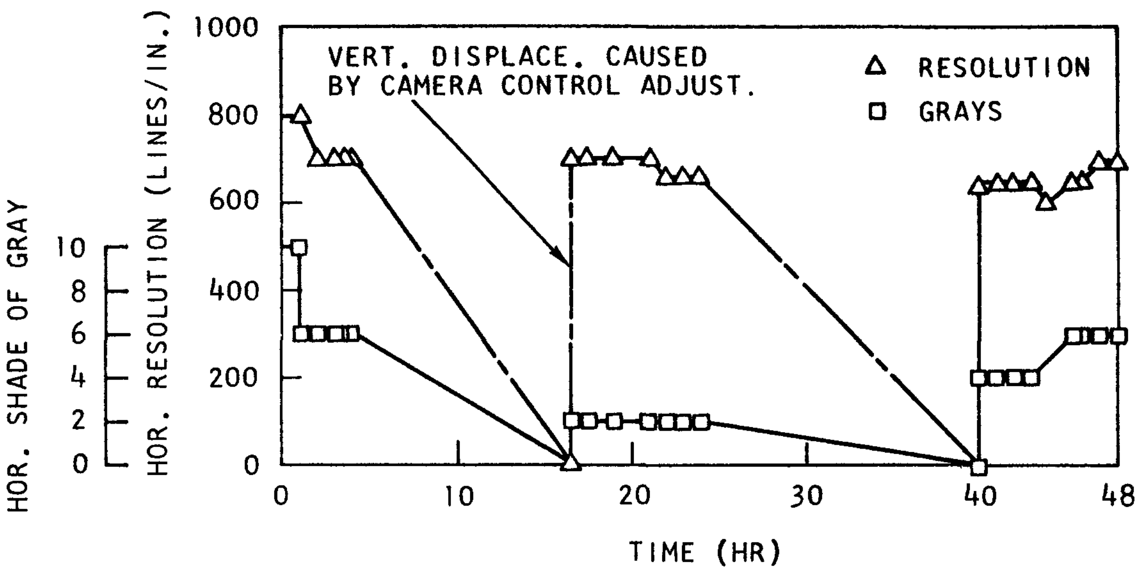

Fig. 1.23--Horizontal resolution and horizontal shades of gray versus time at 200°F

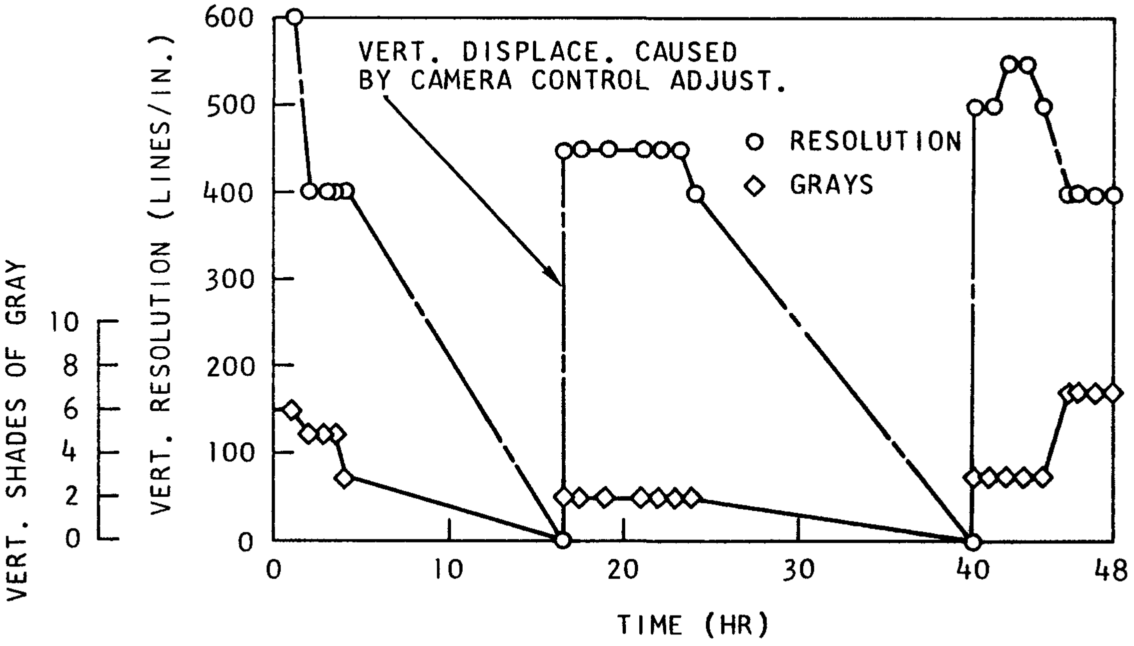

Fig. 1.24--Vertical resolution and vertical shades of gray versus time at 200°F

It was concluded from this test that the camera can reliably transmit a good quality picture over extended periods of continuous operation while operating in a nitrogen atmosphere at a temperature of 170°F and that up to a temperature of 200°F a good picture can be transmitted but with less reliability.

The tests to determine the friction factor of the flexible metallic hose to be used for the reactor viewing device cooling system were completed during the quarter. The results confirm the calculated friction factor.

The test model of the reserve shutdown vacuum tool was completed and installed in the test rig; the preparation and installation of test rig hardware is nearing completion.

RESERVE SHUTDOWN SYSTEM

The objective of this subtask is to determine the most suitable means for providing reserve shutdown capability in the plant, and to establish the basic data needed for detailed design of the system.

A test program is under way to establish the fragmentation characteristics of graphite rupture disks for the reserve shutdown system and also the free-fall characteristics of the absorber material.

As previously reported, a more dense material is to be tried for the rupture disk in order to minimize leakage through the disk. This material has been received, but a change of the absorber material from granules to boronated graphite spheres has held up further testing pending receipt of graphite spheres.

ORIFICING MECHANISM

The objective of this subtask is to develop an orifice valve and mechanism for controlling the inlet coolant flow to the reactor core.

Tests on the rotary orifice valve and its control mechanism have continued in parallel with the control rod drive test. At shutdown of the control rod drive tests the valve mechanism had performed 1710 open-closed-open cycles which exceeds the test requirement by some 200%. When the valve and control mechanism were disassembled there was no evidence of wear or deterioration.

A redesigned valve with reduced bypass flow leakage and a corresponding drive mechanism is currently under construction and will be tested, also in conjunction with the control rod drive test.

References

1. Jones, G., Material Properties of Fibrous Insulation Materials Considered for the PSC Thermal Barrier, USAEC report GAMD-9074, Gulf General Atomic, to be published.

Task II

NUCLEAR ANALYSIS

FUEL CYCLE ANALYSIS

The objective of this subtask is to establish the fuel management program for the reactor based on analyses of the effects of the loadings in the initial and replacement segments, including recycle segments in an equilibrium core, on local power generation, reactor control, reactor safety, and economics.

Status of Nuclear Design

Initial core loadings and fuel zoning for Reference Design 7 are specified. The results of this design iteration will lead to the specification of fuel particles.

Significant improvements have been achieved in coupling the nuclear analysis codes with thermal design codes and in evaluating the nuclear design with respect to compatibility with coolant flow and steam generator design.

Cross-section Evaluation for Reference Design 7

The effective cross sections for most of the nuclides of interest in the HTGR design depend only on the neutron energy spectrum. The reactivity worth of those nuclides can be computed with sufficient accuracy for design purposes by the use of multigroup (<10) calculations. A major exception is Th^{232}, whose resonance structure in the epithermal energy range requires sophisticated methods to evaluate effective cross sections that take into account self-shielding of absorber lumps (fuel rods) and self-shielding due to the grain structure of the fuel. The GAROL code (Ref. 1) is used primarily to determine effective cross sections in the resonance region.

The main, nonfissile absorber in the reactor is Th^{232}. In the initial core, about 30% of the neutrons are absorbed in thorium; 66% of the thorium absorptions occur in the resonance region. An accurate knowledge of the effective capture cross section and its temperature and time dependence is therefore essential to predict and determine the initial core excess reactivity and reactor lifetime behavior.

In the previous quarterly report (GA-8879) the effect of the fuel grain structure and the presence of hydrogen in the fuel rods on the effective thorium resonance integral were discussed in detail. Further investigations of the sensitivity of thorium resonance cross sections against other design parameters have led to a final set of data that were used to generate a consistent cross section set for Reference Design 7.

Sensitivity of the Th Resonance Cross Sections. Summarized in Table 2.1 are a set of calculations that show the sensitivity of thorium cross sections to parameters that are essentially a function of the fabrication process. The first column is the base case. Note that for the other two cases, the total metal load in the system is kept constant. The model itself, which was described in the previous quarterly report, consists of a fuel- and moderator-bearing central region surrounded by an annular moderator region. The second case assumes an arbitrary reduction of the carbon density in the fuel rod by 10%. This variation might be due to fluctuations in average coating thickness or average coating graphite density, because of differences in either matrix volume fraction or density (or both). The calculations indicate a 1.5% reduction of the effective Th resonance integral, compared to the reference case. The third case assumes an arbitrary increase of the effective thorium density in the grains by 2%. At a given metal load, this reduces the grain volume fraction in the rod. The Th resonance integral is reduced by only 0.07%, a negligible amount.

Table 2.1

Th RESONANCE CROSS-SECTION SENSITIVITY STUDY

	Reference Case	Rod Carbon Density -10%	Th Density in Grains +2%
Fuel Region:			
Grain diameter, μm	380	380	380
Mean chord length, cm	1.27	1.27	1.27
Dancoff factor	0.47	0.47	0.47
Volume fraction of grains	0.0976	0.0976	0.0958
Th density in grains, atoms/b-cm	1.948×10^{-2}	1.948×10^{-2}	1.986×10^{-2}
U^{235}	8.543×10^{-4}	8.543×10^{-4}	8.709×10^{-4}
U^{238}	7.00×10^{-5}	7.00×10^{-5}	7.14×10^{-5}
Carbon	4.41×10^{-2}	4.41×10^{-2}	4.50×10^{-2}
Carbon between grains	6.543×10^{-2}	5.841×10^{-2}	6.529×10^{-2}
Average Th	1.902×10^{-3}	---	---
Average U^{235}	8.341×10^{-5}	---	---
Average U^{238}	6.839×10^{-6}	---	---
Average C	6.335×10^{-2}	5.701×10^{-2}	6.335×10^{-2}
Moderator Region:			
Mean chord length, cm	5.08	---	---
Carbon density	6.138×10^{-2}	---	---
Total Cell:			
Average Th	3.8085×10^{-4}	---	---
Average U^{235}	1.3755×10^{-5}	---	---
Average U^{238}	1.3677×10^{-6}	---	---
Average C	6.1776×10^{-2}	6.0509×10^{-2}	6.1776×10^{-2}
Th Resonance Integral	28.91	28.44 (-1.5%)	28.89 (-0.07%)

Variations in kernel metal density and carbon density in the fuel rods have to be expected. Present calculations indicate that ±5% variation in carbon density, obviously the more important parameter, will occur already because of different metal loading densities in the rod. The resulting reactivity uncertainty is in the order of 0.001 to 0.002 Δk.

Reference Cross-section Set. For the generation of the reference fast cross-section set, a series of assumptions has been made concerning cell geometry, particle size, and particle density, based on the present status and knowledge of the over-all design. These data are summarized in Table 2.2. The temperature of the fuel rod and the average thorium density in the rods were chosen as independent parameters. Figure 2.1 shows typical results for the thorium resonance cross section (0.18 Mev $\leq E \leq$ 17.6 ev) as a function of temperature and thorium density in the fuel rod.

Table 2.2

FIXED PARAMETERS FOR RESONANCE CALCULATION

Fuel Region:	
Fuel rod diameter, cm	1.27
Volume fraction of fuel rod in unit cell	0.20
Th density in grains, g/cm^3	7.503
U density in grains, g/cm^3	0.425
C density in grains, g/cm^3	0.880
Grain diameter, μm	400
Moderator Region:	
Outer diameter, cm	2.8398
Mean chord length, cm	5.08
Average carbon density, g/cm^3	1.24

For the thermal cross-section calculations, graphite scattering kernels were generated with the GASKET (Ref. 2) and HEXSCAT (Ref. 3) codes. The independent parameters used were C/U ratio and temperature.

The resulting cross-section sets are a function of four parameters: fuel temperature, Th^{232} density in the fuel rods, C/U ratio, and moderator temperature. In the design calculations, cross-section sets corresponding to a specific fuel composition and temperature are computed by interpolating between the basic data.

Reflector Cross Sections. Neutron energy spectra and the resulting effective carbon cross sections in all reflector regions were revised and updated. GAZE (Ref. 4) calculations (26-group) were performed to take the spatial variation of the spectrum into account. Figure 2.2 shows typical results for the epithermal neutron spectrum in various layers of reflector graphite above the core. The corresponding model, which was as close to the actual reflector geometry and composition as possible, is also given in Fig. 2.2.

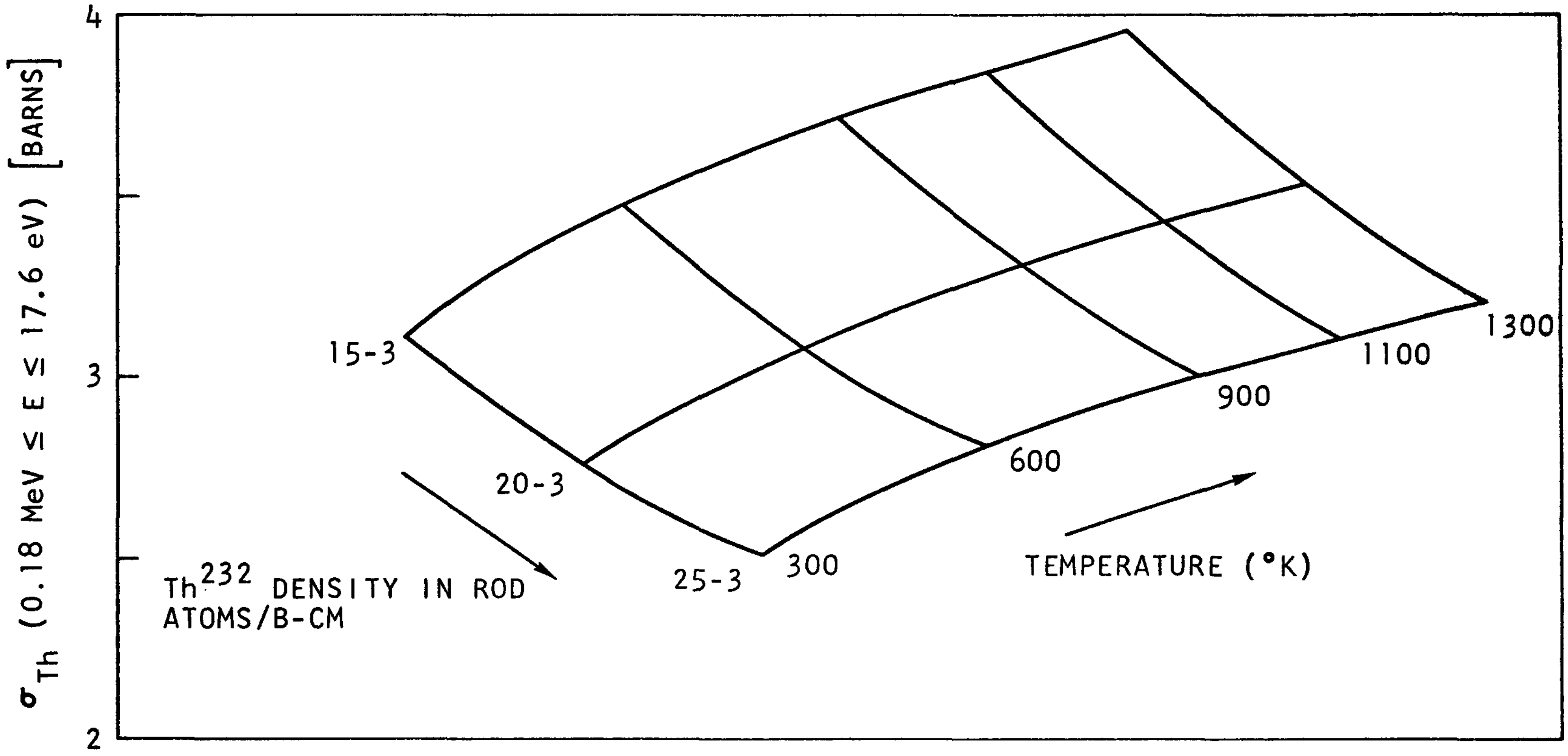

Fig. 2.1--Effective thorium capture cross section

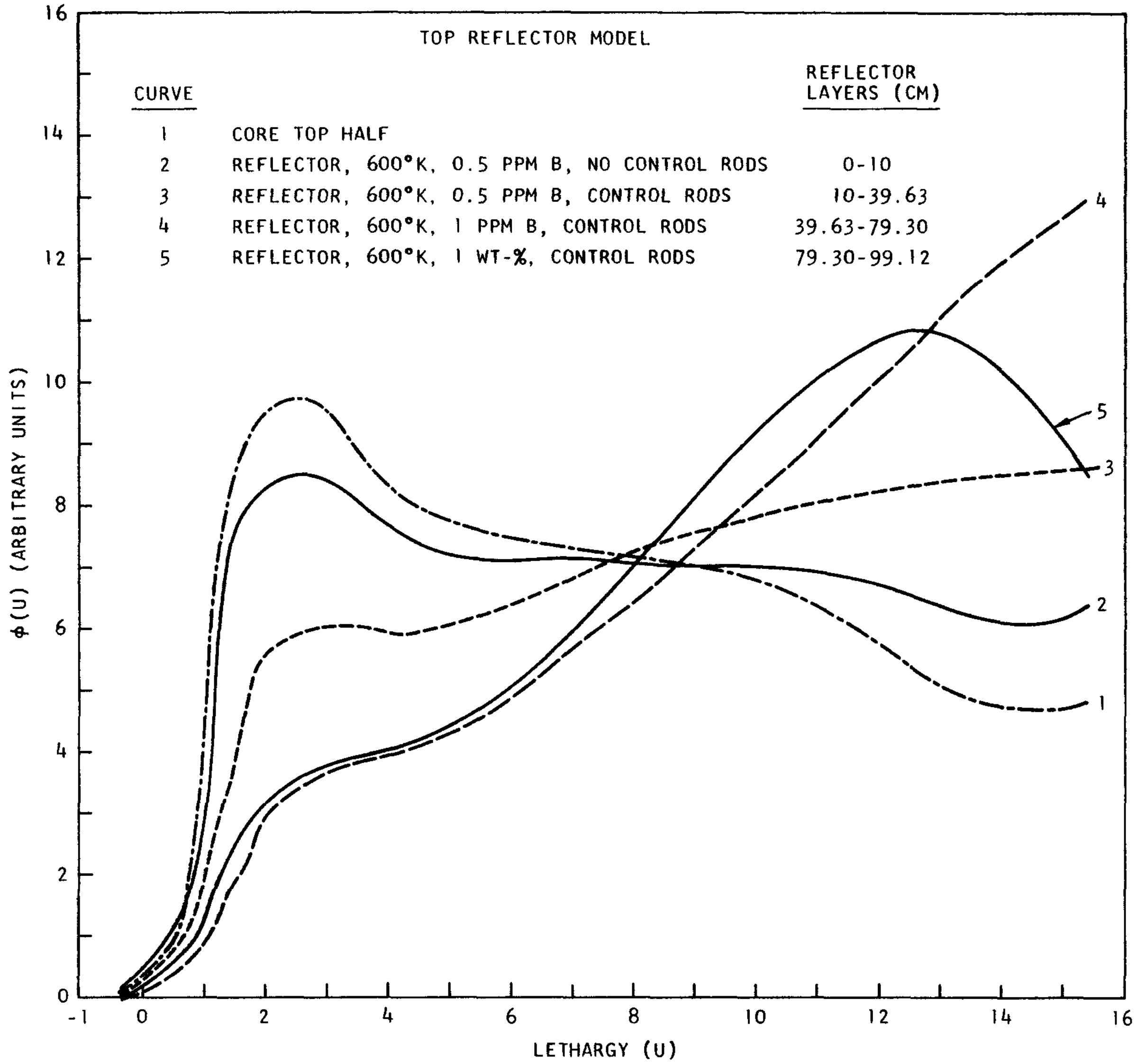

Fig. 2.2--Neutron spectra in top reflector layers

The hardest spectrum, of course, is obtained for the core region. The first 10 cm above the core were assumed to contain no rods. the average spectrum in this region is slightly softer than the core spectrum but has a shape similar to the core spectrum. In the successive layers considered the spectrum changes its general shape and softens more and more. It is primarily the transfer cross section which is affected by these spectrum changes. Previous calculations have shown, that proper treatment of the transfer cross sections is worth about 0.001 Δk in reactivity (see earlier quarterly report GA-7634).

FUEL ZONING AND POWER SHAPING

The objective of this subtask is to establish the fuel and burnable poison distribution and the control rod programming based on analyses of the transverse and axial power distribution as a function of fuel and poison loading, burnup, and control rod positions and considerations of fuel temperatures and economics.

Specifications of the radial and axial fissile and fertile material distributions for Reference Design 7 were completed. Total core loadings were updated and adjusted; the current best estimate of the initial core loading is given in Table 2.3.

Table 2.3

CORE LOADING FOR REFERENCE DESIGN 7

Uranium, kg(%):		
U^{234}	12.08	(1.1)
U^{235}	1,022.78	(93.15)
U^{236}	2.64	(0.24)
U^{238}	60.50	(5.51)
Total U	1,098.00	(100.00)
Thorium, kg	19,241	
Carbon, kg	163,220	
Silicon, kg	5,073	

Loading Distribution

The main difference between the fuel zoning for Reference Design 7 and Reference Design 6 is the extension of the buffer zone at the core reflector interface to encompass a complete fuel element rather than only four rows of fuel holes. The feasibility and implications of this concept were discussed extensively in the previous quarterly report (GA-8879). Refinement of the radial and axial fuel zoning scheme has continued, and the number of fuel compositions required to obtain proper fuel temperatures in the core was reduced to 13, compared to 16 in the last design iteration. Total uranium and thorium load per composition, loadings per fuel element, and the total number of elements per fuel type are summarized in Table 2.4. Each fuel composition consists of, at most, three types of fuel elements: normal fuel elements,

Table 2.4

FUEL LOADING SPECIFICATION INITIAL CORE
(Reference Design 7)

Fuel Type	Block Type[a]	No. of Elements	Loading per Element (g)		Total Load (kg)	
			U	Th	U	Th
1	FUEL	174	639	15865	123.2	3078
	CTRL	33	364	9086		
2	FUEL	174	493	14375	94.2	2748
	CTRL	22	281	8181		
	SCTL	11	209	6105		
3	FUEL	54	953	13502	56.3	798
	CTRL	9	542	7684		
4	FUEL	54	710	11648	41.6	684
	CTRL	6	404	6629		
	SCTL	3	301	4947		
5	FUEL	108	1126	13624	133.2	1611
	CTRL	18	641	7754		
6	FUEL	108	842	12021	98.8	1411
	CTRL	12	479	6842		
	SCTL	6	358	5105		
7	FUEL	72	1343	13579	110.5	1117
	CTRL	18	764	7728		
8	FUEL	72	1028	12220	83.6	994
	CTRL	12	585	6955		
	SCTL	6	438	5190		
9	FUEL	54	956	14820	56.5	876
	CTRL	9	544	8435		
10	FUEL	54	686	12449	40.2	731
	CTRL	6	390	7085		
	SCTL	3	291	5287		
11	FUEL	24	1094	15901	30.0	436
	CTRL	6	623	9050		
12	FUEL	24	921	13859	25.0	376
	CTRL	4	524	7887		
	SCTL	2	391	5886		
13	FUEL	288	666	14241	205.0	4381
	CTRL	30	379	8105		
	SCTL	6	283	6048		
					1098.1	19241

---

[a] FUEL = normal fuel element; CTRL = control rod blocks; SCTL = short control rod blocks.

control rod elements containing holes for control rods and the reserve shutdown system, and short control rod elements. The latter are partially fueled elements and are located at the bottom of each column of control rod elements. Figure 2.3 shows the distribution of the different fuel types in the core. It should be pointed out that in this design iteration all refueling regions are axially zoned. Only the outermost fuel zone, which is one block thick, is not axially zoned. Fuel types 1, 3, 5, 7, 9, and 11 belong to the top half and 2, 4, 6, 8, 10, and 12 belong to the bottom core half.

The number of lumped poison types stays unchanged at three. However, the diameter of the poison sticks was reduced by 0.025 in., at constant boron load, to reduce the reactivity swing during the initial two-year cycle. Table 2.5 summarizes the poison stick characteristics and their distribution within the initial core. No axial zoning is required for the lumped burnable poison.

Table 2.5

LUMPED BURNABLE POISON
(Reference Design 7)

Type	Poison Stick Diam. (in.)	Boron Conc. (g/cm^3)	Refueling Regions
1	0.375	0.0758	2,6,7,9,11,12,14,16,19
2	0.425	0.0688	24,27,30,31,34,37,20,23,26
3	0.375	0.0354	3,13,18,22,29,33

Depletion Analysis

The results of a preliminary depletion analysis of the initial core for Reference Design 7 are shown in Fig. 2.4. In these calculations an axially averaged core was used. Refueling region peaking factors are well within design limits at any time during the initial cycle. A significant difference between this design iteration and Reference Design 6 lies in the use of the control rod groups (see Table 2.6). The adoption of the one-block-thick buffer zone at the core-reflector interface resulted in a relatively low power density in the outer block rings. Insertion of the control rods into the outer refueling regions, as was done in Reference Design 6, pushes the power even further towards the center. However, the use of control rods in the third ring of regions for regulating purposes at full power gives a reasonably flat power distribution. It is believed that the new control rod sequence not only improves the power distribution but also improves the balance in the mixed-mean gas inlet temperature to the steam generators.

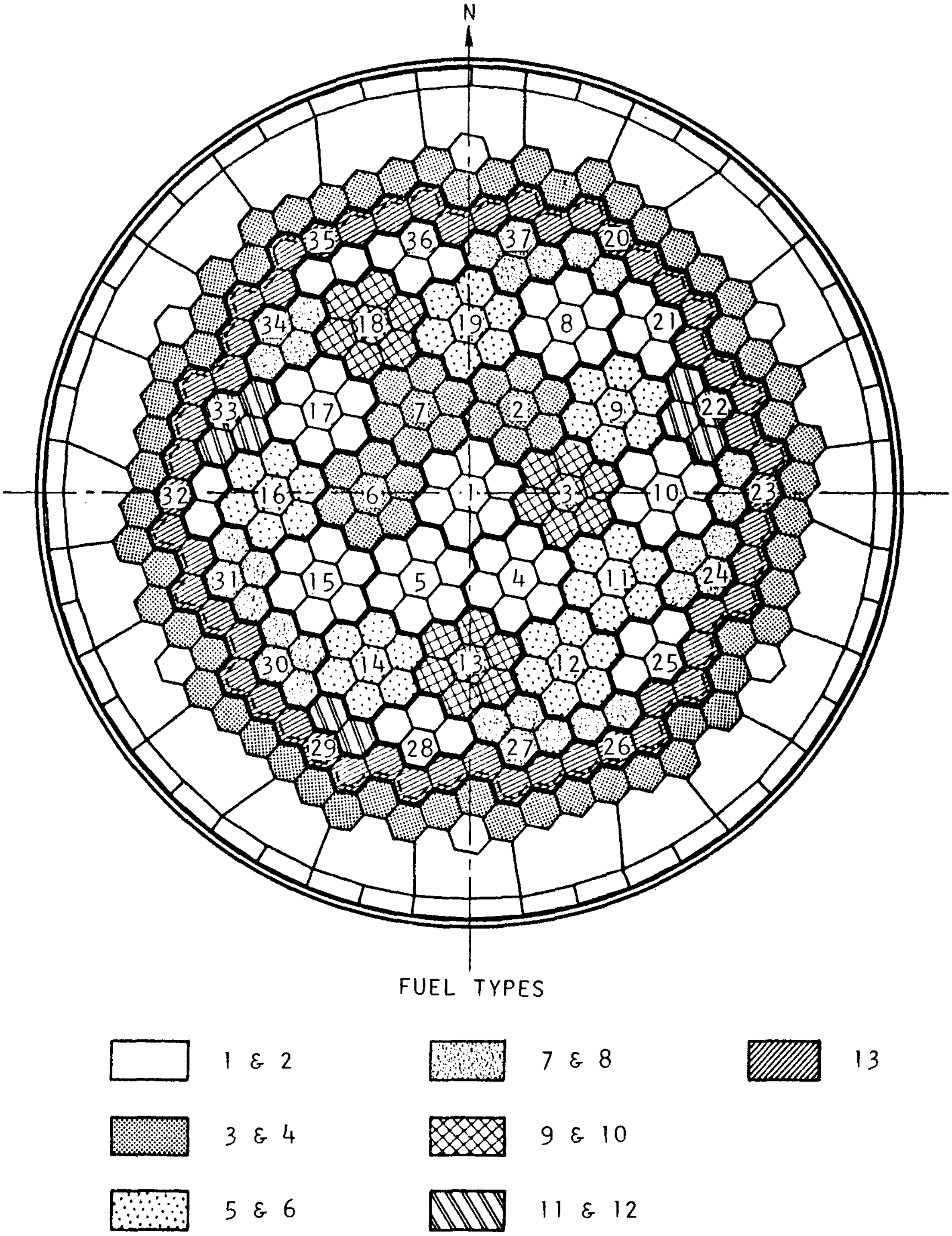

Fig. 2.3--Distribution of fuel types in core

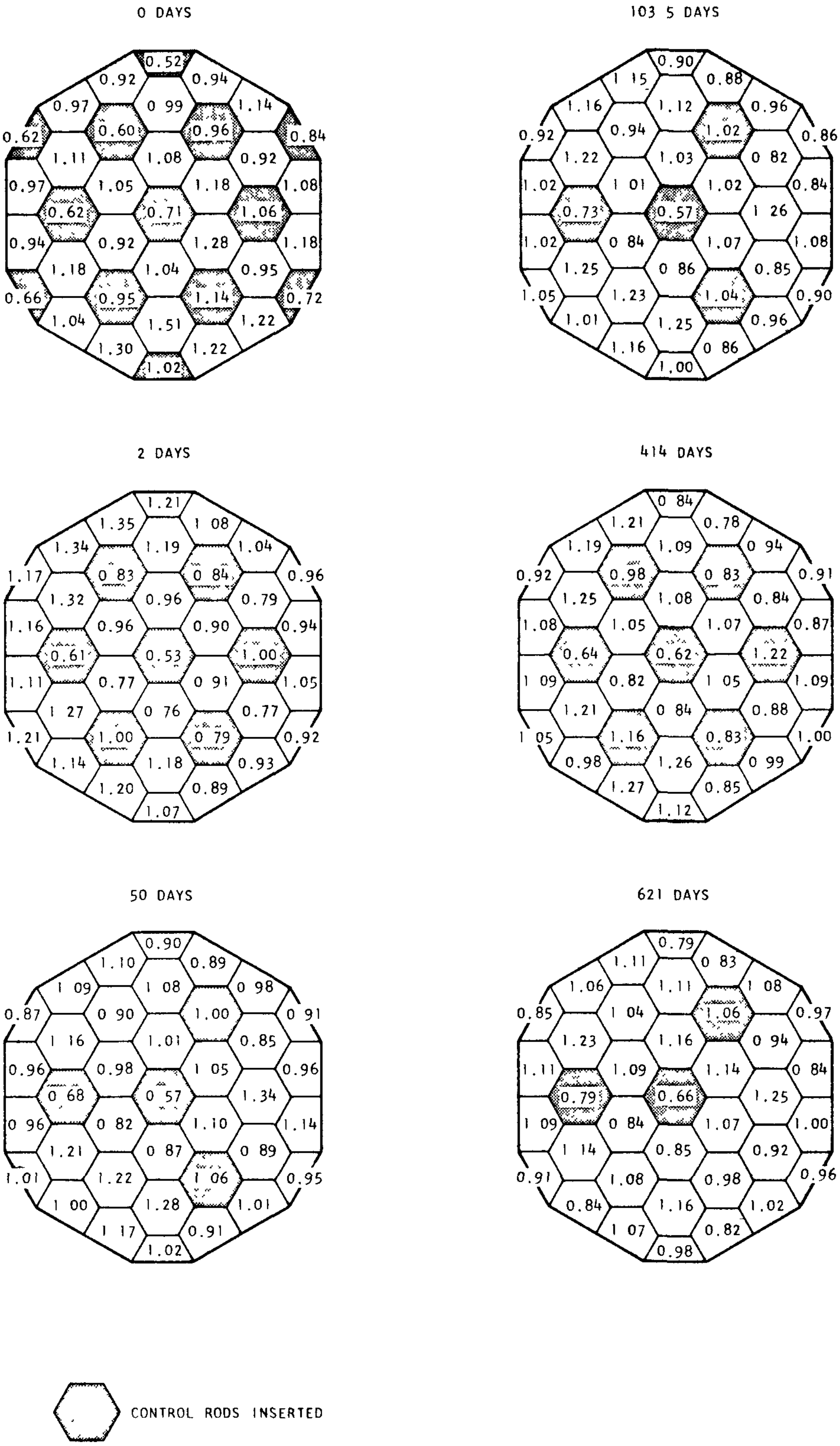

Fig. 2.4--Peaking factors versus time for Reference Design 7 initial core

Table 2.6

CONTROL ROD SEQUENCE
(Reference Design 7)

Bank No.	Rod Pair No.	Group[a]
1	1	1
2	11,15,19	3D
3	9,13,17	3B
4	23,29,35	4D
5	20,26,32	4A

[a] For definitions of rod groups see earlier quarterly progress report GA-8600.

Reactivity Effects in the Initial Core (Reference Design 7)

The loading estimates for Reference Design 7 include secondary reactivity effects, as far as they are known or can be estimated to date. In particular, the following differences between this and the last design iteration had to be compensated for:

1. Total core silicon load increased by about 700 kg, resulting from the adoption of more precise dimensions on particles and coatings. The core reactivity loss is about 0.001 Δk.
2. The average core carbon density dropped by about 0.5%, resulting in a reactivity loss of 0.001 Δk.
3. A more accurate estimate of the isotopic uranium composition was used: 1.1% U^{234}, 93.15% U^{235}, 0.24% U^{236}, 5.51% U^{238}. This compared with 93.5% U^{235} and 6.5% U^{238} used in previous calculations. The resulting reactivity loss is about 0.004 Δk.
4. The consideration of grain shielding effects had only a negligible effect. The prime reason is that different calculational methods had been used in the past. The difference between the effective thorium resonance integral (excluding grain effects) calculated by the GAM code, which was used in the past, and the GAROL code, which was used for this design iteration, is about the same as the difference for GAROL calculations with and without grains. Although the grain shielding effect itself is worth about +0.002 Δk, it had no effect on core loading adjustments.
5. In addition, 0.003 Δk is allowed for burnable and 0.002 Δk for nonburnable impurities (excluding hydrogen).

6. The presence of hydrogen in the fuel rod matrix increases the core reactivity by about 0.008 Δk. It is not yet known how fast this hydrogen is released during full-power operation.

Figure 2.5 shows the current estimate of the excess reactivity in the hot core as a function of time, a result of preliminary depletion studies for Reference Design 7 using nominal initial core loading data (excluding hydrogen). The minimum excess reactivity after 75 days is about 0.013 Δk. If the tolerances on core loading (±1% for thorium, uranium, and graphite) are all assumed to reduce the core reactivity, the minimum excess reactivity is reduced by 0.008 Δk, leaving an acceptable excess of about 0.005 Δk. If hydrogen is taken into account and the assumption is made that all the hydrogen stays in the reactor, the design goal of 0.03 Δk excess reactivity is exceeded. The same is true if all loading biases are such that the core reactivity is raised. In the latter case, core excess reactivity will be reduced by the addition of lumped poison.

Calculational Methods

As in previous design iterations, the depletion analysis for Reference Design 7 will be carried out with single-channel synthesis calculations. Although the nuclear portion of the synthesis package is essentially the same as described in quarterly reports GA-8725 and GA-8879, significant and important improvements have been made in the thermal analysis section of the SCANAL code.

The effects of crossflow (i.e., coolant flow through gaps from one refueling region to another within the active core section) have been found to be significant. As a result, old fuel regions have a skewed axial flow profile with a flow deficiency at the top of the core and a flow excess at the bottom. New fuel regions have a flat axial flow profile, but new regions with a peaking factor greater than 1.5 have a net over-all flow deficiency. The resulting flow distribution in the core is a significant factor in the magnitude and location of maximum fuel temperature.

The COPE code (Ref. 5), a portion of the single-channel synthesis package, has been modified to include a set of built-in empirical factors to account for crossflow effects. These factors were derived from detailed analytical flow distribution calculations.

A new subroutine was added to the SCANAL code to compute steam generator module inlet temperatures. Because of the tight coupling between core and steam generator flow and the sensitivity of steam generator service life against comparatively small variations in gas inlet temperature, a continuous survey of these parameters is necessary to assure proper plant performance.

It is understood that the methods used in the single-channel synthesis analysis to compute crossflow and the resulting fuel temperatures and steam generator module gas inlet temperatures are simplified and approximate. However, it is believed that this is the best way to evaluate the feasibility of control rod programs and over-all core power distribution. A detailed and sophisticated flow and temperature analysis still has to be performed, but

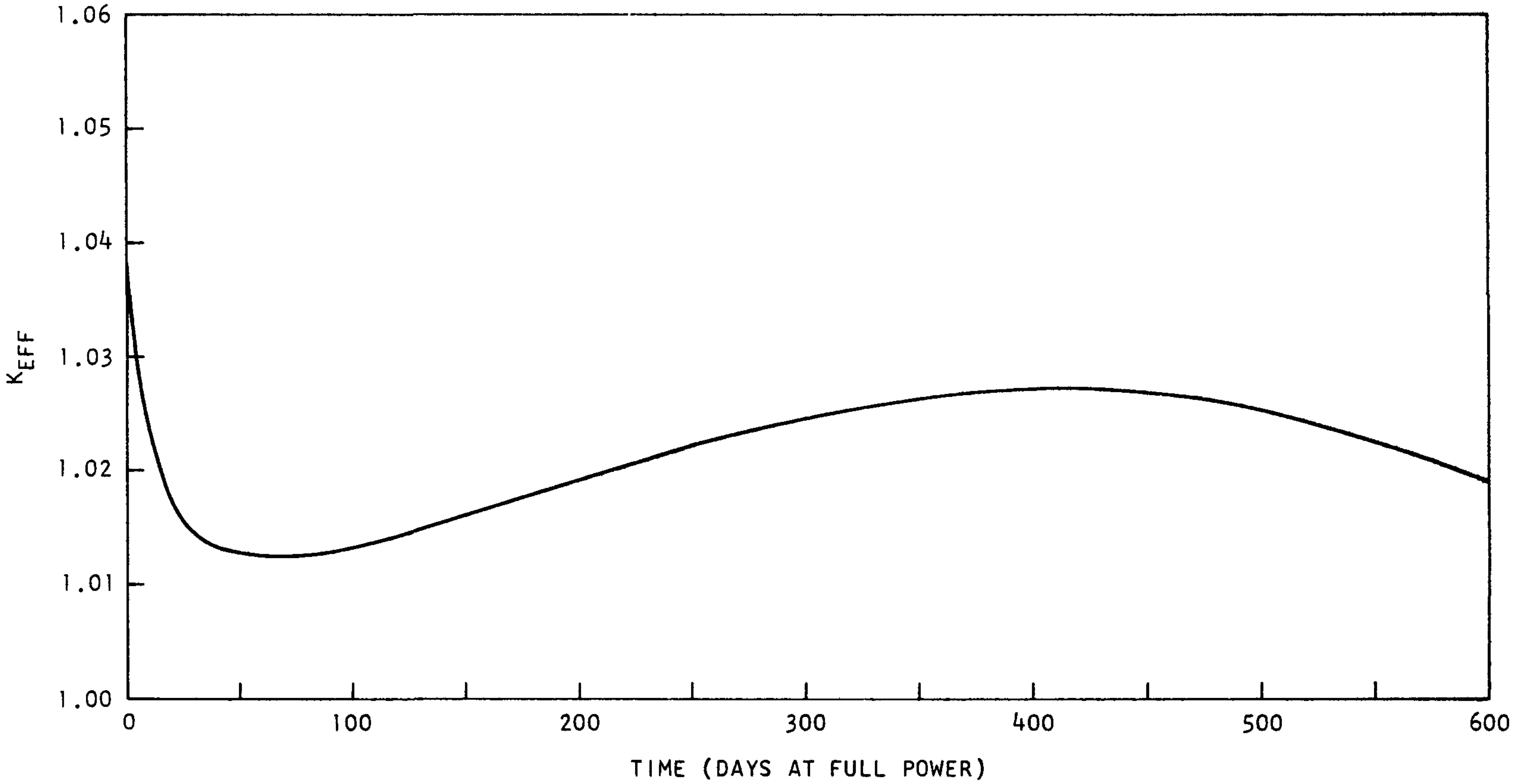

Fig. 2.5--Initial cycle hot core excess reactivity for Reference Design 7

the methods used should be accurate enough to indicate possible trouble spots and to eliminate rod programs that are acceptable from the core physics standpoint but not from an over-all point of view.

To facilitate data transfer to engineering analysis groups, further modification of SCANAL allow the storage of time-dependent power and flux distributions, nuclide concentrations, and fuel loading on magnetic tape.

ANALYTICAL STUDIES

The objective of this subtask is to provide support to other tasks of the program by means of analyses of such items as neutron and flux distributions, nuclear safety of auxiliary equipment, loadings and nuclear properties of irradiation experiments, defining of the need for physics measurements during reactor startup, and evaluating the core response to reserve shutdown system operation.

Fuel Particle Loading

In the current reference design, 13 fuel compositions are used for the initial core to satisfy radial and axial zoning requirements as well as the partial mockup of the equilibrium fuel cycle. As shown in Table 2.7, consistent with the data given in Table 2.4, these compositions differ greatly in their uranium and thorium loading per unit length of fuel. Since a uniform fuel hole diameter of 0.5 in. was adopted for all fuel elements in the core, the loading density variation has to be achieved by proper blending of the four particle types. Their specifications are:

	Kernel Diameter (μm)	Total Coating Thickness (μm)
Fissile:		
A	100 - 175	120 ± 15
B	175 - 275	130 ± 15
Fertile:		
A	300 - 450	130 ± 15
B	450 - 600	140 ± 15

These size ranges were established such that both the most heavily and the most lightly loaded fuel rods could be fabricated without using any diluent material but rather by making use of the difference of actual metal loading per unit bulk particle volume.

However, achievement of the proper loading in a fuel rod or a fuel composition is only part of the problem. Over-all fuel loading requirements and tolerances, particle specifications, and the fabrication process must be compatible to prevent the occurrence of large amounts of residual particles. For instance, if the fabrication process yields more metal in the form of fissile A particles than fissile B particles and the loading requirements and volume restrictions dictate a heavier use of fissile B particles, residual amounts of fissile A particles will result. Thus it must be determined whether all 13 fuel compositions can be fabricated with the present specifications in such a manner that there is a minimum of residual fissile or fertile particles left. If the analysis shows significant amounts of residual particles, the changes in particle specification, fabrication process, or fuel loadings that will assure economic fuel fabrication must be determined. The system must be flexible enough to accommodate changes in fuel loading, variations in the fabrication process, or other modifications that may come up in the final stages of the core analysis.

Table 2.7

INITIAL CORE LOADINGS
(Reference Design 7)

Fuel Rod Composition	Uranium Load (g/in.)	Thorium Load (g/in.)
1	0.104	2.59
2	0.080	2.33
3	0.155	2.19
4	0.115	1.89
5	0.183	2.21
6	0.137	1.95
7	0.218	2.21
8	0.167	1.98
9	0.155	2.41
10	0.111	2.02
11	0.178	2.58
12	0.150	2.25
13	0.108	2.31

The initial effort in this area was directed toward establishing adequate methods for analyzing this set of dependent and independent variables. Linear programming techniques are now being used to determine the distribution of the four particle types into the 13 fuel compositions. The preliminary results clearly indicate that more heavy metal has to be in the form of type B particles, fertile or fissile, if a minimum amount of residual particles is to be achieved.

The analysis of these loading problems will continue to assure that loading tolerances, total loading, and economic fabrication can be achieved.

Burnable Poison Rod Heating

About two-thirds of the fuel blocks in the initial core contain two lumped burnable rods at opposite corners of the block. The poison initially controls about 0.08 Δk of reactivity. At the end of the initial cycle, most of the boron is depleted. During this period proper temperature stability is required so the boron does not diffuse out of the graphite matrix.

The $B^{10}(n,\alpha)\ Li^7$ reaction is the prime source of heat in the poison rods. Heating due to γ-ray absorption is about an order of magnitude lower. Calculations indicate that the highest volumetric heat generation rate in the poison rod occurs in sticks located at the core-reflector interface. The hottest rod produces an average of about 1.5×10^6 Btu/hr-ft^3. Because of the variations in axial flux distribution, a local peaking factor of 1.4 has to be applied for the hottest spot. A thermal analysis is being performed to ensure that temperature limits are not exceeded.

Boron Concentration in Control Rods

The reference control system calls for boronated graphite compacts containing 0.63 g of natural boron per cubic centimeter of compact, approximately 40 wt-% of boron in the matrix. In order to establish purchase specifications and over-all system requirements, the sensitivity of shutdown margins to the boron concentration in the rods was determined.

Minimum shutdown margins occur if one or two rod pairs are withdrawn from refueling regions at the core-reflector interface. A series of calculations has shown that the shutdown margin for these conditions is hardly affected if the poison concentration in the central seven control rod pairs is reduced to below 20 wt-% of boron. A summary of the results is presented in Table 2.8. Clearly, there is a flux tilt if a rod at the core periphery is withdrawn but as one would expect, this tilt is influenced only very slightly by a lower poison concentration in the central portion of the core.

References

1. Stevens, C. A., and C. V. Smith, GAROL, A Computer Program for Evaluating Resonance Absorption Including Resonance Overlap, USAEC report GA-6637, also NASA-CR-71162, General Dynamics, General Atomic Division, August 24, 1965.
2. Koppel, J. U., J. R. Triplett, and Y. D. Niliboff, GASKET, A Unified Code for Thermal Neutron Scattering, USAEC report GA-7417 (Rev.), General Dynamics, General Atomic Division, March 10, 1967.
3. Niliboff, Y. D., and J. U. Koppel, HEXSCAT, Coherent Elastic Scattering of Neutrons by Hexagonal Lattices, USAEC report GA-6026, General Dynamics, General Atomic Division, December 15, 1964.
4. Lenihan, S. R., GAZE-2, A One-dimensional, Multigroup, Neutron Diffusion Theory Code for the IBM-7090, General Dynamics, General Atomic Division report GA-3152, August 3, 1962.
5. Katz, R., Core Performance Code (COPE Code), USAEC report GAMD-1561 (Rev.), General Dynamics, General Atomic Division, March 21, 1963.

Table 2.8

CORE SHUTDOWN MARGINS FOR INITIAL CORE

Case	Description	K_{eff}, Hot
1	Unrodded	1.0508
2	Fully rodded, all rods 40 wt-%	0.8297
3	Fully rodded, all rods 40 wt-%, pair 30 out	0.8928
4	Fully rodded, all rods 40 wt-%, pair 31 out	0.8934
5	Fully rodded, all rods 40 wt-%, pairs 30, 31 out	0.9357
6	Fully rodded, rod pairs 1 to 7 30 wt-%, other 40 wt-%, pair 31 out	0.8935
7	Fully rodded, rod pairs 1 to 7 20 wt-%, other 40 wt-%, pair 31 out	0.8936
8	Fully rodded, rod pairs 1 to 7 10 wt-%, other 40 wt-%, pair 31 out	0.8938
9	Fully rodded, rod pairs 1 to 7 30 wt-%, other 40 wt-%, pairs 30, 31 out	0.9357
10	Fully rodded, rod pairs 1 to 7 20 wt-%, other 40 wt-%, pairs 30, 31 out	0.9358
11	Fully rodded, rod pairs 1 to 7 10 wt-%, other 40 wt-%, pairs 30, 31 out	0.9359
12	Fully rodded, rod pairs 1 to 7 30 wt-%, other 40 wt-%	0.8304
13	Fully rodded, rod pairs 1 to 7 20 wt-%, other 40 wt-%	0.8316
14	Fully rodded, rod pairs 1 to 7 10 wt-%, other 40 wt-%	0.8335

Task III

FUEL DEVELOPMENT

FUEL ELEMENT DESIGN

The objective of this subtask is to develop the design of the fuel elements to be used in the plant by means of mechanical and flow testing, analysis of temperatures under normal and abnormal conditions, analyses of stresses, including effects of temperature, irradiation, and creep, and analysis of fission-product concentrations in the reactor system.

Mechanical Design

The core identification map has been reissued as a reactor construction drawing. Work has continued on the fuel element block drawings; two drawings were reissued and two new drawings were issued.

Work was essentially completed on the preparation of a coupled computer code system for analysis of the stress distributions within the graphite ligaments of the fuel elements throughout life. The stresses arise principally from the thermal gradients due to heat conduction between the fuel and coolant, and due to nonuniform temperature-dependent fast-neutron-induced dimensional change under irradiation. Irradiation-induced creep of the graphite is included in the calculation of the time-dependent stress distributions. The analytical model consists of a representative triangular cell section within the fuel hole array defined by lines of geometric similarity.

A major part of the over-all stress analysis was the preparation of input data routines describing the thermal and irradiation-induced strains during the fuel element life. Computer codes and interface routines were prepared to generate the input data to be used in the SAFE-CREEP stress analysis code. The combined computer code system is identified as SAFE-GRAFITE.

SAFE-GRAFITE handles the following types of two-dimensional problems: plane stress, plane strain, and modified plane strain. The modified plane strain is an approximate computation of the three-dimensional stress distribution. The axial direction stresses are approximate but conservative. Test problems have been solved with the code for a few time steps with satisfactory operation. The code, which appears to be ready for routine use, is now being expanded to perform stress survey calculations to determine the locations in the core at which the maximum stresses may occur. The calculations are based on approximate equations; however, once the locations for possible maximum stress are identified, more precise calculations can be made with SAFE-GRAFITE. The survey code is designed to make approximate stress calculations at 25 axial locations within a fuel column and at approximately 30 time steps during the fuel element life. Thus far, the basic equations have been programmed, but considerable debugging remains to be completed. The survey code will greatly reduce the total computer time required to investigate all regions of the core.

Thermal and Coolant Flow Design

The analysis of flow distribution in the core was interrupted during the quarter in order to improve and automate the calculational methods. Toward this end, the flow analysis code, FLAC, was modified to incorporate branch heat addition in the computational scheme, and a subroutine, HEAT, was added to calculate the appropriate branch heat inputs. In addition, an auxiliary code, SNKMOD, was written to calculate the steam generator module inlet temperatures utilizing the core region outlet flow distribution from FLAC.

Although the code modifications have significantly reduced the amount of hand calculations, it is still necessary to iterate on core ΔP and region orifice settings outside the code. This means that a large number of runs are usually required to obtain a satisfactorily converged solution for each core power distribution. However, at the present time, a systematic method for iterating on orifice settings within the computer code has not been developed.

Using the improved FLAC code with heat addition and the SNKMOD code, a test problem was run corresponding to a solution previously obtained for an equilibrium core based on isothermal flow conditions. A comparison of the results indicates that the heat addition has an appreciable affect on the flow distribution. The affect is most pronounced in the crossflow in the top reflector area. Here, crossflow tends to be appreciable because the orifices create large pressure differences in the x-y plane. In the new solution, the calculated crossflow in the top portion of the core is larger than previously calculated because the true gas density is higher than that used in the previous analysis. In the previous analysis, the gas density was based on the average coolant temperature in the core, which is about 1100°F, while the actual coolant temperature at the core inlet is about 760°F. The net result is that temperature imbalances in the core region outlet gas and steam generator module inlet gas are further aggravated. A quantitative comparison of the isothermal solution and the solution with heat addition is shown in Tables 3.1 and 3.2. The results support the previous conclusion that orifice readjustment alone cannot eliminate the temperature imbalances and that some combination of control rod adjustment and orifice adjustment is necessary.

The analytical results in Tables 3.1 and 3.2 were based on the top reflector plenum elements being keyed with relatively large clearances between elements. An analysis is now being made to determine flow distribution in the core with a revised top reflector plenum element design. The revised plenum element design utilizes raised contact pads to maintain alignment of the fuel columns on region boundaries with radial keys within the region. The raised pads produce an appreciable resistance to the bypass flow entering the external gaps, and thus reduce the magnitude of crossflow entering the gaps at the core inlet.

Several computer runs have been made using the revised plenum geometry; however a satisfactory convergence on core ΔP, total flow through the core, and adjustable orifice settings has not yet been attained. Preliminary results indicate that the revised reflector block design reduces the flow entering the bypass gaps from about 30% to 20% of the flow through the core. The flow at the outlet of the bypass gaps is essentially unchanged at about 5%. A

Table 3.1

COMPARISON OF FLOW ANALYSIS RESULTS

Fuel Region No.	Power Factor	Orifice Loss Coeff.[a]	Deviation in Region Outlet Temperature (°F) $T_{region} - (T_{region})_{avg}$	
			Isothermal	With Heat Addition
1	1.379	---	--	84
2	1.122	63.8	46	83
3	0.907	169	47	63
4	0.854	249	45	-55
5	0.776	300	1	-118
6	1.460	10.2	-11	98
7	1.344	26.8	43	172
8	0.776	300	-5	-2
9	0.981	108	48	73
10	0.794	300	34	19
11	1.125	63.8	56	97
12	1.506	15.3	47	187
13	0.847	230	47	-54
14	0.921	186	43	18
15	0.861	211	47	-71
16	0.963	149	50	19
17	0.744	300	29	-136
18	0.776	300	9	-111
19	1.390	21.7	39	175
20	0.824	197	52	84
21	0.560	300	-246	-240
22	0.731	300	-79	-70
23	0.922	72.8	61	113
24	1.833	5.15	101	199
25	1.032	102	35	64
26	0.869	76.6	49	97
27	1.302	34.5	28	152
28	0.593	300	-218	-246
29	0.461	300	-211	-226
30	1.025	89.4	59	42
31	1.565	7.66	10	104
32	0.518	300	-91	-171
33	0.695	300	-140	-142
34	0.887	287	29	72
35	0.345	300	-327	-362
36	0.645	300	-44	-173
37	0.964	189	54	93

[a] Orifice coefficient range = 5.15 (full open) to 300 (full closed).

significant result of the calculations thus far is that core ΔP is higher than previously estimated with crossflow. Present calculations indicate that the converged core ΔP may be about 8.5 psi versus 7.5 psi from previous calculations. The difference is attributed mainly to the reduced gap flows entering at the top of the core and the fraction of reactor power absorbed by the bypass flows.

Table 3.2

STEAM GENERATOR MODULE TEMPERATURE IMBALANCE

Module No.	Module Temperature Imbalance (°F) T module - $(\text{T module})_{avg}$ I Isothermal	II With Heat Addition
1	30	50
2	-49	-33
3	-10	3
4	68	106
5	50	94
6	20	57
7	-58	-78
8	12	-11
9	16	8
10	-26	-65
11	-27	-66
12	-26	-65

Two special versions of the general-purpose core performance code, COPE, were written to provide a more accurate description of the flow distribution in the core. The main features of the special versions are that a set of empirical factors has been built into the routine to account for crossflow effects and a subroutine SINKMD has been added to calculate steam generator module inlet temperatures. The crossflow factors used in the codes were derived from an analytical solution of the detail flow distribution in the core based on power distribution data for an equilibrium reference 2 core.

One version of the code is designed specifically for use in the fuel depletion studies. The purpose of this version is to provide basic core performance data concurrently with core power distribution results so that realistic decisions can be made concerning control rod patterns during core life. The second version is similar to the first, except that the flexibility of the original code is retained.

Fission-product Transport

The design criteria document for the plateout monitor system was completed, and issued, and a system description was prepared. The monitor probe concept is shown on Fig. 3.1.

Calculations of the Sr^{90} release for the core have been reviewed using updated thermal conductivity data and updated graphite sorption constants.

The PSAR reference "design" case calculations for the bonded rod fuel were conservatively based upon temperatures calculated using the lower limit of loose particle bed conductivity of 1.0 Btu/hr-°F-ft. Subsequent measurements using more refined techniques show values of 2.0 and 4.0 Btu/hr-°F-ft for loose particles and bonded rods, respectively.

Further strontium-graphite vapor pressure measurements have been completed since the PSAR reference "design" release data were compiled. The updated measurements show the strontium vapor pressure at the same concentration and temperature to be lower than the vapor pressure used for the reference "design" calculations. For example at 1000°C and 0.1 mg Sr/g C the updated vapor pressure is about 3×10^{-9} atm compared to about 1×10^{-7} atm for the reference design data.

Retaining the conservatism of using the loose particle thermal conductivity value for temperature calculations, but updated for the more recent higher value, and applying the updated vapor pressure data, the release of Sr^{90} has been recalculated for comparison with the reference case. The FREVAP-8 calculated direct evaporation release accumulated during the 30-year plant life is predicted to be 168 C for the updated case. This compares with 371 C calculated for the PSAR "design" case. The reference precursor Kr^{90} release and assumed contamination release components are not affected by applying these updated values.

MATERIALS

The objectives of this subtask are to:

1. Determine the characteristics of beds of bonded coated particles by means of fabrication technique investigations, thermal property tests, vibration and impact tests, and measurements of packing density and loading uniformity.
2. Select the type of particle bed to be used in the reactor based on the above work and work carried out in other parts of the program, taking into account the expected characteristics, including reprocessing, and determine the suitability of the selected system by means of further tests of the type described above.
3. Determine the characteristics of various candidate graphites for use in the fuel elements by means of measurements of the physical, thermal, and mechanical properties of these graphites.
4. Determine the characteristics of various control materials by means of measurements of physical, mechanical, chemcial, and thermal properties.

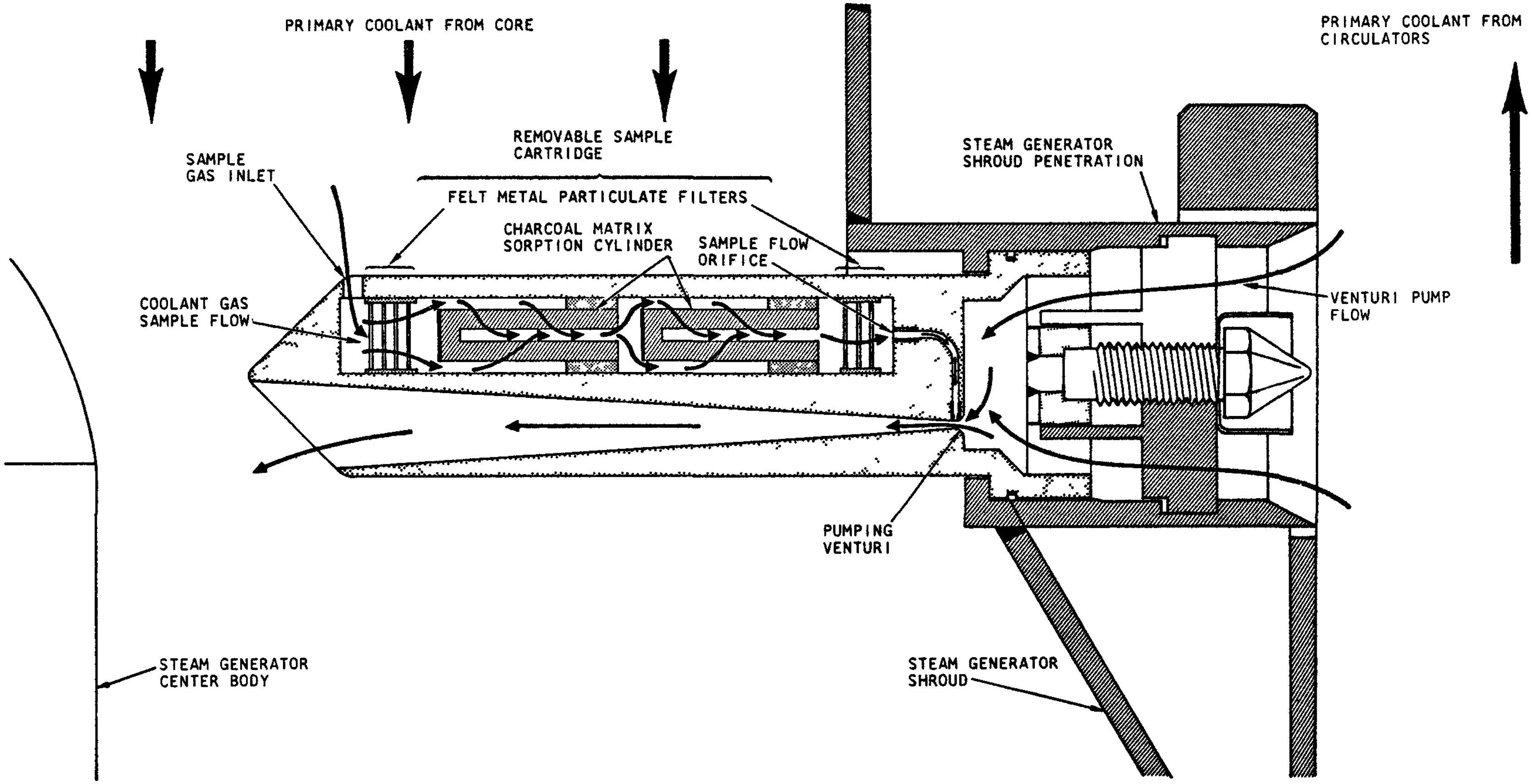

Fig. 3.1--Plateout monitor probe

5. Determine the irradiation stability of candidate graphites for use in the fuel elements by means of irradiation tests conducted in the Engineering Test Reactor at the temperatures and to the integrated fast flux expected in the plant, followed by postirradiation examination.

6. Establish the effect of fast flux on fuel particle coating structural integrity as a function of coating structure and exposure, by means of irradiation tests in the Engineering Test Reactor and other reactors, on unfueled samples of particle coatings, postirradiation measurements of coating properties, such as dimensional changes, flexural strength and crystallite spacing, and subsequent reirradiation to design integrated fast flux and remeasurement. These irradiations will be carried out in the graphite capsules used in 5 above, and in the coated particle capsules used in 7 below.

7. Determine the irradiation stability of coated fuel particles for use in the fuel element by means of a series of (1) short-term tests on coated fuel particles to select a coated fuel particle(s) having over its design life a high degree of structural integrity, followed by (2) longer-term irradiation tests conducted at design temperature, to design burnup, and to a significant fraction of the integrated fast flux expected in the plant. The "significant" integrated fast dosage will be determined from the results obtained in 6. Capsule tests will be followed by postirradiation examination of the particles. Approximately seven short-term and three longer-term capsules are planned for this part of the program.

Particle Fuel Systems

Contamination. As a part of the investigation of gaseous fission-product release from fuel rods, the uranium contamination levels in samples of fuel rod matrix materials and on the surface of fuel rods are being determined. Samples of carbonized matrix material (D-38 formation)* representing the master batches of matrix used in injection-molded fuel rods for the second proof test element were analyzed for uranium by colorimetric and activation analysis.

The samples were first subjected to activation analysis. Values for uranium could not be obtained because the uranium determination was overshadowed by other contaminants, predominantly sodium. The samples were then dissolved and separated by ion exchange, and the resultant solutions subjected to colorimetry. Results of these measurements are shown in Table 3.3. The uranium contamination is shown as "total uranium," since the technique is unable to distinguish between isotopes. In an effort to determine the isotopic distribution (and possible source) of the contamination, three of these solutions were subjected to activation analysis.

---

*D-38 matrix:
47.4 wt-% R-72S phenolic resin
15.8 wt-% maleic anhydride
15.8 wt-% nadic methyl anhydride
21.0 wt-% GP-38 graphite powder filler.

Table 3.3

URANIUM CONTAMINATION IN SECOND PROOF TEST ELEMENT MATRIX MATERIAL

Matrix Batch No.	Fuel Rod No.	Colorimetry	Activation Analysis		
		Total U (ppm)	U^{235} (ppm)	U^{238} (ppm)	Total U (ppm)
1	834	0.110	---	---	---
2	849	0.170	0.100	0.140	0.240
3	870	0.43	---	---	---
4	877-888	0.010	---	---	---
5	889-900	0.043	---	---	---
6	901-912	0.20	---	---	---
7	913-918	0.133	---	---	---
8	919-924	0.610	0.040	0.047	0.087
9	925-936	0.21	---	---	---
10	937-954	0.022	---	---	---
11	1A-12A	0.210	0.020	0.214	0.228
12	13A-28A	0.024	---	---	---
13	45A-56A	0.043	---	---	---

When the observed uranium contamination in each sample of matrix material was plotted against the fission-gas release values (Kr^{87} and Xe^{139}) of the corresponding fuel rods, no correlation was found, as shown in Fig. 3.2. This would indicate that the uranium contamination in the matrix material is at a low enough level that it does not contribute significantly to the fission-gas release.

In addition, alpha-counting studies are being conducted on fuel rods to measure possible surface contamination and to determine any relation to fission-product release. A slight amount of alpha activity has been detected on some rods, but further work with an alpha spectrometer is necessary to identify the specific contamination.

Steady-state Release of Fission Gases from Fuel Rods. In view of the results obtained in studies on the steady-state correction (see Task V, Part II of this report) obtained in fuel rod fabrication studies and presented in Tables 3.8 through 3.11 of the previous quarterly report (GA-8879) are presented again, for documentation purposes, without the steady-state correction. The revised data are given in Tables 3.4 through 3.7. In addition, Figs. 3.11 through 3.14 of GA-8879 have been redrawn without the steady-state correction and are shown here as Figs. 3.3 through 3.6. The lack of a half-life dependence of the gas release is obvious; henceforth, R/B versus half-life plots will be dispensed with in reporting quality control data on fuel rods.

Graphite Development

The evaluation of needle-coke graphite for use in the fuel elements has continued. The graphite under consideration is grade H-327, and additional typical production logs of it have been purchased for machining trials.

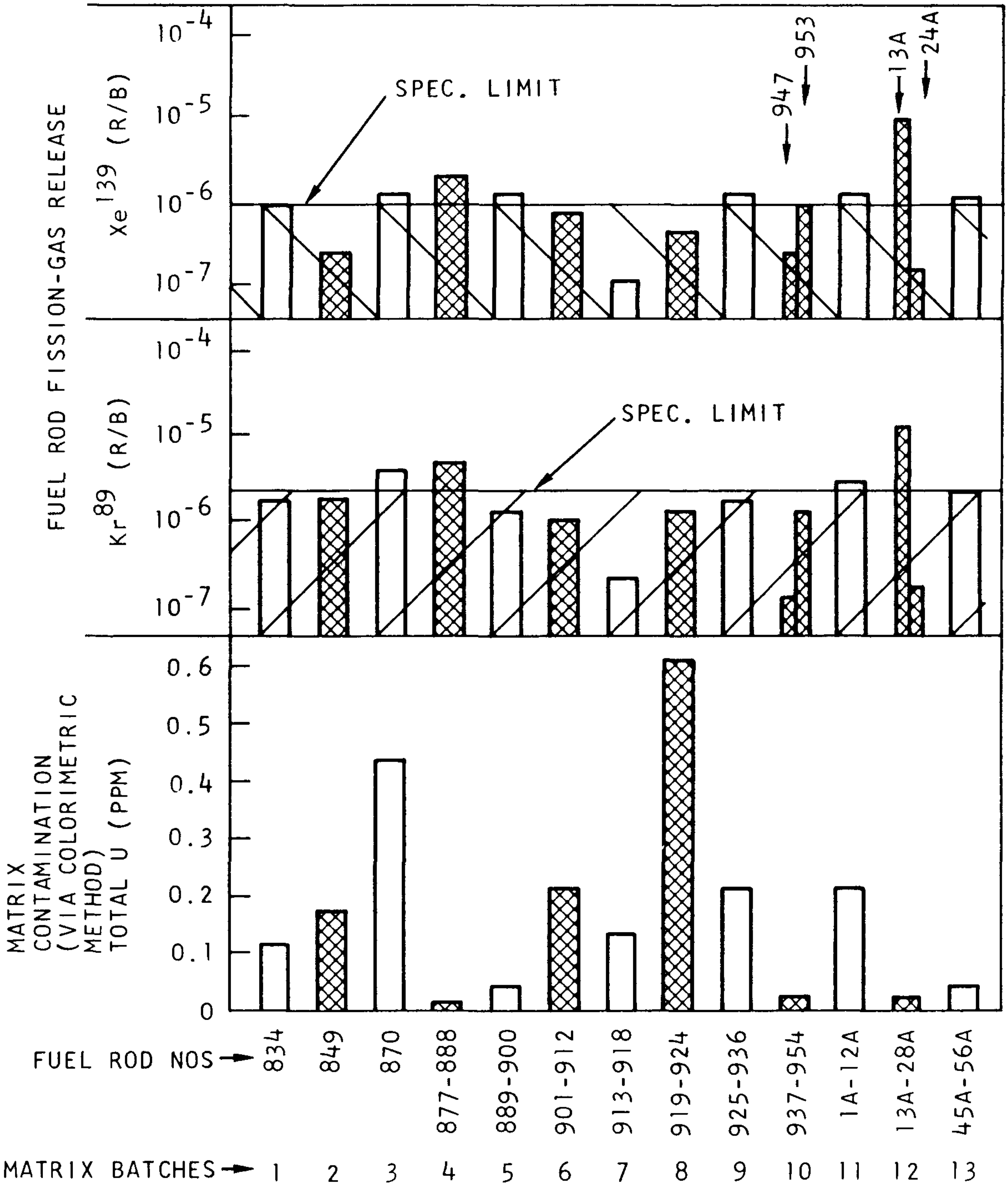

Fig. 3.2--Comparison of uranium contamination in the second proof test element matrix material with corresponding fuel rod fission-product release

Table 3.4

FUEL ROD FISSION-GAS RELEASE SEQUENCE NO. 1
(BISO-leached Coatings)

Sample	Release Fraction, R/B					
	Kr^{85}	Kr^{88}	Kr^{87}	Kr^{89}	Xe^{138}	Xe^{139}
XETK-LTI-HTI-CO2[a] particles (P_1)	$8.4x10^{-6}$	$1.2x10^{-5}$	$1.0x10^{-5}$	$3.3x10^{-6}$	$2.5x10^{-6}$	$2.0x10^{-6}$
D-38 graphite matrix (M_1)	$2.6x10^{-1}$	$3.6x10^{-1}$	$3.3x10^{-1}$	$9.0x10^{-2}$	$1.4x10^{-1}$	$3.2x10^{-1}$
XETK-LTI-HTI-CO2 particles + D-38 graphite matrix ($P_1 + M_1$)	$6.7x10^{-5}$	$1.0x10^{-4}$	$9.3x10^{-5}$	$5.7x10^{-5}$	$4.2x10^{-5}$	$5.3x10^{-5}$
XETK-LTI-HTI-CO2 particles (P_1) separated from matrix (M_1)	$7.5x10^{-6}$	$1.1x10^{-5}$	$7.8x10^{-6}$	$6.3x10^{-6}$	$4.7x10^{-6}$	$3.2x10^{-6}$
New GP-38 graphite matrix (M_2)	$1.5x10^{-3}$	$2.4x10^{-3}$	$1.8x10^{-3}$	$2.7x10^{-3}$	$2.4x10^{-3}$	$3.7x10^{-3}$
Fuel rod X-60 fabricated from ($P_1 + M_2$)	$8.2x10^{-5}$	$1.0x10^{-4}$	$9.9x10^{-5}$	$1.6x10^{-5}$	$2.0x10^{-5}$	$7.6x10^{-5}$

[a] Mixture of fissile particles and fertile particles.

Table 3.5

FUEL ROD FISSION-GAS RELEASE SEQUENCE NO. 2
(TRISO-leached Coatings)

Sample	Release Fraction, R/B					
	Kr^{85}	Kr^{88}	Kr^{87}	Kr^{89}	Xe^{138}	Xe^{139}
T-105A + ET-109A[a] particles (P_1)	$1.5x10^{-7}$	$3.0x10^{-7}$	$1.2x10^{-7}$	$3.7x10^{-8}$	$1.4x10^{-7}$	$1.3x10^{-7}$
D-38 graphite matrix (M_1)	$2.6x10^{-3}$	$4.3x10^{-3}$	$3.2x10^{-3}$	$4.2x10^{-3}$	$3.7x10^{-3}$	$4.4x10^{-3}$
T-105A + ET-109A particles + D-38 graphite matrix ($P_1 + M_1$)	$6.2x10^{-7}$	$8.8x10^{-7}$	$7.7x10^{-7}$	$8.4x10^{-7}$	$9.6x10^{-7}$	$2.8x10^{-7}$
T-105A + ET-109A particles (P_1) separated from matrix (M_1)	$6.8x10^{-8}$	$1.1x10^{-8}$	$6.0x10^{-8}$	$7.8x10^{-8}$	$1.8x10^{-7}$	$7.9x10^{-8}$
New GP-38 graphite matrix (M_2)	$9.2x10^{-4}$	$1.4x10^{-3}$	$4.1x10^{-4}$	$1.0x10^{-3}$	$8.2x10^{-4}$	$8.7x10^{-4}$
Fuel rod X-61 fabricated from ($P_1 + M_2$)	$8.0x10^{-7}$	$9.6x10^{-7}$	$7.7x10^{-7}$	$3.8x10^{-7}$	$8.3x10^{-7}$	$1.1x10^{-6}$

[a] T-105A fertile particles and ET-109A fissile particles.

Table 3.6

FUEL ROD FISSION-GAS RELEASE SEQUENCE NO. 3
(TRISO-unleached Coatings)

Sample	Release Fraction, R/B					
	Kr^{85}	Kr^{88}	Kr^{87}	Kr^{89}	Xe^{138}	Xe^{139}
T-105A + ET-109A[a] particles (P_1)	1.1x10^{-7}	1.3x10^{-7}	8.0x10^{-8}	1.1x10^{-7}	1.6x10^{-7}	1.4x10^{-7}
D-38 graphite matrix (M_1)	2.6x10^{-3}	4.3x10^{-3}	3.2x10^{-3}	4.2x10^{-3}	3.7x10^{-3}	4.4x10^{-4}
T-105A + ET-109A particles + D-38 graphite matrix (P_1 + M_1)	1.5x10^{-6}	2.4x10^{-6}	2.0x10^{-6}	2.5x10^{-6}	2.5x10^{-6}	9.9x10^{-7}
T-105A + ET-109A particles (P_1) separated from matrix (M_1)	4.4x10^{-7}	3.5x10^{-7}	5.7x10^{-8}	1.3x10^{-7}	8.4x10^{-8}	8.8x10^{-8}
New GP-38 graphite matrix (M_2)	8.8x10^{-3}	4.9x10^{-3}	6.2x10^{-3}	1.0x10^{-2}	1.8x10^{-3}	9.9x10^{-4}
Fuel rod X-62 fabricated from (P_1 + M_2)	1.1x10^{-6}	1.8x10^{-6}	8.8x10^{-7}	7.3x10^{-7}	1.0x10^{-6}	7.6x10^{-7}

[a] T-105A fertile particles plus ET-109A fissile particles.

Table 3.7

FUEL ROD FISSION-GAS RELEASE SEQUENCE NO. 4 THROUGH NO. 6
(TRISO-unleached Coatings)

Sample	Release Fraction, R/B					
	Kr^{85}	Kr^{88}	Kr^{87}	Kr^{89}	Xe^{138}	Xe^{139}
T-103C particles[a]	4.7x10^{-4}	6.5x10^{-4}	4.3x10^{-4}	3.1x10^{-4}	2.8x10^{-4}	1.9x10^{-4}
ET-170C particles[b]	7.9x10^{-8}	6.3x10^{-8}	1.5x10^{-8}	6.3x10^{-8}	1.2x10^{-7}	1.5x10^{-7}
T-103C + ET-170C particles	2.6x10^{-7}	2.0x10^{-7}	1.9x10^{-8}	5.2x10^{-8}	7.6x10^{-8}	6.4x10^{-8}
Fuel rod X-63, T-103C particles	3.4x10^{-3}	4.3x10^{-3}	3.8x10^{-3}	5.5x10^{-3}	4.6x10^{-3}	2.2x10^{-3}
Fuel rod X-64, ET-170C particles	4.3x10^{-7}	3.2x10^{-7}	9.9x10^{-8}	7.4x10^{-8}	2.7x10^{-7}	3.1x10^{-7}
Fuel rod X-65, T-103C + ET-170C particles	1.1x10^{-6}	1.6x10^{-6}	3.4x10^{-7}	5.7x10^{-7}	1.9x10^{-7}	2.0x10^{-7}
Graphite matrix used in rod fabrication	8.8x10^{-3}	4.9x10^{-3}	6.2x10^{-3}	1.0x10^{-2}	1.8x10^{-3}	9.9x10^{-4}
2nd irradiation of fuel rod X-63, T-103C particles	3.5x10^{-3}	3.4x10^{-3}	3.5x10^{-3}	3.7x10^{-3}	3.8x10^{-3}	1.9x10^{-3}

[a] Fertile particles.

[b] Fissile particles.

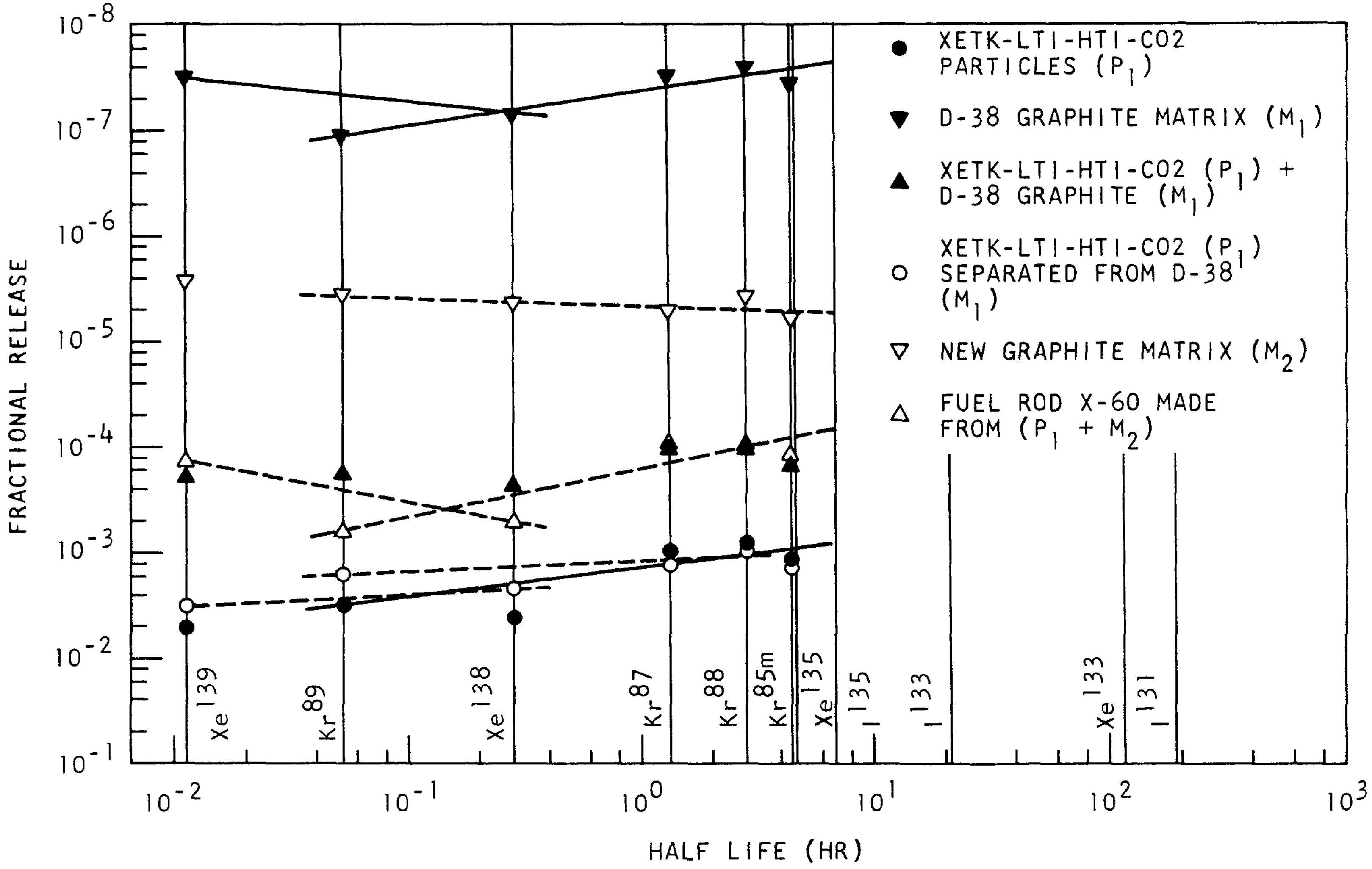

Fig. 3.3--Fuel rod fission-gas release sequence No. 1 (BISO leached particles)

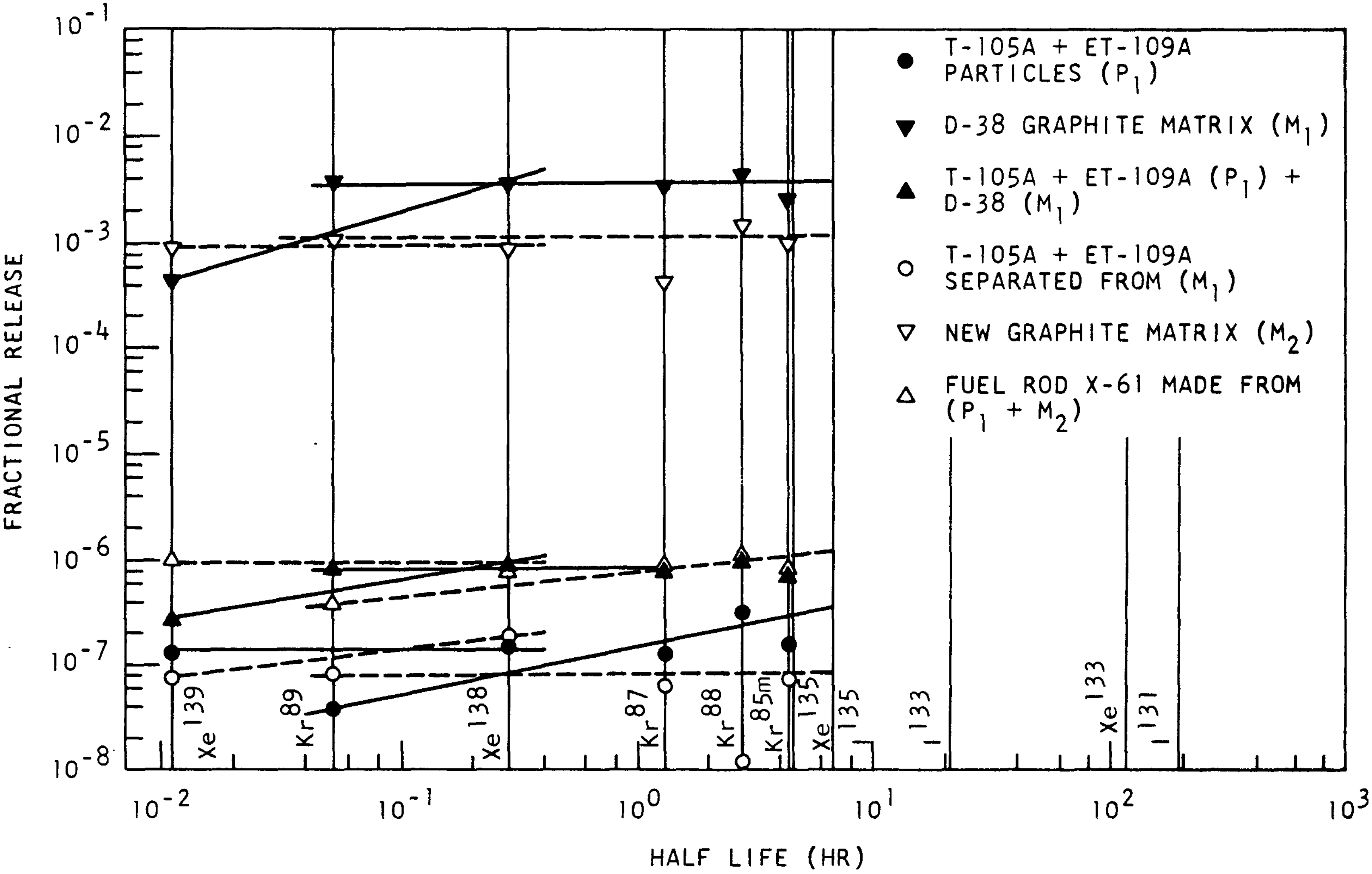

Fig. 3.4--Fuel rod fission-gas release sequence No. 2 (TRISO leached particles)

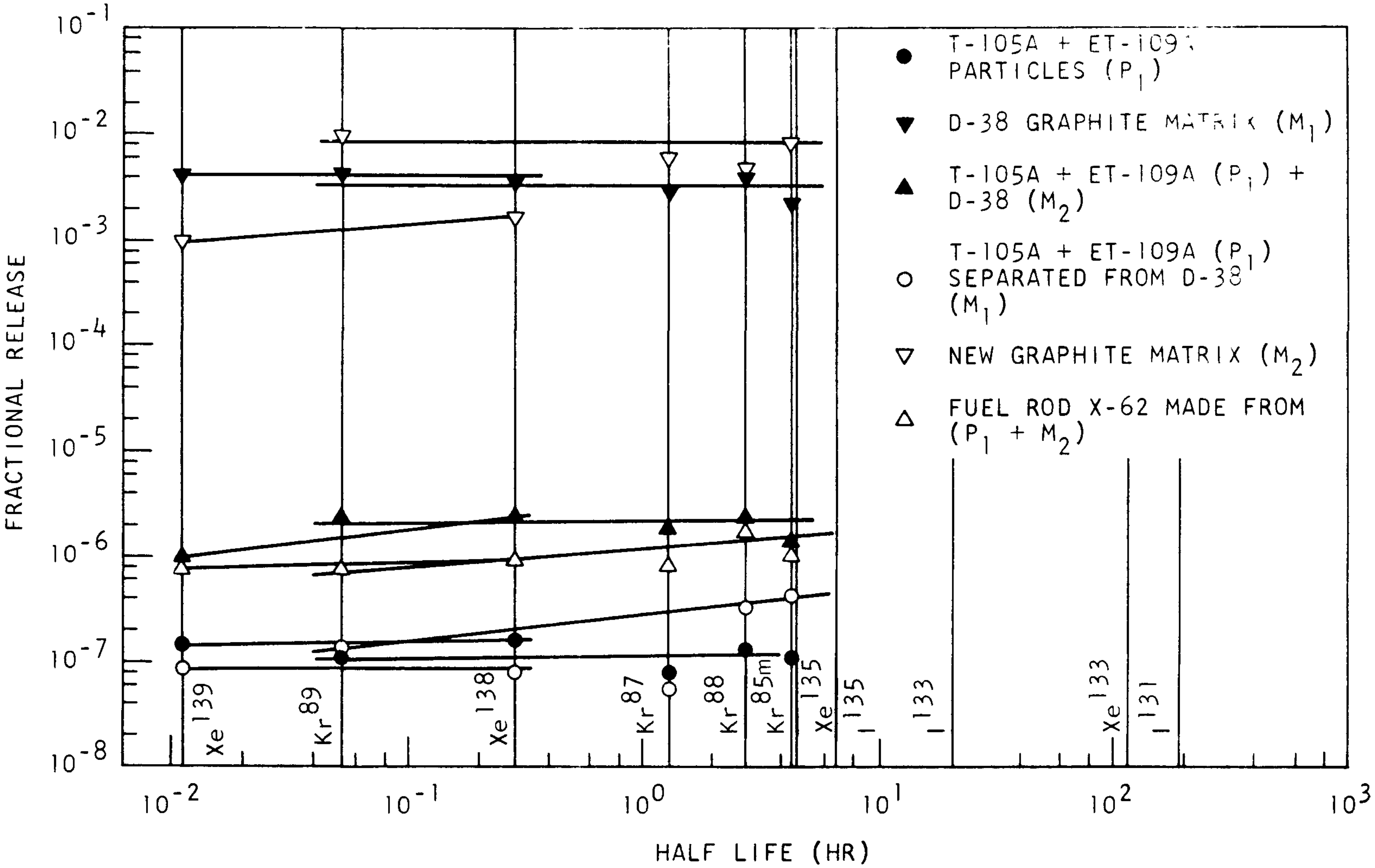

Fig. 3.5--Fuel rod fission-gas release sequence No. 3 (TRISO unleached particles)

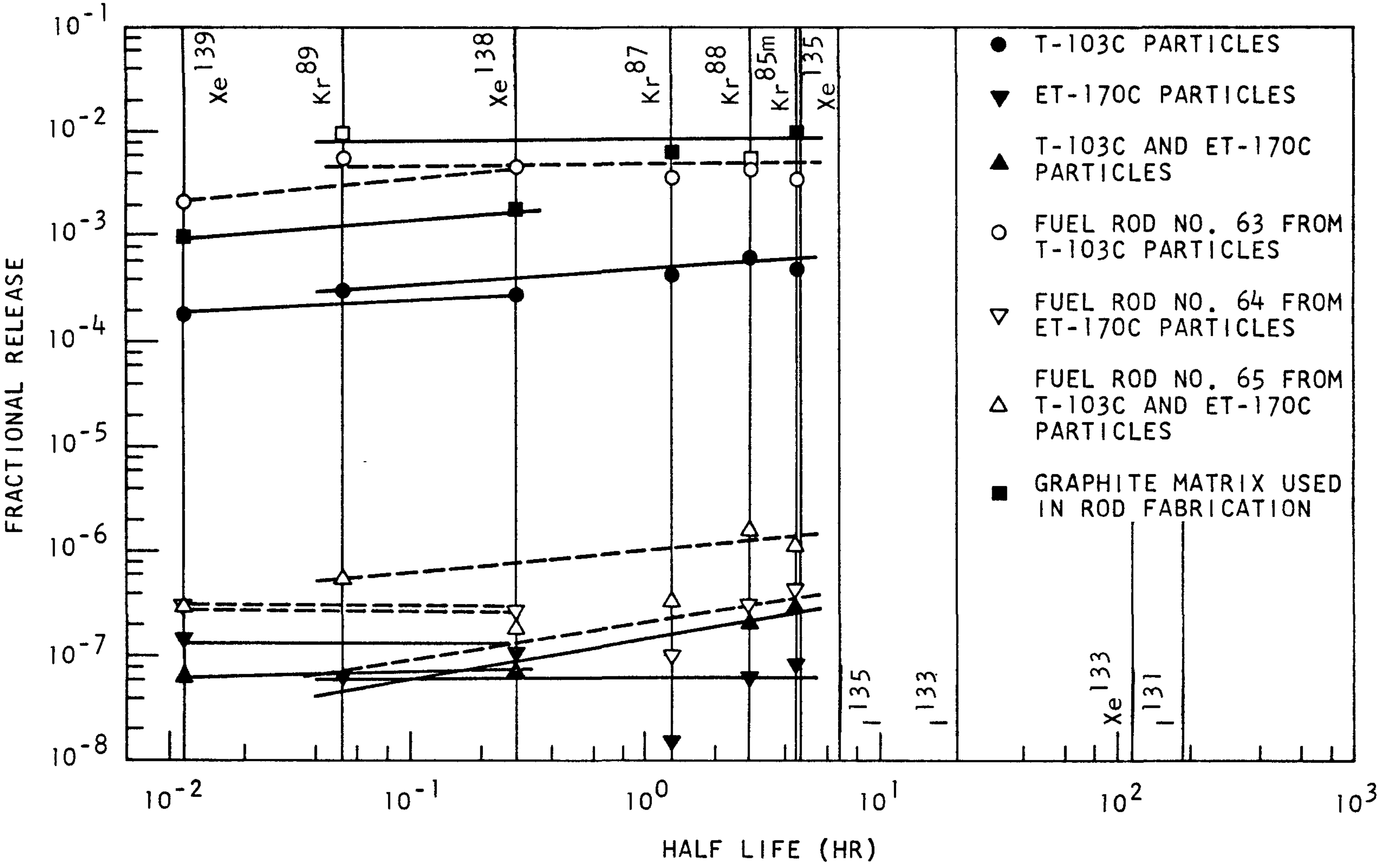

Fig. 3.6--Fuel rod fission-gas release sequence No. 4 through No. 6

Modulus-of-rigidity tests on short-length rectangular samples of typical irradiation sample size have shown the method is adaptable to short-span-type specimens, although evaluation of the results is not complete. Chemical analysis of samples of current H-327 production shows that metallic impurities are well below specified limits. However, there is a greater amount of large porosity in the current samples and further testing is necessary to assess the effects upon permeability.

Control Material

Reserve Shutdown System. During the quarter the boronated reserve shutdown material was changed from B_4C granules to boronated graphite balls. In addition, the use of HfC in graphite balls is being considered for the central seven regions of the core. Design criteria and specifications for the reserve shutdown balls were prepared and are being reviewed.

Before the change in the material, a study of the dusting characteristics of B_4C granules under conditions of vibration was under way. This work was terminated because of the change to boronated graphite balls and also because further study showed that the vibration level in the reactor is insignificant. The results obtained at the termination of the study are presented here.

Dust production in the reserve shutdown materials was of interest because the amount of residual boron left in the reactor core after activation of the system and subsequent cleanup would be related to the tendency of the B_4C to form dust during storage and handling. A PyC coating over the B_4C granules was investigated as a device for reducing the production of B_4C dust. The purpose of this work was to evaluate the relative dusting rates of PyC-coated and uncoated B_4C on accelerated test under severe vibration conditions.

Uncoated and PyC-coated B_4C granules (1/8 to 1/4 in. diameter) were poured into separate glass cylinders to form columns 1 in. in diameter by about 4 in. high. A 140-g plug of Nylon filled with lead was placed on top of the bed to simulate the weight of a longer bed and prevent expansion of the top portion of the bed during vibration.

The beds were vibrated simultaneously on a Syntron Jogger Model DL-1 at 60 cps and a maximum acceleration of 12 g. At the completion of the first 500-hr run the granules were removed from the glass tubes, sieved, and weighed. The granules and dust were then returned to test for another 500 hr, after which the same sieving and weighing cycle was repeated.

After each 500-hr cycle only a few granules at the top of the column would pour out freely. The remaining material had to be pried and scraped from the tubes. At the bottom of each bed was an accumulation of dust that tended to be agglomerated, particularly in the bed with the PyC-coated granules. At the end of 1000 hr of vibration, a crescent-shaped free-standing piece of compacted dust weighing 1.17 g was removed intact from the bed of PyC-coated granules. This piece and two smaller ones are shown in Fig. 3.7. The material crumbled easily under finger pressure.

Photographs of both coated and uncoated B_4C before and after the 1000-hr vibration test are shown in Figs. 3.8 and 3.9. Photomicrographs of the cross

Fig. 3.7--Compacted wear dust formed at the bottom of the bed of PyC-coated B_4C after a 1000-hr vibration test (~6X)

Fig. 3.8--Uncoated B_4C granules 1/4- to 1/8-in. diameter (3471-106): prior to vibration test (left) and after vibration test of 1000 hr, 60 cps, 12-g maximum acceleration (right) (10X)

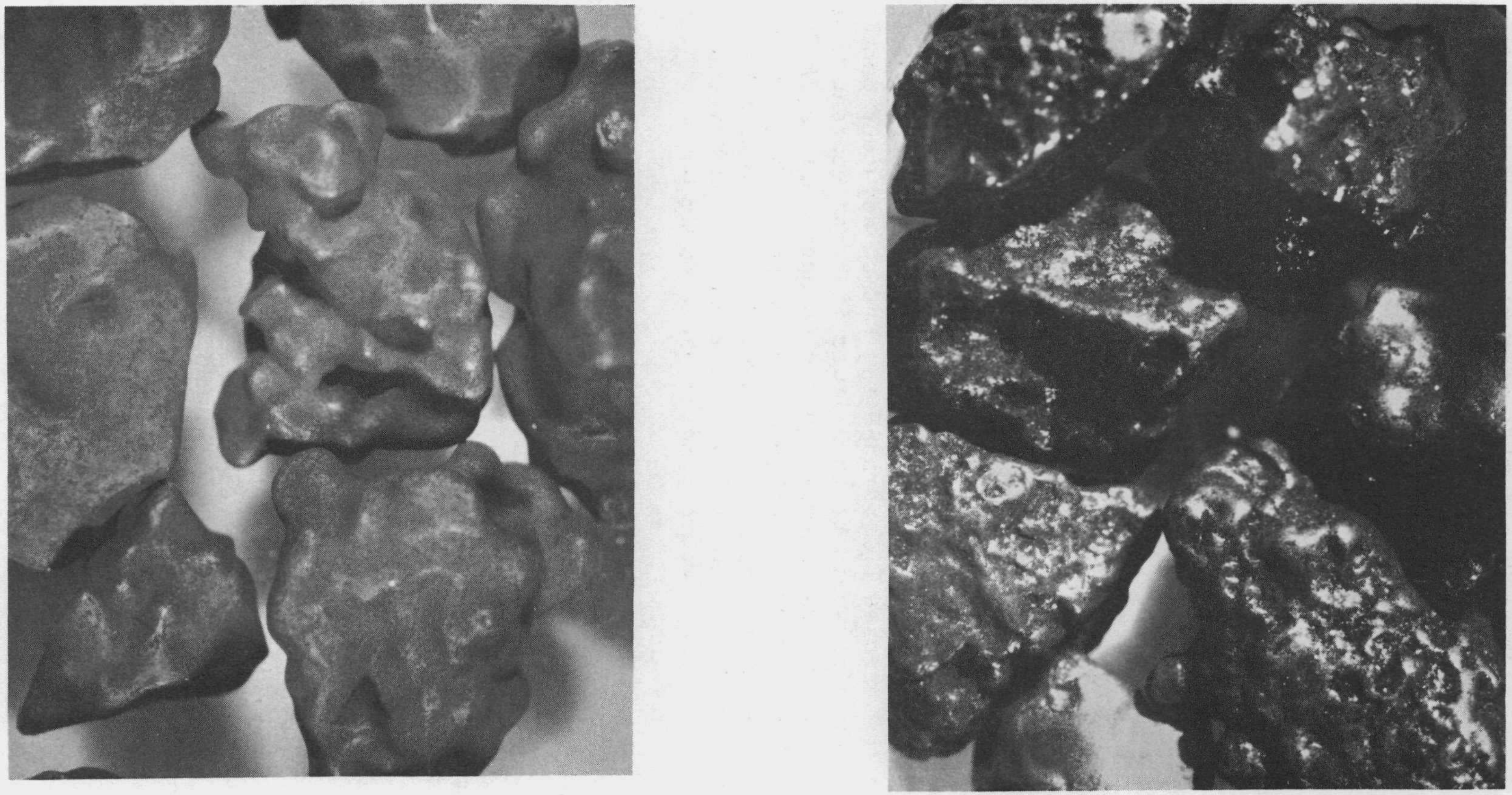

Fig. 3.9--B_4C granules 1/4- to 1/8-in. diameter with 50- to 600-μm PyC coating (3507-57-19): prior to vibration tests (left) and after vibration tests of 1000 hr, 60 cps, 12-*g* maximum acceleration (right) (10X)

section of PyC-coated B_4C showing the coating condition before and after the test are shown in Fig. 3.10. The amount of wear dust at 500 and 100 hr of vibration is shown in Table 3.8.

In the uncoated B_4C (3471-106), the dust particles smaller than 208 μm after vibration for 1000 hr amounted to 5.7 wt-% of the initial weight of sample. This was about 20% greater than at 500 hr and about 10 times greater than at 50 hr under less severe (7 g) loading in a previous test (reported in an earlier quarterly report, GA-8600). Wear on the particles was apparent as a general rounding and reduction in height of asperities (see Fig. 3.8).

In the PyC-coated material, the dust particles smaller than 208 μm after 1000 hr of vibration amounted to 8.1 wt-% of the initial sample weight. This was about 60% greater than at 500 hr. At 50 hr of vibration at the loadings reported in GA-8600 the wear dust from this material was barely detectable (about 0.002 wt-%).

The dusting of B_4C increased approximately linearly with time and further testing might show a decrease in dusting rate as the asperities are worn away. On the other hand, the PyC-coated B_4C, which showed very little wear after 50 hr, showed several orders of magnitude more wear after 500 and 1000 hr of vibration. Presumably the PyC was worn away at localized spots (as shown in Figs. 3.9 and 3.10), and the exposed B_4C abraded the PyC on adjacent particles. The dust produced in this fashion would be much lower in boron content than dust from uncoated B_4C. However, the creation of solid agglomerates of PyC wear dust (Fig. 3.7) would be a detriment, because the granules must remain free flowing in the reserve shutdown system. In fact, the difficulty experienced in removing granules from the cylinder after vibration suggests that neither uncoated nor coated B_4C would remain free flowing under vibration as severe as that used in this test.

Two interesting observations were made during preliminary work with the vibration test apparatus.

1. When a weighted (140 g), graphite crucible (AGOT graphite) was placed on the beds of B_4C granules and severely vibrated for about 8 hr, the uncoated granules wore away the 1/8-in.-thick bottom of the graphite crucible, while the coated particles merely polished the bottom of the crucible.
2. Both coated and uncoated B_4C granules wore through the walls of polyethylene tubes used in preliminary work to hold the beds when vibrated for 288 hr under the conditions previously specified for the 1000-hr test.

The results of the preceding work point out the importance and complex nature of wear in systems, such as these, that undergo significant vibration. Under conditions of severe vibration, the PyC coatings on B_4C do not offer a significant advantage over uncoated B_4C with regard to dust reduction. More moderate vibration levels, inert atmosphere, and higher temperatures might reveal some advantage in having a PyC coating on this material. The fact that both coated and uncoated B_4C became firmly packed in the beds and was not free flowing after the test has serious implications if it is necessary

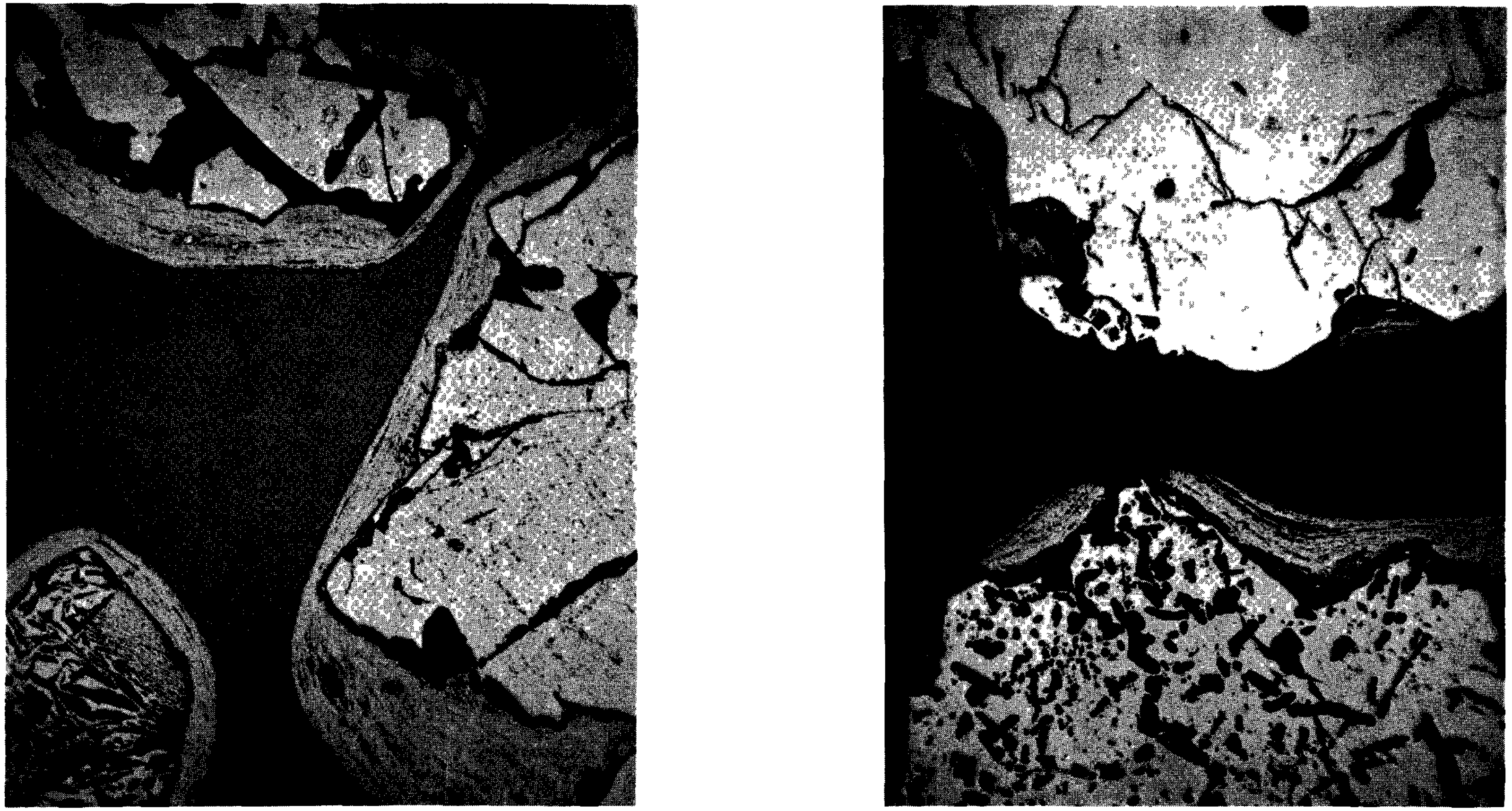

Fig. 3.10--PyC-coated B_4C (3507-57-19) before (left) and after (right) vibration tests of 1000 hr, 60 cps, 12-g maximum acceleration (50X)

Table 3.8

DUST PRODUCTION IN BEDS OF PyC-COATED AND UNCOATED B_4C PARTICLES
(Vibrated Under 140-g Load, 60 cps, 12-g Maximum Acceleration)

Material	Total Sample Weight (g)	Test Time (hr)	Dust in Various Size Fraction (wt-%)			Total Wear Dust for 1000-hr Test (wt-%)
			+208 µm	-208 +74 µm	-74 µm	
3471-106 (uncoated B_4C, ρ=2.3 g/cm^3)	63.6	500	0	2.4	2.4	---
		1000	0	2.8	2.9	5.7
Blend of 3507-51, 53, 55, 57 (PyC-coated B_4C ρ=2.2 g/cm^3)	70.4	500	(Agglomerates of fine powder forced through sieve)	2.1	2.9	---
		1000	1.7 (large agglomerates of fine powder at bottom of column)	3.3	3.1	8.1

that the material remain loose. Vibration at more moderate levels might show a reduced packing and sticking effect.

Control Rod Absorber Material. Specimens of boronated graphite were fabricated for thermal stability experiments to determine the influence of B_4C content and B_4C particle size on the ability of boronated graphite control material to retain its shape and boron content during a postulated loss-of-coolant accident.

Blends of B_4C, graphite flour, and coal tar pitch were made by mixing the dry components together and then dissolving the pitch in Triclene. After the Triclene had evaporated, the powder was divided into 12.5-g charges and pressed in an Incoloy 800 die at 750°C and 4000 $lb/in.^2$ pressure. Cylindrical specimens 0.63 in. in diameter by 1.25 in. long were obtained. A 1% to 2% weight loss was experienced during warm-pressing. The cylinders were baked 2 hr at 2000°C in a vacuum of about 50 μm Hg. The weight loss during the baking cycle was 1% to 2%. The formulation of raw material and the boron concentration after baking are shown in Table 3.9.

The specimens were annealed at 3000 ± 50°C for 1 hr. Specimens with 40 wt-% boron did not retain their integrity during annealing, whereas compacts with 30 and 20 wt-% boron maintained their shape. Boron specimens fabricated with small (<200 μm) B_4C particles seemed less porous after the anneal than specimens with large (>200 μm) B_4C particles.

Experiments were performed to test the compressive strengths of boronated graphite compacts at temperatures of 2500° and 2800°C. The purpose of these tests was to determine the ability of boronated graphite compacts to withstand load pressures simulating those that could occur in the event of a loss-of-coolant accident. The 20, 30, and 40 wt-% B specimens prepared by Gulf General Atomic and a specimen prepared by a vendor (containing about 39 wt-% B) were subjected to loads in the range of 8 to 24 psi.

At a temperature of 2800°C and a pressure of approximately 8 psi, the 40 wt-% B specimen and the vendor specimen showed significant plastic deformation in 5 to 10 hr. At 2500°C the vendor material contracted about 13% in about 20 hr using the same pressure. The 30 wt-% specimen showed no change in geometry during a 50-hr anneal at 2500°C with a compressive load of about 24 psi. At 2800°C, a specimen compressed slightly (5%) under a 15 psi load during a 20-hr test. In a duplicate experiment for 150 hr the 30 wt-% specimen compressed by about 7% of its original length. The 20 wt-% B specimens showed no change in geometry during a 50-hr anneal at 2500°C and 24 psi. At 2800°C and 15 psi, no change was observed after 20 hr.

Tests were carried out at 2500° and 2800°C on 30 wt-% boronated graphite specimens to determine load pressures required to collapse the specimens. The point of failure was taken to be the point at which the compact decreased by more than 20% of its original length within 2 min. At 2800° and 2500°C the fail points occurred at approximately 47 and 85 psi, respectively.

These results indicate that boronated graphite compacts containing up to 30 wt-% boron will maintain their integrity to a satisfactory degree under conditions that could arise in the event of a loss-of-coolant accident.

Table 3.9

FORMULATION OF BORONATED GRAPHITE COMPACTS FOR THERMAL STABILITY EXPERIMENTS

Batch No.	B_4C (76 wt-% B)		GP-38 Graphite Flour Content (wt-%)	Coal Tar Pitch Content (wt-%)	Density After 2000°C Bake (g/cm^3)	Boron Content (wt-%)	Boron Distribution (g B/cm^3-compact)
	Particle Size Range (μm)	Content (wt-%)					
4065-87	100 to 160	51	41.5	7.5	1.7	40	0.70
4065-99	250 to 300	51	41.5	7.5	(a)	40[b]	(a)
4065-100	100 to 160	40	56	5	1.8	30[b]	(a)
4065-103	250 to 300	40	56	5	1.8	30[b]	(a)
4065-93	100 to 160	24.5	64	11.5	1.9	20	0.38
4065-95	295 to 300	24.5	64	11.5	(a)	20[b]	(a)

[a] Not yet determined.

[b] Estimated; not yet determined.

Design criteria and modified specifications were prepared for the control rod absorber material.

Irradiation Testing

Irradiation experiments are being conducted to test BISO- and TRISO-coated particles under PSC design irradiation conditions. These experiments are intended to guide the selection of fuel materials that will meet the performance requirements of the PSC reactor. One experiment currently in progress is a proof test intended to demonstrate the irradiation stability of production BISO-coated particles; postirradiation examination of two other tests of BISO-coated particles have recently been completed. Two tests of TRISO-coated fuel are in progress, and a third was just inserted in the ETR for its first irradiation cycle (cycle 99). A new short-term experiment containing BISO- and TRISO-coated fuel was fabricated and shipped to the ETR. Three irradiation tests of fuel rods containing TRISO-coated particles are in progress. Most experiments are being conducted at the PSC maximum fuel temperature to full design burnup and to a significant fraction of the integrated fast-neutron dose.

Graphite irradiation studies on candidate PSC materials are directed toward obtaining data over the temperature range and lifetime neutron dose of the reactor. A series of capsule experiments is in progress to irradiate production-type graphites at temperatures of 550° to 1100°C to dose levels of the order of 8×10^{21} n/cm^2 ($E > 0.18$ Mev). These capsules were used to irradiate samples of several needle-coke graphites and of a nominally isotropic material.

Capsule P18. Capsule P18 was the second proof test of BISO-coated particles using simulated PSC reactor conditions. It was a longer-term test (8 ETR cycles) than the companion capsule P17 and received a fast-neutron dose that for most batches tested exceeded or approximated the maximum PSC design dose of 8×10^{21} n/cm^2 ($E > 0.18$ Mev). The burnups were between 19% and 25% FIMA for four of the five cells; one cell achieved a burnup of approximately 13% FIMA. The maximum PSC design burnup is 20%.

The particles that were tested in capsule P18 were similar to, and in most cases duplicates of, the particles that were tested in capsule P17 (see Table 3.10). These samples included both HTI- and LTI-coated particles with thick and thin isotropic coatings; the series also included high- and low-density isotropic coatings. As was the case with capsule P17, the buffer coating properties were held constant for all of the particles. The core material was varied in order to invest some flexibility in the test so the desired burnup and fast-neutron flux could be attained.

The postirradiation examination revealed that all 15 sample batches survived. One percent failure occurred in two batches (3742-5E and 3592-151E), in which it was found that the failed particles were defective and had no buffer layers. It is noteworthy that the preirradiation examination of both of these batches showed that 2% to 4% of the particles were without buffer coatings, and therefore these particles are very likely responsible for the observed failure. Similar types of failures were also observed in the P17 capsule with sample 3742-5E, which tends to confirm this conclusion.

Table 3.10

DESCRIPTION OF COATED PARTICLES TESTED IN CAPSULE P18
(8-cycle ETR Irradiation)

Lot No.	Coating						Particle			Irradiation Conditions					Postirradiation Examination		Remarks
		Buffer		Isotropic							Temperature (°C)						
	Type[a]	Thickness (μm)	Density (g/cm^3)	Thickness (μm)	Density (g/cm^3)	Anisotropy Factor	Type[b]	Size (μm)	Th:U Ratio	Burnup (% FIMA)	Avg	Max	EOL	Fast Dose (10^{21} nvt)	Micro Exam[c] (% Fail)	Met Exam (% Fail)	
3592-137E	BISO(2000)	59	1.14	48	1.96	1.05	$(Th,U)C_2$	150-250	2.2	25	1130[d]	1335	975[d]	8.4	0[e]	0	HTI thin isotropic series
3663-49E	BISO(1900)	61	1.10	43	2.04	1.12	$(Th,U)C_2$	150-250	2.8	21	1135	1325	950	7.7	0[e]	0	
3742-15E	BISO(1900)	61	1.10	40	1.94	1.04	$(Th,U)C_2$	150-250	3.4	12	1090	1280	935	4.3	0.1	0	
3742-11E	BISO(1900)	59	1.14	73	1.89	1.00	$(Th,U)C_2$	150-250	2.2	25	1130[d]	1355	975[d]	8.4	0	0	HTI thick isotropic series
3742-5E	BISO(1900)	61	1.10	61	2.03	1.05	$(Th,U)C_2$	150-250	2.8	20	1140	1345	925	7.7	0[e]	1.5	
3592-151E	BISO(1900)	61	1.10	61	2.03	1.01	$(Th,U)C_2$	150-250	3.4	18	1145[d]	1345	975[d]	8.4	1.3[e]	1.3	
3592-141E	BISO(1400)	59	1.14	47	1.93	(f)	$(Th,U)C_2$	150-250	2.2	17	1095[d]	1340	930[d]	4.3	0	0	LTI thin isotropic series
3663-53E	BISO(1400)	61	1.10	49	1.96	(f)	$(Th,U)C_2$	150-250	2.8	22	1130[d]	1305	975[d]	8.4	0[e]	0	
3592-143E	BISO(1400)	61	1.10	49	1.90	(f)	$(Th,U)C_2$	150-250	3.4	12	1100	1280	935	4.3	0	0	
3592-145E	BISO(1400)	59	1.14	61	1.98	(f)	$(Th,U)C_2$	150-250	2.2	26	1130[d]	1370	975[d]	8.4	0[e]	0	LTI thick isotropic series
3663-39E	BISO(1400)	61	1.10	56	1.91	(f)	$(Th,U)C_2$	150-250	2.8	20	1055[d]	1230	890[d]	7.7	0[e]	0	
3592-147E	BISO(1400)	61	1.10	61	1.96	(f)	$(Th,U)C_2$	150-250	3.4	19	1140[d]	1330	975[d]	8.4	0[e]	0	
3742-17E	BISO(1900)	61	1.10	61	1.94	(f)	$(Th,U)C_2$	150-250	2.8	18	1130[d]	1360	935[d]	6.4	0	0	LTI and HTI low-density isotropic series
3663-51E	BISO(1900)	61	1.10	66	1.82	1.02	$(Th,U)C_2$	150-250	2.8	19	1130	1355	945	6.4	0	0	
3663-35E	BISO(1400)	61	1.10	61	1.83	(f)	$(Th,U)C_2$	150-250	2.8	18	1125	1345	925	6.4	0	0	

[a] Deposition temperature (in °C) of isotropic layer is given in parentheses.
[b] All particles are spheroidal and 90% of theoretical density.
[c] Determined by stereographic examination of 2000 particles.
[d] Estimated. Thermocouple failed during test.
[e] Some particles stuck to graphite thimble.
[f] Not determined.

A slight increase in the anisotropy of the high-density isotropic coatings ($\rho > 2.00$ g/cm^3) was inferred from the appearance of the coatings under polarized light. The causes and implications of this phenomenon are undetermined at this time, however.

Particles were again found to have stuck to the thimble walls, but there was no indication of a cause for the sticking. There were no observed detrimental effects caused by the sticking. This situation is currently being investigated.

In summary, capsule P18 is by far the highest exposure test of coated particles that has ever been conducted with significant burnup, and the BISO-coated particles have now been proven to the full PSC fast-flux exposure with burnups that equal or exceed the PSC maximum.

Representative photomicrographs are presented in Figs. 3.11 through 3.25.

Capsule P19. Capsule P19 is the first P-capsule proof test of BISO-coated particles prepared in large-scale (production) equipment. Several different isotropic-layer-density and anisotropy-factor combinations are being tested for both HTI and LTI to determine the most economical combination that will survive HTGR design irradiation conditions. A detailed description of the coated particle samples in P19 was given in an earlier quarterly report (GA-8600).

Capsule P19 was designed to achieve full PSC fuel burnup of 20% FIMA and a fast-neutron dose of 6×10^{21} n/cm^2 at the maximum PSC fuel temperature of 1300°C. The fuel temperatures are again being programmed to simulate the thermal history of a typical HTGR maximum-temperature core region, and one cell is designed to operate at 900°C.

The capsule has completed its fifth cycle in the ETR in core position I13NW. The fuel has reached an estimated burnup of 19% FIMA with an estimated fast-neutron dose of 4.3×10^{21} n/cm^2 ($E > 0.18$ Mev). The fuel temperatures are 1090° to 1110°C in the four high-temperature cells, which are now programmed for a design temperature of 1100°C at the burnup that capsule P19 reached. The low-temperature cell (cell 1) is operating at 860° to 900°C. Five of the 15 fuel thermocouples are still operative.

Capsule P20. Capsule P20 is the first proof test of PSC TRISO-coated particles. Both TRISO-I- and TRISO-II-coated particles are being tested to a fast-neutron dose of 5 to 6×10^{21} n/cm^2 ($E > 0.18$ Mev) and to the full PSC fissile particle burnup of 20% FIMA. The samples are being irradiated at both 1300° and 900°C, which are near the PSC maximum and average temperatures, respectively. Variations in several coating parameters are being tested in this experiment to guide the optimization of mechanical stress relationships in the coating layers under high fast-neutron exposures. These parameters include PyC type (LTI versus HTI), PyC thickness, PyC density, and SiC thickness. A detailed description of the samples tested was given in an earlier quarterly report (GA-8725).

The capsule has completed its fourth of five to six cycles in the ETR in the I13SE core position. It is operating satisfactorily with fuel temperatures close to the design value of 1100° and 900°C. The fast-neutron

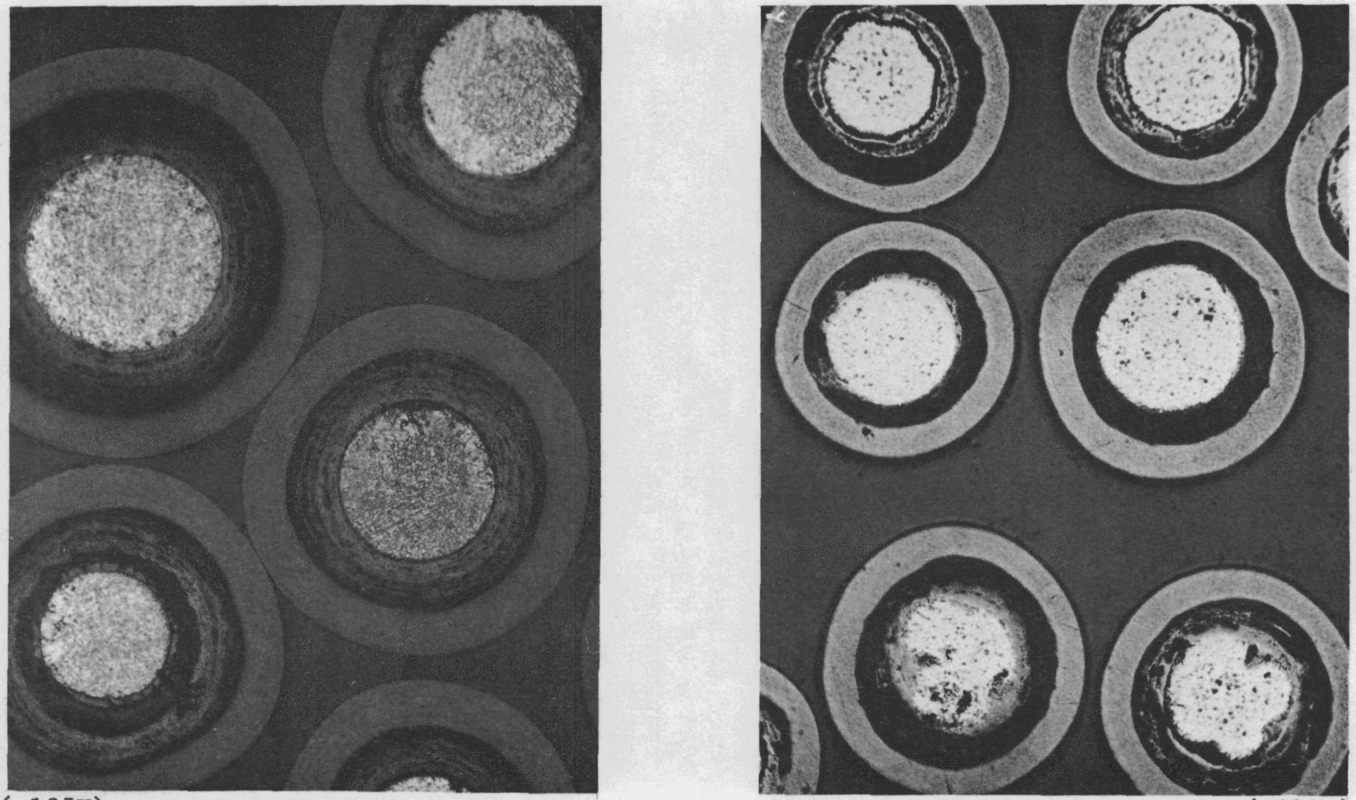

(~125X) (~100X)

Fig. 3.11--BISO-coated particles from lot 3952-137E before (left) and after (right) irradiation in capsule P18

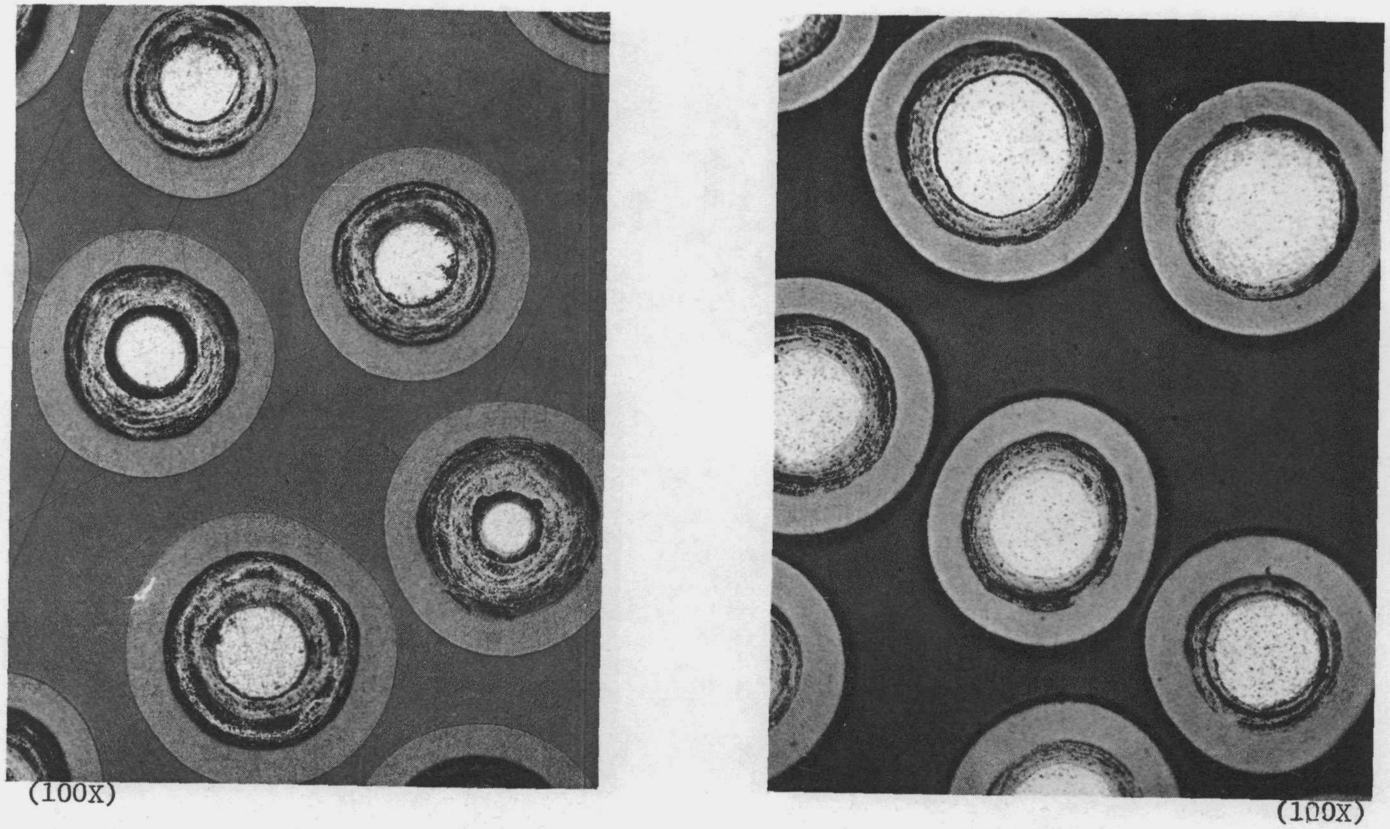

Fig. 3.12--BISO-coated particles from lot 3663-49E before (left) and after (right) irradiation in capsule P18

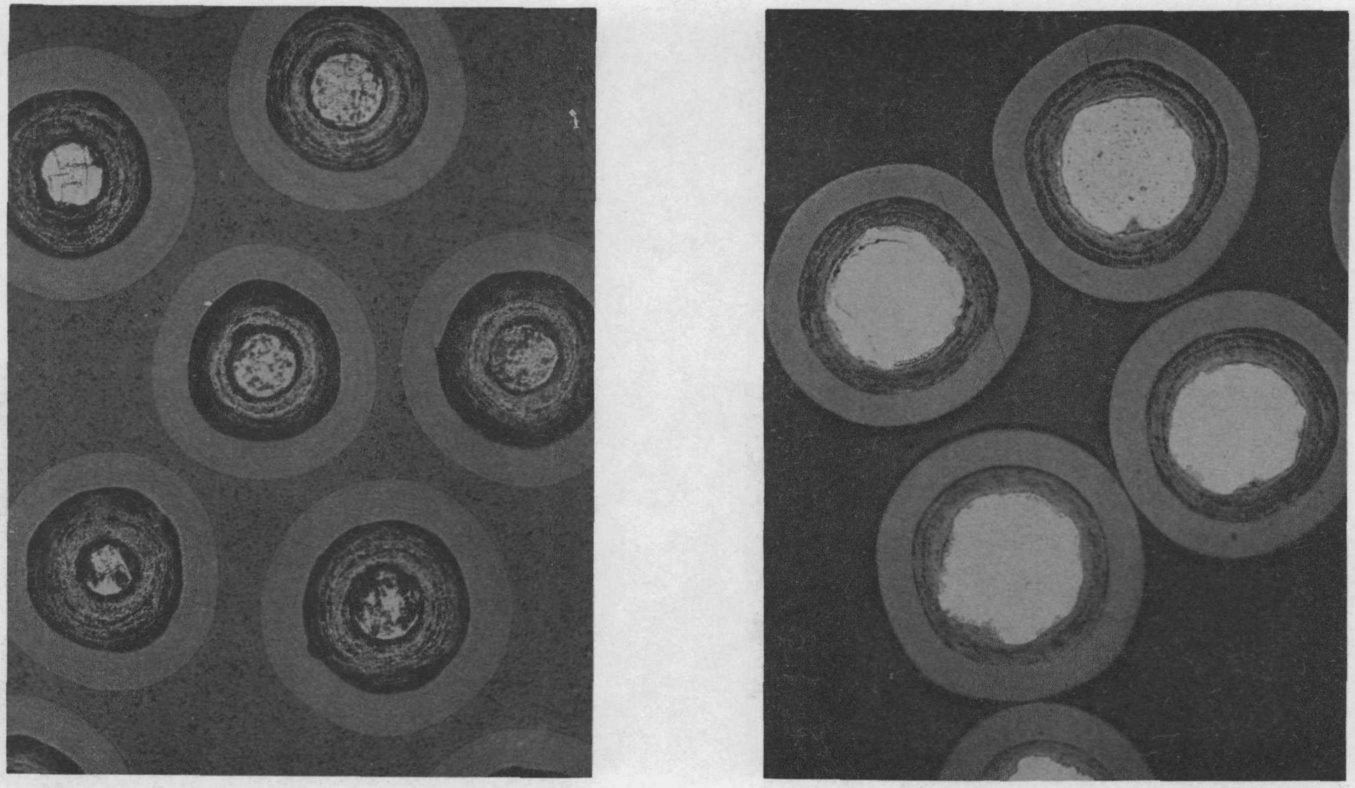

(100X)

(100X)

Fig. 3.13--BISO-coated particles from lot 3742-15E before (left) and after (right) irradiation in capsule P18

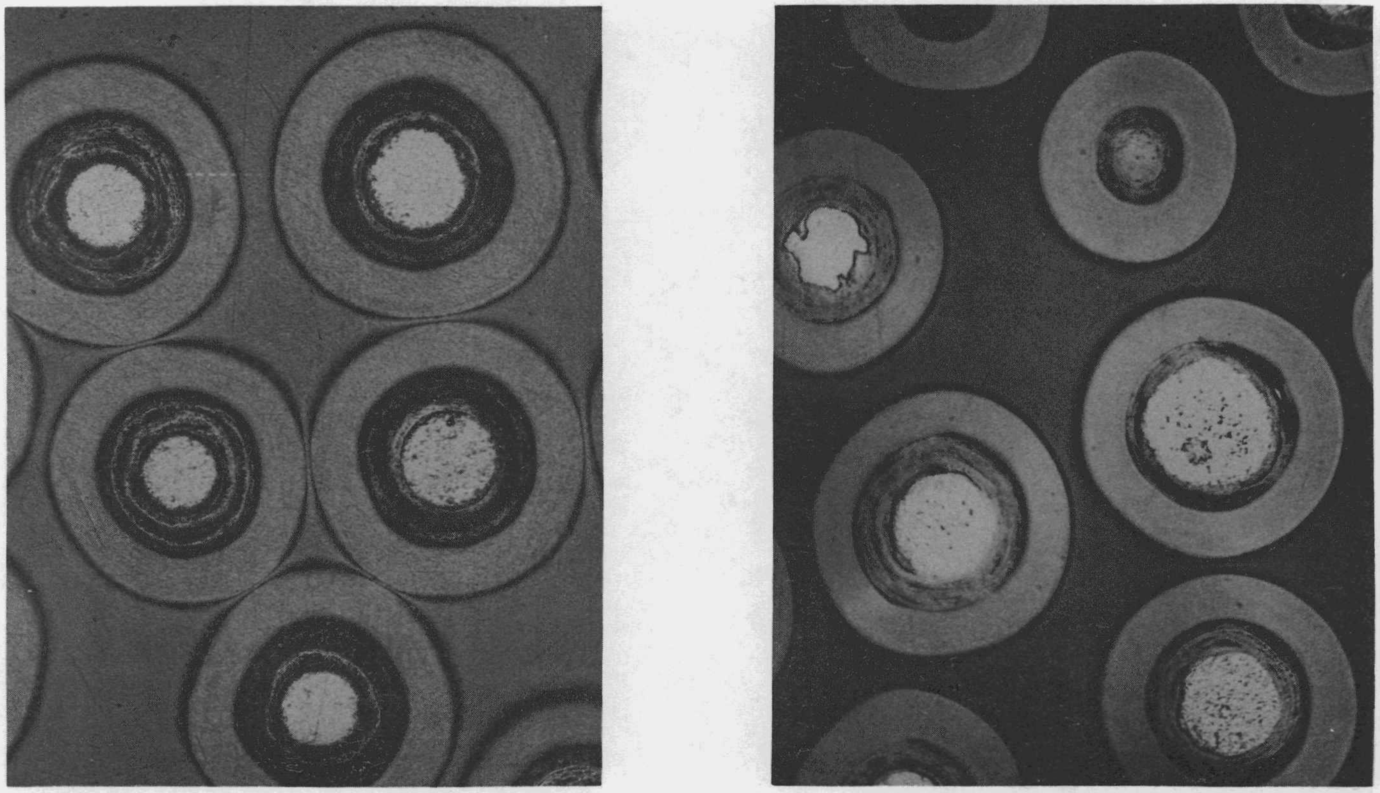

(100X)

(100X)

Fig. 3.14--BISO-coated particles from lot 3742-11E before (left) and after (right) irradiation in capsule P18

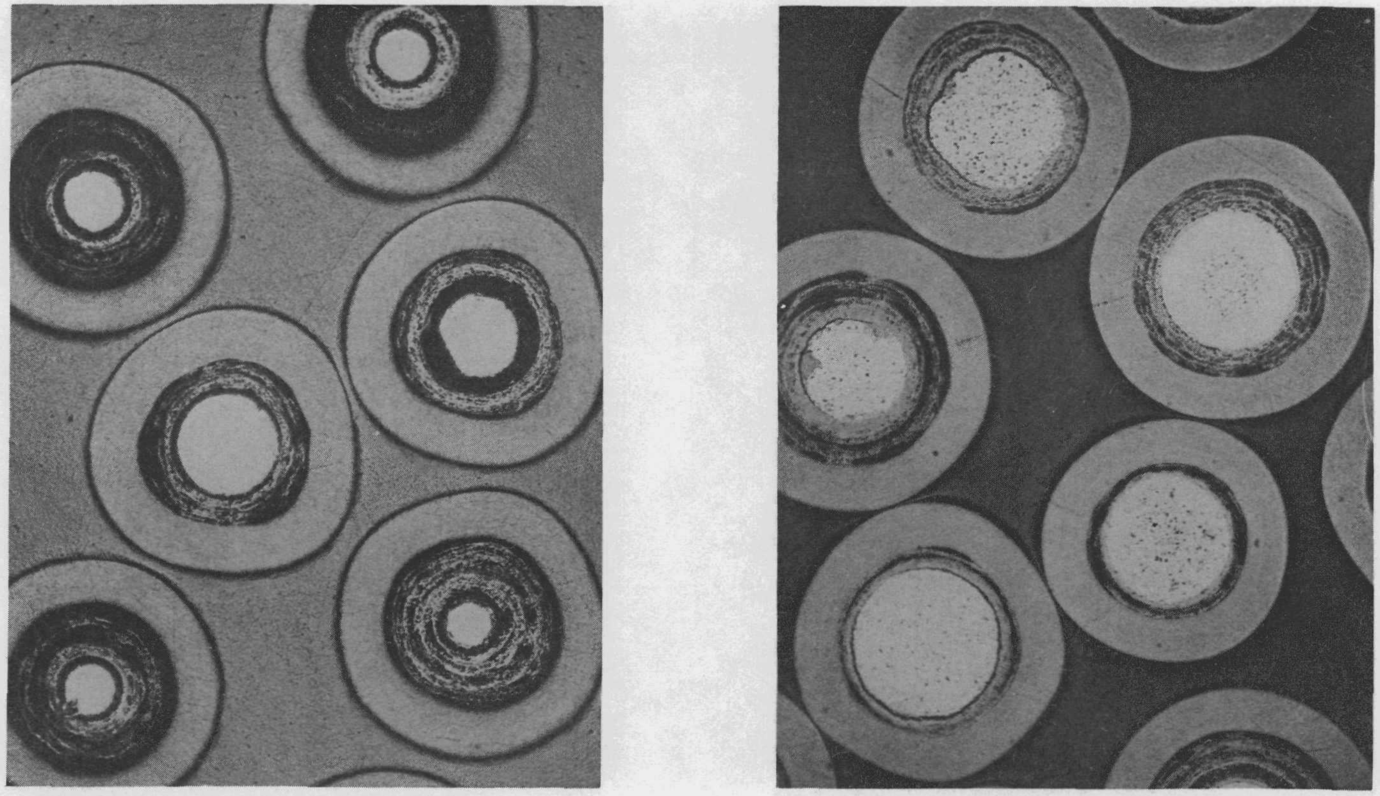

(100X) (100X)

Fig. 3.15--BISO-coated particles from lot 3742-5E before (left) and after (right) irradiation in capsule P18

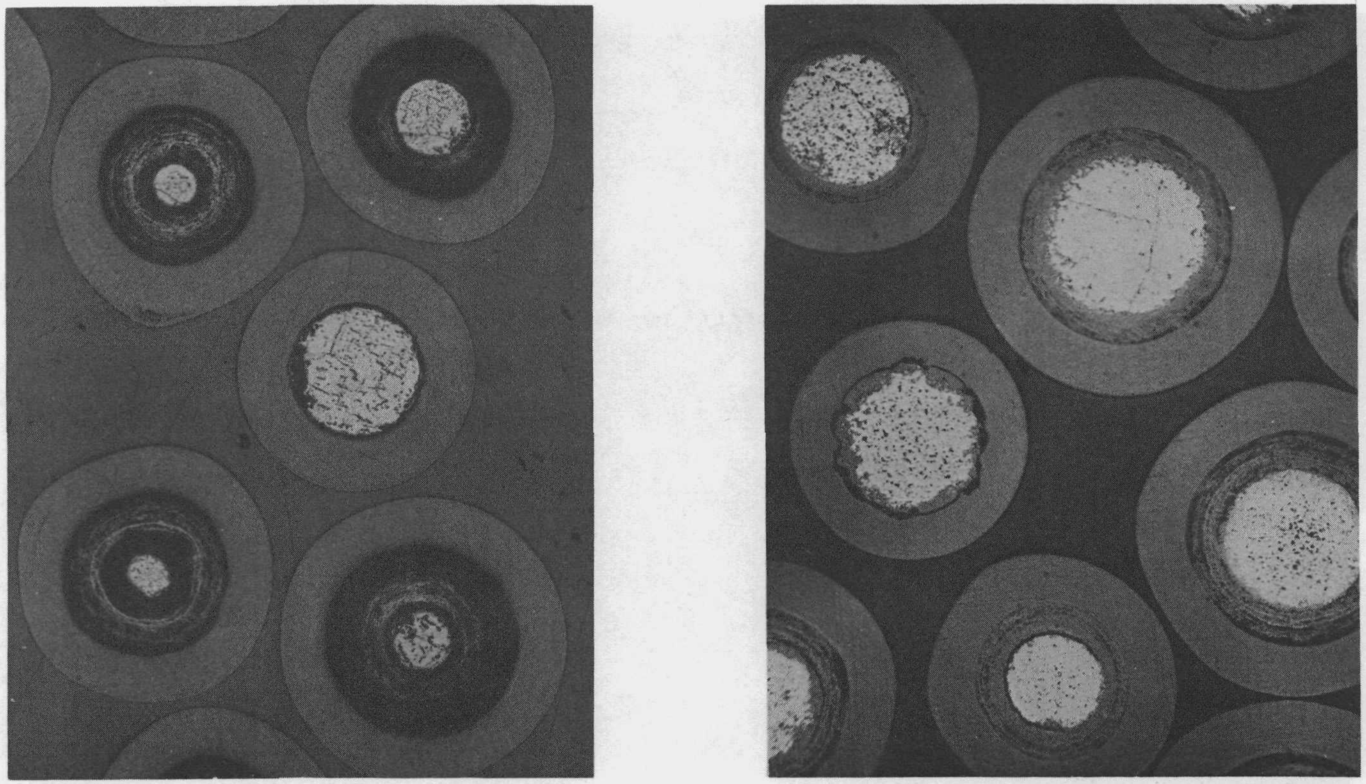

(100X)

(100X)

Fig. 3.16--BISO-coated particles from lot 3592-151E before (left) and after (right) irradiation in capsule P18

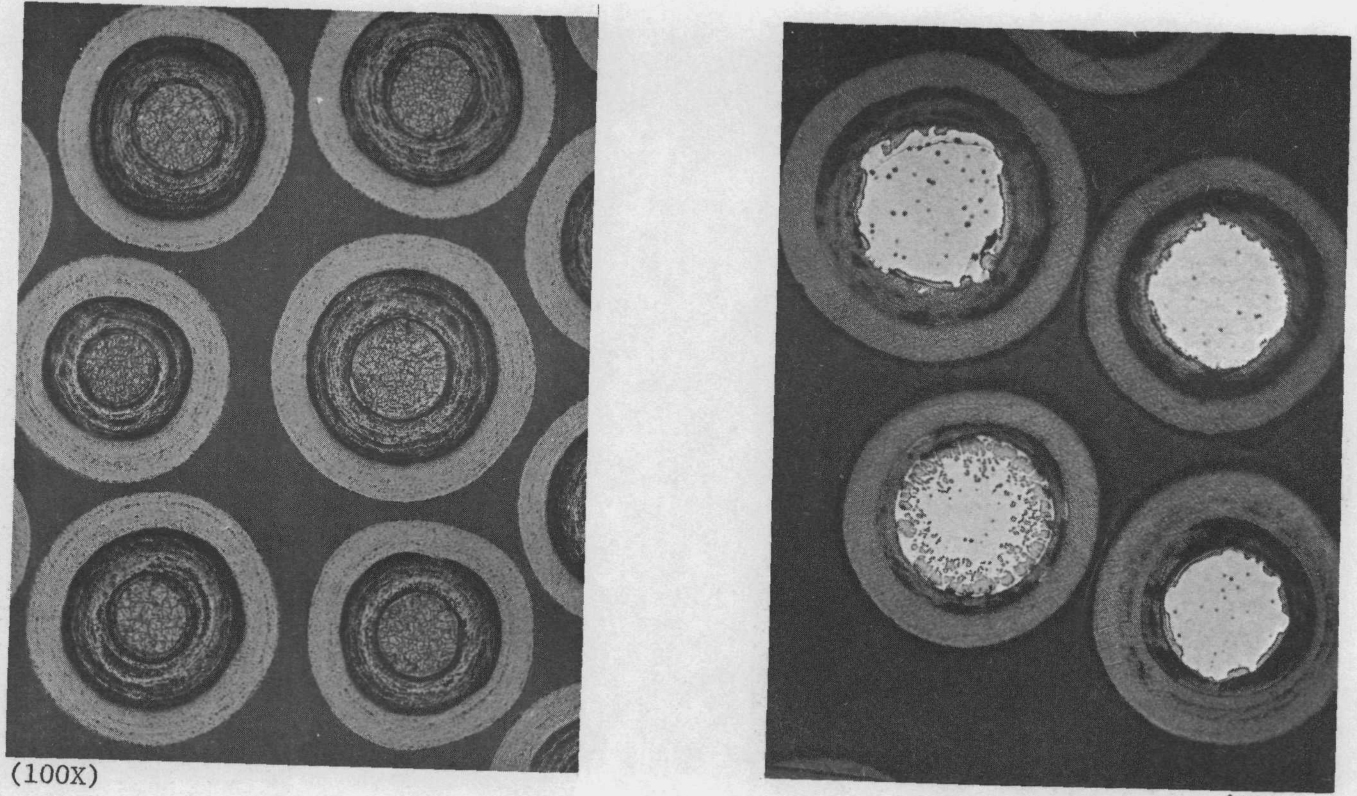

(100X)

(100X)

Fig. 3.17--BISO-coated particles from lot 3592-141E before (left) and after (right) irradiation in capsule P18

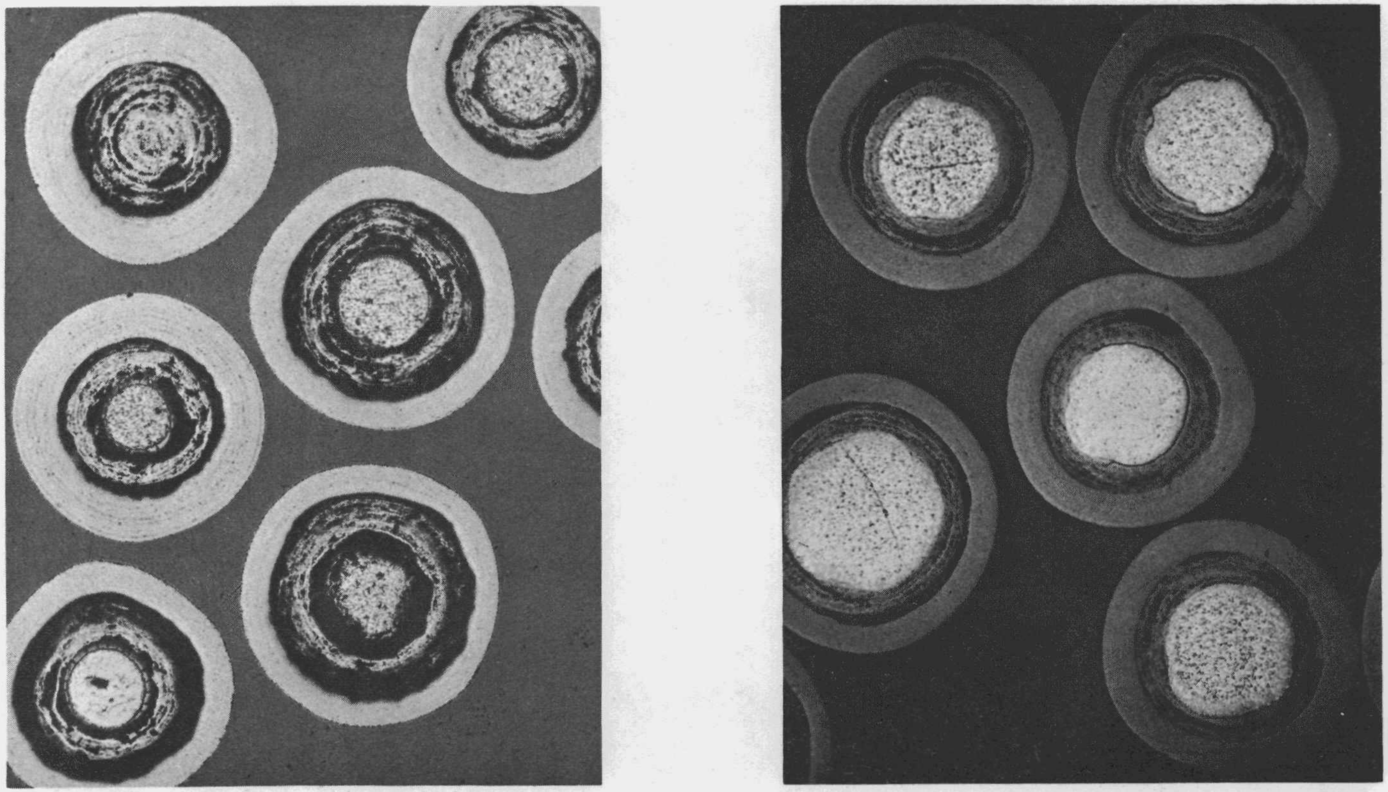

(100X)

(100X)

Fig. 3.18--BISO-coated particles from lot 3663-53E before (left) and after (right) irradiation in capsule P18

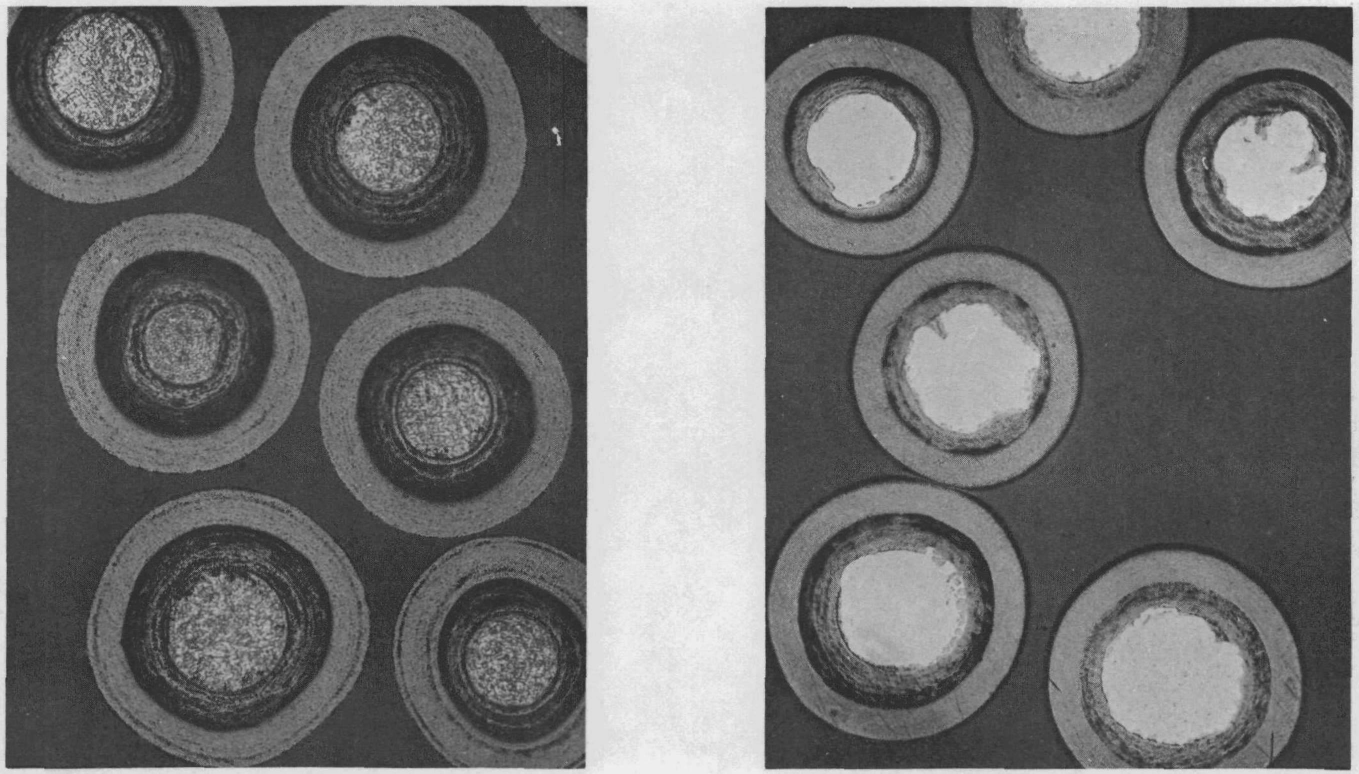

(100X) (100X)

Fig. 3.19--BISO-coated particles from lot 3592-143E before (left) and after (right) irradiation in capsule P18

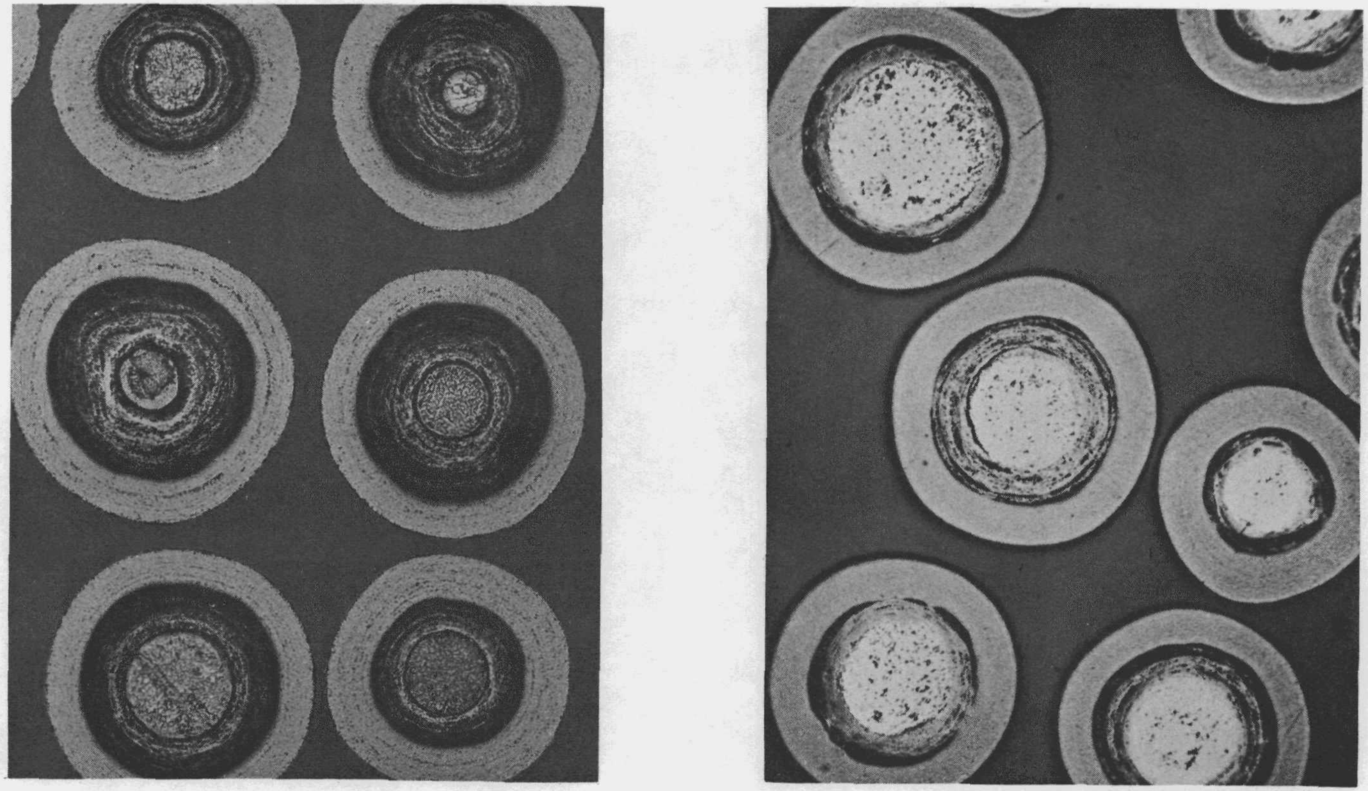

(100X) (100X)

Fig. 3.20--BISO-coated particles from lot 3592-145E before (left) and after (right) irradiation in capsule P18

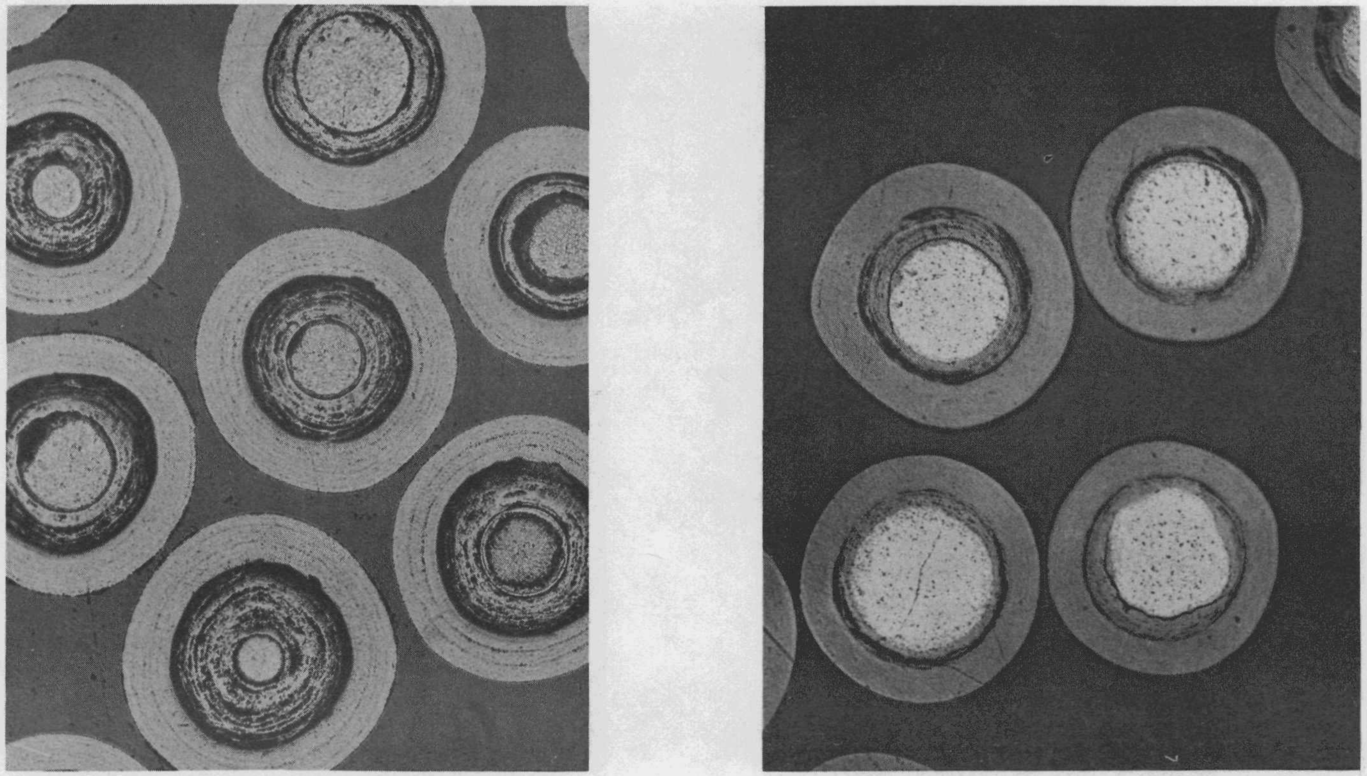

(100X) (100X)

Fig. 3.21--BISO-coated particles from lot 3663-39E before (left) and after (right) irradiation in capsule P18

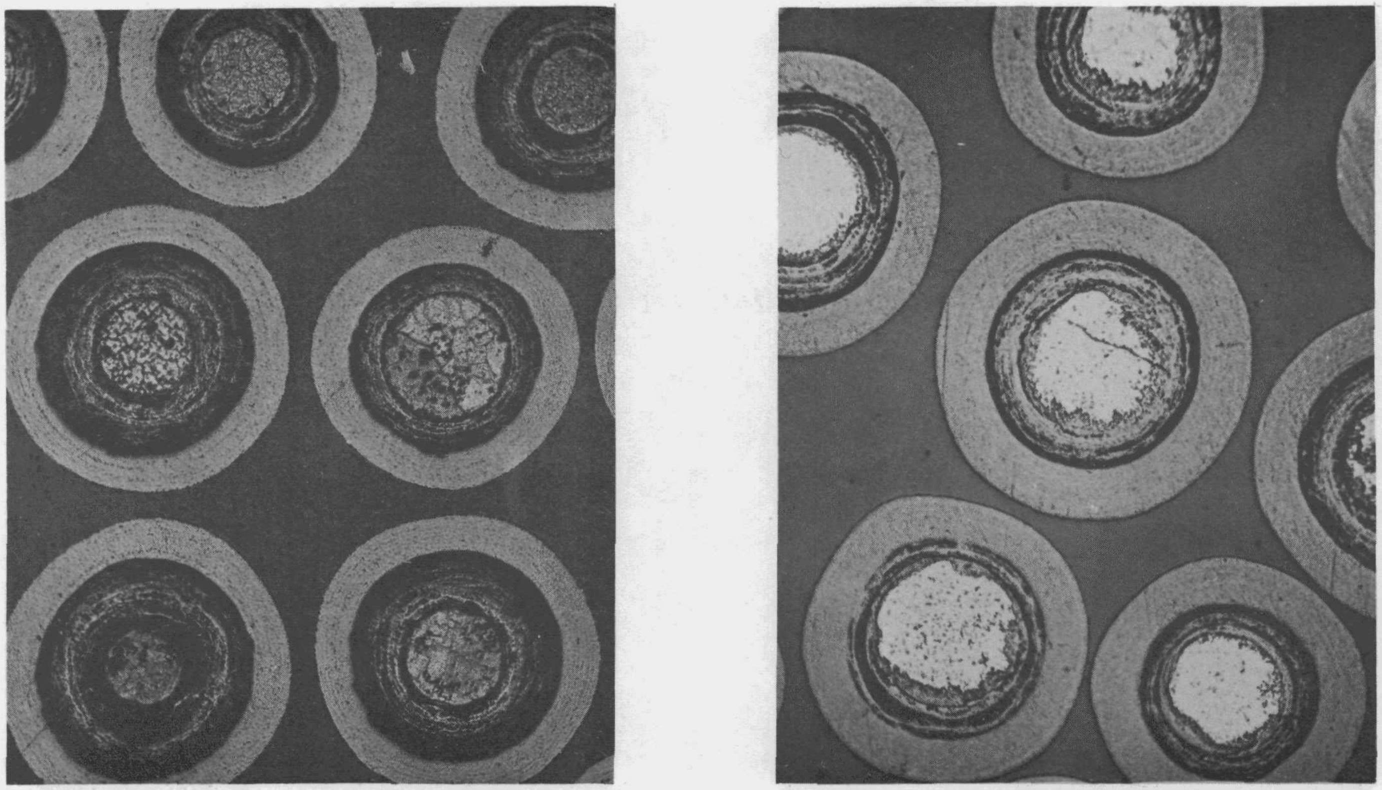

(100X)

(100X)

Fig. 3.22--BISO-coated particles from lot 3592-147E before (left) and after (right) irradiation in capsule P18

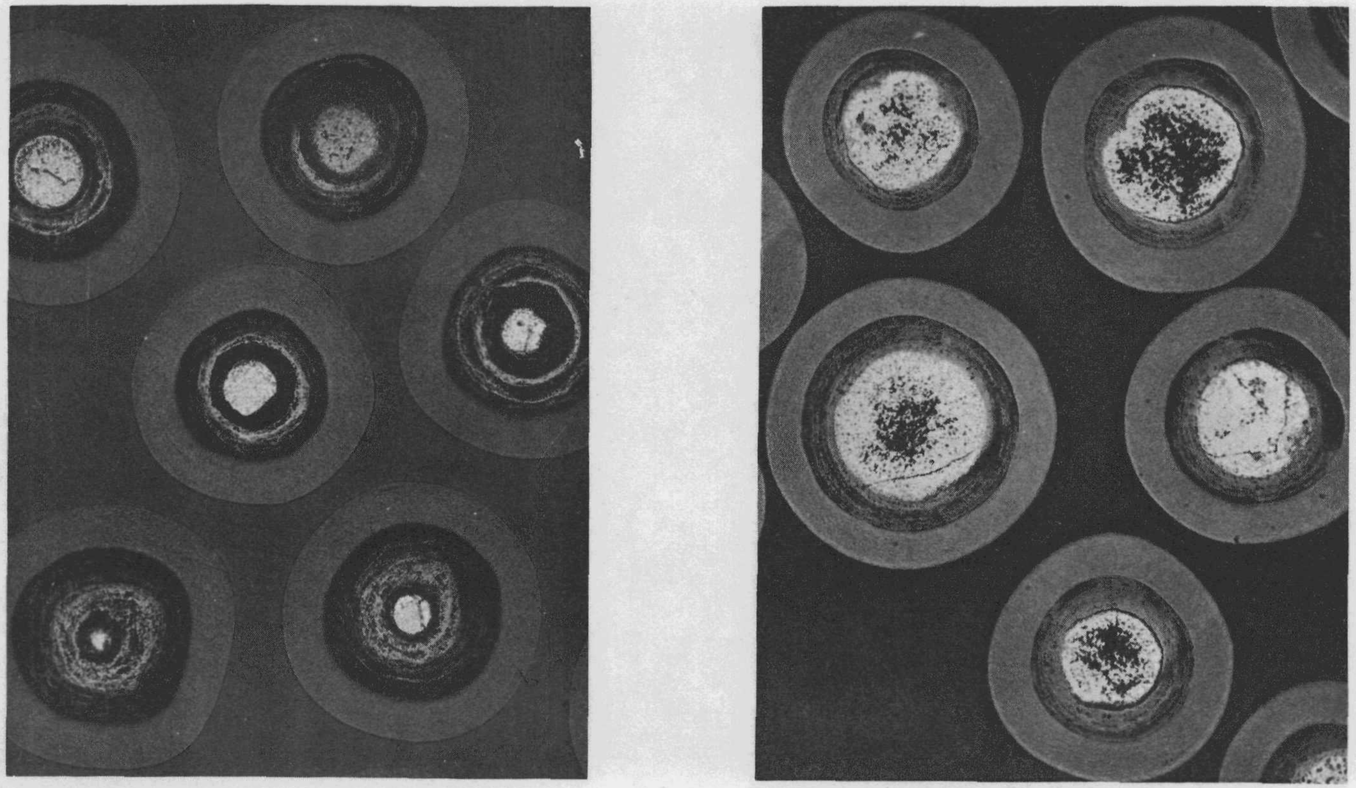

(100X)

(100X)

Fig. 3.23--BISO-coated particles from lot 3742-17E before (left) and after (right) irradiation in capsule P18

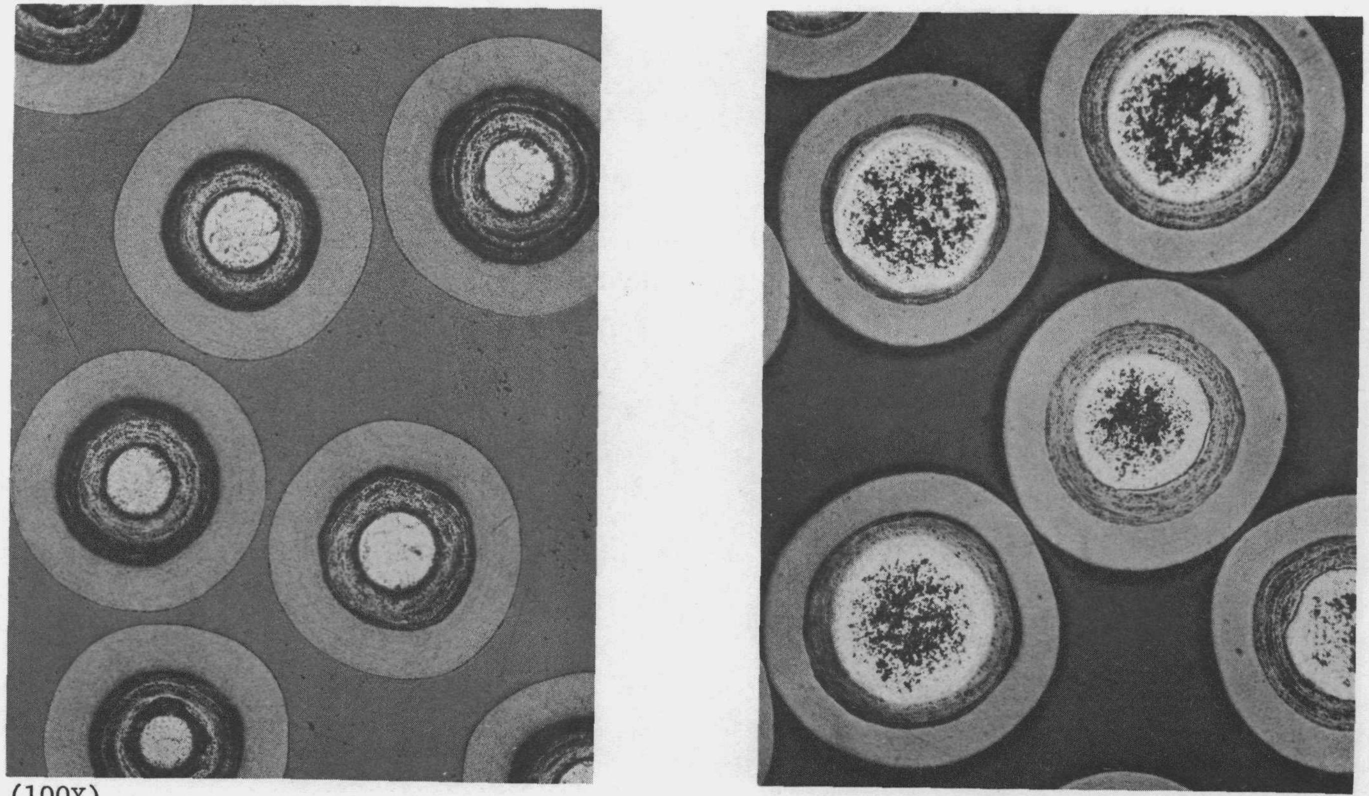

(100X)

(100X)

Fig. 3.24--BISO-coated particles from lot 3663-51E before (left) and after (right) irradiation in capsule P18

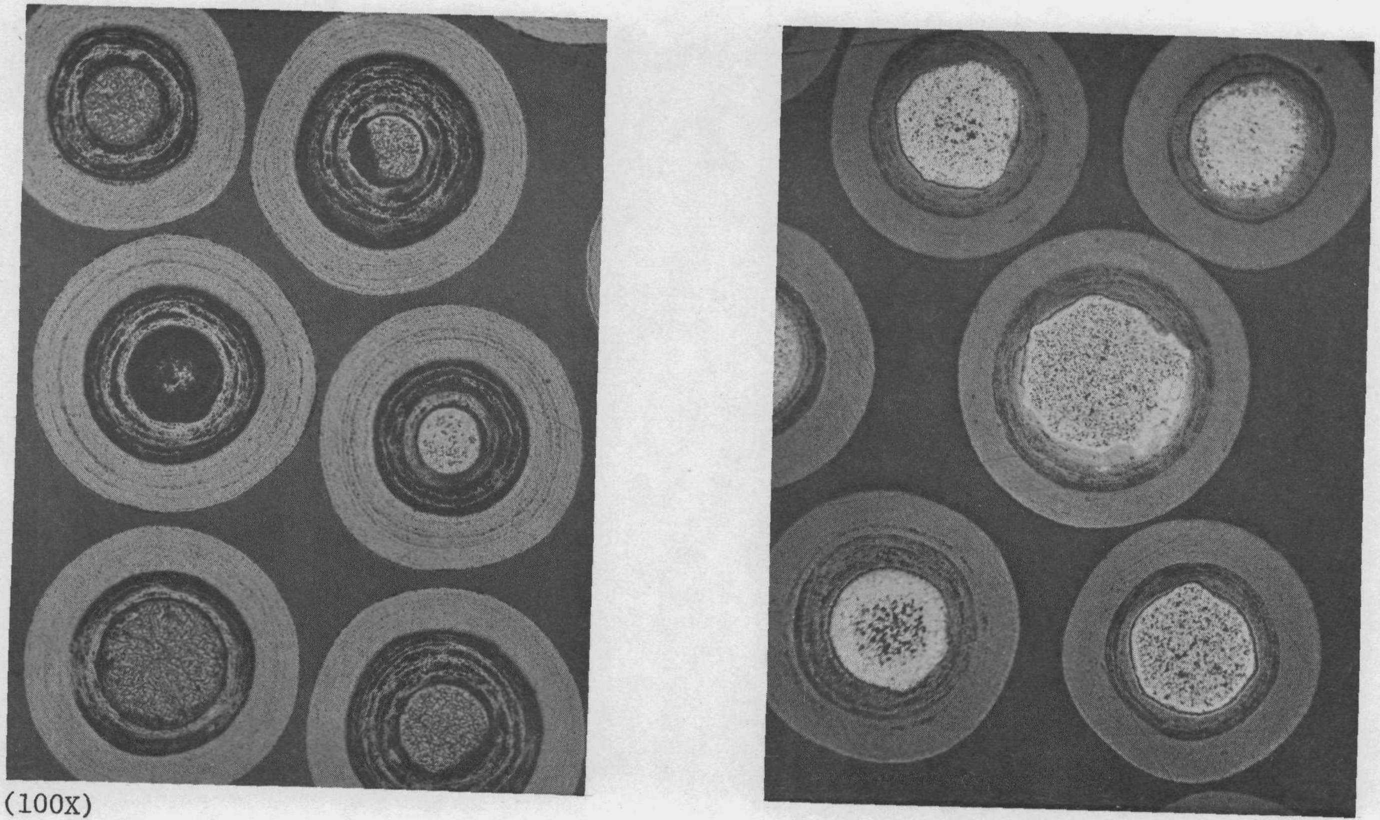

(100X)

(100X)

Fig. 3.25--BISO-coated particles from lot 3663-35E before (left) and after (right) irradiation in capsule P18

dose is estimated at 3.3×10^{21} n/cm^2 (E > 0.18 Mev) with an estimated fuel burnup of 18% FIMA.

Capsule P21. Capsule P21 is a second proof-test experiment to demonstrate the stability of TRISO-I- and TRISO-II-coated particles similar to those in capsule P20 to a higher fast-neutron exposure (85% to 100% of the full PSC fast-neutron exposure of 8×10^{21} n/cm^2) and full PSC fuel burnup. TRISO-coated samples prepared in both laboratory and production equipment are included. A detailed description of the samples being tested was given in an earlier quarterly report (GA-8725).

The capsule has completed its fourth of seven to eight cycles in the ETR in the I13NE core position. All samples are operating close to design temperatures of 1100° and 900°C. The fuel has reached an estimated fast-neutron dose of 3.3×10^{21} n/cm^2 (E > 0.18 Mev) with an estimated fuel burnup of 15% FIMA. The capsule experienced radiation activity in the lead tube junction box during its first cycle, but this problem appears to have been corrected. Six of the 15 fuel thermocouples are operating.

Capsule P22. Capsule P22 is the third proof-test irradiation experiment of TRISO-coated particles. The capsule design has been modified to allow 30 different samples to be tested instead of the 15 samples tested in previous capsules.

The samples are primarily TRISO-II-coated fissile-size particles prepared in large-scale (production) equipment, and also some TRISO-I particles; these are designed to evaluate the effects of PyC type, PyC density, and SiC thickness on stability at high fast-neutron exposures. Also included are laboratory-prepared TRISO-II, TRISO-I, and advanced-design SiC-coated fissile-size particles, as well as TRISO-II design coatings on fertile-size cores.

The experiment is designed to be irradiated to a fast-neutron dose of 7 to 8×10^{21} n/cm^2 (E > 0.18 Mev), which is 85% to 100% of the PSC maximum dose. The fuel is designed to achieve the maximum PSC burnups of 20% and 7% FIMA for fissile and fertile particles, respectively. The design temperatures are 1300°, 1100°, and 900°C.

The capsule has completed its second cycle of irradiation. It will be irradiated for seven to eight cycles in the I13SW core position. The temperatures in the three high-temperature cells range between 1095° and 1325°C. The greater temperature difference occurs between thimbles of fissile particles and thimbles that contain mixed fissile and fertile particles. A reevaluation of the thermal characteristics of mixed fissile-fertile beds indicates that the observed temperature difference could result. Correction for the mixed-bed loadings will be made in future capsules. The lower-temperature cells have been operating close to design. The estimated fast-neutron dose is 1.3×10^{21} n/cm^2, and the burnup is estimated at 8% FIMA. Nineteen of the 25 fuel thermocouples are still measuring temperatures.

Capsule P23. Capsule P23 is a new short-term (two-cycle) irradiation test in ETR to evaluate the ability of low-density PyC coatings to survive the initial rapid densification at low fast-flux exposures. (These lower-density coatings offer promise of improved performance at high exposures because of greatly reduced anisotropic dimensional changes.)

The capsule was inserted in the ETR for cycle 99 and will be irradiated to a fast-neutron dose of about 2 x 10^{21} n/cm^2 at temperatures of 900° and 1200°C. The burnup will be about 13% FIMA. Both TRISO- and BISO-coated particles will be tested. One fuel rod is also included.

Capsule FR-1. The objectives of the FR-1 fuel rod irradiation experiment are to test 1/2-in.-diameter by 1-in.-long fuel rods to a fast-flux exposure of 5 to 6 x 10^{21} n/cm^2 at 1300° and 900°C with full burnup of the fissile particles. Three different matrix compositions (D-25, D-38, and D-24) and two particle types (LTI TRISO-II and HTI TRISO-II) are being tested in the five fuel rod samples. Blends of fissile and fertile TRISO-coated particles are used in each rod, and loose fissile- and fertile-coated particles are tested with each fuel rod for a direct comparison of coated particle performance loose and in the rods.

Capsule FR-1 has completed its third cycle of irradiation in the ETR in the F13NE core position. It is operating satisfactorily with temperature of 1210° to 1240°C in the four fuel rods designed to operate at 1250°C, and 1030°C in the one rod designed for 900°C. Temperatures in the control samples of loose-coated particles in each cell are approximately 1000°C in the high-temperature cells and approximately 700°C in the low-temperature cell. The fuel has reached an estimated burnup of 14% FIMA for fissile particles with an estimated fast-neutron dose of 2.1 x 10^{21} n/cm^2.

Capsules FR-2 and FR-3. Fuel rod capsules FR-2 and FR-3 are companion experiments to capsule FR-1, but are designed to achieve higher exposures. Both will be irradiated to fast-neutron doses of 7 to 8 x 10^{21} n/cm^2 with fissile particle burnups of 20% FIMA. The design temperatures in FR-2 are 1250°C (three rods), 900°C (one rod), and 600°C (one rod); in FR-3 four rods are at 1250°C and one is at 900°C. Both capsules have been completed and shipped to the ETR for irradiation beginning with ETR cycle 100. Figure 3.26 shows the fuel rod samples that were included in capsule FR-3.

Capsule G13. Capsule G13 is a follow-on experiment to capsule G12. It contains needle-coke graphite grades H-327, 9567 (Nuclear II purity), NC-8 (EGCR), and isotropic grade RC-4. This capsule, after completing a six-cycle irradiation in ETR, has been returned to Gulf General Atomic and dismantled for examination. The five-cell capsule was subjected to fast-neutron doses of 4.6 to 5.5 x 10^{21} n/cm^2 ($E > 0.18$ Mev) in cells one through four and 2.8 x 10^{21} n/cm^2 in cell five; the irradiation temperatures were 600° to 1050°C.

Test procedures being adapted to hot-cell techniques include, in addition to uniaxial tensile tests, burst tests on hollow cylinders. These tests will be developed to assess the effects of uniaxial and biaxial stresses on graphites at web positions of a fuel element. A preliminary survey shows the feasibility of hydraulically pressurizing cylinders of graphite, and it is intended to pressurize closed cylinders with oil to obtain shear stress values and to pressurize a rubber tubular insert in an open-ended cylinder to obtain tensile stress values.

Fixtures have been designed and manufactured for tensile testing 1-in.- and 2-in.-long specimens from capsule G13. Preliminary results indicate that short specimens can be used for generating test data providing grips are glued to their ends in a special fixture. Subject to further test trials on

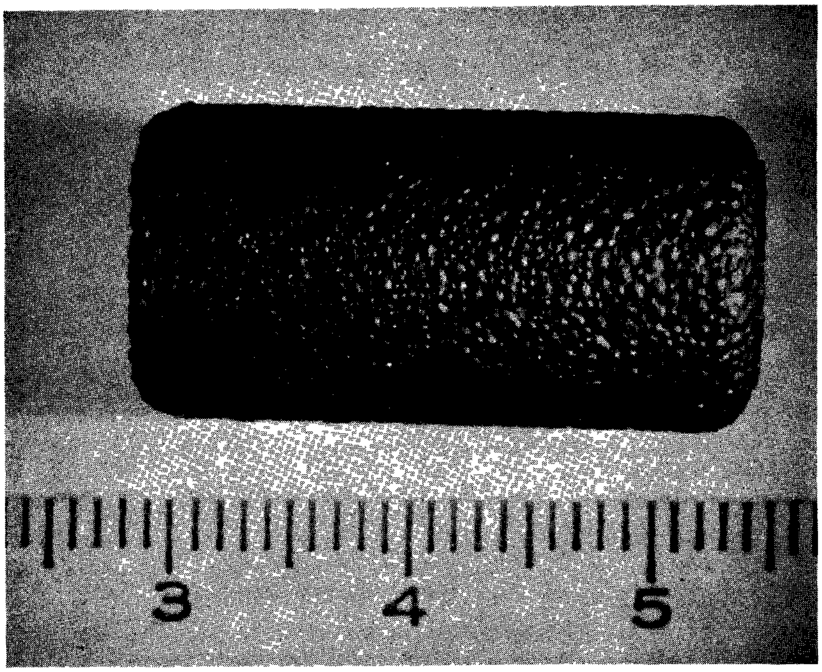

Rod C-70, cm scale (3X)

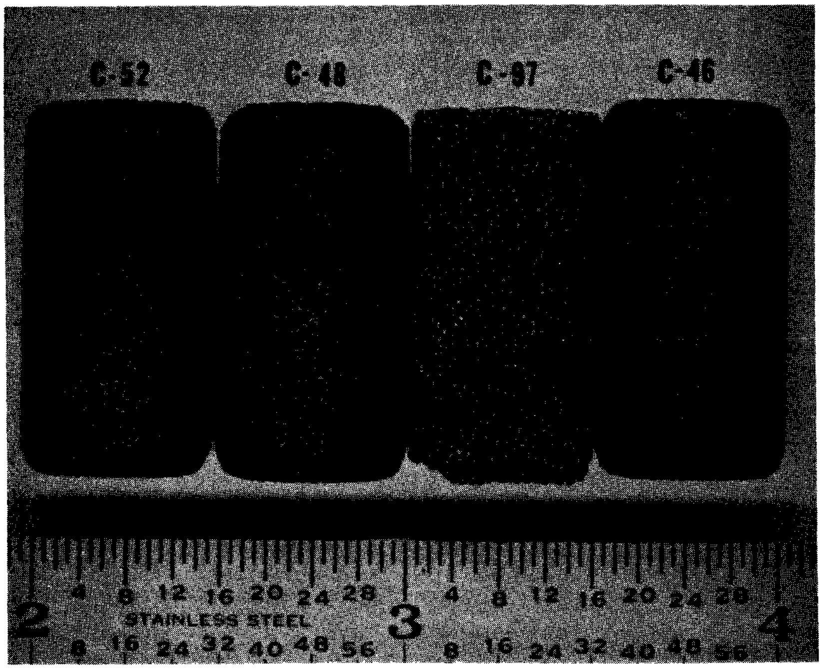

Rods C-52, C-48, C-97, and C-46, inch scale (2X)

Fig. 3.26--Fuel rod samples for FR-3 irradiation capsule; samples contain TRISO-II-coated particles and are fabricated by the injection-molding (C-52, C-48, C-46, and C-70) and the overcoat-matrix (C-97) processes

unirradiated materials and satisfactory decontamination of selected samples taken from the above capsules, the various graphites will be vibration-cycled and mechanically tested to establish any changes in their mechanical properties.

HELIUM PURIFICATION SYSTEM

The objective of this subtask is to determine operating conditions of the helium purification system's sorbent beds as a function of bed temperature, coadsorbate interference, regeneration techniques, aerosol removal, and adsorption bed materials, by means of laboratory-type experiments.

Sorbent Beds

Low-temperature Adsorption Studies. Low-temperature adsorption studies have been performed to test various candidate activated carbons for the ultimate selection of an adsorbent to be used in the low-temperature sorber beds. The adsorbent should have the highest capacity per unit volume for carbon monoxide while restricting the breakthrough of krypton.

The procedure used for determining CO adsorption isotherms employed an automatic recording electro-microbalance to determine the amount sorbed, and a McLeod gage to determine the amount of CO in the gas phase.

On the basis of low-temperature adsorption data presented in previous quarterly reports (GA-8038, GA-8725, and GA-8879), MI-6736 activated carbon appeared to be the logical choice. However, it was found that the manufacturer's designation applied only to one specific mesh size of the particular type of activated carbon. The mesh size desired for the sorber beds (6-10 mesh) is designated by the manufacturer as BC-582 and is presumably the same material as MI-6736. Accordingly, the BC-582 carbon was selected as the low-temperature adsorbent, though previous tests with it had not been performed at Gulf General Atomic. When the material was received from the manufacturer carbon monoxide isotherms at -300°F and -320°F were determined and were compared to those of MI-6736 at -320°F (see Fig. 3.27). The data indicate no significant difference in the behavior of the two materials. No low-temperature determinations of krypton dynamic adsorption coefficients and breakthrough fronts were made, and work on the low-temperature adsorber screening tests has been concluded.

Hydrogen Gettering Studies. The hydrogen gettering tests were initiated to provide information on the suitability of hot titanium sponge for the removal of hydrogen and tritium from the reactor coolant. Specifically, information was needed on (1) the capacity of titanium metal for hydrogen absorption as a function of temperature, (2) the dynamic absorption characteristics of the hydrogen-titanium sponge system under simulated reactor conditions, and (3) desorption or regeneration characteristics of hydrogen-saturated titanium sponge bed at design reactor conditions.

The experimental work in this area is complete. The procedure and results of studies for items (1) and (2) above have been presented in previous quarterly reports. The results of a final desorption experiment are reported below.

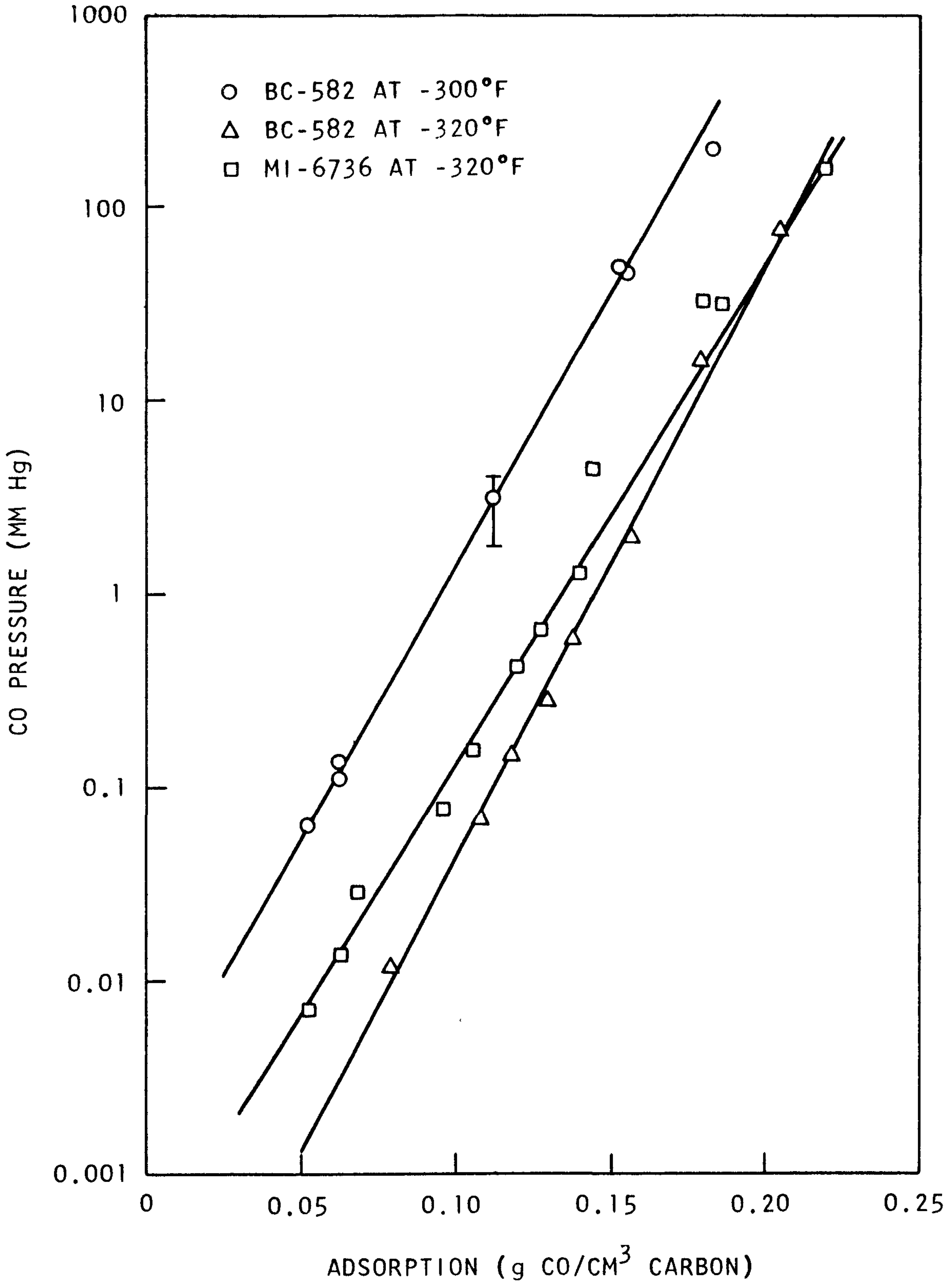

Fig. 3.27--CO adsorption isotherms for BC-582 and MI-6736 at -300° and -320°F

A packed bed of titanium sponge weighing 3320 g, 1.75 in. in diameter and 30 in. long, was heated in a clamshell furnace. A hydrogen supply was connected to one end of the system and a vacuum pump was provided at the other. The pumping speed (15 cfm at pump throat) and the pumping conductance of the vacuum line (4 ft of 3/4-in. -ID tubing) were chosen to simulate the pumping conditions of the reactor units. A mercury manometer and a McLeod gage were provided to monitor the hydrogen pressure at either end of the titanium sponge bed during regeneration.

The furnace was first brought to the design temperature while the packed bed was evacuated to less than 10 μm. The measured axial temperature of the bed ranged from 500° to 660°C, though the bulk of the material was above 600°C.

Hydrogen was then slowly admitted to the titanium sponge until 31 ft^3 was absorbed. This loading corresponds to an average empirical formula of TiH. At this point, the hydrogen overpressure was observed to be 300 mm of mercury. Evacuation was then started and the pressure at each end of the packed bed was monitored frequently. The experimental data are shown in Fig. 3.28 in a plot of hydrogen pressure versus time. Pressure data were obtained both during evacuation, while the main pump valve was open, and after the main valve had been closed for 1 to 5 min. The latter measurement should more closely reflect the true equilibrium hydrogen pressure above the titanium sponge.

It was observed that after 32 hr of evacuation at 630°C, the equilibrium hydrogen pressure was still in excess of 100 μm of mercury. At this pressure and temperature, however, the average hydrogen concentration in the sponge would correspond to approximately $TiH_{0.01}$. Thus, the material was considered to have been 99% regenerated.

Strength of Sorbent Materials. The purpose of these tests was to determine the extent of degradation of the sorber material to be used in the PSC reactor in the event of rapid increase in flow rate during a sudden depressurization, or during the thermal cycling of beds as a result of regeneration procedures.

The high-flow experimental procedure was to flow dry laboratory air through a 4-in.-diameter by 10-ft-high column of the sorbent materials of interest. The materials tested were activated carbons AC and BC-582, Type 5A molecular sieve. Gas velocities up to about 250 ft/min were used. Both upflow and downflow tests were conducted. A full-flow millipore filter was used downstream from the bed to collect the dust generated.

The runs were made for 1/2 hr, followed by 5 to 6-1/2 hr at each specific velocity. Table 3.11 contains the results. The two time intervals were used to determine whether the dust collected was from constant generation or from liberation of trapped dust generated during the loading operation. It was observed, during the molecular sieve run, that the walls of the vessel were heavily coated with dust during the filling operation and, further, that the walls tended to clear up during the run periods.

The amount of dust collected during the runs was small. The data indicate that the largest part of the dust collected during the tests was liberated

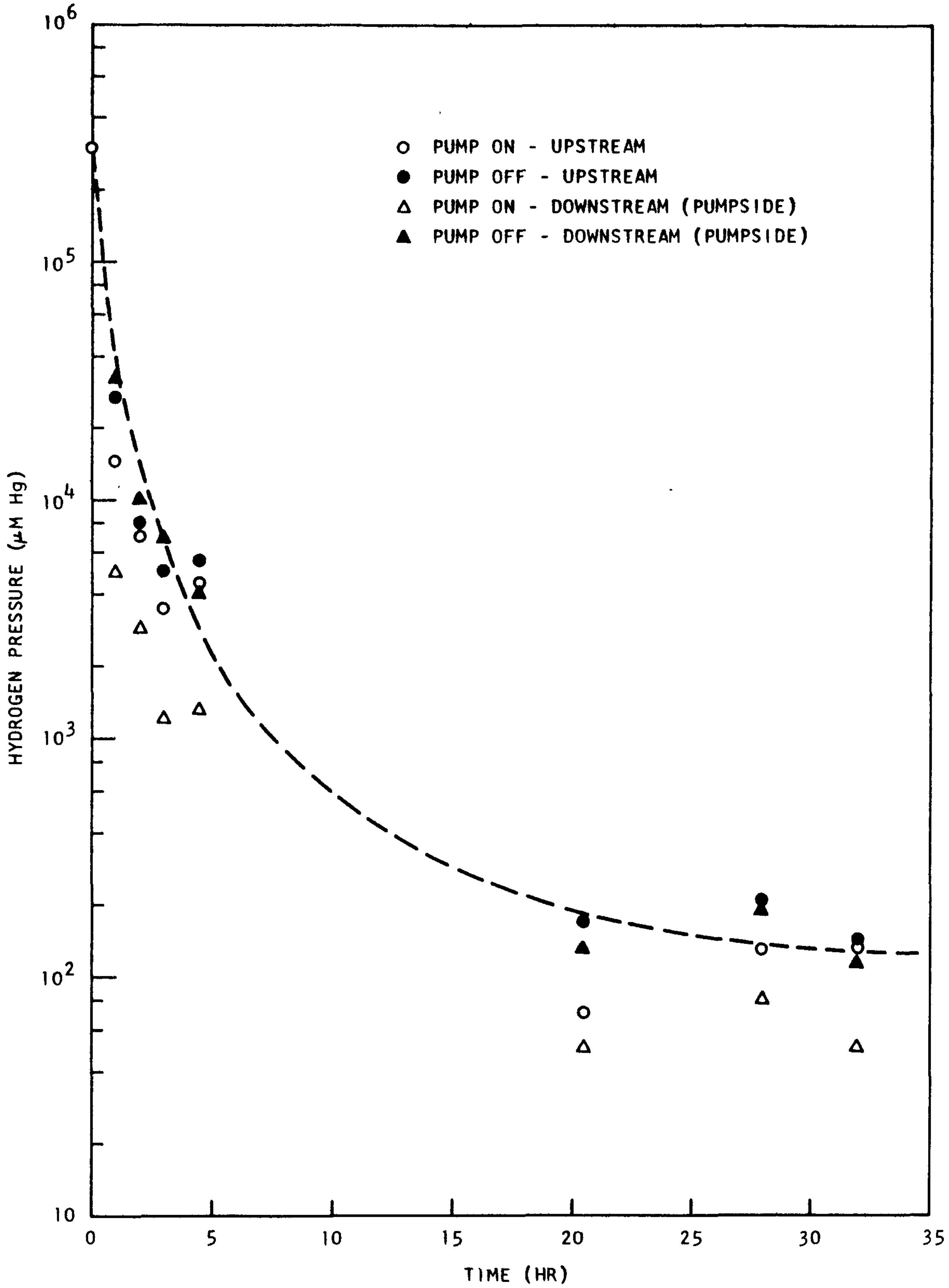

Fig. 3.28--Desorption of hydrogen from titanium sponge

Table 3.11

EFFECT OF GAS FLOW VELOCITY ON DEGRADATION OF TRAPPING SYSTEM MATERIALS

Material	Packed Density (lb/ft^3)	Time to Fill (hr)	Run Time (hr)	Superficial Flow Velocity (ft/min)	Flow Direction	Δp (psi)	Dust Collected (mg)	Notes
AC Charcoal, 6-10 mesh (31-1/2 lb)	36.3	1	0.5	50	Down	1.5	4.1	Dust removed appears to be that trapped during filling operation.
			5.0	50	Down	1.5	0.6	
			0.5	100	Down	4.3	3.2	
			6.0	100	Down	2.8-5.3	2.2	
			0.5	200	Down	12-14	(a)	Filter discolored evenly.
			6.0	200	Down	13-18	(a)	Trace.
			0.5	267	Down	26	(a)	Filter discolored evenly.
			0.5	200	Down	13	(a)	Trace.
			0.5	50	Up	1.5	(a)	Trace.
			0.5	123	Up	6-7	4.6	Bed swelled 3 mm, resettled 2 mm.
							14.7	
BC-582 Charcoal, 6-10 mesh (29-1/4 lb)	33.2	3/4	0.5	50	Down	1.8	2.1	
			6.5	50	Down	1.8	(b)	
			0.5	100	Down	5.2	2.2	Bed settled 1/16 in.
			0.5	200	Down	16	2.4	Additional fines discolored filter, bed settled additional 1/6 in., total 1/8 in.
			0.5	248	Down	27	0.5	Additional fine discolored filter.
			0.5	50	Up	1.5	(b)	
			0.5	123	Up	7	0.6	Bed swelled about 2 in., did not resettle.
							7.8	
Type 5A Molecular Sieve (1/8-in. pellets)	46	2	0.5	50	Down	---	44.2	Dust removed during entire experiment appeared to be that generated and trapped during filling operation.
			6.5	50	Down	---	10.1	
			0.5	100	Down	3.5	37.0	
			6.5	100	Down	3.5	<10	
			0.5	200	Down	10.8	93.0	Glass tower became coated with dust while loading and cleared up during testing operations.
			6.5	200	Down	10.8	9.3	
			0.5	316	Down	23	42.3	
			0.5	50	Up	1.1	(b)	
			0.5	100	Up	3	(b)	
			0.5	200	Up	9.6	249.2	Top 10 in. swelled 2-1/2 in., settled only 1/4 in.
			0.5	200	Up	9.6	79.4	All but bottom 4 in. swelled by 2-1/2 in. over-all.
							574.5	

[a] Not weighable.

[b] None visible.

rather than generated. It was concluded that the dust generation rate as a result of particle abrasion under these test conditions in insignificant.

The thermal cycling procedure consisted of saturating a sample of activated carbon (BC-582) with nitrogen at -320°F and regenerating as rapidly as possible to 300°F with preheated helium. This procedure was repeated ten times. A sample of Type 5A molecular sieve was treated similarly, except that it was saturated with water vapor at ambient conditions and regenerated to 600°F with preheated helium. This procedure was also repeated ten times. At the conclusion of the tests the materials were examined. No appreciable degradation was observed. The molecular sieve material, however, appeared much harder after completion of the test, suggesting that the clay binder of the as-received material is substantially unfired.

Within the limits of the tests reported here, there appears to be no evidence that the adsorbents experience appreciable physical degradation during thermal cycling or during periods of increased gas velocity. These experiments have been concluded.

Task IV

FUEL ELEMENT PROOF TESTING

The objective of this task is to demonstrate suitable performance of a test fuel element(s) based on the plant fuel element design by means of irradiation testing at expected fuel operating temperatures at greater than expected temperature gradients and up to or exceeding approximately one third of the planned fuel element burnup in the plant.

During the quarter the fabrication and assembly of the second proof test element was completed. The test element was shipped to the site and is awaiting insertion into the reactor during the current outage. The element will be installed into the E10-01 instrumented core position.

All of the required rods were carbonized in place in the different graphite sections with the exception of the annular thermocouple rods, which were carbonized separately. Various "piggyback" samples were also included in the test element. Prior to carbonization a gamma-scan was made on each cured rod. The values obtained indicate that all rods were well within ±5% fuel loading. Representative rods were removed from each section after carbonization and inspected. The external appearance and dimensions of the rods were satisfactory. Photographs and careful dimensional measurements were taken on each rod used in the element. A typical 14.3-in.-long rod is shown in Fig. 4.1, and four 1.0-in.-long rods are shown in Fig. 4.2.

The element has a total uranium loading of 450.18 g (419.35 U^{235}). The total thorium loading is 2153.41 g. The weight of the completed element is 88.1 lb.

The as-built primary coolant gaseous activity contribution from the second proof test element computed by the RAD code is 0.06 C. The activity as seen by the Peach Bottom Cary primary coolant activity monitor is predicted to be 0.03 C. This compares directly with 1.59 C computed using the same methods for the first proof test element.

The calculated maximum fuel centerline temperature for the initial operation in core position E10-01 is 2150°F using a fuel rod conductivity of 4.1 Btu/hr-ft-°F for a thermal power of 225 kw. After 300 full-power days, the thermal power will decrease to about 200 kw, and the maximum fuel centerline temperature is calculated to be 2090°F using a fuel rod thermal conductivity of 2.0 Btu/hr-ft-°F.

The information package for the second proof test element was completed and sent to the Philadelphia Electric Company.

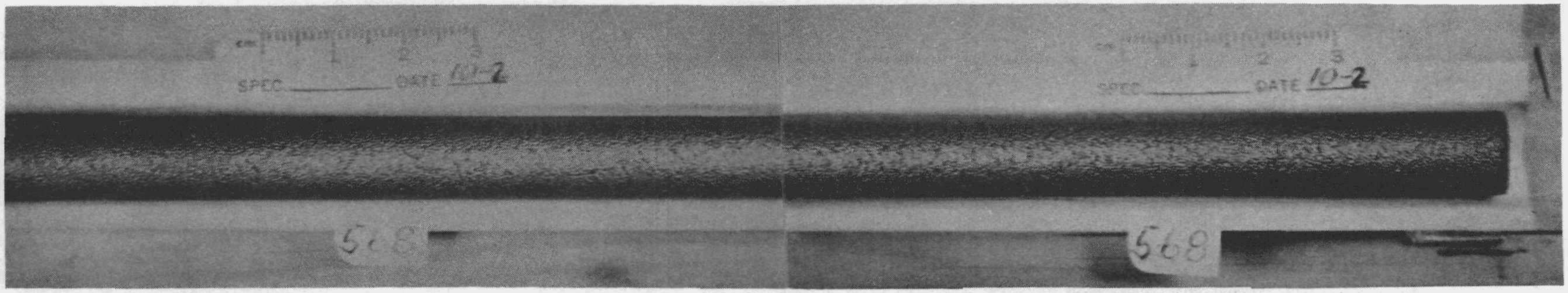

Side view

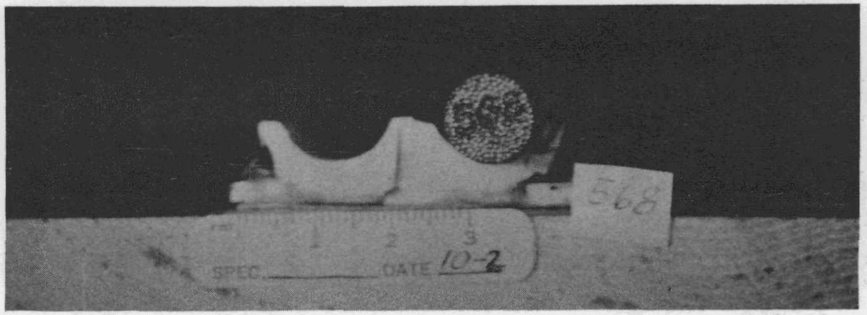

End view

Fig. 4.1--Typical injection-molded fuel rod 14.3 in. long fabricated for proof test element No. 2

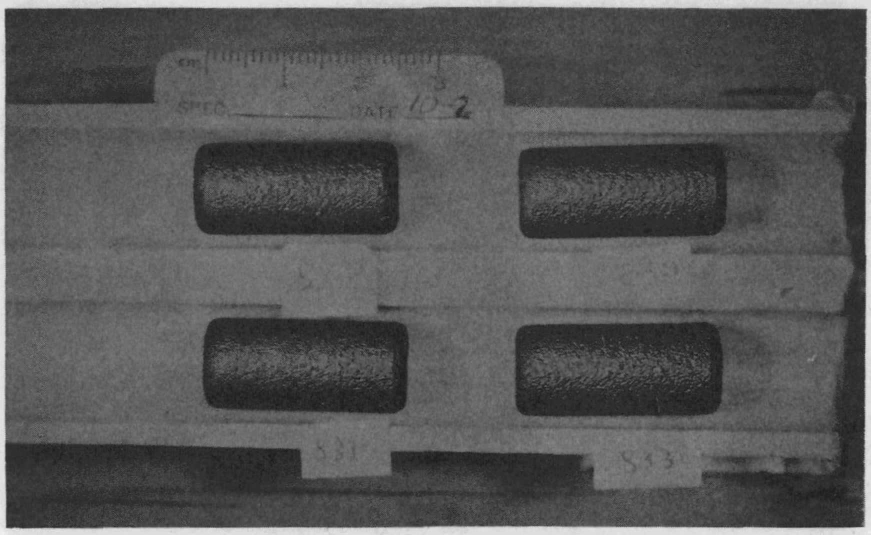

Fig. 4.2--Four typical injection-molded fuel rods 1.0-in. long fabricated for proof test element No. 2

Task I

FUEL TRANSFER MACHINE

The objective of this task is to establish the suitability and maintainability of the fuel transfer machine for use in the plant by means of testing of the fuel transfer machine with a segment of a dummy core, and by carrying out tests in helium at the temperature and chemical impurity level expected in the plant of critical components, as necessary.

DESIGN AND FABRICATION

The study initiated during the previous quarter of the fuel transfer machine operation over the fuel shipping cask was completed. It was found necessary to provide a stop ring on the outer tube to properly operate on the shipping cask. Drawings of this ring were completed, and the part is being fabricated.

Another interference study was initiated and completed this period. It was found that the remote electrical disconnect for the grapple head would interfere with the fuel storage rack when the machine was translating in the up direction. The mounting bracket for this connector was redesigned, and fabrication is under way.

Assembly of the fuel transfer machine progressed during this period. The main drive mechanism is approximately half complete, and assembly work on the telescoping tubes is under way.

The upper housing for the fuel handling machine was received from the fabricator and assembly of this unit is now being completed.

Figures I.1, I.2, and I.3 are photographs of components for the index arm drive assembly and azimuth drive assembly all of which were fabricated by Gulf General Atomic.

CONTROL SYSTEM

Electrical design of the machine wiring and hardware is complete. The design of the cabling and interlocks with all other equipment is complete and drawings have been released for fabrication.

Effort is now being directed to detailing the test procedures to be used during the Phase III and IV programs.

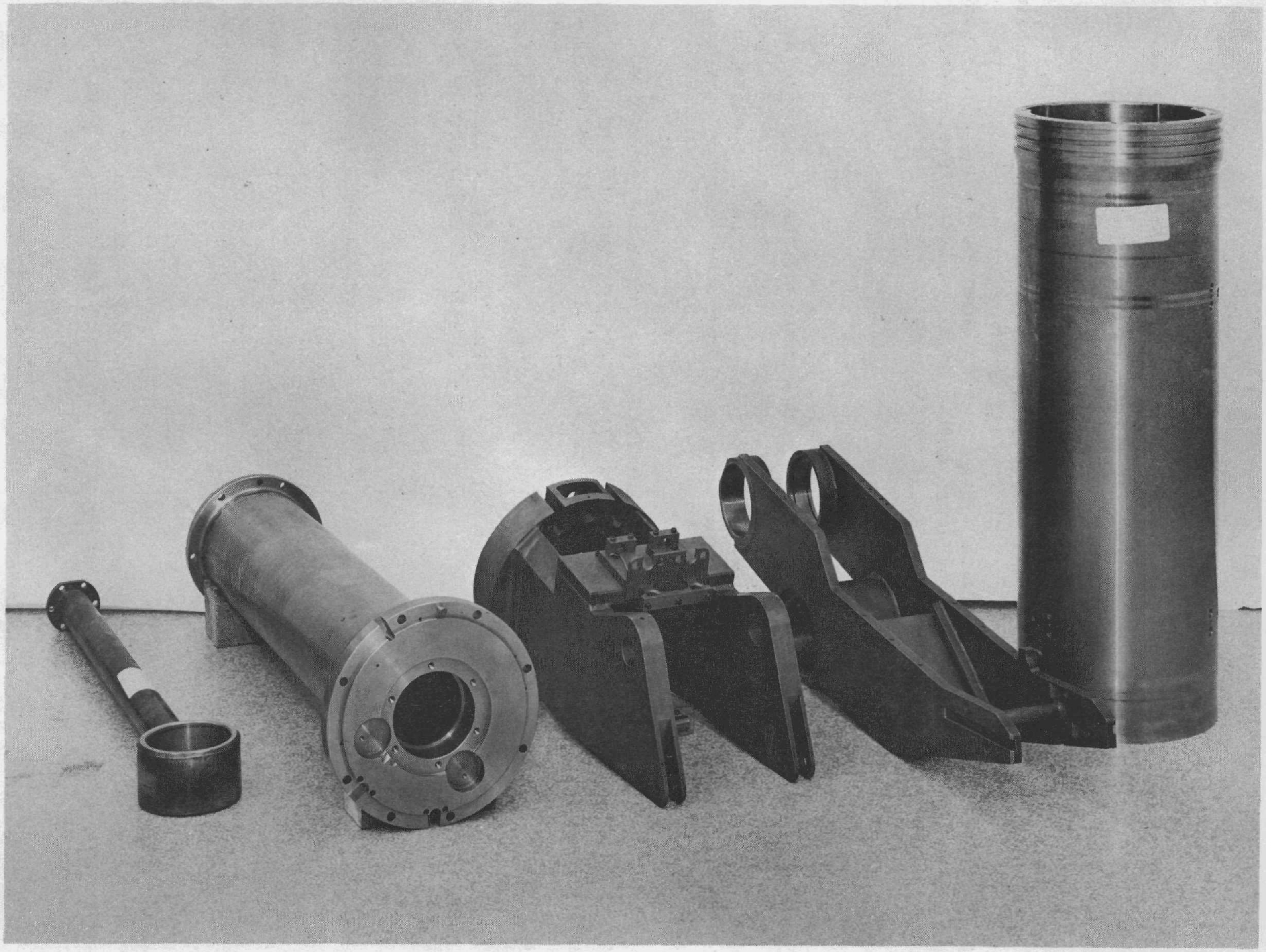

Fig. I.1--Index arm and support assemblies

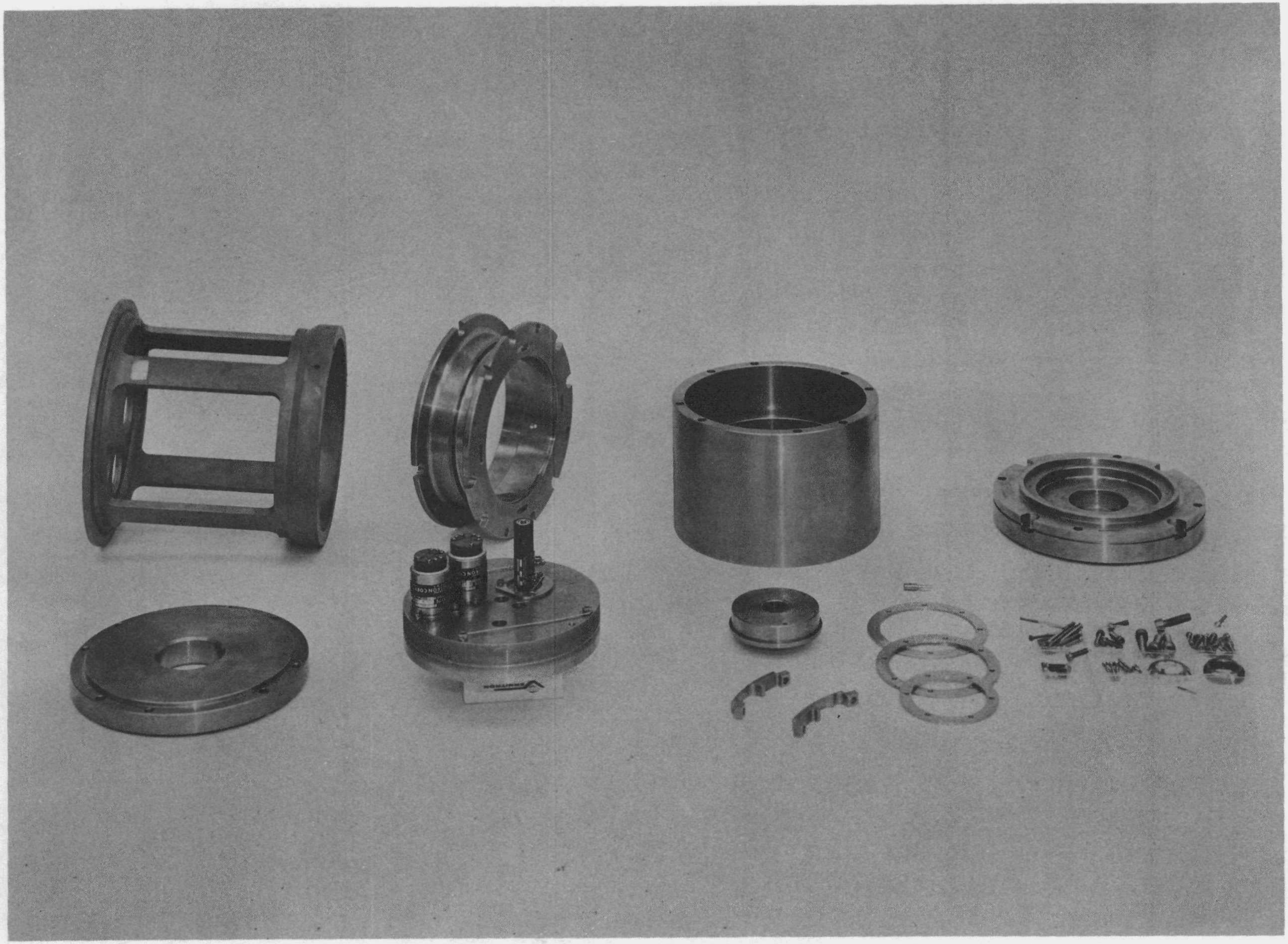

Fig. I.2--Index arm motor drive components

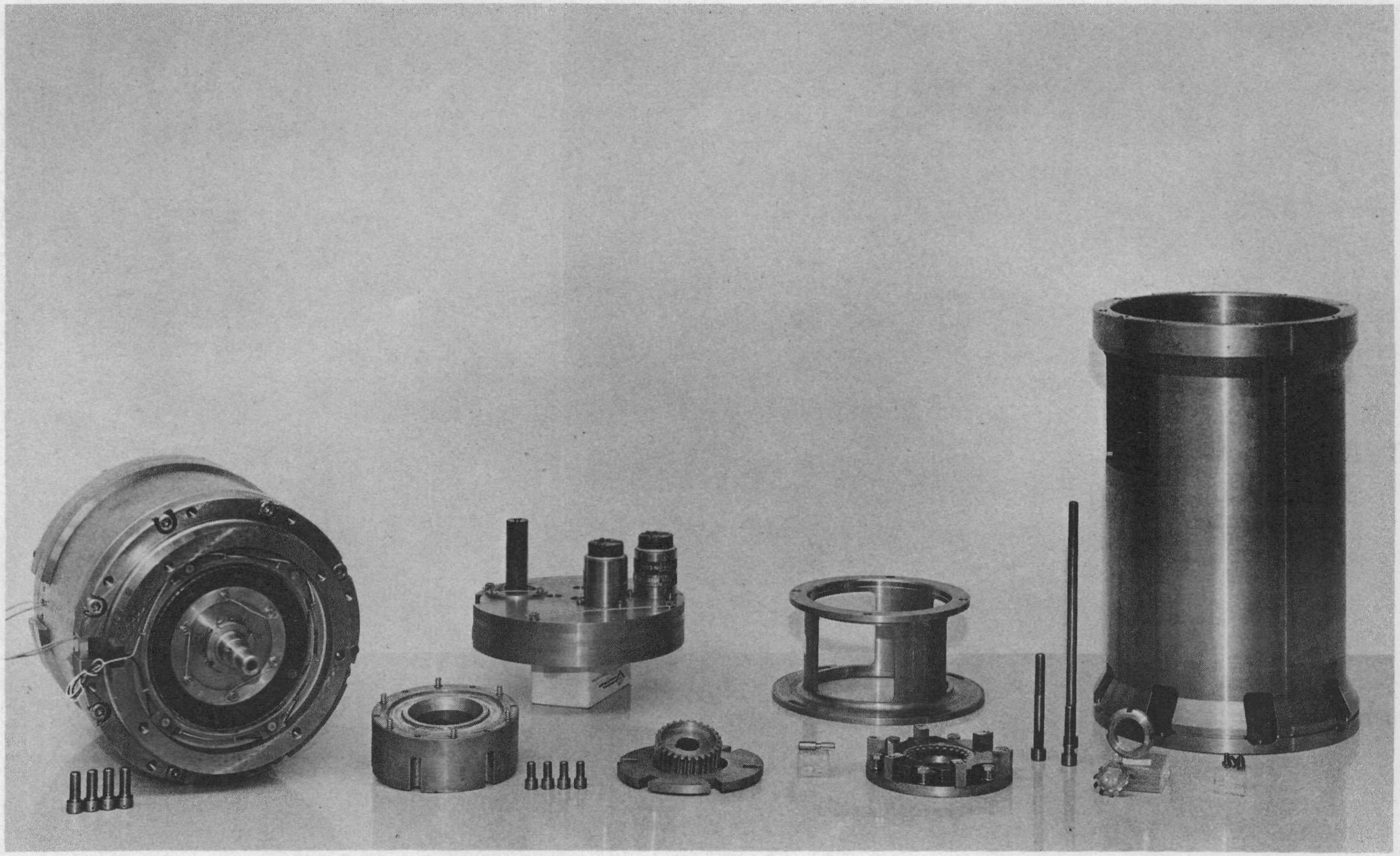

Fig. I.3--Azimuth drive motor assembly and connecting spool piece

PART II

PRIVATELY SPONSORED RESEARCH AND DEVELOPMENT PROGRAM

(Not the Subject of AEC Reimbursement)

The fuel handling machine controls are now well into the fabrication stage. The checkout of final hardware is progressing as individual areas are completed, and computer programming is now moving from flow block diagrams to actual machine language routines.

Assembly is under way on the controls sections of the operator's console and all of the equipment cabinets. Essentially all metal work has been designed and released for fabrication. The manual control panel and punched tape control panel are assembled and ready to be installed in the system. Schematics of the ac and dc power distribution systems are complete. These include the switching circuits of the master control that turn the system on and off.

Wire lists are being prepared for wiring the last section of the digital logic rack. The vertical drive logic is complete and has been successfully tested with a simulated mechanical drive. The high-speed tape reader has been connected with the digital computer and is being used for data input during system checkout.

The grapple head rotation control has been received and, along with other equipment necessary for a closed-loop system, has been assembled for testing with the grapple head. The synchro-to-digital converters were rejected and returned to the vendor for rework. Basic control system analysis is being performed for the vertical drive, arm extension drive, and azimuth drive loops. These will be used to determine initial constants for the closed-loop systems at the start of testing.

A tape punch has been added to the Gulf General Atomic 1108 computer which will allow it to be used to produce control data tapes and to assemble programs for the control computer. The basic flow block diagram for the fuel handling machine program is complete and work is now being initiated on supervisory routines.

TEST PROGRAM

The major facility preparations were completed for the first portion of machine testing. The graphite core and support structure were installed and checked out in both the upper and lower positions. The machine main support ring was installed and aligned along with the autoclave nozzle extension. The refueling sleeve was installed and aligned. The autoclave and refueling sleeve were sealed, leak-checked, evacuated, and heated to complete the functional check of the test facilities.

Due to the late delivery of the transfer cask storage rack and its effect on the over-all test schedule, a study was made of alternate test schemes. Since the alternate schemes would possibly extend the test schedule, it was decided to await the availability of the rack.

The testing of the grapple head is continuing. After the failure of the rotation bands discussed in the previous report, new bands were fabricated and installed into the head. A stop pin was also added to provide protection for the bands in the event of overpressurization of the rotation bellows. Following this work, the grapple head was returned to the test facility to complete the previously postponed air cycles for rotation and to continue with the environmental testing. The 200 cycles of air testing were completed and the environmental testing was initiated. During the planned 1000 cycles with head rotation, the grapple head bound in rotation on the 709th cycle. The cause was found to be a galled and seized armature in the rotation system LVDT. The threaded portion of the transducer armature caused a ceramic bushing to break up by the rubbing or "filing" action of 709 cycles. Chips from the ceramic bushing were lodged in and around the armature which ultimately caused the system to completely bind and hold.

The ceramic bushings were replaced with new hardened steel bushings, and the armatures were replaced with hardened or chrome-plated steel units; the armature alignment was also improved.

The grapple head was then installed in the autoclave to resume the originally planned 5000 cycles. The test was initiated in the helium environment and the planned 1000 cycles with rotation were completed. The testing was terminated, however, after an additional 1604 cycles because of the failure of an electrical wire and the loosening of a fastener holding another electrical wire. The grapple head was removed from the autoclave and repair was completed in the tower. It was determined that the see-saw action of the electrical wire at its terminal lug during the cyclic motion of the grapple head caused the wire to break. Repair consisted of rerouting and modifying wire supports so that the cyclic motion of the wiring would not occur at the terminal lug. Also, the fasteners securing the electrical wires were lock-wired to provide positive locking.

The grapple head has been returned to the autoclave and testing has resumed with test counts starting at zero.

Figure I.4 is a photograph of the grapple head at the test facility.

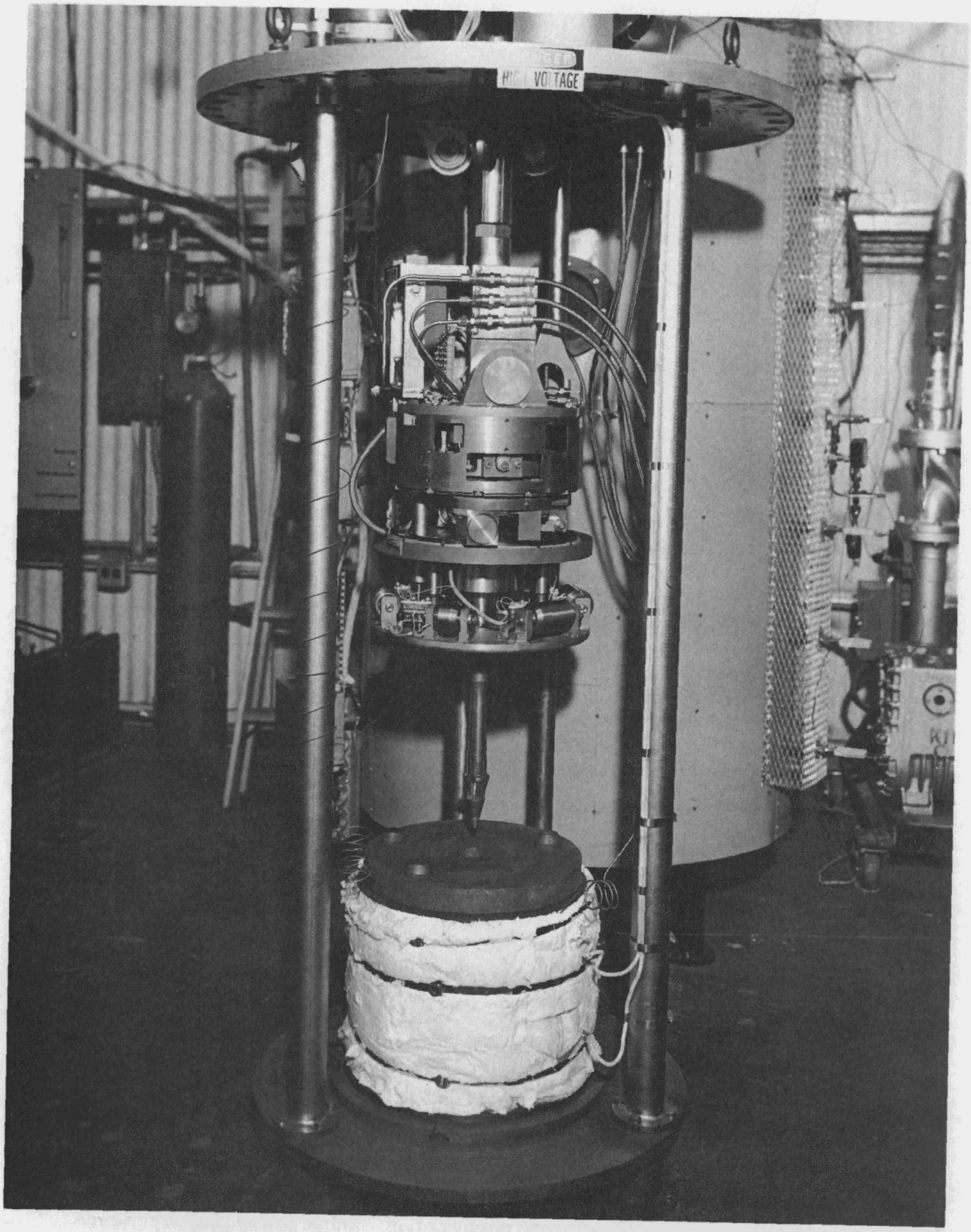

Fig. I.4--View of grapple head at test facility

Task II

SERIES-STEAM-TURBINE-DRIVEN HELIUM CIRCULATOR

The objective of this task is to establish the suitability of the main helium circulators and steam turbine drives for use in the plant by means of analysis, component tests, and prototype testing under conditions of temperature and speed expected in the plant and up to at least 50% of design horsepower. Compressor blade and rotor vibration measurements will be made during these tests. The duration of the full-scale prototype testing will be approximately 200 hr.

DISK CATCHER TESTING

A program is under way to provide information needed for the design of the disk catcher. The initial phase of this program is an analogous explosive test in which a simulated disk fragment is accelerated with an explosive charge and the fragment is then caught in a candidate disk catcher ring. Arrangements were made to have a vendor carry out this portion of the program. Unfortunately, the vendor was unable to measure the fragment velocity, although several approaches to the problem were attempted. The required parts and tooling have therefore been returned to the Gulf General Atomic Green Farm facility, where the velocity will be determined photographically. This facility has been used extensively for high-speed photography work combined with explosive testing. The photographic capability of the facility permits the measurement of particle velocities far in excess of the velocities required by this program.

CIRCULATOR DISCHARGE CHECK VALVE

A series of tests on the light-weight check-valve was run to gather additional loss coefficient data. The valve plates were taped open to simulate the actual plate positions in helium at the Reynolds numbers investigated. The range of test flows used covers most of the relevant operating conditions. Static pressure differential across the valve was measured more accurately than before in the low-flow range by using inclined manometers. Dynamic pressure in the duct below the valve was also recorded on inclined manometers with the exception of the high-flow range. These data were collected for the three spoiler configurations previously tested and for no spoilers.

Data reduction consisted of calculating the loss coefficient (static ΔP/dynamic pressure) and Reynolds number for each data point by means of an elementary computer program. Loss coefficient versus Reynolds number was plotted for each configuration.

The plots show excessive data scatter and present little justification for drawing a curve. It was noted that the spoiler configuration or lack of spoilers has no noticeable effect on loss coefficient. It varied from 0.001 to more than 0.1 with an over-all average of 0.03 for all configurations. Using this value, a ΔP of 0.0023 psi may be calculated. The specified performance requirements at 0% power with one circulator and pressurized condition amounts to 0.0022 psi ΔP for a valve. Choosing a specific, rather than average, flow (dynamic pressure) close to the above conditions given a ΔP of 0.0021 psi.

MICROPHONE SYSTEM

An acoustic transmission line and microphone housing for the next series of Mark II steam and helium tests has been designed and fabricated. This system was calibrated to determine its performance in helium at pressure. The unit performs well and faithfully transmits the sound up to 5000 cps. Above this frequency, however, the unit does not follow a calibrated signal. The system has been slightly redesigned to improve the high-frequency response.

PROTOTYPE CIRCULATOR TESTS

During a spin test of the Mark II prototype helium compressor disk assembly, a failure occurred causing destruction of the disk assembly which was being test spun up to 16,000 rpm at room temperature for the first time within a specially constructed vacuum spin facility. This condition simulates the disk stress differential (between yield and operating level) that occurs at 13,500 rpm (141% overspeed) at reactor operating temperature (750°F) - a test condition planned as part of future circulator tests.

The spinning operation was apparently normal until after 16,025 rpm was reached. Various noises were heard and the vacuum was lost thirty seconds after closing the drive turbine supply valve.

The disk was found essentially intact upon disassembly, but all 31 rotor blades were separated from the disk. The test vacuum chamber showed considerable impact damage (at the level at which the disk had been spinning) including several gaping holes caused by impingement of the flying blades. Blades and blade fragments were found both inside and outside the vacuum chamber. The lower disk catcher was intact but the upper disk catcher had been ripped away.

An evaluation of the incident resulted in the following findings:

1. There was no apparent error in the operation of the spin facility.
2. No manufacturing or material deficiencies were evident.
3. There was no apparent malfunction of the spin facility.
4. The blade dovetail roots exhibited evidence of yielding and the dovetails of some blades had broken into two pieces.

5. Further investigation of two sets of blades that had previously been spun to 14,000 rpm showed slight deformation in the dovetail region apparently caused by yielding at high stress levels.
6. The calculated shear stress in the blade dovetail was very high in relation to the material capabilities. Analysis has confirmed that shear failure will occur under the 16,000-rpm test conditions.
7. Because of the different characteristics of the blade and disk material, the 16,000 rpm test condition imposed stresses on the blade roots higher than anticipated. The yield strength of the disk, Ladish D6AC, drops off more rapidly with temperature than the blade material, Greek Ascoloy.

It should be noted that this failure occurred on the prototype compressor disk configuration and occurred because of the effort to simulate the maximum stress ratio at operating temperatures in a room-temperature spin pit. A full review has been carried out on the production circulator disk and some changes have been instigated to assure adequate margin for future room temperature spinning operations.

TEST FACILITY OPERATIONS

No tests were carried out during this period. The major effort has gone into facility preparation and assembly of the Mark II prototype helium circulator. It is anticipated that testing with the Pelton wheel drive will start on December 10, 1968 and steam testing should commence on January 13, 1969.

TEST DOCUMENTS

The test specification that outlines the initial checkout tests to be performed on the Mark II helium circulator system using the Pelton wheel as the source of power has been prepared. These tests will precede the operation of the Mark II system using steam and helium.

Test specifications for the shutdown seal and brake and the reverse thrust bearing were released.

The test specification for the seal system transients is being reviewed.

Task III

CONTROL ROD DRIVE

The objective of the work under this task is to determine the suitability, maintainability, and reliability of the control rod drives for the plant under the expected temperature and helium chemical impurity conditions predicted for the reactor by means of testing, including accelerated life testing, of a full-scale prototype of the control rods and drive.

Environmental testing of the control rod drive was resumed at the start of the quarter. As previously reported, the motor bearings were replaced with a special construction of nitralloy and Bearite retainer and tungsten carbide balls. The fast scram retarder and scram clutch were also included in this test.

With 88% of the jog test target achieved, the test was shut down for what was found to be a failure of the motor pinion teeth (see Fig. III.1). This failure was attributed to wear and the consequent development of excessive radial play in the bearings supporting the mating gear. The bearings concerned, in common with most other bearings and gears in the unit, had been subjected to several times their anticipated service life; therefore they could reasonably be expected to wear out at this time.

At the time of failure, all other components in the drive mechanism were operational.

Failure of the motor pinion caused ultimate seizure of the drive and was attributed to wear due to high tip loading at the gear teeth. High tip loading was caused by a combination of wear in the bearings of the pinion mating gear, and by undersized pitch diameters on both the pinion and its mating gear. The net result of these two conditions was inadequate tooth engagement.

A metallurigical examination of the failed pinion together with an examination of other parts substantiate the conclusion as to the cause of failure of the pinion. Results show evidence of fatigue failure in the nitrided surface of a third stage pinion and evidence of destructive pitting on the mating gear.

Several failures to slow scram are attributed to a general increase in friction throughout the drive system as a result of the accumulation of debris in addition to general wear of parts that had been on test since the start of the test program. The most sensitive part of the drive to debris is at the 1750-rpm motor bearings in that a minimum resistance is needed at this point to inhibit a scram.

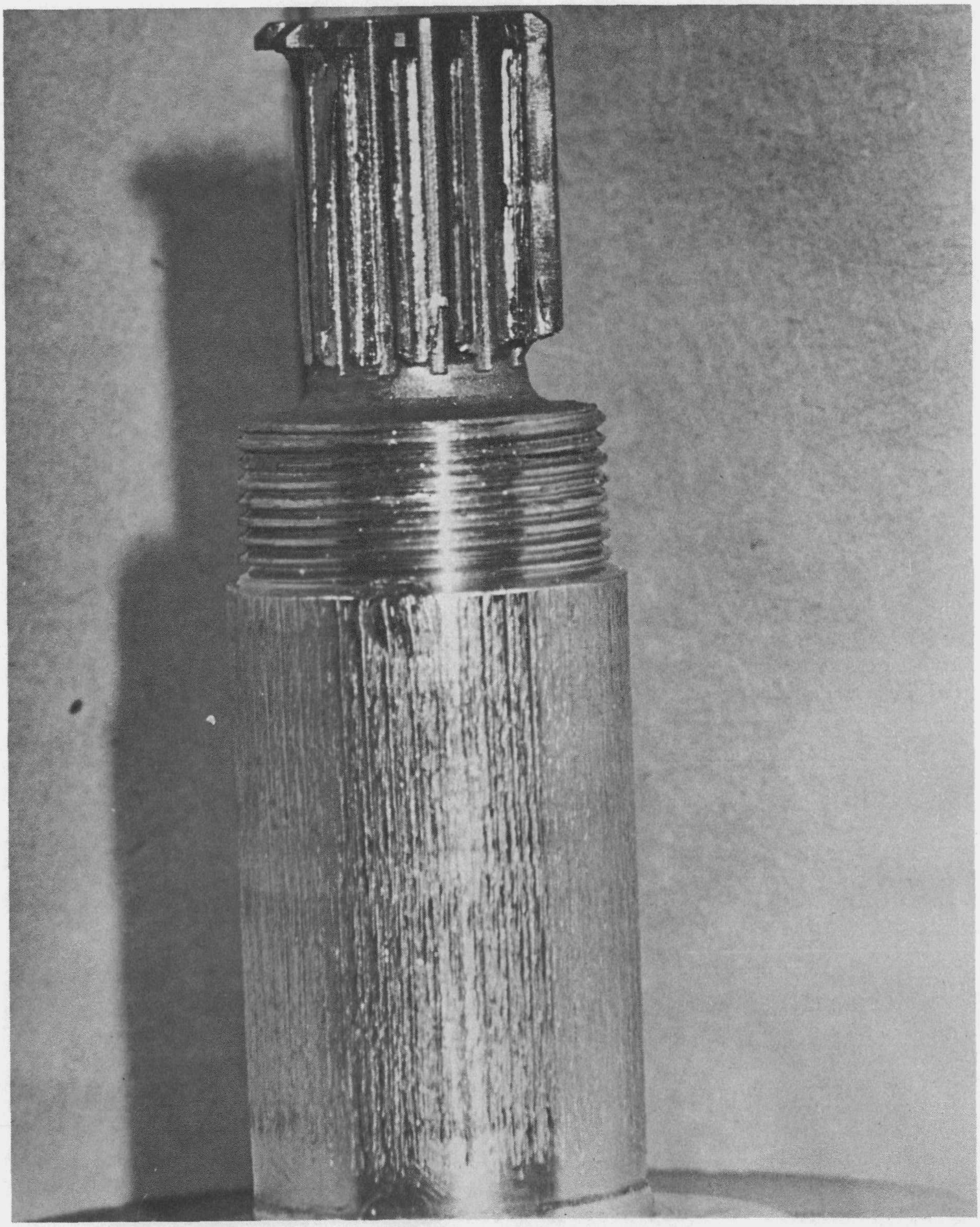

Fig. III.1--Failed motor pinion

Failures to fast scram that occurred during the test were attributed to a failure of the clutch to release properly. These failures have not been fully assessed at this time.

In view of the above, it is planned to replace the 1750-rpm induction motor with the 450-rpm backup unit currently under construction. The effect will be an increase in motor bearing life expectancy because of the smaller number of motor revolutions required to achieve the test objectives. For the same reason, less debris should be generated in the area of the motor bearings and pinion.

Further, because a lower gear reduction ratio is used with the 450-rpm motor, a higher holding torque becomes necessary at the motor end to maintain the rods in a withdrawn position. This makes for a scram capability less sensitive to any frictional resistance brought about by the accumulation of debris in the various gears and bearings.

The drive will be refurbished with new bearings, gears, and other parts subject to wear, and the applicable parts of Phases I and II testing will be repeated with all test counts starting from zero.

SUMMARY OF TEST ACCOMPLISHMENTS TO DATE

In testing a single prototype drive the intent is to demonstrate the adequacy of one drive for regulating service for a one-year period and 36 drives in shim service for a six-year period. The regulating drive is expected to see some shim service during its operation and all drives must demonstrate their ability to scram during their periods of service.

The anticipated service requirements for the PSC drive in the regulating mode and in the shim mode are tabulated below. The test goals established to demonstrate the adequacy of the drives in each mode are also given.

Regulating Mode

Service period, one year
Anticipated jogs during service period, 130,000
Desired jogging reliability, 0.66 demonstrated 80% confidence
Test jogs to demonstrate, 500,000 (3.8 years equivalent operation)
Anticipated shim travel during service period, 350 ft
Desired shimming reliability, 0.977 demonstrated to 60% confidence
Test shim travel to demonstrate, 13,500 ft (38.6 years equivalent operation)
Anticipated scrams during service period, 6
Desired scram reliability, 0.968 demonstrated to 60% confidence*
Test scrams to demonstrate, 167 (27.8 years equivalent operation)*

Shim Mode

Service period, six years
Anticipated shim travel in service period, 2100 ft
Desired shim reliability, 0.977 demonstrated to 60% confidence
Test shim travel to demonstrate, 80,000 ft (229 years equivalent operation)

Anticipated scrams during service period, 36
Desired scram reliability, 0.968 demonstrated to 60% confidence*
Test scrams to demonstrate, 1000 (167 years equivalent operation)*

---

[*] This reliability requirement has been subsequently revised from 0.968 to 0.982. When testing is resumed, 300 scrams will be required to demonstrate the regulating mode and 1800 to demonstrate the shim mode drives.

For comparison with the above, the upper portion of Table III.1 shows the actual performance of the drive at failure, together with the confidence levels attained. The lower portion provides similar information except that the point in time is that at which the first failure to slow scram occurred. The data shown for slow scrams is the same in both cases because testing to demonstrate scram adequacy is considered to have failed as of the first slow scram failure. A review of Table III.1 shows the drive had demonstrated its adequacy in the shim mode, had essentially demonstrated its adequacy in the regulating mode, but further testing will be required to demonstrate the adequacy in scramming mode.

3

Table III.1

PERFORMANCE OF PROTOTYPE DRIVE

	Actual Performance		Confidence Level Attained			
			Regulating		Shim	
	Original Parts	Replaced Parts	Original Parts (%)	Replaced Parts (%)	Original Parts (%)	Replaced Parts (%)
			At End of Test			
Jogs	1,013,407 (7.8 yr)	439,528 (3.66 yr)	96	76	---	---
Shim travel	230,590 ft (673 yr)	119,234 ft (331 yr)	99	99	93.9	74.6
Slow scrams	1,209 (200 yr)	334 (55.6 yr)	99	86.5	67.2	26
			At Time of First Scram Failure			
Jogs	800,000 (6.15 yr)	226,000 (1.74 yr)	92.4	51.7	---	---
Shim travel	101,432 ft (460 yr)	50,176 ft (145.3 yr)	99	99.4	88	31
Slow scrams	1,209 (200 yr)	334 (55.6 yr)	99	86.5	67.2	26

NOTE: Original parts refer to all parts which have been on test since its inception. Replacement parts refer to those parts which had been replaced or refurbished as a prerequisite to returning to test on August 27, 1968.

Task IV

STEAM GENERATOR

The objective of this task is to establish the suitability and maintainability of the design of the steam generators for the conditions of temperature and pressure expected in the plant by means of conceptual design, analyses, and testing of the critical aspects of the design. The tests are expected to include gas flow distribution and pressure drops, helium-side heat transfer, steam-water flow stability, tube vibration, and experimental investigation of material compatibility with coolant impurities. The development of a high-temperature design basis and investigation of experience relative to tube integrity is also planned.

STEAM-WATER FLOW STABILITY TEST PROGRAM

The boiling stability test loop was used to simulate PSC thermal-hydraulic operating conditions at full load and 1/4 load for a main steam coil circuit operating between subheaders. Pressure level and steam-water temperature distributions were duplicated. Local conditions were duplicated for the economizer-evaporator I locations with respect to mass velocity and heat flux. Since the test coil employs a thin wall in the superheat regime relative to the PSC design, various exit orifices and inlet throttling adjustments were used to simulate PSC hydraulic conditions by duplicating the pressure drop ratios. The hydraulic simulation involved Δp values at 60% of those in the PSC design. Exit orifices with nominal Δp values of 25 and 60 psi were used to simulate leadout tubing and the relative increase in hydraulic resistance in the superheat coils.

Testing at simulated 1/4-load conditions was performed while recording the response of the wall thermocouples. The 1/4-load flow oscillation instability observed in previous testing (see GA-8725, an earlier quarterly report) was accompanied by periodic wall temperature oscillations with an amplitude of about 20°F (maximum/minimum) with a 20-sec period (see Fig. IV.1). Possible loop coupling was studied to determine if the coil instability was truly self-excited or induced by loop resonance. This was studied by altering the natural frequency of various containment volumes. For example, an accumulator Helmholtz mode computed at a period of 10 to 20 sec was within the range of the 1/4-load oscillatory frequency. Isolating this component from the system had no detectable effect on the coil oscillation. All efforts to date indicate that a 1/4-load coil circuit instability does exist in the form of a mild oscillation. However, the associated fatigue stresses are calculated to be less than 1000 psi for the tubing in the economizer-evaporator-superheater I bundle.

A search was made for random fluctuations in wall temperature associated with the DNB transition zone. Visicorder records of the tube coil surface temperatures developed at full-load conditions did not disclose any

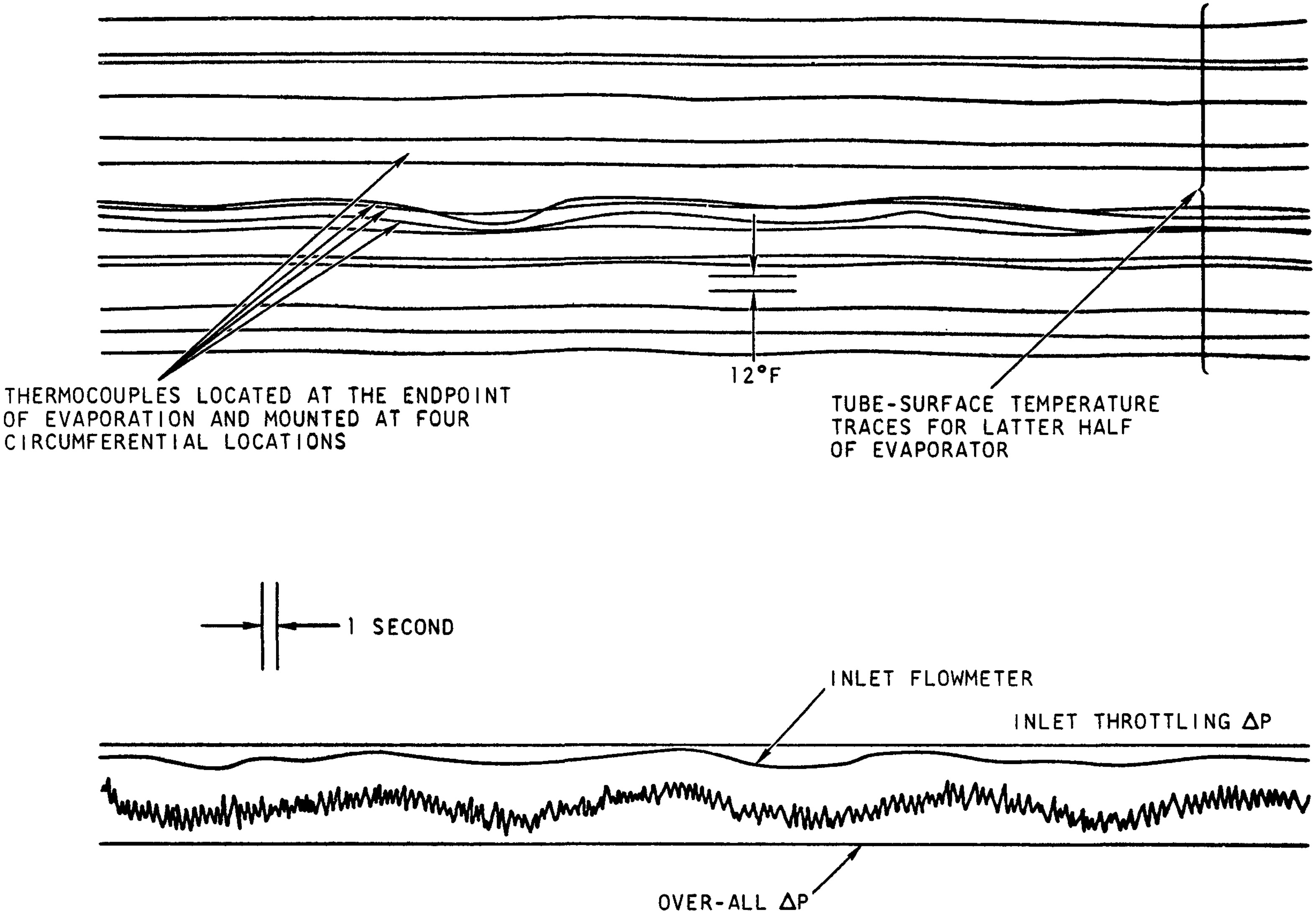

Fig. IV.1--Record of hydraulic and temperature measurements in one-quarter-load simulation fluctuations. Testing was performed with stable flow in the test section and with a gradual displacement of the evaporator zone. This procedure involving evaporator movement was an attempt to place the boiling heat transfer regimes in positions coincident with one or more of the fixed thermocouple locations. Predicted surface temperature response ranges in attenuation magnitude from 0.05 to 0.80 over a corresponding frequency range from 1.0 to 0.10 cps. This indicates that the measurement response should be adequate to disclose the anticipated fluctuations. Additional effort is planned to determine if the expected fluctuations are so highly localized in axial and circumferential directions that the fixed thermocouple locations are missing the event.

The main circulating pump failed early in November, halting the current test series. Primary water leaked from a stator cavity which is normally isolated from the circulated water. Indications are that the stator liner has failed. The pump has been removed and returned to the manufacturer for inspection and repair.

TUBE JOINT DAMPING TEST

The energy method for determining the vibration magnification factor of the GAVEL wedge has been applied. Results are shown in Figs. IV.2, IV.3, and IV.4. Figure IV.2 is a plot of magnification factor versus strain for several positions of applied force. Figure IV.3 is a cross plot of Fig. IV.2. Figure IV.4 is a plot of mean magnification factors versus strain which will be used in the analysis of the GAVEL strain gage data.

GAVEL VIBRATION TEST

A review of the lift coefficient data shown as first reduced on Fig. IV.5 was completed. It was found that the occasional high lift coefficients shown are from strain gages with very small strains near nodes. The data analysis has large uncertainties for this condition because the magnification factor is indeterminate with data from a nodal point. The data reduction program has been appropriately corrected and additional data plots are being run showing the least-squares fit and confidence limits.

AIR FLOW TEST

The air flow test is planned to be conducted at a site to be constructed near the Sorrento Valley Test Tower. Designs for the test site, air supply, and water supply have been completed and issued for bids.

Design for the strain gage data acquisition system is proceeding. Plans are presently being made to install strain gages on the test module.

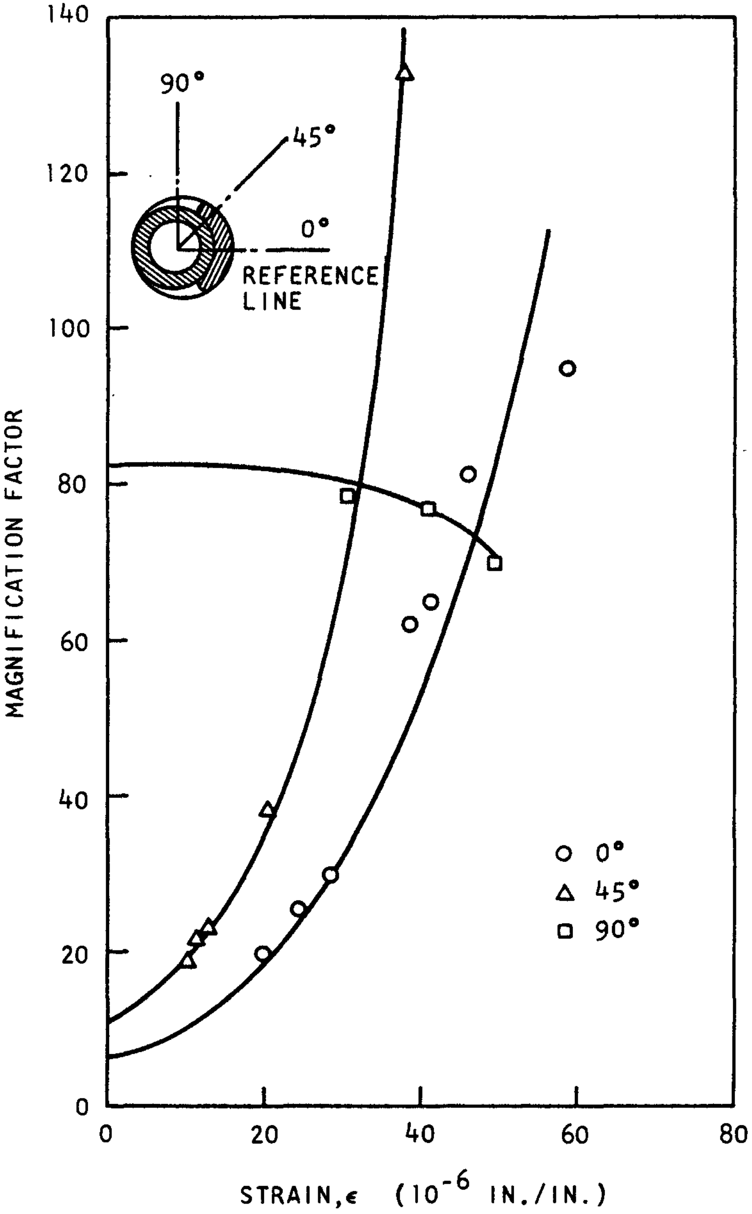

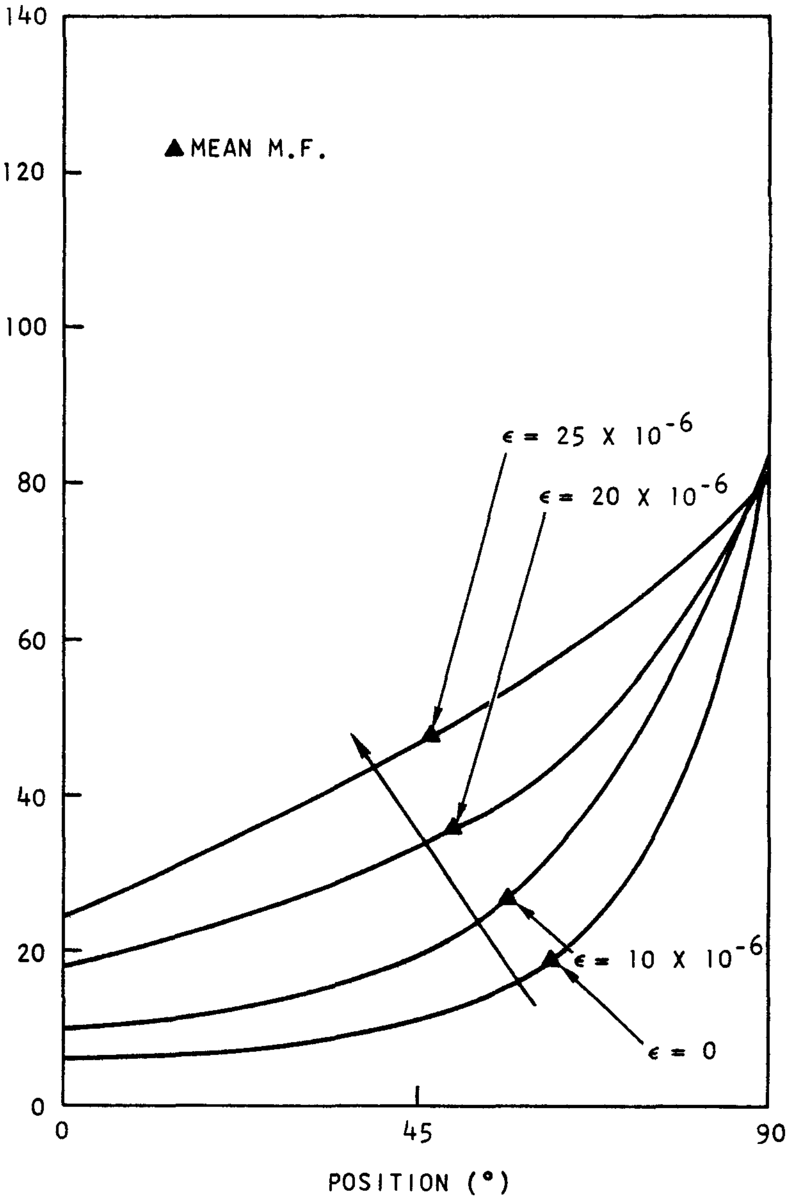

Fig. IV.2--Magnification factor versus strain Fig. IV.3--Magnification factor versus position

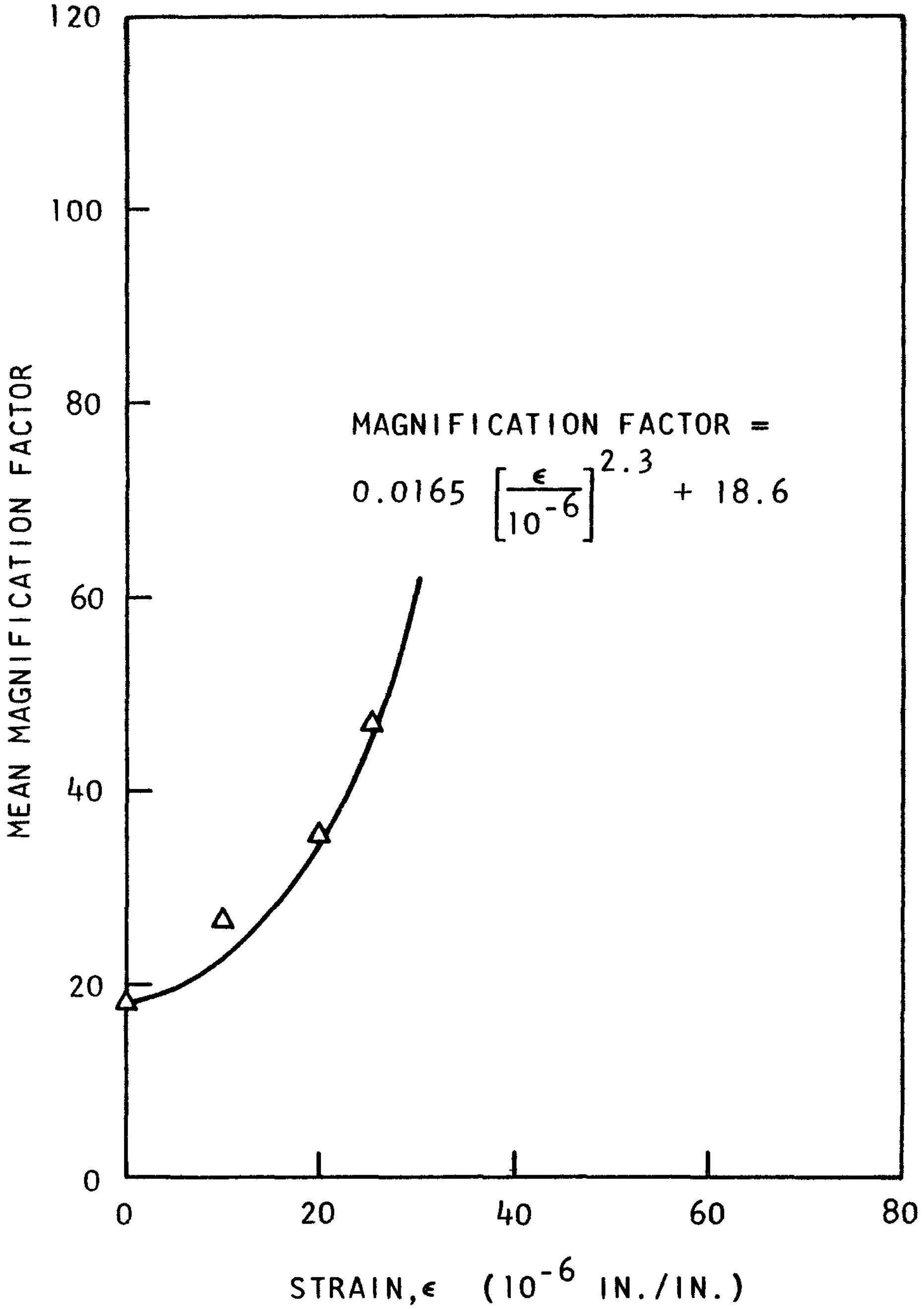

Fig. IV.4--Mean magnification factor versus strain

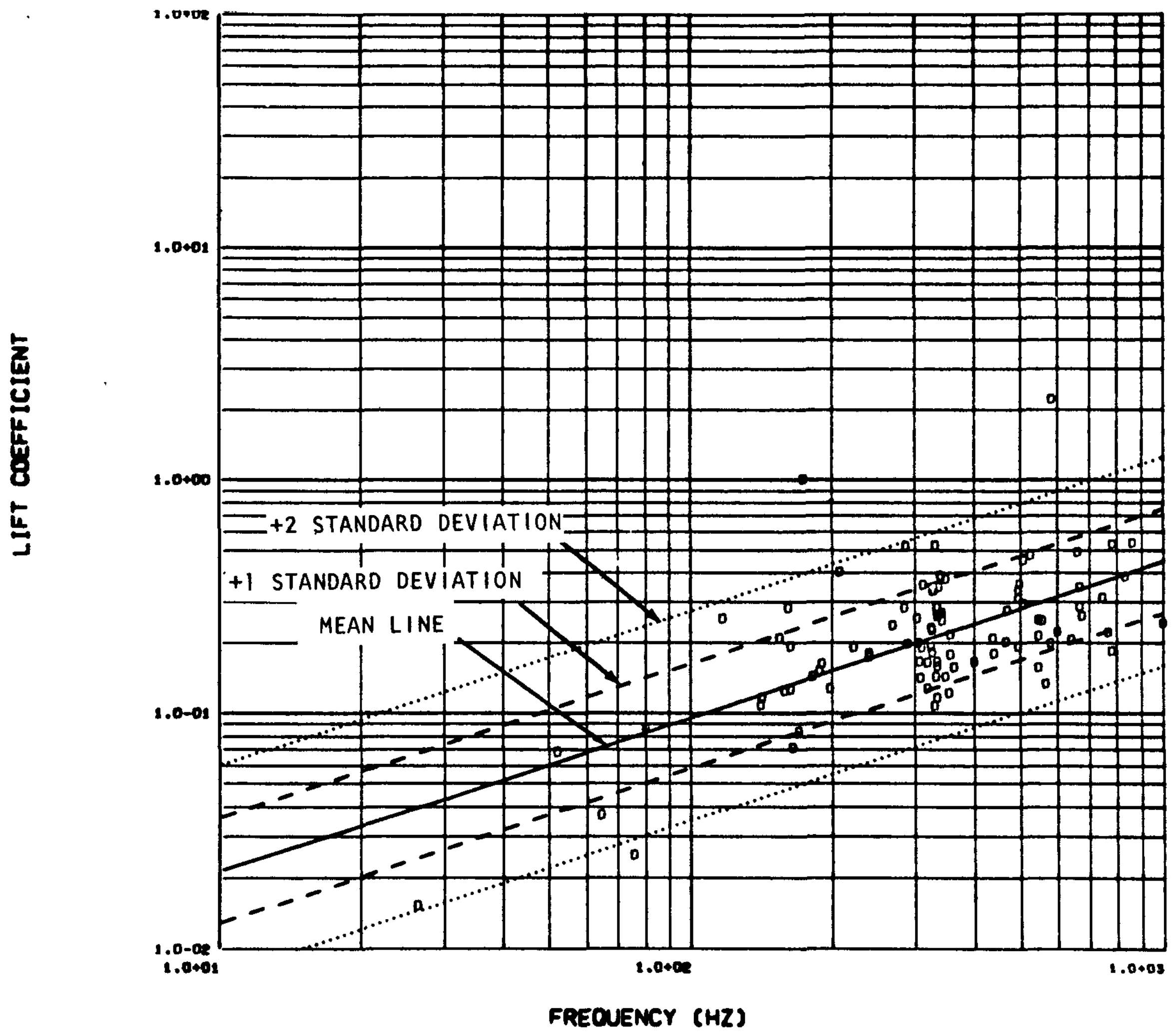

Fig. IV.5--Lift coefficient as computed with GAVEL code; Reynolds number = 35894, built-in boundary condition

STEAM GENERATOR TUBE PLUGGING MACHINE

The electrical control console diagrams for construction of the console were completed during the quarter. Construction of the console enclosure is complete and mounting of equipment on and in the enclosure has begun.

The electrical control console provides electric power, controls, and instruments for operation of the tube plugging machine. The console is located on the tube plugging machine service equipment cart. It is a rigid, free-standing cabinet. Access into the front or rear of the console is provided through gasketed hinged doors.

The main electric power supply to the tube plugging machine is 480 v, single phase, 60 cps. This power will be fed to the console via a three-conductor portable cable. One of these conductors will be used as a ground wire. A molded case circuit breaker is used for the 480-v power circuit protection. The molded case circuit breaker is accessible through a front access door and is interlocked with the door latching mechanism so that the breaker must be opened before the door can be opened. Also, all 480-v wiring will be contained behind this same access door so that access to any 480-v wiring will be prevented except when the circuit breaker is open disconnecting the power supply. Main power will be turned on and off by energizing and deenergizing a magnetic contactor with a selector switch on the front panel after the circuit breaker is closed and power is available. A green indicating light beside the selector switch will be energized when power is available and the contactor is deenergized. A red indicating light beside the selector switch will be energized when the contactor is energized indicating that main power is on.

The 480-v power will feed the welder and a 480-120/240-v, single-phase, 60 cps, 5-kva transformer. Both feeders are protected with fuses. The transformer provides all power for the tube plugging machine and its service cart with the exception of the welder.

On the front panel of the console, the mode of operation will be selected by positioning two selector switches. One selector switch is used to select the main mode of operation: (1) tube plugging or (2) reheat pipe seal welding. The other selector switch has eight positions for selecting (1) off, (2) turret, (3) position sensing, (4) leak detection, (5) cleanup, (6) weld preparation, (7) plug insertion, and (8) welding. The second position (turret) will be used for both tube plugging and reheat pipe seal welding and the other positions are for tube plugging operation only. These selector switches will provide control power for the selected positions only, which will help minimize the possibility of operator error.

Color-coded nameplates are used on the front panel to identify the different control and instrument groups.

A bell inside the console and a red indicating light on the front panel will indicate an unsatisfactory condition. The alarm bell may be silenced with an acknowledge push button next to the red light, but the light will clear only after all conditions are normal. A red indicating light is also provided for each of the alarm conditions. Alarms are provided for the following conditions:

1. High or low middle-seal pressure.
2. High or low end-seal pressure.
3. High or low centering plungers pressure.
4. Dome high pressure.
5. Television camera and seal welding coolant high temperature.
6. Turret tube bank position in error.

All controls, position readouts, and limit indications for the various operations of the tube plugging machine are located on the front panel, along with instrumentation for monitoring the operation.

Task V

COATED PARTICLE DEVELOPMENT

The objective of this task is to determine the process variables for fabrication of coated fuel particles suitable for use in the plant by means of investigation of various methods of fabricating fuel particles, investigation of coating process variables, and preirradiation evaluation of coated particles.

LOWER-DENSITY PYROCARBONS

It is desirable to use coated fuel particles that are dimensionally stable under fast-neutron doses (out to about 8 x 10^{21} n/cm^2) in order to maintain coating stresses at low values and ensure fuel integrity at the end of life. In the development of such fuel, both long-range and short-term experiments are under way to assess the stability of the fuel coatings. Capsule P23 is a short-term experiment that is being conducted to evaluate lower-density (1.50 to 1.90 g/cm^3) outer pyrolytic carbon (PyC) coatings at low fast-neutron doses where the irradiation-induced shrinkage rate is maximum.

In order to obtain LTI and HTI coatings in the above density range, temperature adjustments were made, resulting in higher deposition temperatures for the propane (LTI) coatings and lower deposition temperatures for the methane (HTI) coatings. Portions of this work have been reported in the previous quarterly report (GA-8879).

Additional studies have been conducted at lower and higher LTI coating temperatures than reported last quarter using the same constant coating parameters. In addition, coatings that had been deposited using different coating gas concentrations have been evaluated and the data included. The coating conditions that were employed in all cases are as follows:

Tube configuration	2.5-cm-diam. graphite
Inlet distributor	Single nozzle, conical
Total gas flow	6000 std cm^3/min*
Carrier gas type	Helium
Initial bed surface area	540 cm^2
Estimated contact time	0.73 sec
Coating gas concentration:	
Propane	20, 30, 40 vol-%
Methane	12, 15, 20 vol-%
Coating temperature range:	
Propane coatings	1125° to 1700°C
Methane coatings	1690° to 1960°C

---

[*] Measured using flowmeters calibrated against a constant 24 mm Hg back pressure.

Coating thicknesses were measured optically by viewing contact radiographs through a microscope. The PyC densities were measured using sink-float techniques on PyC samples stripped from graphite disks that had been coated along with the particles. The degree of preferred orientation was measured by X-ray diffraction using the modified Bacon technique and reported as BAF (Bacon anisotropy factor).

The data that were obtained using the above coating conditions are presented in Fig. V.1. These data show the LTI density values to be uninfluenced by the propane concentration over the range used in these experiments. These data show that increasing deposition temperature results in an initial density increase at about 1300°C, followed by rapidly decreasing densities at temperatures beyond 1350°C. At 1600°C, the propane coating densities reach a minimum value of about 1.40 g/cm^3, increasing with temperature beyond this.

Inspection of the coating and growth rate values shows that the best fit of data occurs with the deposition rate (g/min or moles/min) values. These data are shown in Fig. V.2 for coatings deposited from 40% propane. This plot shows that the deposition rate is maximum at the minimum-density temperature (approximately 1600°C) and falls off rapidly beyond this temperature. Since the propane concentration and bed surface area are essentially constant, the deposition rate is being controlled by the rate of formation of a pyrolyzate that reaches its maximum abundance at about 1600°C.

This pyrolyzate is probably the large gas-borne droplets (with graphite-like crystallites forming on the surface) described by Grisdale (Ref. 1) for rotary coaters and extended to fluidized beds by Bokros (Ref. 2). The formation of these large droplets occurs when high concentrations of polymerizing species are present with small bed areas (A_i < 1000 cm^2). When these conditions are obtained, high-molecular-weight, complex molecules form, coalesce, and grow until they form gas-borne droplets that are then deposited on the substrate. The size and abundance of these droplets is controlled by gas residence time (contact time), bed surface area, and temperature. Since only the temperature was varied in these experiments, the effects of this parameter can be directly measured.

Another essential part of the Bokros model that applies to the data shown in Figs. V.1 and V.2 is that at lower temperatures (<1350°C for this case) the formation of the gas-borne droplets is inhibited and planar molecules condense and align directly on the substrate, yielding higher densities, higher BAF values, and reduced cooling rates. Applying the above model to the data shown in Figs. V.1 and V.2 seems to result in good agreement with the experimental evidence. At temperatures in the range of 1100° to 1350°C, condensation and alignment of planar molecules appears to be the principal deposition mechanism. This observation is supported by the higher densities obtained (1.94 to 2.05 g/cm^3), low deposition rates (0.01 to 1.3 g/min), and higher BAF (1.12 to 1.42). The crystallite size obtained in this temperature range was about 29 to 33 Å.

As the temperature is increased from 1350° to 1600°C, the deposition rate increases to its maximum value, suggesting total saturation of the coating

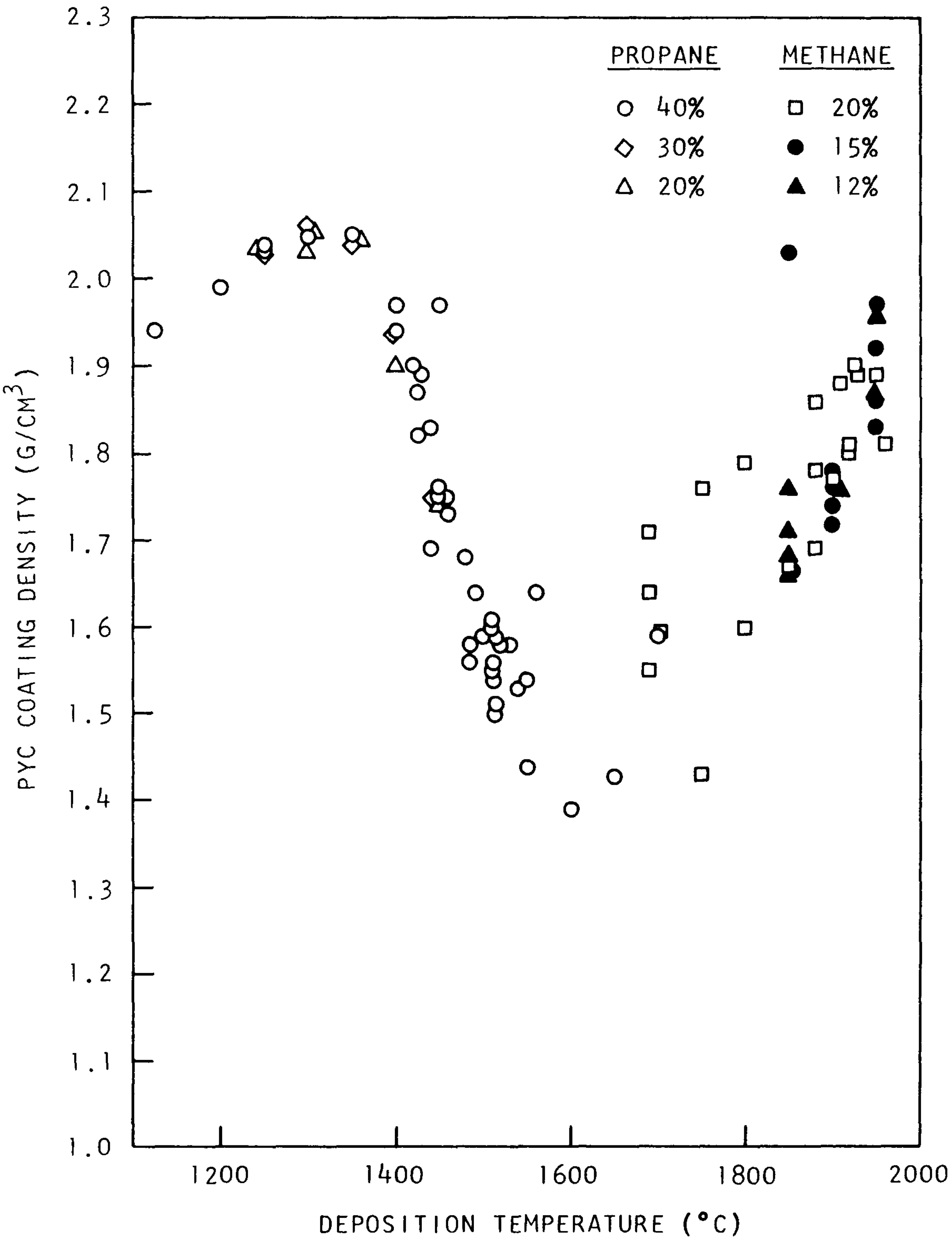

Fig. V.1--Pyrocarbon densities obtained with various concentrations of propane and methane coating gases over the temperature range of 1100° to 1950°C. Data were obtained using constant coating conditions in a 2.54-cm-diameter coater

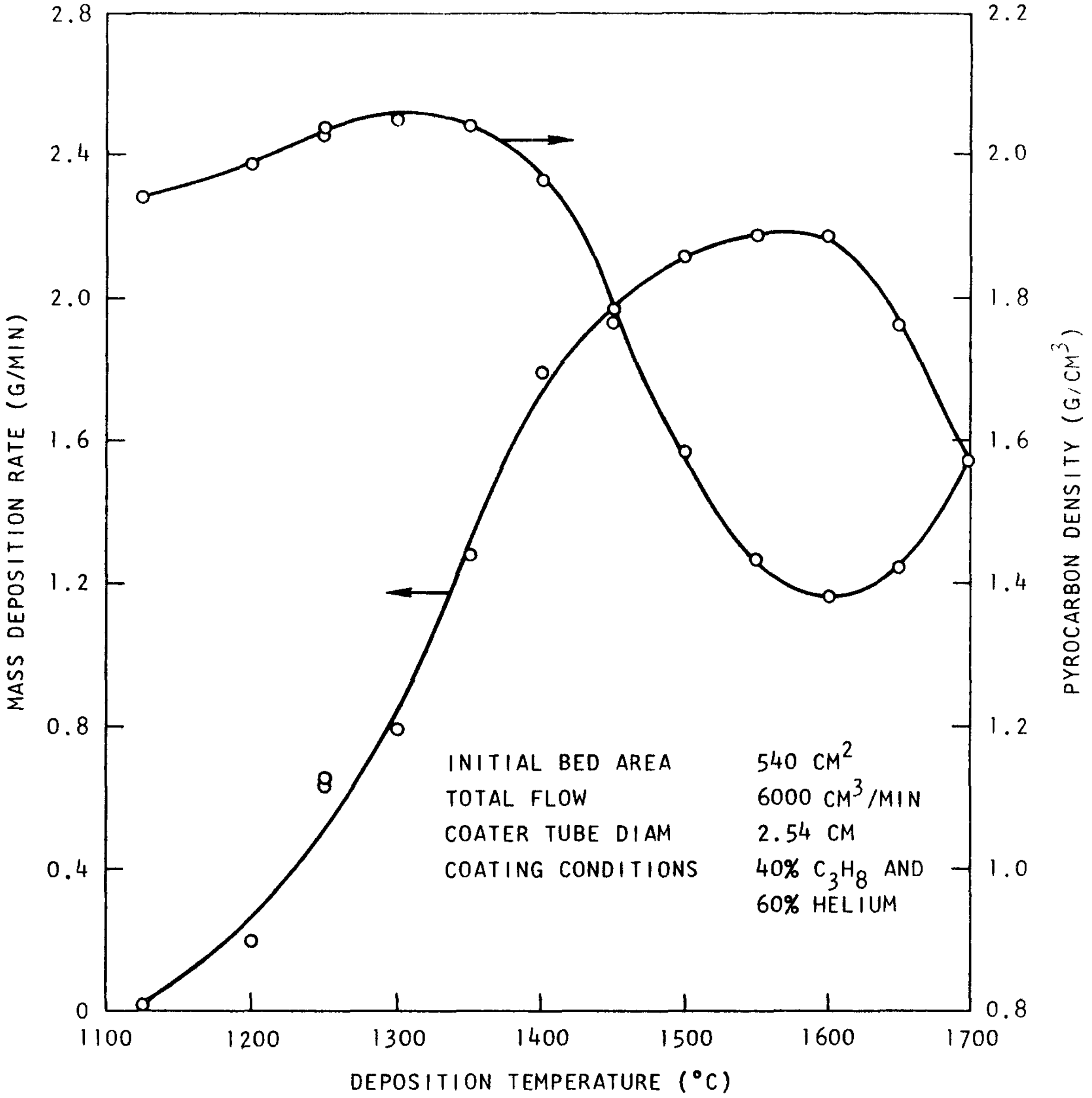

Fig. V.2--Deposition rate and pyrocarbon density as function of deposition temperature. Minimum density deposit occurs at maximum deposition rate atmosphere with droplets. Also, at higher temperatures, increased polymerization and coalescence would result in larger droplets, which in turn would increase deposition rates. The higher deposition rates obtained with these nonoriented droplets will result in lower-density, isotropic, carbon coatings. The decreasing density with increasing deposition rate is clearly shown in Fig. V.2. The coatings are isotropic (BAF = 1.00 to 1.07) and have slightly increasing crystallite sizes at temperatures >1500°C (size range = 44 to 56 Å), which is in good agreement with the Bokros model. At temperatures greater than 1600°C, the density values begin increasing while deposition rate falls off. The coatings were isotropic and very much like those obtained at temperatures between 1450° and 1600°C. The presence of more soot at temperatures greater than 1600°C indicates that the orderly pyrolysis and polymerization of propane is being replaced by dissociation and formation of carbon (soot) and hydrogen (higher temperatures appear to promote this reaction (Ref. 3)). This would reduce the deposition rate; higher densities are obtained since dehydrogenation occurs more readily, and, in addition, the carbon mobility is increasing, leading to a denser deposit.

It is interesting to note that the propane-produced coating density is essentially uninfluenced by the propane feed concentration (20 to 40 vol-%). This observation indicates that the atmosphere in the fluidized bed is saturated with gas-borne droplets at concentrations as low as 20 vol-%. Since droplet size and abundance is controlled by temperature (other parameters being constant), one would not expect a large variation in density. There would be a large variation in deposition rate, however, since more of the uniform-sized droplets can deposit per unit time at higher propane concentrations. This effect should diminish at lower temperatures, because of the mechanisms described above. That this seems to be the case is supported by the curves shown in Fig. V.3, where deposition rates for the three propane concentrations used in this experiment are shown plotted versus deposition temperature. These data show that the rates are more nearly the same at lower temperatures and increase with propane concentration at higher temperatures.

The foregoing experimental observations indicate that the lower-density pyrocarbon coatings obtained by increasing the propane deposition temperature should not be structurally different from those obtained at lower temperatures. The slight increase in crystallite size observed should be beneficial with regard to irradiation stability (Ref. 4). A possible problem that may be associated with these coatings is high hydrogen levels in the deposited droplets; however, the higher temperatures may allow more thorough dehydrogenation to occur. The actual hydrogen levels would probably be low, perhaps below accurate detection limits. Experiments to evaluate this possible problem have been initiated.

The deposition mechanisms for the methane-produced coatings shown in Fig. V.1 are discussed in considerable detail in Ref. 2. All of these coatings were isotropic, with fairly constant crystallite heights (88 to 107 Å).

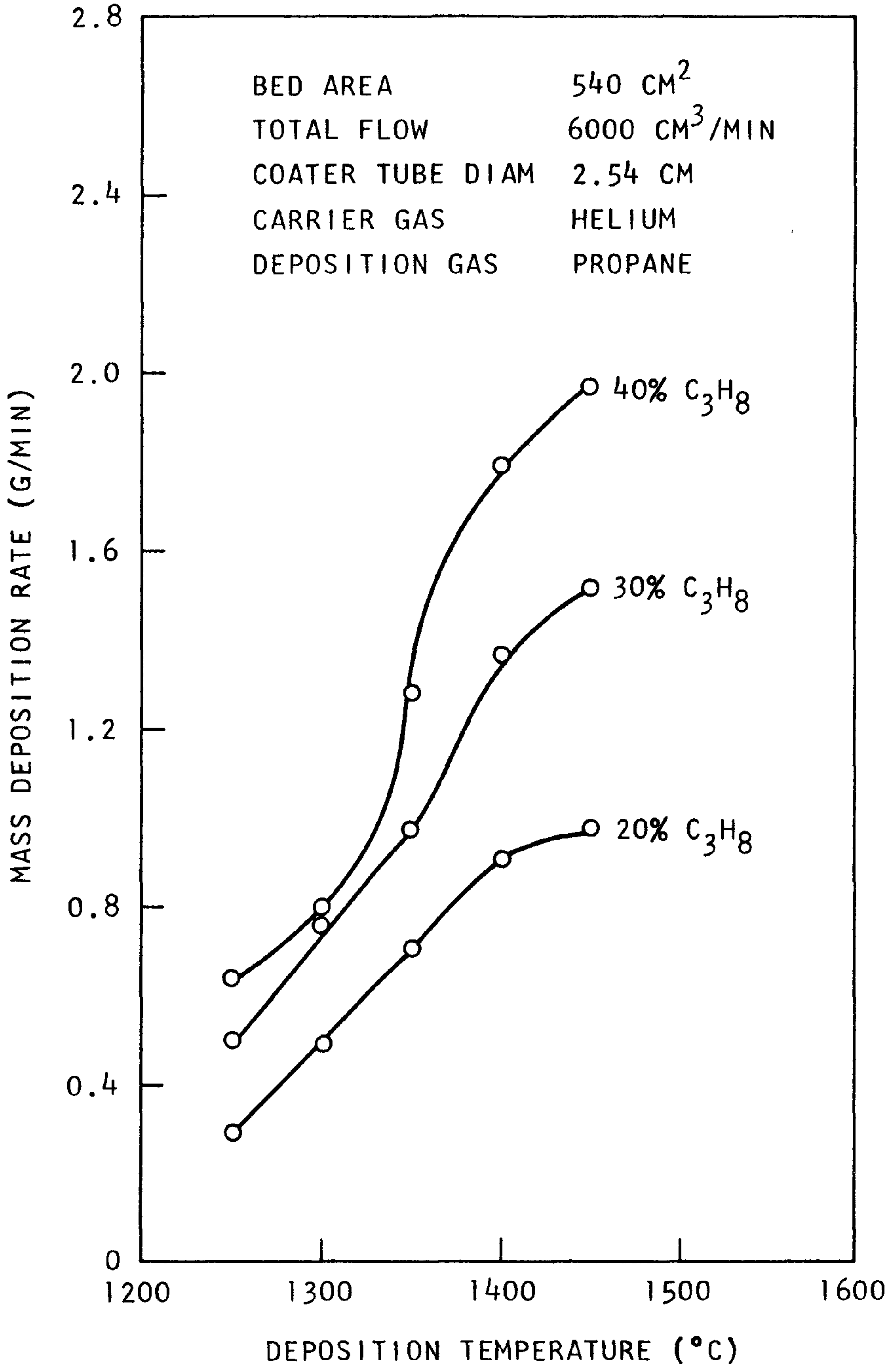

Fig. V.3--Variation in deposition rates obtained for different propane concentrations at different temperatures

COATING CONTAMINATION STUDIES

Coating Contamination in Fissile Particles Using the Mica-foil Technique

The mica-foil technique (Ref. 5) has been further developed and applied to the study of coating contamination in fissile fuel particles. The particles are mounted metallographically, polished down to remove the cores, and then irradiated in contact with mica foil. The fission fragments released as a result of thermal fissioning of the U^{235} nuclei produce straight tracks of damaged material 10 to 15 μm long in the mica. These tracks are then etched out in 50% HF and become visible in the optical microscope, their densities being directly related to the U^{235} contamination in the given particles. Mica-foil traces recently obtained for fissile particles were sufficiently detailed to permit calculation of U^{235} contamination in the buffer and outer isotropic coatings of different particles and different batches. The results are listed in Table V.1, and the basis for the calculations is shown below.

According to Price and Walker (Ref. 6), the number of fission fragments crossing a given surface in the interior of a thick sample having a uniform uranium distribution is given by

$$\rho = nN_0\sigma IR_0C \quad , \qquad (1)$$

where ρ = measured track density per cm^2,

n = thermal-neutron dose,

N_0 = number of atoms per cm^3 of sample,

σ = thermal-neutron cross section for U^{235} fission,

I = isotopic abundance of U^{235},

R_0 = average fission fragment range in matrix, and

C = atom-fraction of uranium in the sample.

In the case of a mica foil in contact with a cross-sectioned particle, it is assumed that the PyC represents a semi-infinite medium, and therefore

$$\rho = \frac{nN_0\sigma IR_0C}{2} \quad . \qquad (2)$$

For the particular conditions prevalent here,

$n = 3.3 \times 10^{15}$,

$N_0 = 1 \times 10^{23}$,

$\sigma = 5.82 \times 10^{-22}$,

$I = 0.93$ (for enriched uranium), and

$R_0 = 14 \times 10^{-4}$.

Table V.1

COATING CONTAMINATIONS IN TRISO FISSILE PARTICLES

Batch No.	Type	Area Examined	Tracks/cm^2	U^{235} in Coating (ppm)	Fraction U^{235} in Outer PyC		Comments
					Mica-foil Technique	PyC Burnoff Method	
3923-79E	TRISO-I HTI	Outer PyC	1.4×10^{6}	0.22	4.2×10^{-7}	3.5×10^{-7}	Average particle
		Average over buffer	$>2 \times 10^{8}$	>30	---	---	
3923-85E	TRISO-I LTI	Outer PyC	$\sim 5 \times 10^{5}$	~0.08	$\sim 1.5 \times 10^{-7}$	$\leq 1.9 \times 10^{-7}$	Average particle
		Outer PyC	1.7×10^{6}	0.27	5.1×10^{-7}	---	Particle after annealing 200 hr at 1300°C
3923-81E	TRISO-II HTI	Outer PyC	3.7×10^{5}	0.06	1.1×10^{-7}	$\leq 1.9 \times 10^{-7}$	Average particle
		Average over buffer	$>2 \times 10^{8}$	>30	---	---	
3923-87E	TRISO-II LTI	Outer PyC	1.3×10^{5}	0.02	4×10^{-8}	2×10^{-8}	Average particle
		Average over buffer	8×10^{6}	1.25	---	---	
		Just inside SiC	1.4×10^{7}	2.2	---	---	
		Outer PyC	3.6×10^{5}	0.06	1.1×10^{-7}	---	Particle with heavy buffer contamination
		Average over buffer	1.2×10^{8}	18.7	---	---	

Therefore

$$C = \rho \cdot 8 \times 10^{-15} \text{ atom fraction of } U^{235}, \text{ or}$$

$$C' \text{ (in ppm)} = \rho \cdot 1.56 \times 10^{-7} \quad . \qquad (3)$$

Expression (3) is the one used to obtain the parts per million values quoted in Tables V.1 and V.2. A more detailed explanation of the method and calculations is presented in Ref. 1.

As may be noted in Table V.1, the contamination levels are very low in all the fissile particles examined, and it appears that the HTI batches are slightly more contaminated than the LTI. Agreement between the figures obtained using the mica-foil technique and those obtained for the same batches of material using an activation and PyC burnoff method is very good. The parts per million figures quoted are considered more accurate than the fractional U^{235} contamination values, since they do not assume an average core size, particle diameter, and PyC thickness for each batch of material.

Uranium Contamination in Fertile Particles Using the Mica-foil Technique

The mica-foil technique has also been applied to the determination of uranium contamination in fertile particles (Ref. 5). Two mounts from each of six batches of fertile material were prepared and irradiated in the TRIGA reactor in contact with a mica foil, one set of six mounts being encased in 0.03-in.-thick cadmium. The cadmium prevented thermal fissioning of the U^{235}. By determining the differences in the numbers of fission fragment tracks in the mica between the two samples of each batch, it was possible to determine the magnitude of U^{235} contamination in each batch and its distribution.

The results listed in Tables V.2 and V.3 indicate that all six batches of fertile particles have U^{235} contamination in the outer PyC. In two of these, the U^{235} concentration is markedly greater on the particles surfaces, as illustrated in Fig. V.4. In four other batches, including T103(B)SH and T161(B)SL, shown in Figs. V.5 and V.6, respectively, contamination is slightly greater at the outer edge of the PyC. Only in batch T103(C)SL is the surface contamination equal to or somewhat less than that within the PyC (see Table V.1). Approximately 1 ppm of U^{235} distributed fairly evenly throughout the PyC of batch T103(B)SH particles is the highest contamination level observed, while the lowest is about 0.01 ppm, in batch T253(B)SL. Only in batch T103 (B)SH does the contamination in the PyC appear markedly greater than that in the inner isotropic and buffer coatings, as shown in Fig. V.2.

In Table V.3, the mica-foil results are compared with the results obtained by the PyC burnoff method on particles from the same batches. It will be seen that values of uranium contamination in the PyC coatings and on the surfaces are in close agreement. In calculating the U^{235} contaminations in grams of U per gram of particles, 2500 fertile particles per gram were assumed, and the weight of PyC on an average fertile particle was calculated to be close to 8.5×10^{-5} g.

Table V.2

LEVELS OF URANIUM CONTAMINATION IN FERTILE PARTICLES

Batch No.	Fertile Particle Type	Area Examined	A Tracks/cm^2 Due to Total Fissions	B Tracks/cm^2 Due to Fast Fissions	(A-B) Tracks/cm^2 Due to Thermal Fission of U^{235}	U^{235} in Coating (ppm)	Comments
T103(B)SH	TRISO-II HTI	Outer edge of PyC	$6.9x10^{6}$	$5.8x10^{5}$	$6.3x10^{6}$	0.98	Relatively high U and Th concentrations at surface and throughout PyC.
		Inner section of PyC	$5.4x10^{6}$	$4.3x10^{5}$	$5.0x10^{6}$	0.78	
		SiC	$\sim 3x10^{5}$	$<3x10^{4}$	$\sim 3x10^{5}$	~0.04	
		Inner Iso/Buffer	$2.7x10^{6}$	$2.3x10^{5}$[a]	$\sim 2.5x10^{6}$	~0.39	
		Background	$2x10^{4}$	~Zero[b]	$2x10^{4}$	0.003	Slight polishing contamination plus U present in mica.
T103(C)SL	TRISO-II LTI	Outer edge of PyC	$2.3x10^{6}$	$8x10^{5}$	$1.5x10^{6}$	0.23	Contamination fairly constant beneath particle surfaces.
		Inner section of PyC	$3.5x10^{6}$	$1.3x10^{6}$	$2.2x10^{6}$	0.34	
T161(B)SL	TRISO-II LTI	Outer edge of PyC	$2.9x10^{6}$	$1.0x10^{6}$	$1.9x10^{6}$	0.30	Contamination present on surface of PyC, SiC, and inner Iso. Contamination on SiC surface is just U.
		Center of PyC	$1.5x10^{6}$	$6x10^{5}$	$9x10^{5}$	0.14	
		PyC/SiC interface	$4.1x10^{6}$	~Zero	$4.1x10^{6}$	0.64	
		SiC/Inner Iso interface	$7.0x10^{6}$	$1.3x10^{6}$	$5.7x10^{6}$	0.89	
T169(B)SH	TRISO-II HTI	Outer edge of PyC	$4.5x10^{6}$	$4.4x10^{5}$	$4.1x10^{6}$	0.64	Concentration of U much higher at outer edge of PyC.
		Inner section of PyC	$1.2x10^{6}$	$4.4x10^{5}$	$8x10^{5}$	0.13	
T176(C)SH	TRISO-II HTI	Outer edge of PyC	$1.6x10^{6}$	~Zero	$1.6x10^{6}$	0.25	Uranium contamination higher at surface of PyC particularly in some small areas. Thorium contamination very low.
		Highly contaminated edge of PyC	$1.2x10^{7}$	~Zero	$1.2x10^{7}$	1.81	
		Inner section of PyC	$9x10^{5}$	~Zero	$9x10^{5}$	0.14	
T253(B)SL	TRISO-II LTI	Outer edge of PyC	$1.6x10^{6}$	~Zero	$1.6x10^{6}$	0.25	Uranium contamination concentrated on particle surfaces, very little inside PyC. Thorium contamination very low.
		Inner section of PyC	$4x10^{4}$	~Zero	$4x10^{4}$	0.006	

[a] Projected, based on PyC counts.

[b] Approximately zero is taken to mean, perhaps, 10^2 tracks/cm^2.

Table V.3

COMPARISON OF URANIUM CONTAMINATIONS IN FERTILE PARTICLES DETERMINED BY DIFFERENT METHODS

Batch No.	U^{235} Contamination, Mica-foil Technique (ppm)		U^{235} Contamination, Mica-foil Technique (10^{-7} g U/g particles)		U^{235} Contamination Burn-leach Method (10^{-7} g U/g particles)	
	Within PyC	On Surface	Within PyC	On Surface	Within PyC	On Surface
T103(B)SH	0.78	0.98	1.6	2.0	0.7	1.0
T103(C)SL	0.34	0.23	0.7	0.5	0.6	≤0.3
T161(B)SL	0.14	0.30	0.3	0.6	0.2	0.7
T169(B)SH	0.13	0.64	0.3	1.3	0.2	1.0
T176(C)SH	0.14	0.25	0.3	0.5	---	<0.3
T253(B)SL	0.006	0.25	0.013	0.5	0.008	<0.4

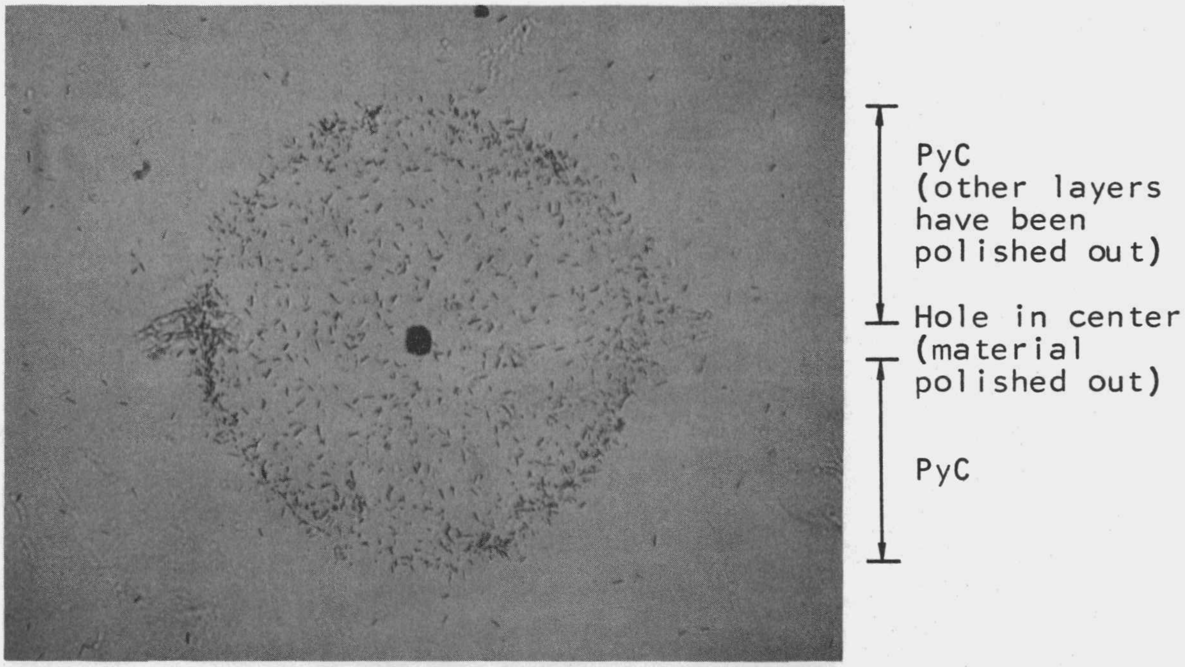

(150X)

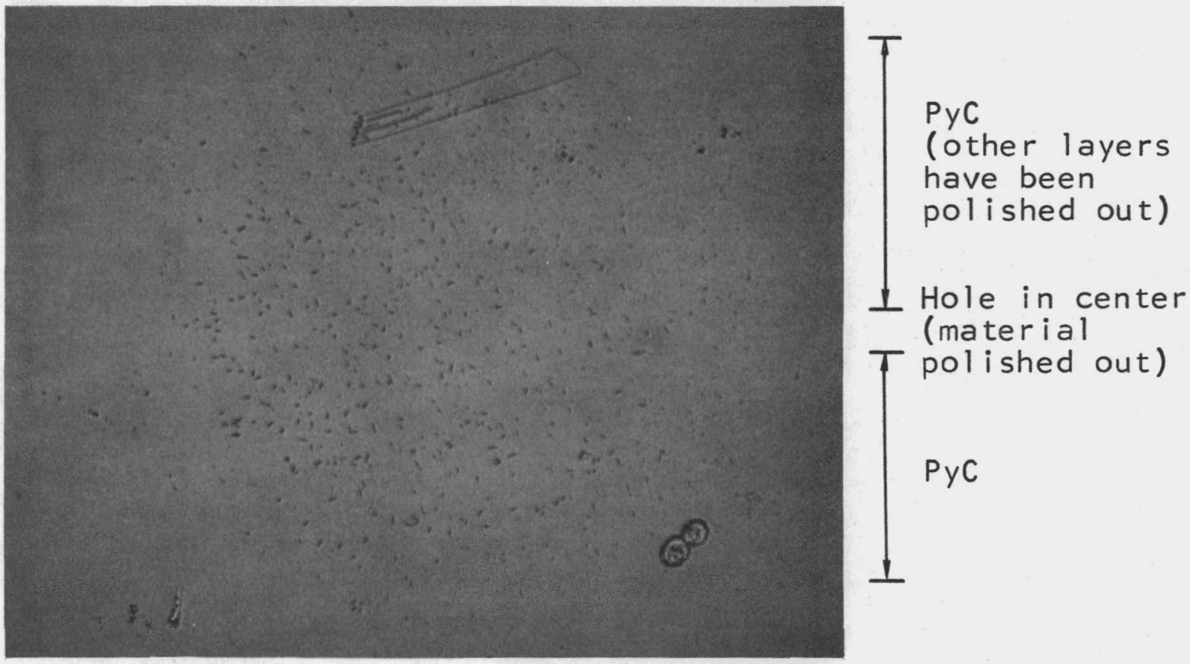

(150X)

Fig. V.4--Mica foils corresponding to particles from batch T169(B)SL, showing fission fragment tracks due to contamination in the PyC irradiated normally (above) and irradiated inside cadmium foil (below). The cadmium prevents thermal fissioning of U^{235} and consequently the difference in numbers of tracks per square centimeter between the two samples is a direct function of the amount of U^{235} present

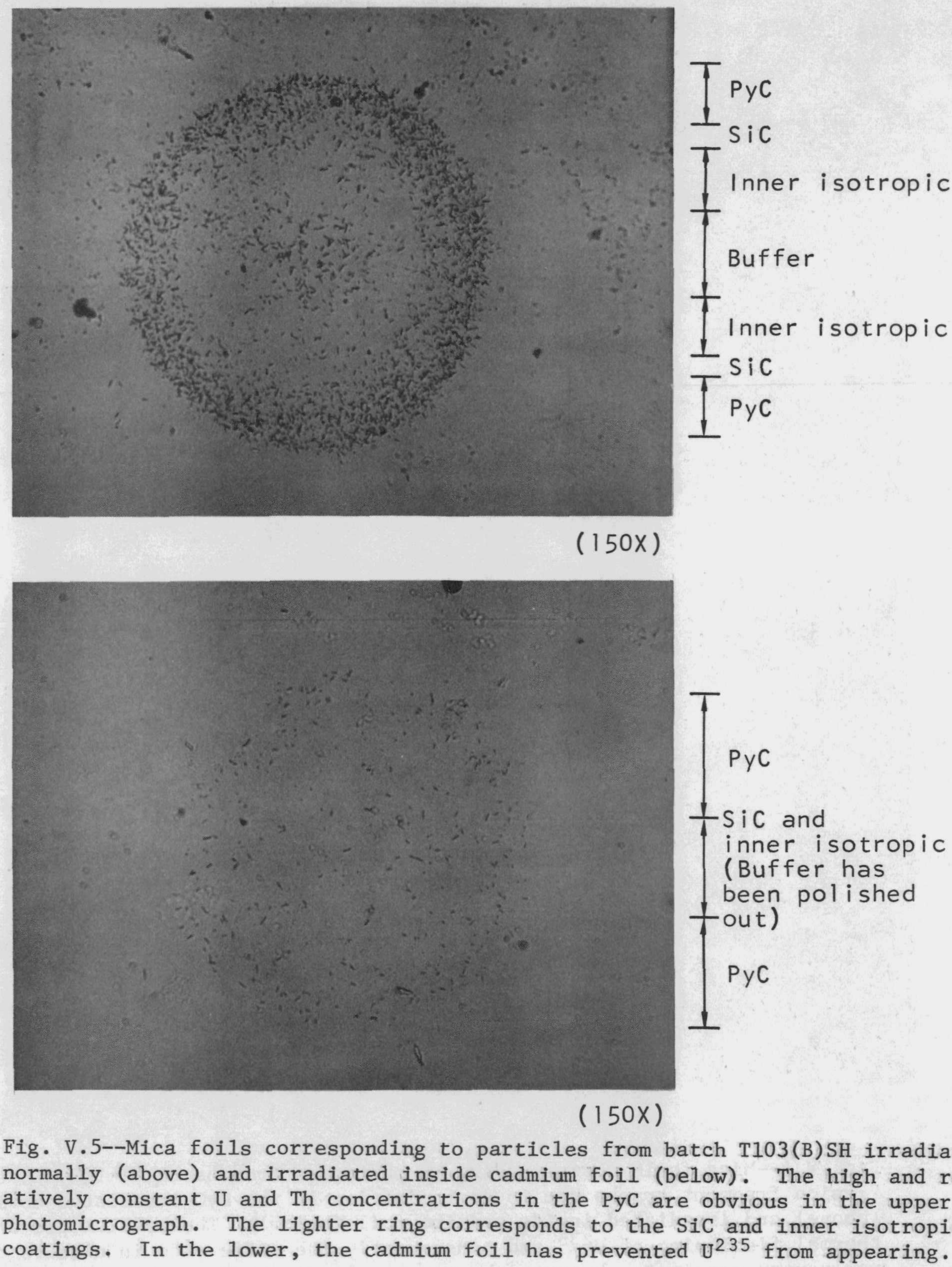

Fig. V.5--Mica foils corresponding to particles from batch T103(B)SH irradiated normally (above) and irradiated inside cadmium foil (below). The high and relatively constant U and Th concentrations in the PyC are obvious in the upper photomicrograph. The lighter ring corresponds to the SiC and inner isotropic coatings. In the lower, the cadmium foil has prevented U^{235} from appearing.

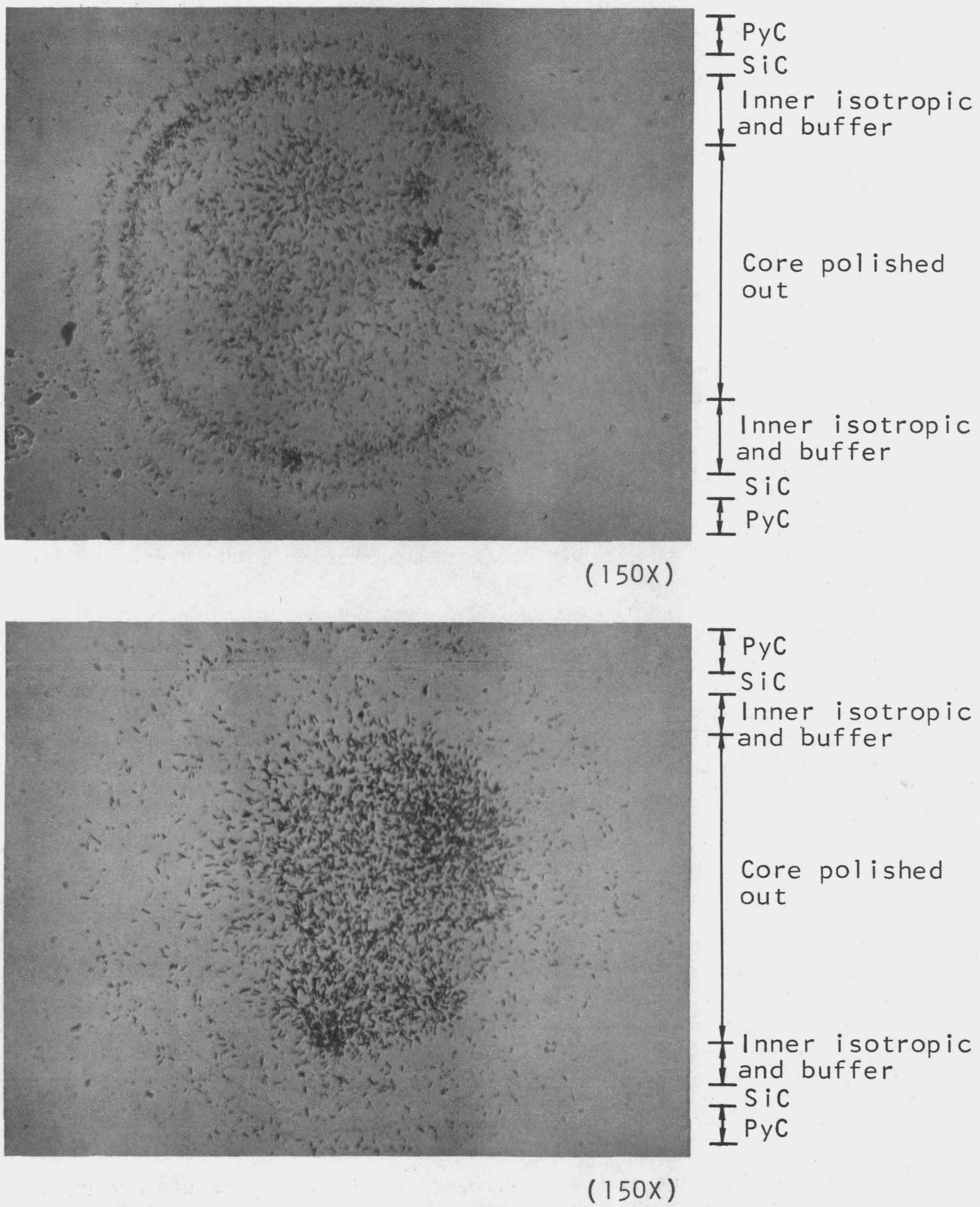

Fig. V.6--Mica foils corresponding to particles from batch T161(B)SL irradiated normally (above) and irradiated in cadmium foil (below). Three rings of contamination are visible in the upper photomicrograph, corresponding to the outer surfaces on the inner isotropic, SiC, and PyC layers, respectively. Contamination on the SiC is not visible in the lower photo indicating that it is almost entirely uranium

As in the case of the fissile particles, the uranium contamination appears greater in the HTI than in the LTI batches (the batch numbers prefixed by T103, etc., represent the chronological order of production). It may also be noted that uranium contamination levels in the outer PyC of these fertile particles are about the same as those in the fissile particles examined previously (Tables V.1 and V.3). Uranium contamination of fertile particles produced for PSC should not occur, however, as a result of separation of production of the fertile and fissile materials.

Contamination Measurement by PyC Burnoff

A study was initiated this quarter to determine the levels of thorium and uranium in and on the outer PyC layers of both fissile and fertile TRISO-coated particles. This work consisted of two parts: (1) measurements of fuel contamination on the surfaces of TRISO-coated particles and (2) measurements of fuel contamination in the PyC layers and on the surface of the SiC-substrate material.

In these studies a much more selective sample was used than had been used in earlier contamination studies. The integrity of the SiC layers was determined after each treatment by microradiography. These samples were carefully selected to contain only fuel particles with intact PyC and SiC coatings.

Approximately 500 radiographed particles (approximately 0.20 g) were placed in a 125-ml Erlenmeyer flask fitted with an air condenser. Five ml of $HClO_4$ and five drops of HCl (surface-leach solution) were added and the mixture was refluxed for an hour at about 200°C. The liquid was decanted, and the particles were washed three times with distilled water, twice with acetone, and then dried at about 150°C in an oven. The leach solution was evaporated to dryness and the residue was dissolved in 10 ml of HNO_3. The HNO_3 was evaporated and the extract was again treated with HNO_3 to remove all the chlorine. The residue was finally dissolved in 1 ml of HNO_3 and irradiated in the lazy Susan of the TRIGA reactor with the appropriate thorium and uranium standards.

The leached TRISO-coated particles were then irradiated for approximately 2 hr in the TRIGA Mark F reactor at ambient temperature to about 10^{14} fissions. After irradiation, the PyC layers were oxidized in a gas flow of about 100 cm^3/min of 10% O_2 - 90% He, which was passed over the particles at 1000°C and into a liquid-nitrogen-cooled silica gel trap where the Xe^{135} was collected. The oxidation unit and the particles were leached after oxidation with a solution consisting of 5 ml of $HClO_4$ and 5 drops of HCl (burn-leach solution).

The leach solutions were analyzed for fission products and protactinium using gamma spectroscopy with a Li-Ge 40-cm^3 crystal. The SiC-substrate particles were then microradiographed to detect broken SiC layers and then were gamma-counted. The Xe^{135} traps were gamma-analyzed using a 3-in. by 3-in. NaI crystal.

The data obtained in these experiments have been interpreted in the following manner: (1) For fissile particles, the ratio of the specific activity of a given fission product nuclide in the burn-leach solution to its specific activity in the SiC-substrate particle yields directly the fraction of U^{235} in the outer PyC coating and on the surface of the SiC-substrate. (All of this uranium will contribute to the release of metallic fission products, but only about 10% of it will contribute to the release of gaseous fission products.) The contribution of the thorium contamination to the fission-product yield is insignificant. (2) The ratio of the specific activity of Pa^{233} in the burn-leach solution to that in the SiC-substrate particle yields directly the fraction of thorium in the outer PyC coating. (3) The fission-product activity in the surface-leach solutions (compared with the uranium standard) was used to calculate the total amount of U^{235} contamination on the surface of the particles. These data can then be converted into the surface fraction of uranium on the sample. (4) Similarly, the Pa^{233} activity in these surface-leach solutions permitted quantitative estimates of the surface thorium contamination but only on fertile particles. (The amount of surface thorium contamination on fissile particles was below the limits of detectability. See footnote (b) of Table V.6). (5) For fissile particles, the ratio of the fractions of U^{235} and Th in the coating were generally the same as the Th/U ratio in the kernel. However, for fertile particles, which contain no uranium in the kernel, a difference between the fission product and the Pa^{233} levels in the coating indicates the presence of U^{235} contamination in the coating.

After leaching and gamma analysis, the SiC-substrate particles were annealed at 1300° or 1400°C for 5 hr to confirm, by strontium release measurements, the observations made on the microradiograph slides. With one exception, the annealing data showed that the SiC layers remained intact.

The thorium and uranium contamination levels in the PyC layers of fissile TRISO-coated particles are given in Table V.4. These data on fissile particles indicate that:

1. The thorium-to-uranium contamination ratio of the PyC layers of fissile particles usually approximates that of the core material.
2. Uranium contamination levels calculated from various fission-product spectra are in good agreement.

The contamination levels in the PyC layers of the fertile samples are given in Table V.5. The values represent the amount of a particular fission nuclide found in the PyC layer divided by the total amount of that nuclide produced in the kernel during irradiation. If these fission products originated only from fissioning of thorium, then the protactinium fractions in the PyC layers should equal the fission-product fractions. However, these data show a difference of three orders of magnitude between the thorium contamination fraction and the fission-product fractions in PyC layers. This difference indicates that a substantial amount of uranium was present in the PyC layers of fertile TRISO-coated particles, while little or no uranium was present in the SiC-coated substrate. The sample from lot T253(B)SL was an exception; the level of uranium contamination in this sample appeared to be significantly lower than in the other fertile particles.

Table V.4

FUEL CONTAMINATION IN THE OUTER PyC LAYERS OF FISSILE TRISO-COATED PARTICLES

Sample Lot No.	Fraction of U^{235} Based on					Fraction of Th Based on	U^{235}/Th Ratio (kernel)	Contamination Ratio U^{235}/Th
	Xe^{135}	Sr^{91}	Nb^{97}	Ba^{140}	Mo^{99}	Pa^{233}		
4000-886	7×10^{-8}	---	---	---	---	---	0.4	---
4000-889	6×10^{-7}	---	---	---	---	4×10^{-5}	0.4	0.015
3923-87E	1×10^{-8}	---	---	---	---	---	0.4	---
3923-111E	1×10^{-7}	---	---	---	---	$<4\times10^{-6}$	0.4	>0.2
ET49(B)SL	2×10^{-6}	3×10^{-6}	2×10^{-6}	2×10^{-6}	---	6×10^{-6}	0.4	~0.3
ET48(A)SH	2×10^{-6}	2×10^{-6}	1×10^{-6}	4×10^{-6}	---	5×10^{-6}	0.4	~0.5
ET49(A)SH	1×10^{-5}	2×10^{-5}	1×10^{-5}	2×10^{-5}	---	2×10^{-5}	0.4	~1
ET109(A)SH	2×10^{-6}	2×10^{-6}	1×10^{-6}	4×10^{-6}	---	$<2\times10^{-5}$	1.7	>0.10
ET1(B)SL	2×10^{-7}	---	---	7×10^{-7}	4×10^{-7}	$<2\times10^{-6}$	0.4	>0.2
ET48(B)SL[a]	2×10^{-3}	---	---	---	---	---	0.4	---
ET109(B)SL	---	2×10^{-6}	8×10^{-7}	2×10^{-6}	1×10^{-6}	$<8\times10^{-6}$	1.7	>0.12
ET255(A)SL	3×10^{-6}	1×10^{-6}	8×10^{-7}	1×10^{-7}	1×10^{-6}	$<7\times10^{-6}$	1.7	>0.14

[a] This sample contained broken particles, as indicated by the high Xe^{135} release.

Table V.5

FUEL CONTAMINATION IN THE OUTER PyC LAYERS OF FERTILE TRISO-COATED PARTICLES

Sample Lot No.	Fraction of Fission Products[a]					Fraction of Th Based on Pa^{233}	Contamination Ratio U^{235}/Th
	Xe^{135}	Sr^{91}	Nb^{97}	Ba^{140}	Mo^{99}		
T161(B)SL-1	$1x10^{-3}$	$2x10^{-3}$	$1x10^{-3}$	$2x10^{-3}$	---	$2x10^{-6}$	1000
T161(B)SL-2[b]	$2x10^{-3}$	$1x10^{-3}$	$1x10^{-3}$	$4x10^{-3}$	---	$3x10^{-6}$	1000
T169(B)SH-1[c]	$2x10^{-3}$	$3x10^{-3}$	$2x10^{-3}$	$3x10^{-3}$	---	$1x10^{-4}$	30
T169(B)SH-2[b]	$3x10^{-3}$	$3x10^{-3}$	$1x10^{-3}$	$3x10^{-3}$	---	$1x10^{-6}$	2000
T103(C)SL	$3x10^{-3}$	---	---	$4x10^{-3}$	---	$5x10^{-7}$	6000
T103(B)SH[c]	---	$3x10^{-3}$	$2x10^{-3}$	---	$1x10^{-3}$	$6x10^{-5}$	50
T253(B)SL	$3x10^{-5}$	$2x10^{-5}$	$1x10^{-5}$	---	$1x10^{-5}$	$5x10^{-6}$	>2

[a] Value given is amount of fission-product isotope found in PyC layers divided by total amount produced in particles.

[b] Duplicate samples.

[c] Sample contained at least two broken SiC-substrate particles, noted on examination of the microradiograph slide taken after oxidation of PyC layers. The thorium cores were only partially dissolved.

The amount of uranium present in the PyC layers can be estimated from the following relation:

$$\text{Weight of } U^{235} = \frac{\text{Total fissions in PyC layer} \times \text{mol wt of } U^{235}}{6.023 \times 10^{23} \times \text{cross section} \times \text{flux} \times \text{irradiation time}} \ .$$

This relation was used to calculate the average amount of uranium in the PyC layers of the particles tested. Ten nanograms of U^{235} irradiated in the TRIGA Mark I reactor for 4 hr would produce the observed levels of fission products in the PyC layers of the fertile particles. This is a small amount of uranium when compared with the thorium present in the test samples (each 0.2-g sample contained about 0.1 g of thorium).

The SiC-substrate particles were annealed at 1300° or 1400°C to confirm, by strontium release measurements, the integrity of the SiC-substrate particles.

In an unleached TRISO-coated particle, the release of fission products may be strongly influenced by the level of surface fuel contamination. The surface fuel contamination levels of the five fertile and the twelve fissile TRISO-coated particle samples and an additional fertile particle sample from lot T176(C)SH were determined by the activation analysis technique described above. The surface-leach solution from a weighed amount of particles was irradiated with a blank, a 1-μg thorium standard, and a 0.01-μg uranium standard in the TRIGA reactor to approximately 1 Mw-hr. The amounts of uranium and thorium in the surface-leach solutions were determined by gamma-analyzing the solutions and standards for Mo^{99} and Pa^{233} and comparing the relative activities. The data for these experiments are given in Table V.6. These data indicate that the levels of surface contamination are roughly the same as the levels of coating contamination given in Tables V.4 and V.5. The data obtained for U^{235} contamination on the surface and in the outer pyrolytic carbon coatings are summarized in Table V.7.

The data in Tables V.6 and V.7 indicate the following:

1. Uranium contamination on the surface of the fissile particles appeared to be slightly higher than that on the fertile particles. The surface area of the fissile particles was approximately 2.5 times larger than that of the fertile particles. If the surface area difference was considered, the contamination levels (g U^{235}/cm^2 surface area) were approximately equal.
2. The thorium contamination was approximately an order of magnitude greater than the uranium contamination on the fertile TRISO-coated particles.
3. The fraction of thorium on surfaces of the fertile particles was low (approximately 10^{-6} fraction).
4. The surface fuel contamination was high ($>10^{-5}$ fraction) for only one fissile sample, lot 4000-886.
5. The U^{235} contamination on the surface of fertile particles generally exceeds that in the coating.

Table V.6

SURFACE FUEL CONTAMINATION ON TRISO-COATED PARTICLES

Sample Lot No.	Surface Fraction Th^{232}	Surface (g Th^{232}/ g particles)	Surface Fraction U^{235}	Surface (g U^{235}/ g particles)
Fertile Particles				
T103(B)SH	$2x10^{-6}$	$1x10^{-6}$	(a)	$1x10^{-7}$
T103(C)SL	$2x10^{-6}$	$8x10^{-7}$	(a)	$\leq 3x10^{-8}$
T161(B)SL	$9x10^{-7}$	$5x10^{-7}$	(a)	$7x10^{-8}$
T169(B)SH	$2x10^{-6}$	$1x10^{-6}$	(a)	$1x10^{-7}$
T176(C)SH	$2x10^{-6}$	$1x10^{-6}$	(a)	$<3x10^{-8}$
T253(B)SL	$1x10^{-6}$	$6x10^{-7}$	(a)	$<4x10^{-8}$
Fissile Particles				
4000-886	$1x10^{-4}$	$3x10^{-5}$	$1x10^{-4}$	$8x10^{-6}$
4000-889	(b)	---	$5x10^{-6}$	$4x10^{-7}$
3923-87E	(b)	---	$\leq 4x10^{-7}$	$<3x10^{-8}$
3923-111E	(b)	---	$<5x10^{-7}$	$\leq 4x10^{-8}$
ET49(B)SL	(b)	---	$2x10^{-6}$	$1x10^{-7}$
ET48(A)SH	(b)	---	$4x10^{-6}$	$4x10^{-7}$
ET49(A)SH	(b)	---	$<8x10^{-7}$	$7x10^{-8}$
ET109(A)SH	(b)	---	$9x10^{-7}$	$2x10^{-7}$
ET1(B)SL	(b)	---	$1x10^{-6}$	$1x10^{-7}$
ET48(B)SL	(b)	---	$1x10^{-6}$	$7x10^{-8}$
ET109(B)SL	(b)	---	$2x10^{-6}$	$5x10^{-7}$
ET255(A)SL	(b)	---	$7x10^{-7}$	$2x10^{-7}$

[a] Not meaningful. See text.

[b] The lower detection limit for Th^{232} on fissile particles was 2×10^{-5} fraction.

Table V.7

URANIUM CONTAMINATION IN PyC LAYERS OF TRISO-COATED PARTICLES

Sample Lot No.	Layer Contamination (g U^{235}/g particles)	Surface Contamination (g U^{235}/g particles)
	Fertile Particles	
T103(B)SH	7×10^{-8}	1×10^{-7}
T103(C)SL	6×10^{-8}	$\leq3\times10^{-8}$
T161(B)SL	2×10^{-8}	7×10^{-8}
T169(B)SH	2×10^{-8}	1×10^{-7}
T176(C)SH	(a)	$<3\times10^{-8}$
T253(B)SL	8×10^{-10}	$<4\times10^{-8}$
	Fissile Particles	
4000-886	6×10^{-9}	8×10^{-6}
4000-889	5×10^{-8}	4×10^{-7}
3923-87E	8×10^{-10}	$\leq3\times10^{-8}$
3923-111E	8×10^{-9}	$\leq4\times10^{-8}$
ET49(B)SL	2×10^{-7}	1×10^{-7}
ET48(A)SH	2×10^{-7}	4×10^{-7}
ET49(A)SH	1×10^{-6}	7×10^{-8}
ET109(A)SH	4×10^{-7}	5×10^{-7}
ET1(B)SL	2×10^{-8}	2×10^{-7}
ET48(B)SL	(a)	1×10^{-7}
ET109(B)SL	4×10^{-7}	7×10^{-8}
ET255(A)SL	3×10^{-7}	2×10^{-7}

[a] No PyC contamination level was obtained because of particle failures.

6. The U^{235} contamination on the surface of fissile particles is approximately the same as that in the coating.

Coating Contamination in Long-term-anneal BISO Particles

Radiography of certain batches of long-term-anneal BISO particles heated for either 9,000 or 18,000 hr at 1400°C in helium revealed that many of the particles had bright rings at or very close to the PyC surfaces, indicating high concentrations of heavy metal in this area. A gradation in brightness of the rings could be observed by considering different particles on a X-ray plate (see Fig. V.7). In addition, a considerable number showed no radiographically detectable contamination at all. Specific particles from two batches were therefore picked out to include different amounts of radiographically detectable heavy metal, and these were sectioned and analyzed using the electron microprobe.

Coating contamination, visible radiographically as bright rings at the surfaces of the particles, was present in about 30% of the unleached particles from batch 3023-77E (18,000-hr anneal) and in about 65% of those from batch 3363-77E (9,000-hr anneal). The variations between different particles from each batch are shown in the two radiographs of Fig. V.7. In addition to the bright rings, many of the batch 3363-77E particles exhibited spotty contamination, which in several instances could be seen standing up from the surface of the particles by 2 or 3 μm. Figure V.8 shows typical particles having this type of surface contamination, but lacking the uniform contamination associated with the bright rings. The particle shown in Fig. V.9, which was found in batch 3363-77E, revealed that the spotty contamination originated from a broken or defective particle.

After leaching, most of the particles in both batches that originally showed the bright rings appeared clean (see Table V.8). In batch 3363-77E, the spotty surface contamination had been completely removed. Several particles in each of the batches, however, still showed contamination as light rings near the surfaces. Among these particles, it was noted that, in batch 3023-77E, these all appeared to exhibit core migration also. A detailed count of 300 leached particles from this batch showed 36 with core migration, of which 35 still had contamination near the surface. The remaining 264 particles exhibited neither phenomenon (Table V.8). An identical evaluation of batch 3363-77E revealed a similar correlation, as shown in Table V.8; in this case, however, core migration or breakdown was considerably less obvious. The excellent correlation between the occurrence of bright rings (which were indicative of the most highly contaminated particles originally) and the core migration in these leached particles shows that in both batches the rings at or very close to the outer surfaces originated from the diffusion of Th and U outward from the core, and not from external contamination as a result of broken particles.

The electron microprobe analyses were performed on the particles by first scanning each particle (nine were selected and mounted from each batch) for the region of highest thorium and uranium contamination at the outer edge of the coating. Uranium and thorium determinations were then made every 1 μm across this zone, starting in the mounting material and continuing to

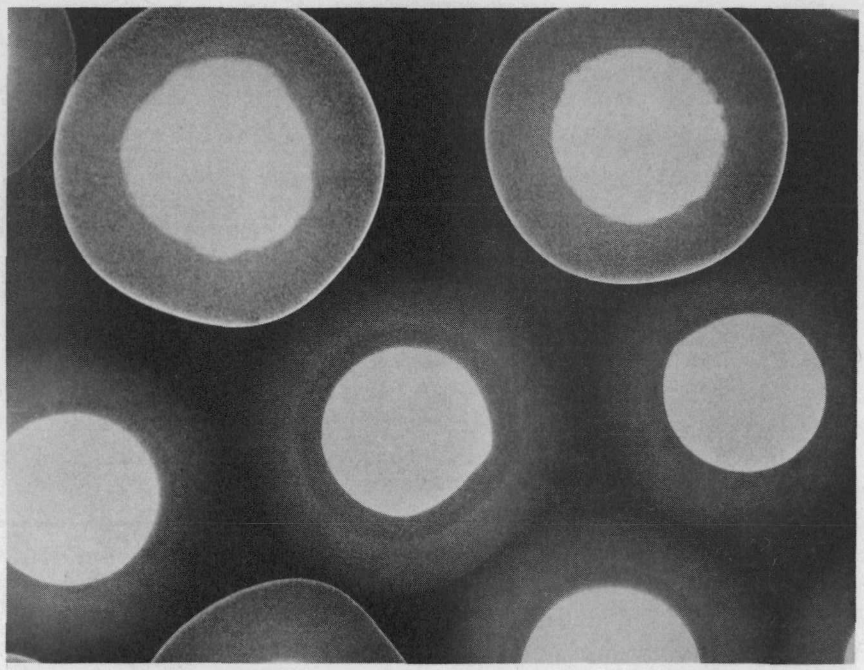

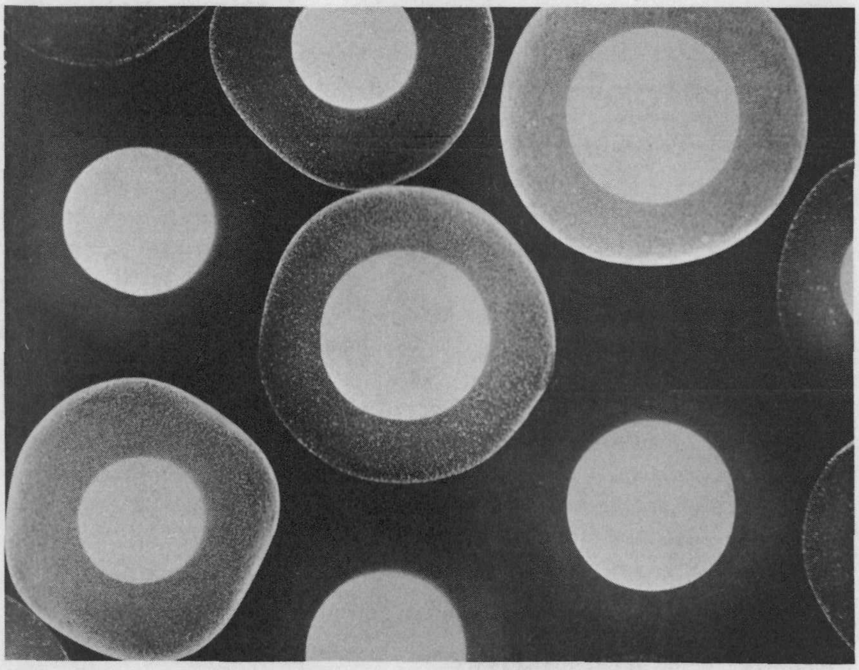

Fig. V.7--Radiographs of long-term-anneal BISO particles from batch 3023-77E (above) and from batch 3363-77E (below). Particles from both batches show various degrees of radiographically detectable contamination in the outer coatings, evident by the brightness of the outer rings (150X)

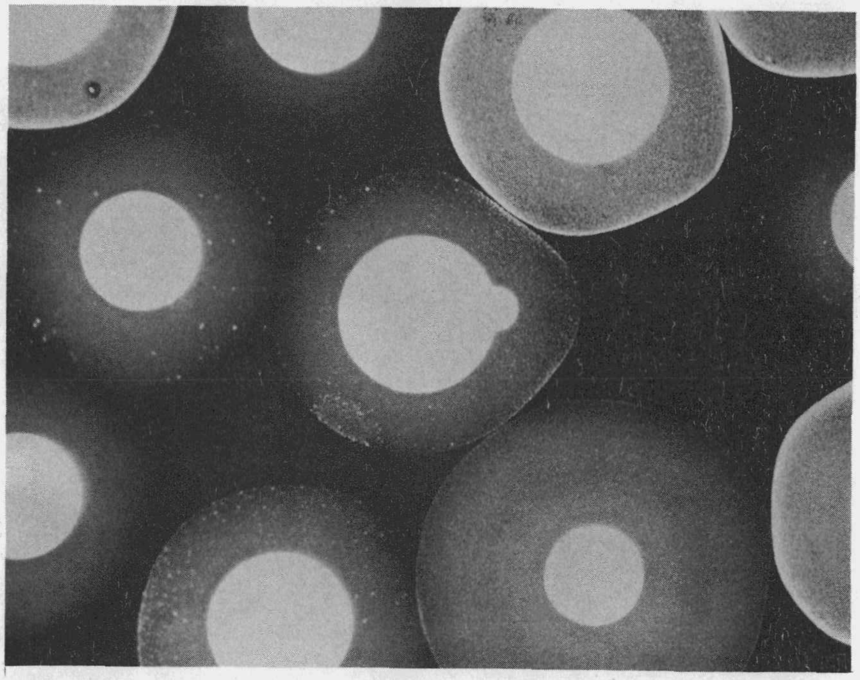

Fig. V.8--Spotty contamination detected radiographically in unleached particle from batch 3363-77E. This type of contamination is raised up from the particle surfaces, and arises as a result of external contamination by broken particles (100X)

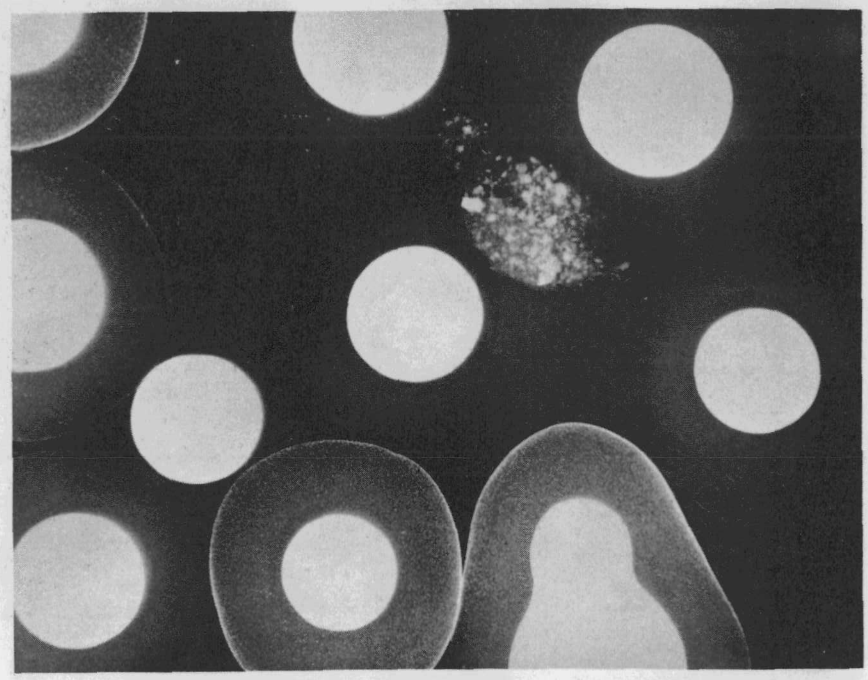

Fig. V.9--Defective particle and foreign material present in batch 3363-77E. Defective particle has only about 10 μm of either buffer or PyC coatings, and the foreign material was unidentified. Either or both could account for the external spotty contamination observed in unleached particles of batch 3363-77E (see Fig. V.8) (100X)

Table V.8

NUMBER OF PARTICLES SHOWING CORE MIGRATION AND COATING CONTAMINATION BEFORE AND AFTER LEACHING

Batch No.	No. of Particles Examined	No. of Particles With Rings Before Leaching	No. of Particles With Rings After Leaching	No. of Particles With Core Migration After Leaching	No. of Particles With Rings and Core Migration After Leaching
3023-77E	300	93	35	36	35
3363-77E	300	194	24	23	22

the inner edge of the PyC. Two typical contamination profiles are shown in Figs. V.10 and V.11, and the maximum uranium and thorium concentrations measured in the rings around the different particles are shown in Table V.9.

In general, the microprobe analyses bore out the radiographic observations extremely well. In every case the uranium and thorium concentrations were at maxima about 3 to 4 μm below the particle surfaces, and dropped down to approximately constant, just-above-background levels at distances greater than 20 μm into the PyC. In many particles these low constant levels of uranium and thorium contamination (0.01 to 0.04 wt-%) were attained within 10 μm of the particle surfaces. As shown in Table V.9, the maximum uranium and thorium concentrations occurred at the same place, except in four of the most contaminated particles from batch 3363-77E. In these latter particles, secondary peaks were present, as shown graphically in Fig. V.11.

The combined uranium and thorium concentrations listed in Table V.9 for each particle showed that the brightness of the rings visible radiographically varied in direct relation to the amount of contamination present, as would be expected. Particle 3 from batch 3023-77E and particle 10 from batch 3363-77E, however, were exceptions to this rule, but since the brightness was not judged quantitatively, for example by a microdensitometer, interpretation of the order of severity depended on the observer.

Table V.9 indicates that the detectable limit for radiographically observable heavy metal is in the region of 1 wt-%. Both particle 4 of batch 3023-77E and particle 3 of batch 3363-77E showed very light rings corresponding to this level of contamination, but the particles with less heavy-metal contamination than these showed nothing. Since particle 3 of batch 3363-77E had the least contamination of the two (about 1.5 wt-% heavy metal maximum), this is about the least amount visible when evenly distributed around the PyC.

Probably the most significant factor in the investigation is that the uranium and thorium concentrations throughout most of the PyC are 0.01 to 0.04 wt-%, and these concentrations are relatively constant. Only near the surfaces of the particles are the uranium and thorium concentrations higher than this, building up to maxima of 3 or 4 μm beneath the particle surfaces. Since "uphill" diffusion is impossible, the uranium and thorium near the surface must be in a different state from that diffusing through the PyC. For example, oxygen may be diffusing into the particles to form very stable oxides just beneath the surface. The exact mechanism of contamination buildup beneath the particle surfaces is not known, however, and experiments are continuing.

Alpha-count Data Versus Contamination in PyC Coating

The α-count data obtained since April 1966 for capsule and proof test element material have been evaluated. An end-window proportional counter was used for detecting and counting, and an alpha chamber housed the planchette that contained the fuel particles. The 2-in.-diameter planchette was filled with fuel particles several layers deep; by this means, the alpha chamber saw a continuous surface of infinite thickness. This meant that the method of

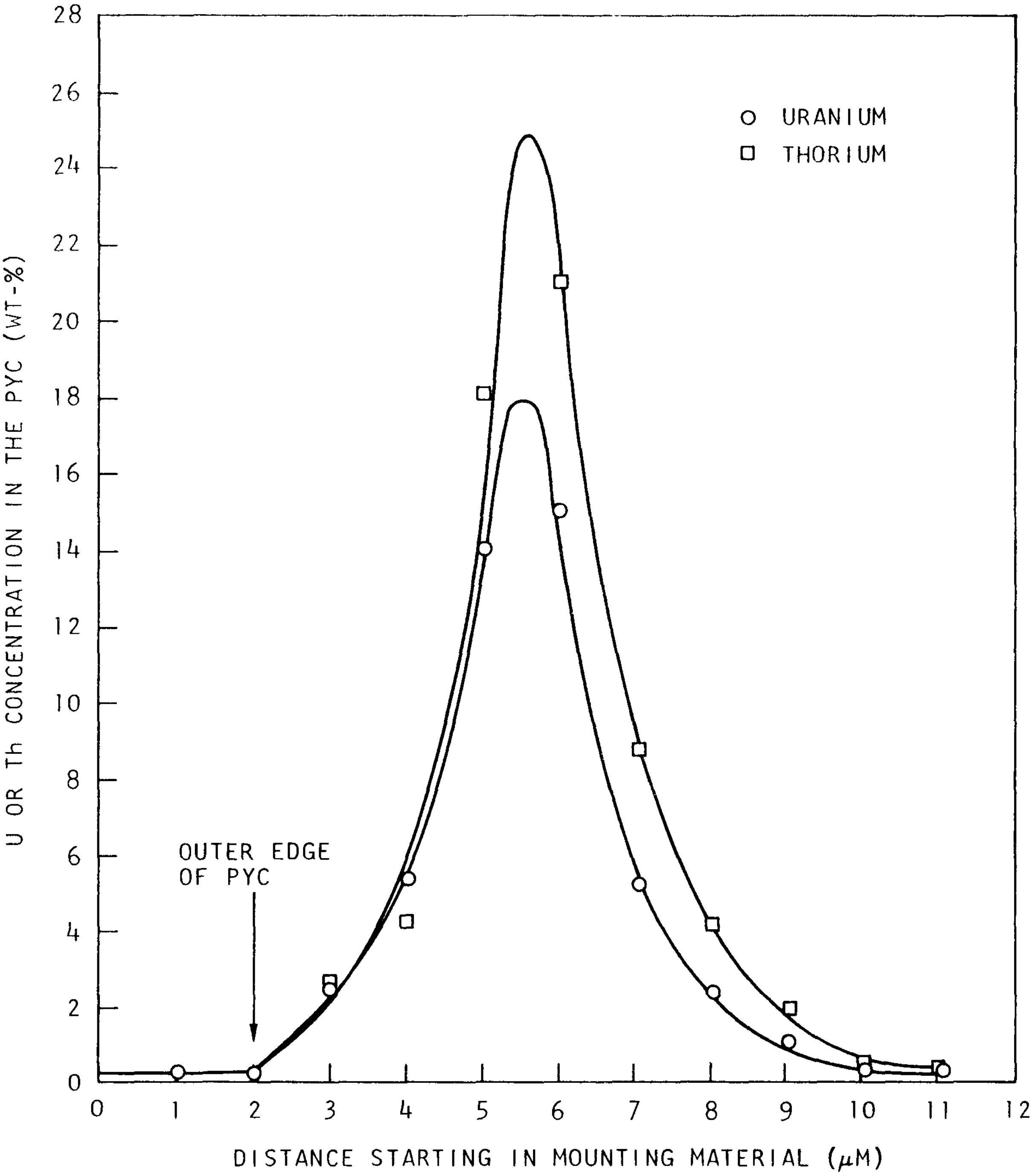

Fig. V.10--Typical contamination profile in PyC of a long-term anneal BISO particle from batch 3023-77E (No. 6)

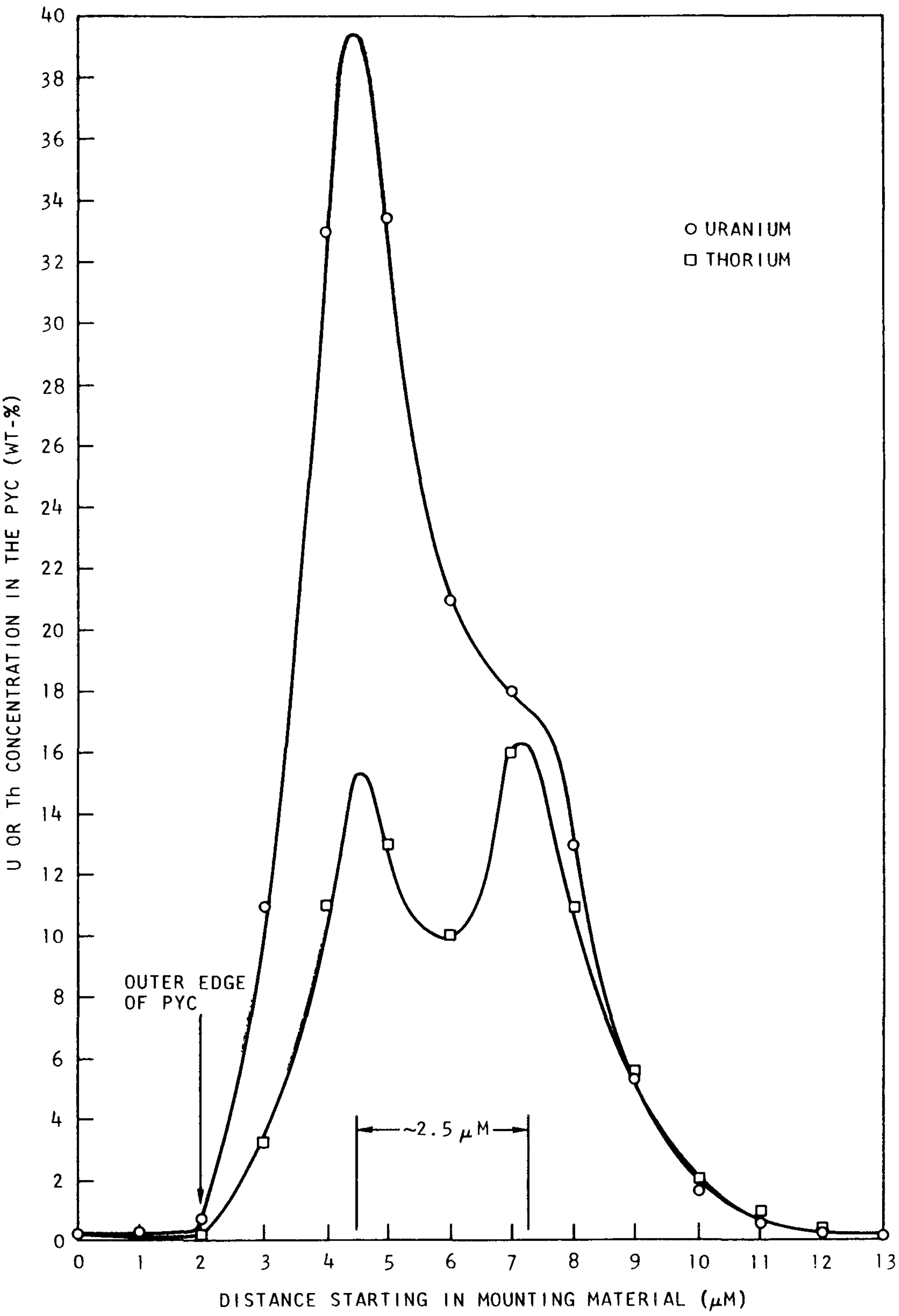

Fig. V.11--Typical contamination profile in the PyC of long-term anneal BISO particle from batch 3363-77E (No. 23)

Table V.9

MAXIMUM URANIUM AND THORIUM CONCENTRATIONS IN THE PyC COATINGS

ID No.[a]	Apparent Order of Severity Radiographically	Max. U Concentration (wt-%)	Th Concentration at Same Place (wt-%)	Max. Th Concentration If Different (wt-%)
		Batch 3023-77E, Th:U ratio = 4:1		
16	1[b]	0.02	0	---
15	1[b]	0.06	0.03	---
14	1[b]	0.14	0.07	---
4	2	1.6	2.3	---
5	3	5.4	4.5	---
7	4	6.7	7.0	---
8	5	11.6	15	---
6	6	15	21	---
3	7	13	11	---
		Batch 3363-77E, Th:U ratio = 1.6:1		
5	1[b]	0.10	0.03	---
1	1[b]	0.18	0.01	---
3	2	1.3	0.16	---
2	3	1.1	0.08	---
12	4	4.9	2.0	2.1
10	5	18	7.4	---
16	6	14	2.0	3.4
18	7	22	6.7	9.8
23	8	33	13	16

[a] Particle identification number on slide F-785 for batch 3023-77E; slide F-786 for batch 3363-77E.

[b] No contamination visible radiographically.

counting was independent of particle size, shape, and weight if the PyC coating was greater than 15 μm thick. About 5 g of particles was sufficient to fill the planchette adequately.

The particles were generally counted for 60 min or to 10,000 counts, if the latter took a shorter time. The background was determined by counting an empty planchette for the same length of time. Knowing the α-standard factor, the alpha activity in counts per minute per square centimeter were then calculated from the formula

$$\frac{(C_p - C_b}{T} \times \frac{\alpha_s}{A} = n \qquad \text{counts/min-cm}^2 \quad ,$$

where C_p = α-counts from particles in time T,

C_b = background α-counts in time T,

α_s = alpha standard factor, and

A = area of planchette.

The results are listed in Table V.10 and Fig. V.12; for clarity, the BISO HTI, BISO LTI, and TRISO results are also presented separately in Figs. V.13, V.14, and V.15.

Figure V.12 shows most obviously that the quality of particles has improved markedly since November 1965. Alpha-count values, taken as an indication of contamination within 15 μm of the particle surfaces that were obtained for most recent BISO HTI and LTI batches are an order of magnitude lower than for the P13 and P14 samples. All recent TRISO particles also give values less than 10 counts/min-cm^2 and as low as 0.01 count/min-cm^2, the present limit of detection for the method.

In general, BISO LTI batches appear to be far less contaminated than BISO HTI batches, which might be expected considering the times at temperature involved during processing. TRISO batches are generally less contaminated than either type of BISO particle. No distinction can be made between the TRISO-I and TRISO-II material on an α-count basis, since both show values between 0.01 or less than about 0.7 count/min-cm^2. Likewise, no distinction is possible between TRISO-I (or TRISO-II) HTI and LTI batches.

A correlation was attempted between the α-count readings determined for various batches of enriched fissile particles and the U^{235} contamination present in the outer 15 μm of the outer PyC of these particles. Coating contamination values were obtained from several sources, as noted in Table V.11, and were normalized to estimate the amount of U^{235} in the outer 15 μm of PyC, in each case assuming a constant level of contamination throughout the outer coating. Any α-particles originating deeper than this within the particles would not escape from the particle surfaces, and thus could not affect the α-count values determined.

Table V.10

ALPHA ACTIVITY AND FABRICATION DATES OF CAPSULE MATERIALS

Date Fabricated	Material Type[a]	Number of Batches Included	Capsule	Th:U Ratio	α-counts/min-cm^2
Nov. 1965	BISO HTI	9	P14	3.0	25-47
	BISO HTI	3	P14	12.0	15-24
Feb. 1966	TRISO HTI	7	P13F	3.0	3.2-10
Mar. 1966	BISO HTI	11	P15	1.6	73-109
	BISO HTI	4	P15	8.0	40-55
June 1966	TRISO HTI	5	P13H	1.6,8.0	7.8-15.3
	TRISO HTI	4	P13H	1.6,8.0	28-124[c]
Aug. 1966	BISO LTI	5	P16	1.6	7.3-12
	BISO LTI	2	P16	8.0	20-23
	BISO HTI	2	P16	8.0	30-35
Feb. 1967	TRISO LTI	7	P13J2	1.9	0.8-3.4
	BISO LTI	1	P13J2	1.9	0.8
	BISO HTI	1	P13J2	1.9	82
Mar. 1967	TRISO LTI	2	P17, P18	1.9	0.6-8.8
	BISO LTI	11	P17, P18	1.6,2.2,2.8,3.5	1.2-8
	BISO HTI	13	P17, P18	1.6,2.2,2.8,3.5	8.5-20
Dec. 1967	BISO LTI	6	P19	2.5	0.4-1.9
	BISO HTI	8	P19	2.5	2.1-36
Mar. 1968	TRISO-I[b]	7	P20	2.25	≤0.01-0.9
	TRISO-II	5	P20	2.25	0.02-0.07
Mar. 1968	TRISO-I	5	P21	2.75	≤0.01-0.57
	TRISO-II	4	P21	2.75	0.02-0.31
	TRISO-I	1	P21	2.75	0.96
	TRISO-II	1	P21	2.75	0.7
Apr. 1968	TRISO-I	1	P22	2.75	0.72
	TRISO-II	3	P22	2.75	0.08-1.24
	TRISO-II (fertile)	2	P22	∞	≤0.01-0.07
	TRISO-I	2	P22	2.75	0.88-1.5
	TRISO-II	9	P22	2.75	0.85-3
	TRISO-II (fertile)	2	P22	∞	0.1-0.14
July 1968	TRISO-II	9	P23	2.24	0.47-0.80
	BISO LTI	3	P23	2.24	0.48-0.56
Aug. 1968	TRISO-II	12	PTE[d]	0.6	0.55-2.93
	TRISO-II (fertile)	18	PTE[d]	∞	0.29-3.42

[a] Fissile particles unless otherwise stated.

[b] No distinction is apparent between TRISO-I (or TRISO-II) HTI and LTI batches made during and after this period.

[c] Bare cores present.

[d] Second proof test element.

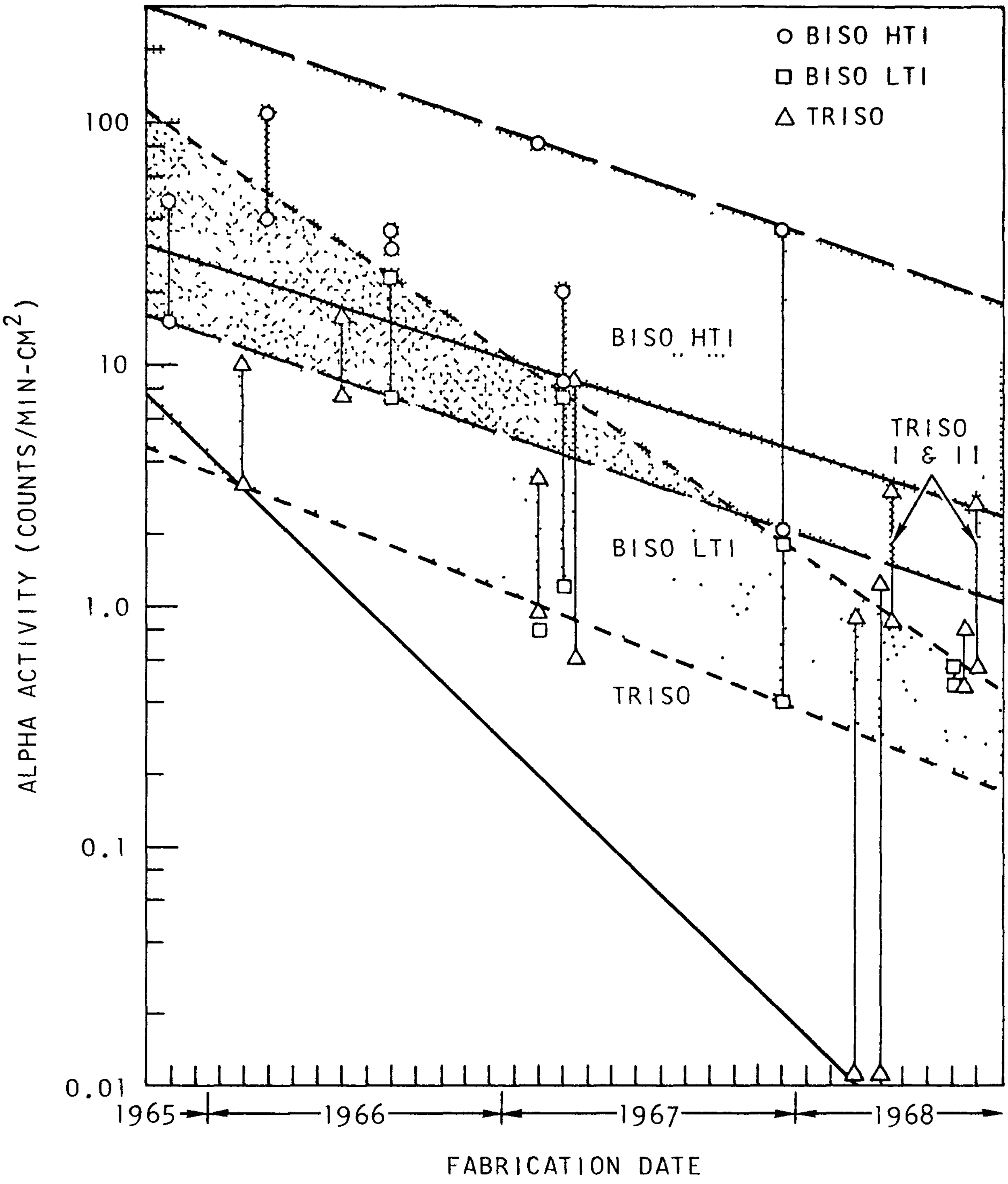

Fig. V.12--Alpha activity of capsule materials versus fabrication date

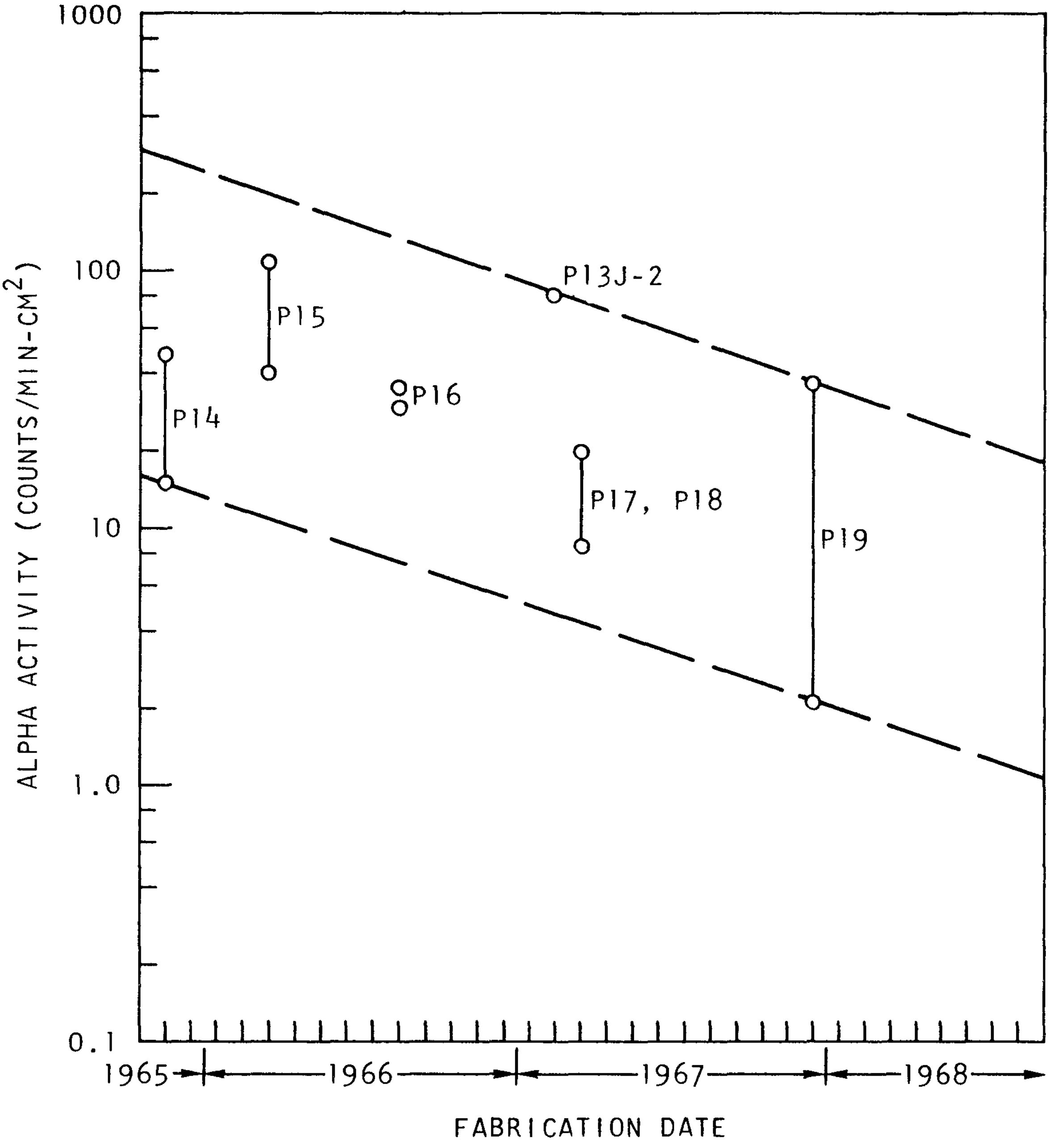

Fig. V.13--Alpha activity of capsule BISO HTI particles versus fabrication date

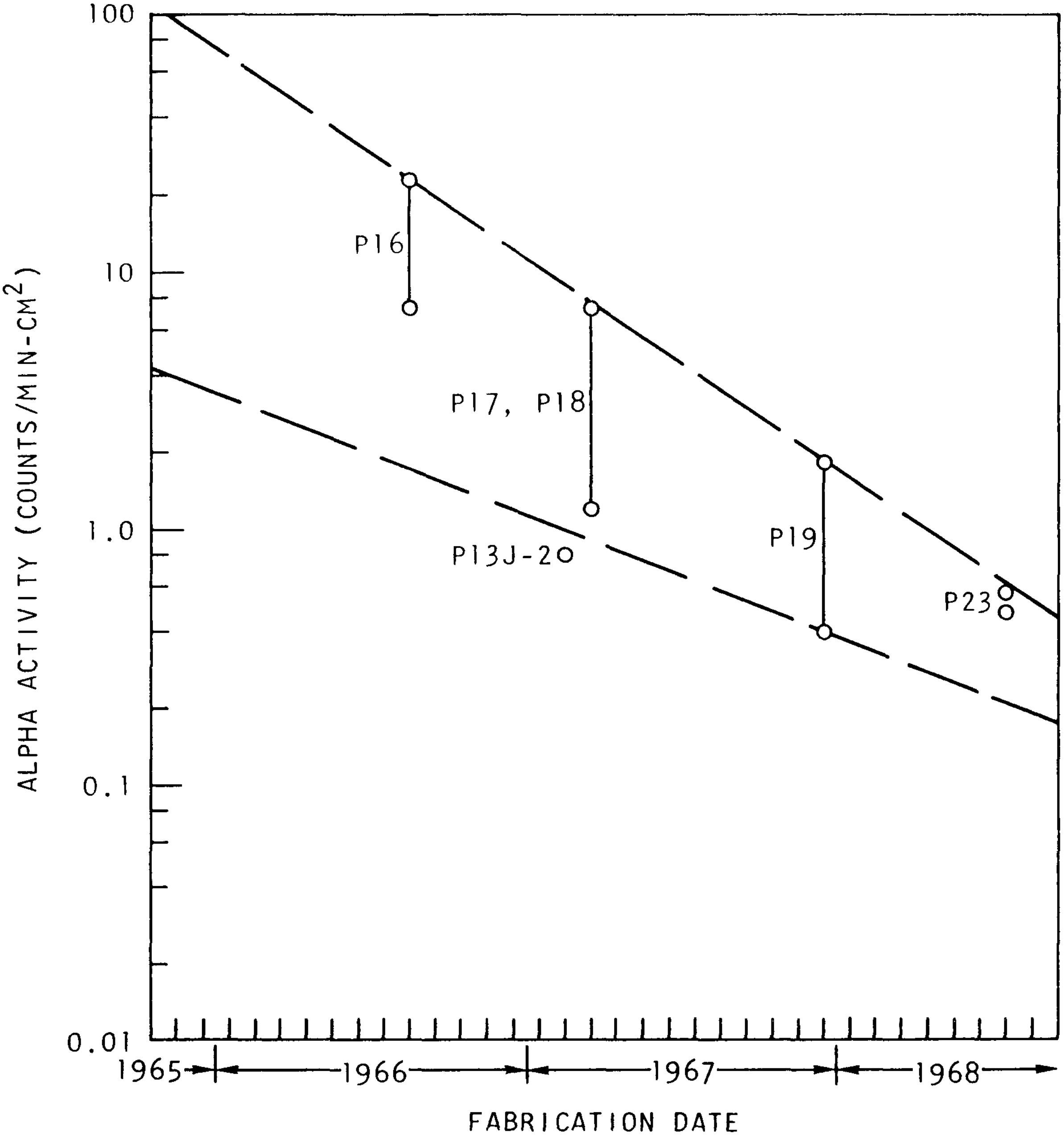

Fig. V.14--Alpha activity of capsule BISO LTI particles versus fabrication date

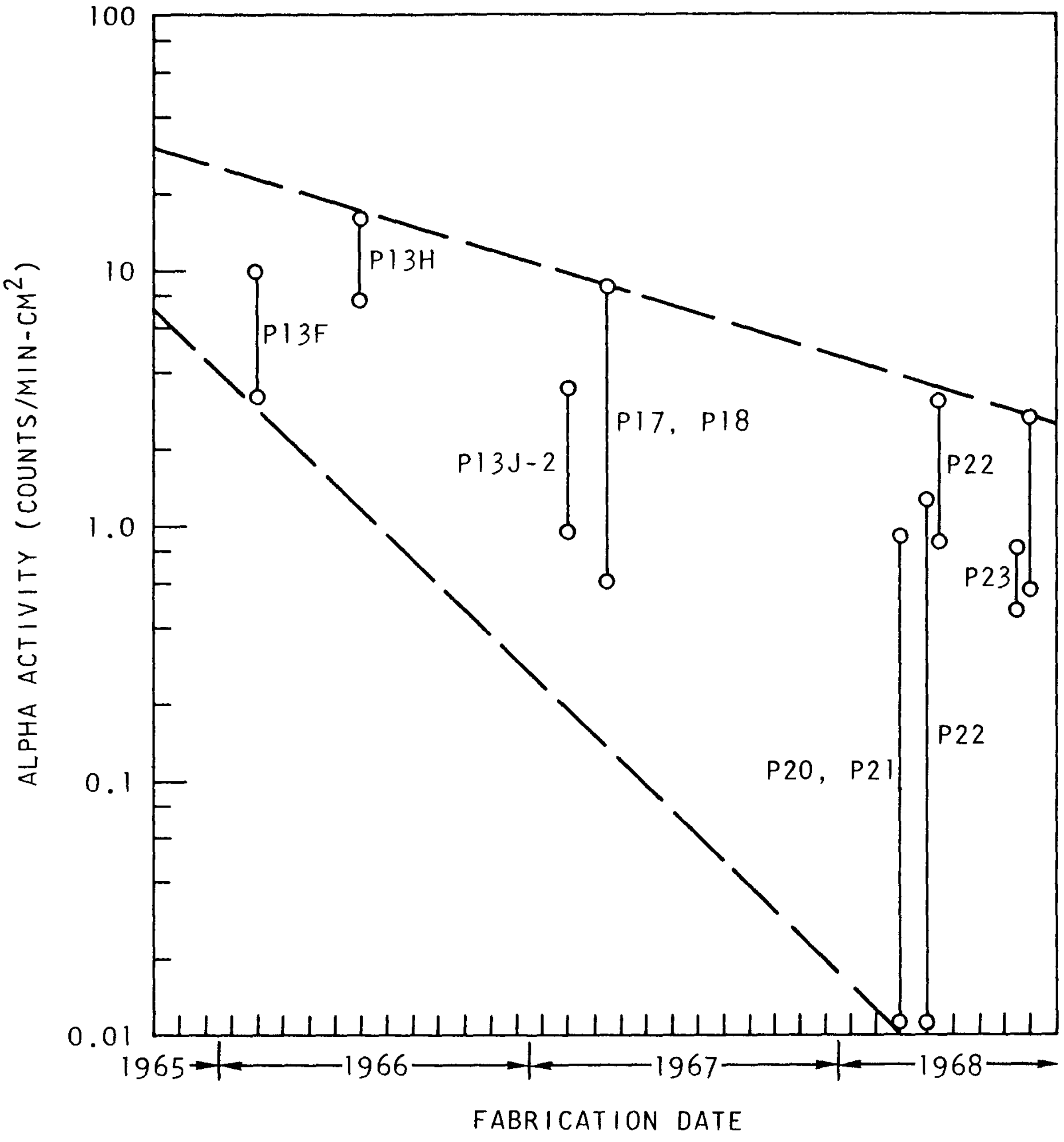

Fig. V.15--Alpha activity of capsule TRISO particles versus fabrication date

Table V.11

ALPHA ACTIVITY AND FRACTIONAL U^{235} CONTAMINATION IN OUTER 15 μm OF ENRICHED FISSILE PARTICLES

Batch No.	Particle Type	Alpha Activity (counts/min-cm^2)	Fractional U^{235} Contamination in Outer 15 μm
2824-19E	BISO HTI	97	2.8×10^{-4} 2.5×10^{-4}
2824-9E	BISO HTI	81	3.7×10^{-4} 5×10^{-4}
3363-149E	BISO HTI	71	1.1×10^{-4} 2.5×10^{-4} 3.3×10^{-4}
4000-691E	BISO HTI	27	2.2×10^{-4}
3742-11E	BISO HTI	17	3.8×10^{-4} 3.2×10^{-4}
3363-103E	BISO LTI	12	2.6×10^{-5} 8×10^{-5} 4.4×10^{-5}
3592-147E	BISO LTI	7.5	2.3×10^{-4} 2.4×10^{-4}
3325-123E	TRISO-I HTI	124	3.2×10^{-4} 4.1×10^{-4}
3325-87E	TRISO-I HTI with ZrC barrier	47	6.8×10^{-6} 7.3×10^{-6}
3592-35E	TRISO-I LTI	3.0	3×10^{-7}
3592-45E	TRISO-I LTI	1.2	4×10^{-7}
3923-85E	TRISO-I LTI	0.16	1×10^{-7}
3332-101E	TRISO-I/II HTI	3.2	1×10^{-5} $<4\times10^{-7}$[a] $<5\times10^{-7}$[a] $<1\times10^{-7}$[a]
3923-111E	TRISO-II HTI	0.03	5.5×10^{-8}
4000-717E	TRISO-II HTI	0.86	1.2×10^{-6}
4155-133E	TRISO-II HTI	0.99	1.4×10^{-6}
3923-87E	TRISO-II LTI	0.02	2×10^{-8} 5.5×10^{-9}
4000-719E	TRISO-II LTI	2.66	1.4×10^{-6}
4155-139E	TRISO-II LTI	1.43	1.0×10^{-6}
4000-747E	TRISO-II LTI	1.13	7×10^{-7}
4000-889E	TRISO-II LTI	0.70	3.2×10^{-7}

[a] No defective particles present.

Figure V.16 shows that there appears to be a reasonably good correlation between α-activity and U^{235} contamination of the outer PyC when these values are plotted on a log-log scale. That this is fortuitous over four orders of magnitude seems unlikely, although to justify a relationship of this sort theoretically would be extremely difficult. Several "open" points are plotted on Fig. V.16; these are not considered significant because they are the result, in general, of defective particles. All the batches plotted as open points showed many defective particles; in particular, radiographs of representative material from batches 3592-45E and 3592-35E showed bare cores. Consequently, the open points probably represent the correct fractional contaminations for the good particles but the wrong α-count values, since the latter consider the batch as a whole.

Support for the above argument is gained from the investigations of batch 3332-101E, which contained a relatively large number of PyC-coated cores and other defective particles (Ref. 7). As shown in Table V.3, three independent determinations on good particles from this batch showed that the fractional U^{235} contamination in the outer 15 μm was less than 5×10^{-7}. A fourth determination, on the other hand, found 1×10^{-5} fraction for the same material. This determination involved removing increments of coating from about 500 particles and determining the amount of removed U^{235} by activation analysis. It is quite likely, therefore, that one or more defective particles were included in the 500 particles abraded, giving the high value noted.

At this stage it is not known precisely what a particular α-count value corresponds to in terms of relative abundances of U^{235}, U^{234}, Th^{232}, and other isotopes. Consequently, considerable work may be necessary to standardize the present procedure in order to obtain fractional contamination values with respect to certain elements or isotopes.

Alpha Spectroscopy for Quality Control of Fuel Particles

It has been suggested that alpha spectroscopy, as distinct from simple alpha-counting, may be a useful quality-control method for fuel particle production to determine levels of fuel contamination in coatings. Consequently, preliminary studies of the alpha spectra of fissile and fertile particles were started during the quarter.

Alpha spectroscopy not only reveals the presence of alpha emitters on the surface of particles but also reveals the alpha-emitting species. Thus, in several fertile particle samples, in addition to the expected thorium contamination, it has been possible to show that U^{235} is also present on the surface of the particles.

DEFECTIVE PARTICLE STUDIES

Nature of Specks in the PyC of Certain TRISO Particles

Various types of radiographically detectable defective particles are present in varying numbers in all batches of fuel particles. The chief types of defective TRISO particles, their origins, and frequencies of occurrence

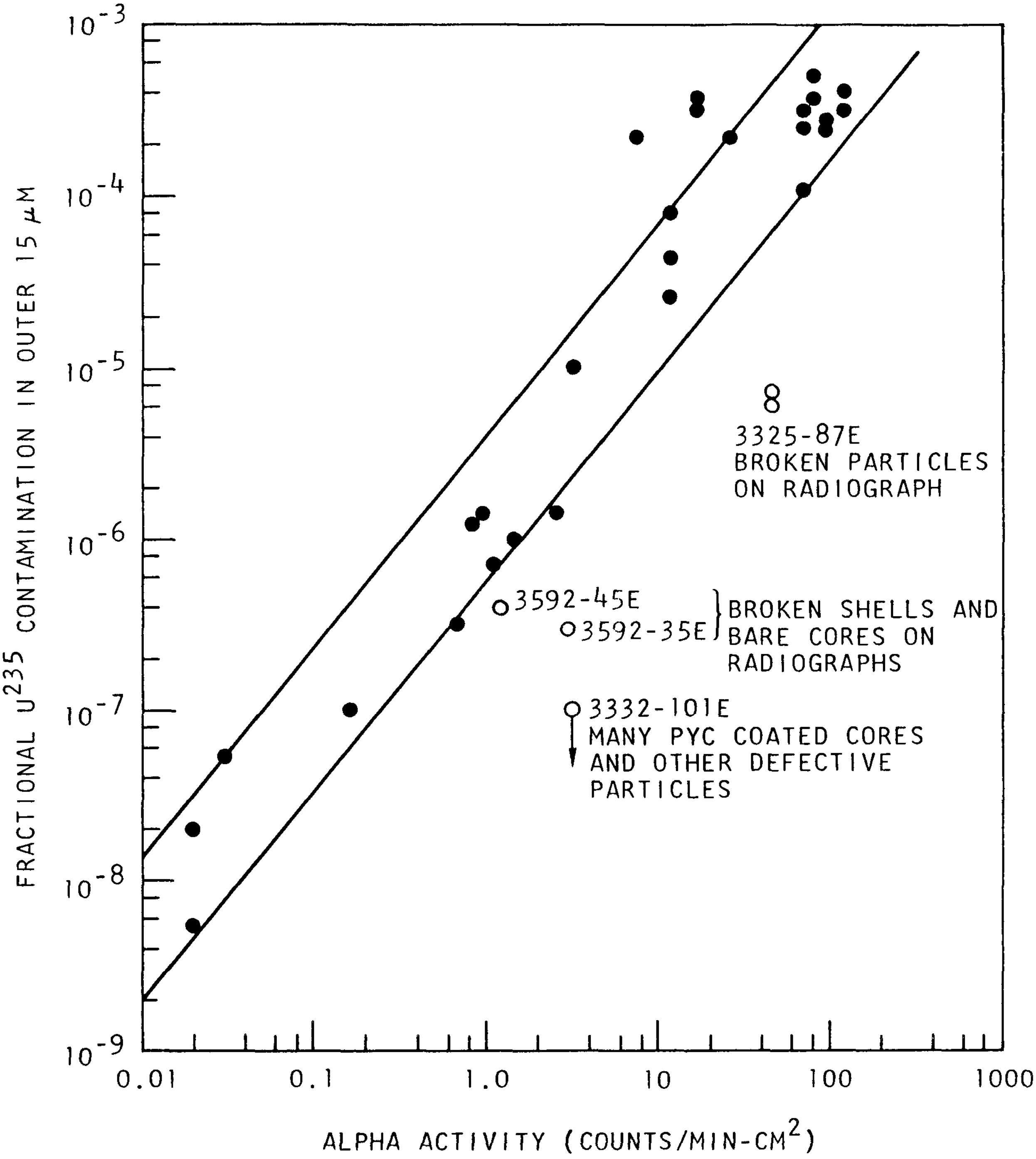

Fig. V.16--Alpha activity of enriched fissile particles versus PyC coating contamination have been reported (Ref. 7). Several types of defective TRISO particles have been identified that would show poor performance in a reactor, such as those with no SiC layers, cracked SiC, and no buffer. Other types, such as particles with leached cores and those with specks in the outer PyC, may be inferior to regular particles if the cores are still leachable and if the specks are of fissionable material, respectively (Ref. 7).

During this quarter, particles with specks in the PyC have been separated out from two batches of TRISO particles showing relatively large numbers of these defects. Since the specks were visible radiographically (see Fig. V.17), it was likely that they were quite dense and could be detected by electron microprobe analysis. About 10 particles from each batch were therefore mounted, polished down to remove the core material, and examined using the electron microprobe.

All the elements commonly found in fuel particles were looked for briefly. Only Th and Si were found to occur in any significant amounts in the coatings, and U was just detectable in some areas of one or two particles. The relatively high Th and Si concentrations occurred only at the outer edges of the PyC on all the particles, as shown in Fig. V.18. The "very high" thorium specks were only a few micrometers square, and were not found in all of the particles (as would be expected considering a random cross section through specks of this size). The largest number detected was six or seven around any one particle (Fig. V.18), and probably considerably more than 10 wt-% Th was present in these small specks. The fewer specks of high Si (less than 10 wt-%) detected were in some cases coincident with areas of high Th, but generally were not (Fig. V.18), suggesting no chemical combination of the Th and the Si.

The uranium concentration in the high-thorium specks was extremely low in every case, probably a few hundredths percent only (see Fig. V.19). The Th:U ratio in the specks is therefore estimated to be at least 10:1 and is probably more than 100:1. Since the core material has a Th:U ratio of about 2.75:1, the specks are not due to contamination either by polishing or by broken particles from either of the two batches examined.

It is concluded that the specks in the PyC detectable radiographically are due in part to silicon but mainly to thorium, probably in the form of oxide. The specks are on the particle surfaces and have very much higher Th:U ratios than the core material in the particles; they are contamination that occurred outside the coaters, possibly due to broken fertile particles. As has also been noted above, uranium contamination is observed on the surfaces of fertile particles. The number and size of the high-thorium specks are considered small enough that they would not affect the fission-product release characteristics of these fissile particles significantly.

THERMAL STABILITY OF COATED PARTICLES

The purpose of this work is to determine the mechanism for chemical interaction of core and coating in TRISO-coated fuel. The ultimate goal, with regard to the reaction, is to establish the operating limits of time

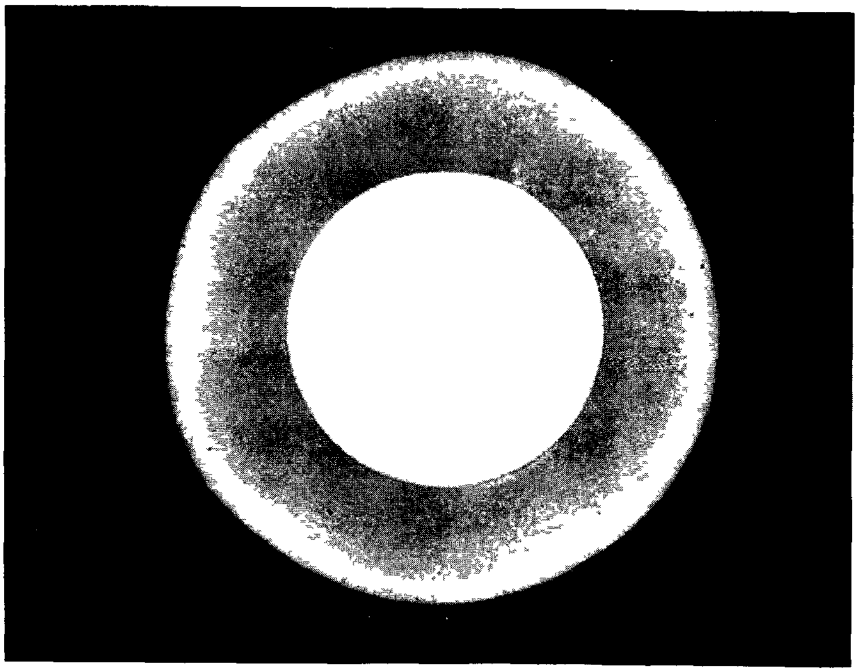

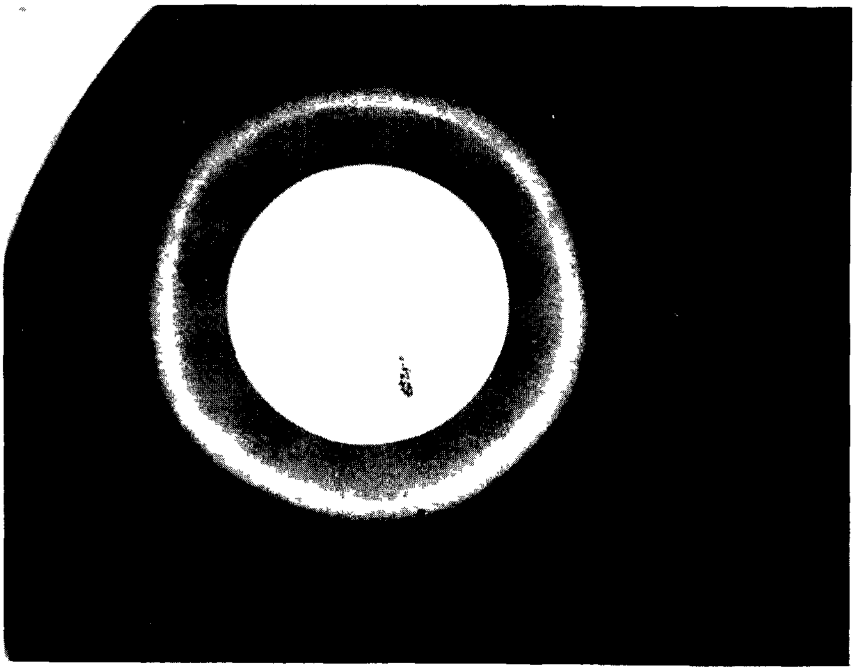

Fig. V.17--Typical defective particles exhibiting radiographically detectable specks in the outer PyC: batch ET109(B)SL (above) and batch 4000-886E (below) (200X)

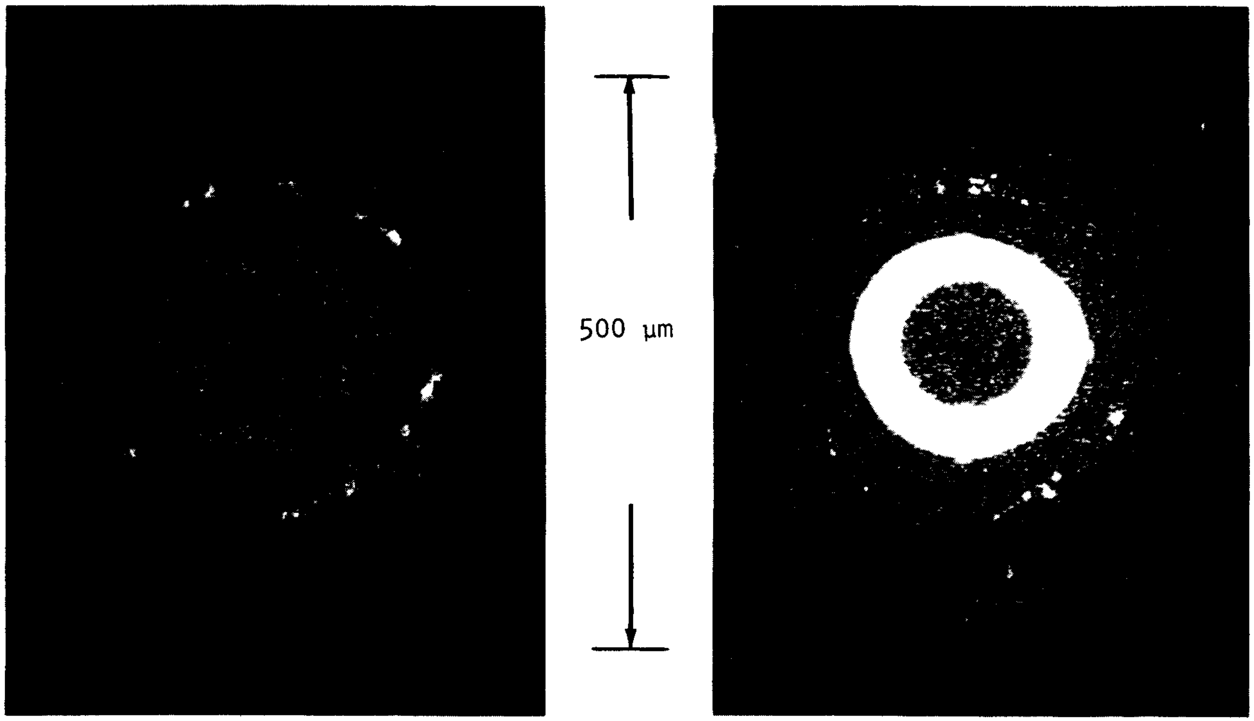

Fig. V.18--Electron microprobe backscatter photographs of particles from batch with specks in the PyC; thorium Mα (left) and silicon Kα (right). The high-Th and high-Si specks are on the surface of the particle, but do not necessarily occur together, suggesting no chemical combination of the two elements (150X)

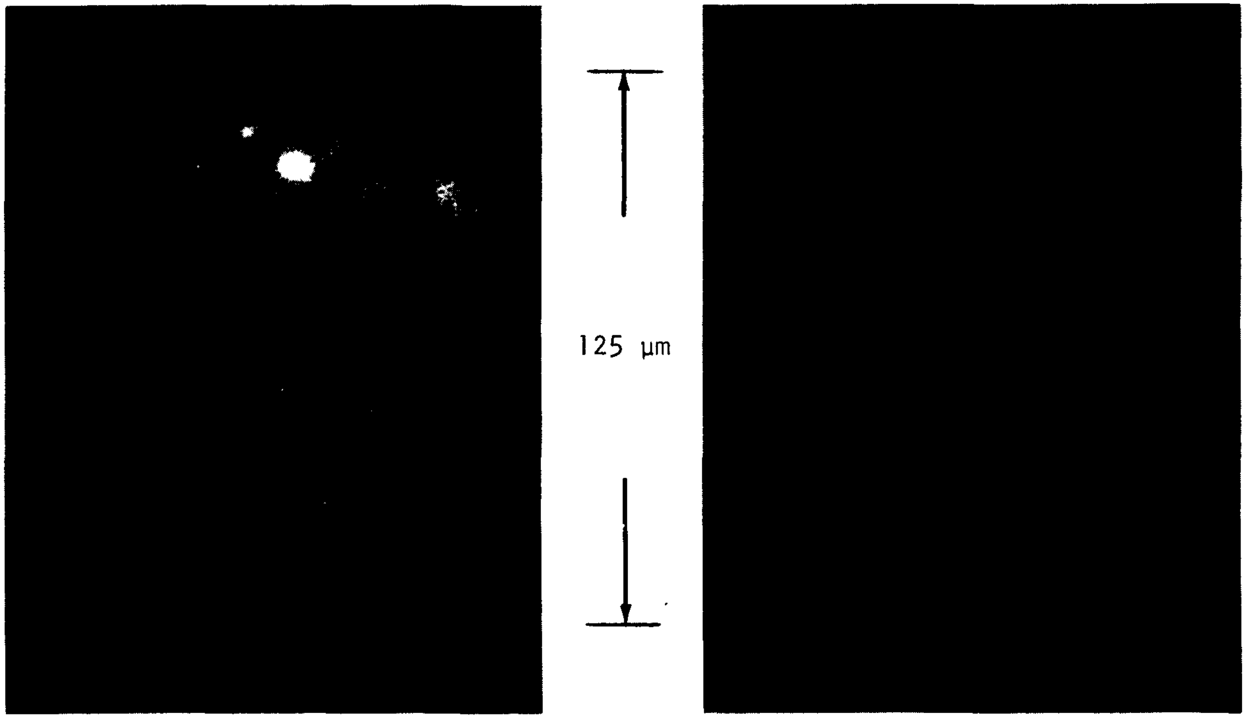

Fig. V.19--Electron microprobe backscatter photographs of specks on the PyC; thorium Mα (left) and uranium Mα (right). The same area is shown in both photographs, and it is apparent that the uranium content of the specks is extremely low, whereas the thorium content is probably greater than 10 wt-% (600X) and temperature for TRISO-coated fuel. During this report period, work on the problem has been concentrated on microprobe analysis of irradiated fuel, and experiments in which coated particles were heated in a thermal gradient or isothermally.

Microprobe Analysis

The examination of TRISO-I-coated particles (batch 3592-35) irradiated at 1300°C in capsule P13J was discussed in the previous quarterly report (GA-8879). During this report period, analysis of unirradiated particles from batch 3592-35 and of particles irradiated at 600° and 1000°C was completed. The results of this work and conclusions regarding the sequence of events leading to chemical reaction between coating and core are reported here.

The concentration of elements derived from the microprobe analysis have been reported as approximate weight percent. The reported values were determined from the ratio of the characteristic X-ray intensity from the sample and a standard. The unknown porosity of the material, the complex blend of elements, the effects of topography, and X-ray absorption rendered accurate quantitative work impractical. The concentrations reported here should therefore be considered approximate at about ±50% of the reported value. The fact that the chemical inventory from a given location may not add up to 100% is due partially to this uncertainty in measurement and partially to the fact that not more than three elements were monitored at precisely the same location in the particle.

Unirradiated Particles. Fifteen unirradiated particles from batch 3592-35 were examined with the electron microprobe. The particles were similar in their chemical distribution and microstructure. A representative particle is shown in Fig. V.20, with the elemental distribution indicated. The indicated thorium and uranium contents of the core were less than standard quantitative analysis showed should be present. The carbon content indicated by microprobe analysis was higher than the more accurate value obtained by quantitative analysis, but the microprobe shows how carbon tended to be segregated at the grain boundaries. The actual carbon content of the cores (about 10 wt-%) was about 0.8% in excess of stoichiometric carbon concentration.

There was a significant but unmeasured amount of thorium in the buffer extending about 10 μm from the core into the buffer and also at the buffer-SiC interface. Uranium was also found in the buffer, but not as great a quantity as the thorium, and only at the buffer-core interface. Apparently the thorium was much more mobile than the uranium during the coating process. Silicon was found throughout the buffer, with concentrations highest at the SiC-buffer interface. The thorium, uranium, and carbon concentrations in the cores were about 55, 30, and 12 wt-%, respectively. At the dark boundaries between grains, the carbon concentration increased; typical concentrations of thorium, uranium, and carbon in those regions were 45, 25, and 20 wt-%, respectively. The thorium and uranium concentration within a core was uniform from region to region. However, there was a variation of about ±2 wt-% in average thorium and uranium concentration from one particle core to another.

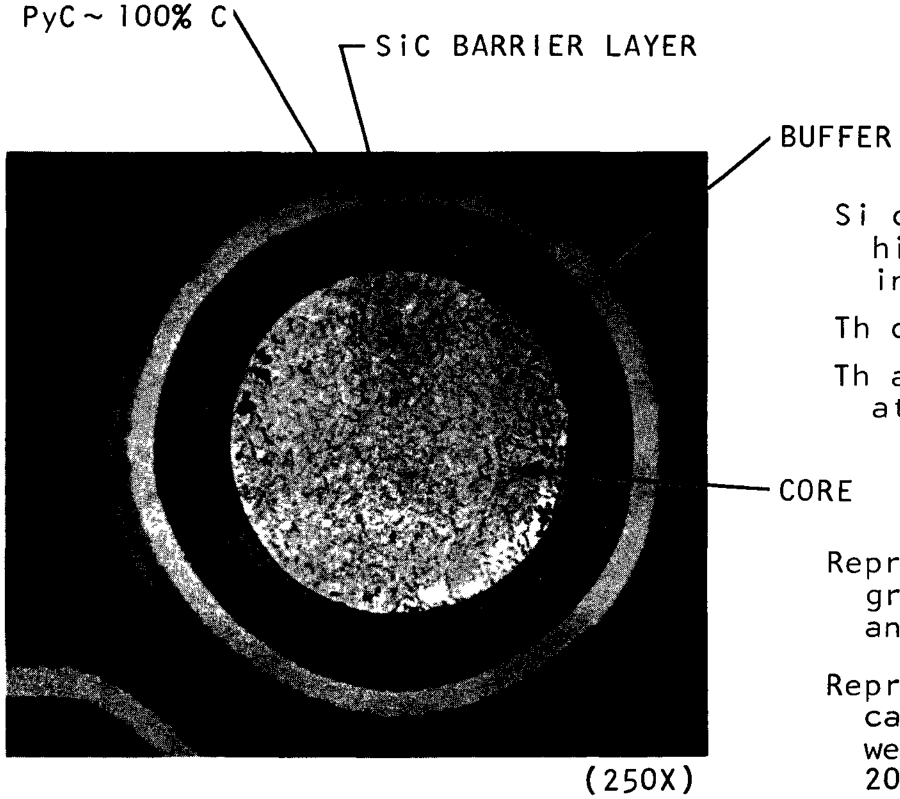

Si detected throughout buffer, with highest concentration at SiC-buffer interface

Th detected at SiC-buffer interface

Th and U detected in a diffuse band at the core-buffer interface

Representative concentrations within grains were 55 wt-% Th, 30 wt-% U, and 12 wt-% C

Representative concentrations in high-carbon dark regions between grains were 45 wt-% Th, 25 wt-% U, and 20 wt-% C

(Typical quantitative analysis of core: 60 wt-% Th, 30 wt-% U, and 10 wt-% C)

Fig. V.20--Elemental distribution in representative unirradiated particles from batch 3592-35E (TRISO-I, LTI coating); typical coating thicknesses were 40-μm buffer, 15-μm SiC, and 10-μm PyC; nominal Th:U ratio 2:1. Particles from this batch were irradiated 2300 hr in capsule P13J at 600°, 1000°, and 1300°C. Particles irradiated at each temperature were then examined by electron microprobe

Iron was found to be barely detectable (probably less than 1 wt-%) in several small regions near the interface of the buffer and SiC coating. Chlorine was sought and not detected.

Particles Irradiated at 600°C. A sample from particle coating batch 3592-35, irradiated at 600°C, was mounted and polished for microprobe examinations. The fast-neutron exposure was about 2.7 x 10^{21} n/cm^2 (E > 0.18 Mev) and burnup was 13% FIMA. Because of a scarcity of sample particles and difficulty experienced in metallographic polishing, microprobe examination was limited to a single particle. The following elements were sought but not detected in the particle: Cu, Sm, Pm, I, Te, Se, Rb, Y, Nb, Rh, and Pd.

The elemental distribution of detected elements within the particle is shown in Fig. V.21. Discontinuities in the SiC and outer PyC coating were presumed to be due to polishing damage. Earlier postirradiation examination of a large number of companion particles (reported in an earlier quarterly report GA-8725) had shown no disruption of the coatings, and no core-coating chemical reaction was revealed in the microprobe examination.

Fission products were evenly distributed throughout the core. Some fission products were detected in a diffuse band extending from the core about 15 μm into the buffer. These elements were Cs, Ce, La, Pr, Nd, Xe, Zr, and Mo. A 10-μ-thick ring at the periphery of the core had a highly reflective surface and was found to be much higher in carbon (approximately 60 wt-%) and lower in thorium and uranium (about 8 and 4 wt-%, respectively) than the rest of the core. The concentration of fission products in this ring decreased from typical core concentrations on the inner surface to low values, typical of the buffer, at the outer surface.

The thorium, uranium, and carbon content of the carbide core inside the outer ring was uniformly distributed, with concentrations of 55, 20, and 25 wt-%, respectively. Unlike the unirradiated particles, grain boundaries containing high carbon content were not detected within the core.

The measured carbon content of the core was probably greater than the true concentration, which was estimated as 10 to 12 wt-%. The observation of the high-carbon ring suggests that excess carbon in the particles migrated down the thermal gradient from the center of the core to the periphery during irradiation to form a shell of high carbon content.

Particles Irradiated at 1000°C. Fifteen particles were polished in a single mount. There was no evidence of chemical interaction between the core and coating. In order to reduce the high radiation level, all but four of the particles were picked from the mount before the examination. Three distinctly different microstructures had been observed in the original field of particles, and examples of these were retained in the mount. One type of particle had sharply defined globular-shaped regions within the core near the periphery. A second type had elongated precipitates within the core near the periphery, with a ring of apparent porosity adjacent to the precipitates, but nearer the center of the particle. A third type had a featureless core except for a ring of slightly more reflective material at the periphery of the core. These three microstructures will be referred to in the order

REPRESENTATIVE COMPOSITIONS (approx. wt-%)
(ratio of characteristic X-ray intensity from sample & standard)

	C	Th	U	Si	Ru	Sr	Cs	Ba	Fe	Xe	Zr	Mo	Tc	Pr	Nd	Ce	La
BUFFER																	
Near SiC	40	-	-	10	-	-	-	-	(a)	-	-	-	-	-	-	-	-
Middle	70	-	-	0.1	-	-	-	-	-	-	-	-	-	-	-	-	-
Near core	40	2	-	0.1	-	-	0.4	-	-	0.5	0.2	0.1	-	0.5	2.0	0.8	0.2
CORE																	
Bright band at edge of core	60	8	4	0.06	-	-	0.2	-	-	1.0	0.7	0.3	-	0.5	2.0	0.5	0.2
Core adjacent to bright band	(b) 30	58	22	-	0.3	0.2	0.7	0.6	-	1.7	1.3	0.6	0.2	0.9	2.5	1.0	0.4
Center	25 (b)	55	20	0.05	0.4	0.2	0.8	0.6	-	1.7	1.5	9.9	0.4	0.9	2.9	1.5	0.5

Note: The dashes indicate values not determined.

(a) Fe detected at SiC-buffer interface in discontinuous regions, concentration not measured.

(b) Probably greater than true concentration, estimated as 10 to 12 wt-%.

K-64377

Fig. V.21--Elemental distribution in particle from batch 3592-35 irradiated 2300 hr in capsule P13J at 600°C to a neutron exposure of 2.7 x 10^{21} n/cm^2 (E > 0.18 Mev) and burnup of 13% FIMA. Discontinuities in the coating were from polishing damage. No chemical attack of the coating was detected discussed above as types 1, 2, and 3, respectively. Photomicrographs of each type of particle and elemental distribution are shown in Figs. V.22, V.23, and V.24.

The silicon content of the buffer was relatively high (3 to 20 wt-%) in the three microstructures. While the microstructure of the cores in the particles varied considerably, with the exception of the high-carbon precipitates of types 1 and 2, the thorium, uranium, and carbon content of the core was uniformly dispersed and similar at about 50, 12, and 32 wt-%, respectively. Fission-product distribution within the cores was also uniform and similar, except for the high-carbon precipitates in the type 2 microstructure (Fig. V.23), which had a higher Sr, Cs, Ba, Ce, Xe, and Mo content than the rest of the cores. There was no visual evidence of coating failure in the three types of particles; however, in view of the greater abundance of Cs and Sr in the carbon precipitates of the type 2 microstructure, it is plausible that this coating was more effective in retention of these relatively volitile fission products. Other variables, such as nominal temperature, thermal gradients, or starting core composition, however, may have caused the difference.

The type 1 microstructure had sharply defined globular-shaped carbon precipitates at the periphery of a relatively dense and otherwise featureless carbide core. The type 2 microstructure had elongated and irregular high-carbon deposits at the core periphery, with an adjacent region of 10- to 20-μm-diameter voids nearer the center. The ring of voids corresponded to a boundary between the inner carbide with high (approximately 1.7 wt-%) xenon concentration and the outer carbide with a lower (approximately 0.3 wt-%) xenon concentration. The xenon was presumably trapped in microscopic porosity within several micrometers of the polished surface.

The concentration of carbon at the core periphery in types 1 and 2 was probably related to the effect observed in the particle irradiated at 600°C (Fig. V.21). The formation of high-carbon globules at 1000°C rather than a continuous ring at the surface of the carbide may reflect greater mobility of thorium and uranium in the carbide at 1000°C and the tendency of the high-carbon phase to assume a lower-energy condition by reducing surface area. The fact that the high-carbon phase was not completely rejected by the core under the radial thermal gradient that must have existed is an important observation that will be useful in the eventual understanding of the core movement (amoeba effect) to be discussed later.

The type 3 microstructure did not contain a high-carbon phase like that of types 1 and 2. The bright ring at the core periphery was examined and found to have essentially the same composition as the rest of the core. While the reason for this lack of a high-carbon phase is not known with certainty, one reasonable possibility is that the unirradiated core had little or no excess carbon that could be rejected under the influence of the thermal gradient during irradiation.

Conclusions and Possible Reaction Sequence. The microprobe examination of two particles from batch 3592-35 irradiated at 1300°C was discussed in the previous quarterly report (GA-8879). Results of that work and subsequent microprobe work reported here, combined with out-of-pile thermal gradient

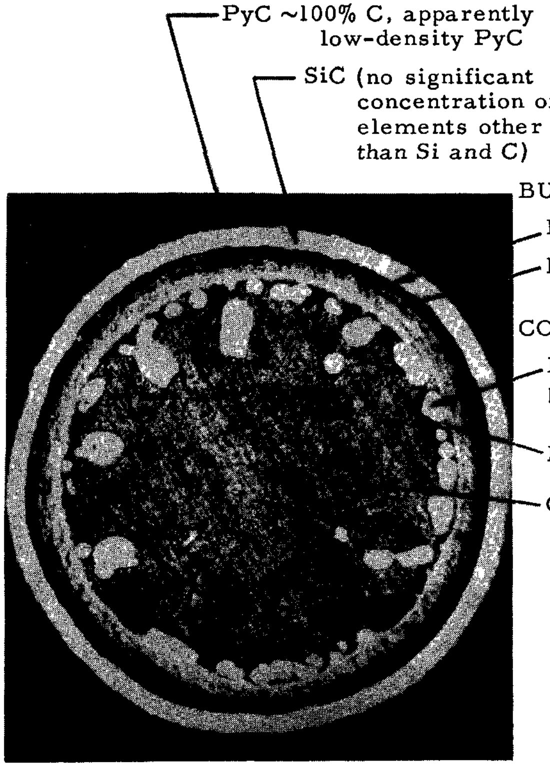

K-63780

REPRESENTATIVE COMPOSITIONS (approx. wt-%)
(ratio of characteristic X-ray intensity from sample & standard)

	C	Th	U	Si	Ru	Sy	Cs	Ba	Fe	Xe	Zr	Mo	Y	Te	Pr	Nd	Ce	La	Tc
BUFFER																			
Near SiC	(a)	-	-	>3	-	0.1	-	-	(c)	0.05	0.3	0.02	-	-	-	1.1	-	-	-
Near core	(a)	-	0.5	3	0.2	0.4	0.02	0.2	0.02	0.5	0.9	0.4	-	-	0.4	1.6	0.4	0.3	-
CORE																			
High-carbon precipitates	75	9.3	4.5	0.3 to 0.4	0.3 to 0.6	0.5	0.8	0.4	<0.02	1 to 2	1 to 2	1.4	-	-	0.6	1.4	0.5	<0.1	(d)
Edge (12 μm)	(b) 20	50	12	0.4	0.6	0.4	0.6	0.55	<0.02	1.4	1.6	0.8	0.2	0.2	0.8	2.3	1.0	0.3	-
Center	20 (b)	50	12	0.5	0.6	0.4	0.6	0.60	<0.02	1.5	1.7	1.3	0.2	0.2	0.8	2.3	1.2	0.4	-

Note: The dashes indicate values not determined.

(a) Buffer region primarily carbon.

(b) Probably greater than the true concentration, estimated as 10 to 12 wt-%.

(c) Occasional, high-Fe (several wt-%), μm-sized regions on both the PyC-SiC and the SiC-buffer interface.

(d) Tc uniform throughout core, probably less than 0.4 wt-%, somewhat lower in the white phases than in rest of core.

Fig. V.22--Type 1 microstructure and elemental distribution in a particle from batch 3592-35 irradiated 2300 hr in capsule P13J at 1000°C to a fast-neutron dose of 3.1 x 10^{21} n/cm^2 (E > 0.18 Mev) and burnup of 17% FIMA. This was a companion particle to those shown in Figs. V.23 and V.24

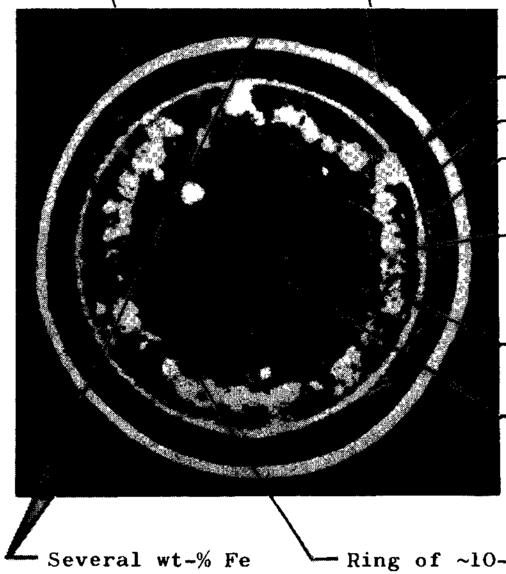

REPRESENTATIVE COMPOSITIONS (approx. wt-%)
(ratio of characteristic X-ray intensity from sample & standard)

	C	Th	U	Si	Ru	Sr	Cs	Ba	Fe	Xe	Zr	Mo	Y	Te	Pr	Nd	Ce	La	Tc
BUFFER																			
Near SiC	(a)	---	---	~15	---	0.4	0.4	0.1	<.01	0.3	0.4	---	---	---	<.5	0.1	---	---	---
Near core	(a)	0.2	0.3	~3	0.2	0.6	1.4	0.1	<.01	1.2	0.8	0.5	---	---	<.5	2.2	0.8	---	---
High Cs, Ru, La, Ba band	(a)	(b)	(b)	(b)	2.5	(b)	3.7	1.4	(b)	(b)	(b)	1.0	(b)	(b)	<.5	(b)	(b)	.25	(b)
CORE																			
High carbon precipitates	75 to 65	8 to 15	5	0.5	0.6	1.0	2.0 to 3.0	1.0	<.01	2.5	1.6	(c) 1.2 to 3.4	---	---	<.5	1.5	1.2	0.4	(d)
Edge	20[e]	50	12	0.5	0.4	0.2	0.6 to 0.9	0.2	<.01	0.3	1.5	0.7	0.2	0.2	0.5	2.1	1.2	0.2	---
Center	20[e]	48	12	0.5	0.4	0.5	1.2	0.4	<.01	1.7	1.7	1.0	0.2	0.2	0.9	2.4	1.0	0.3	---

Note: The dashes indicate values not determined.

(a) Buffer primarily carbon.

(b) Value not measured.

(c) The mo content was uniform within a single precipitate but varied from one precipitate to another.

(d) Tc was uniform throughout the core, including high-carbon precipitates; probably <0.4 wt-%.

(e) Probably greater than true concentration estimated as 10 to 12 wt-%.

(f) Occasional low-level Th and Nd in PyC.

Fig. V.23--Type 2 microstructure and elemental distribution in a particle from batch 3592-35 irradiated 2300 hr in capsule P13J at 1000°C to a neutron exposure of 3.1 x 10^{21} n/cm^2 (E > 0.18 Mev) and burnup of 17% FIMA. This was a companion particle to those shown in Figs. V.22 and V.24

PyC ~100 wt-% carbon; apparently low-density PyC

SiC (no significant concentration of elements other than Si and C)

REPRESENTATIVE COMPOSITIONS (approx. wt-%)
(ratio of characteristic X-ray intensity from sample and standard)

	C	Th	U	Si	Ru	Sr	Cs	Ba	Fe	Xe	Zr	Mo	Y	Te	Pr	Nd	Ce	La
BUFFER																		
Near SiC	45[a]	--	--	17	--	--	<.4	<.4	(b)	0.04	0.1	<.1	--	--	<<.9	<<2.1	0.08	<.2
Mid	100	--	--	4	--	--	<.4	<.4	<.03	<.9	<2.9	<.1	--	--	<.9	<2.1	<.9	<.2
Near core	80[a]	0.6	--	0.5	0.2	0.4	0.4	0.4	<0.3	0.9	2.9	0.1	--	--	<.9	<2.1	0.9	0.2
CORE																		
Edge (6 μm)	20[c]	50	11	0.5	0.4	0.4	0.4	0.5	<.03	1.6	1.4	0.8	0.1	0.2	0.9	2.1	1.3	0.1
Center	20[c]	50	11	0.3	0.4	0.4	1.1	0.4	<.03	1.6	1.6	1.2	0.2	0.3	0.9	2.1	1.3	0.4
High SiC region	20[c]	50	11	2-5	0.4	0.4	0.7	0.4	<.03	1.6	1.6	1.2	0.2	0.3	0.9	2.1	1.3	0.4

Note: The dashes indicate values not determined.

(a) Buffer region primarily carbon; the low carbon measurement is probably due to density or topography effects.

(b) At SiC-buffer interface, occasional high-Fe inclusions (several μm in diameter; 0.6 to 2.8 wt-% Fe).

(c) Probably greater than true concentration estimated as 10 to 12 wt-%.

Fig. V.24--Type 3 microstructure and elemental distribution in a particle from batch 3592-35 irradiated 2300 hr in capsule P13J at 1000°C to a neutron exposure of 3.1 x 10^{21} n/cm^2 (E > 0.18 Mev) and burnup of 17% FIMA. This was a companion particle to those shown in Figs. V.22 and V.23

heating experiments to be discussed later, have provided evidence that suggests the sequence of events leading up to chemical interaction of the core and coating observed at 1300°C.

After irradiation at 1300°C, the particles had high-carbon phases within the core at the periphery. One particle showed two distinct and different high-carbon phases. This particle had a coating which had failed by chemical interaction of the core and coating. A microphotograph of the particle is shown in Fig. V.25. Electron microprobe scanning micrographs of the same particles (Fig. V.26) show the distribution of uranium, thorium, carbon, and ruthenium.

The high-carbon precipitates within the core and opposite the reaction zone are not distinct in the photographic reproduction in Fig. V.25, but the scanning micrographs of Fig. V.26 provide evidence of their presence. Regions of low Th, U, and Ru in the core correspond with regions of high carbon. These high-carbon phases probably were produced in the same manner as those of the types 1 and 2 microstructures of particles irradiated at 1000°C. Presumably, this particle had a significant thermal gradient along its diameter because of its position in the bed of particles, superimposed on the radial thermal gradient as a result of fission within the core. Instead of the occurrence of a radial dispersion of high-carbon phases within the core, the excess carbon tended to migrate toward the cool side of the particle, where it precipitated in the core near the surface as high-carbon phases containing thorium and uranium (5 to 30 wt-%).

The distinct crescent-shaped deposit of essentially 100% carbon opposite the reactor zone and adjacent to the core was a feature observed in some particles irradiated at 1300°C. It was never observed in particles irradiated at lower temperatures. It appeared to be on the surface of the core and not an integral part of it. It seems unlikely that this carbon could have been rejected from the core, since there was a region of high thorium and uranium between this deposit and the high-carbon precipitates in the core. It is more probable that the carbon in the crescent-shaped deposit was transported to the cool side of the particle by some undetermined mechanism, perhaps surface diffusion or vapor transport through the buffer. Conditions at the cool side were such that carbon was precipitated at the interface between the core and buffer, forcing the core to mechanically move toward the hot side. The buffer on the hot side was either crushed or the carbon removed and transported to the cool side. This process continued until contact between the core and SiC was possible. The fission products Ru and Tc in the core then alloyed with silicon and thorium to form the observed reaction zone and destroy the SiC.

The movement of the core observed here resembles the amoeba effect observed earlier (Ref. 8) under a thermal gradient. In that work, however, dissolution of carbon on the hot side of the core followed by rejection on the cool side was the proposed mechanism of carbon transport. Results of the work discussed here do not disprove this original hypothesis; however, it seems that other mechanisms of carbon transport may also be important. Since the ability of cores to penetrate PyC by the amoeba effect has been demonstrated

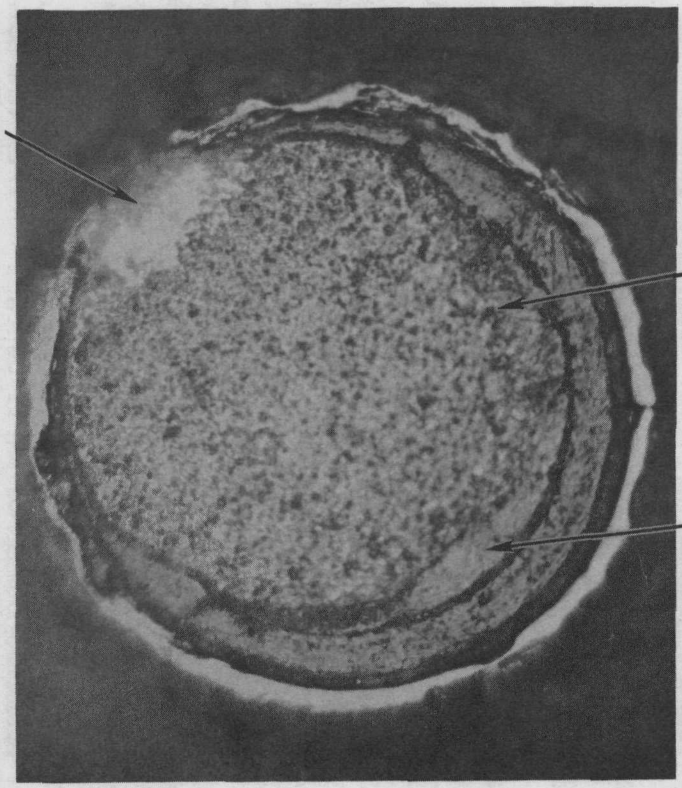

Reaction zone containing Th, Ru, Si, and Tc compound in relative amounts by weight of 5, 3, 2, and 1, respectively

Ring of high-carbon globules in the core, containing Th and U and 40 to 90 wt-% C

Crescent-shaped deposit adjacent to the core, containing essentially 100 wt-% C

MC-27066-1 300X

Fig. V.25--TRISO-I-coated particle from batch 3592-35E showing core-coating interaction and high-carbon phases in and adjacent to the core after irradiation in capsule P13J for 2300 hr at 1300°C to a fast-neutron exposure of 3.6×10^{21} n/cm^2 (E > 0.18 Mev) and burnup of 17% FIMA

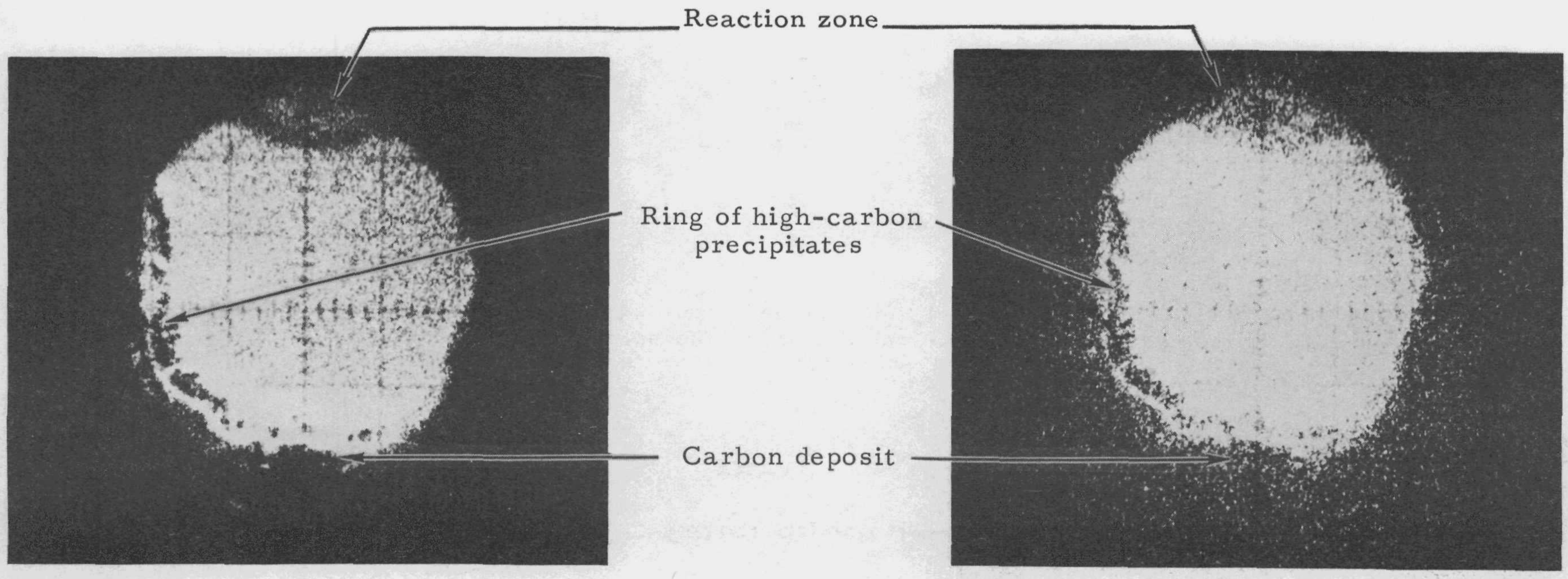

K-63622 200X

(a)

K-64374 200X

(b)

Fig. V.26 (Part I)--Electron microprobe scanning photographs of the particle shown in Fig. V.25. The bright regions indicate relative abundance of the indicated element: (a) Th(Mα) and (b) U(Mα)

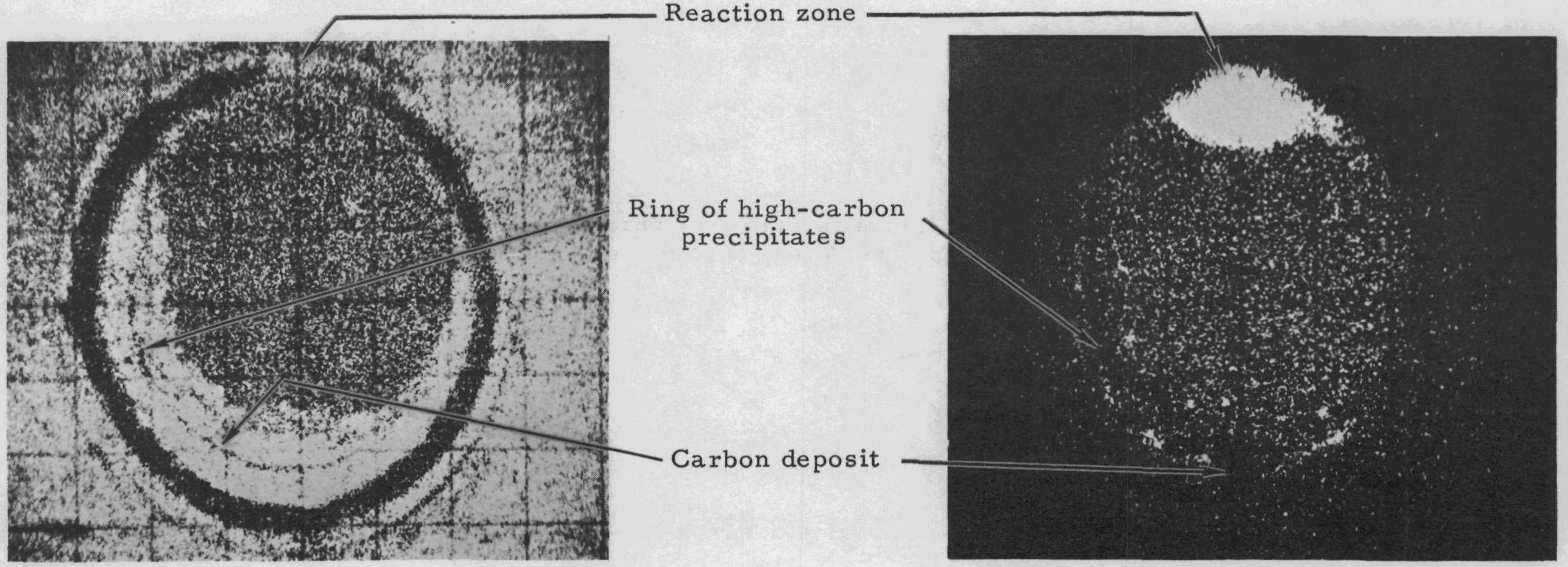

K-63620 200X

(c)

K-63621 200X

(d)

Fig. V.26 (Part II)--Electron microprobe scanning photographs of the particle shown in Fig. V.25. The bright regions indicate relative abundance of the indicated element: (c) carbon (Kα) and Ru (Lα)

(Ref. 8), complete understanding of the parameters contributing to the core movement is essential to prediction of chemical stability of TRISO-II coatings, as well as TRISO-I and BISO.

Thermal Gradient Experiments

The purpose of this work was to study, out-of-pile, the effects of thermal gradient, fission-product additions, Th:U ratio, coating type, and coating composition on chemical compatibility of $(Th,U)C_2$ cores and coatings. The experiments were designed as screening tests in which a large number of variables were examined with selected samples in order to identify parameters important to chemical compatibility.

Experimental Procedure. Fission-product-doped cores with TRISO-I or TRISO-II coatings were included in Experiments 4283-13 and 4283-17. The description of the fission-product-doped specimens was included in the previous quarterly report (GA-8879). All other specimens were selected from historical samples of particles included in particle irradiation capsules. The apparatus and procedure for loading, heating, and preserving orientation during metallographic examination after the test were the same as those described previously (GA-8879). The only difference in procedure was that enough particles were poured into the 1/8-in.-diameter hole in the crucible to form a bed about 3/16 in. deep. In previous work a monolayer of particles was used.

Fission-product-doped TRISO-I particles and undoped TRISO-I, TRISO-II, and BISO particles were included in Experiment 4283-31. The procedure for loading, heating, and metallographic examinations was the same as that for the experiments discussed above, except that there were four crucible holders arranged axially along the heating element. This resulted in the two end holders operating at about the same temperature, which was 50° to 75°C lower than that of the two middle holders. The operating temperatures of the middle holders were about the same.

Two sample beds were bonded in place with phenolic resin carbonized at 1500°C prior to heating in the thermal gradient.

It was desirable to obtain radiographic evidence for migration of particle constituents during heating. Therefore, cylindrical rings with a 0.12-in. OD and a 0.08-in. ID were cut from baked carbon. A monolayer of each of the various particle types was cemented across the end of a cylinder using phenolic resin dissolved in acetone. After the resin was carbonized for 10 min at 1500°C, these cylindrical-ring holders were placed on a photographic plate and radiographed. The holders were then placed in the holes in the crucibles that contained particles from the same batches, and heating was begun. The orientation of the particles relative to the thermal gradient was maintained; the condition of individual particles in the monolayer could be monitored by radiograph at selected time intervals during the experiment. A photograph of crucibles and radiograph holders is shown in Fig. V.27, and a loaded radiograph specimen holder is shown in Fig. V.28.

Results. Specimens were heated for 120 hr in a thermal gradient resulting from temperatures ranging from 1725° to 1925°C in Experiment 4283-13. This resulted in an estimated temperature difference across a particle of 10°

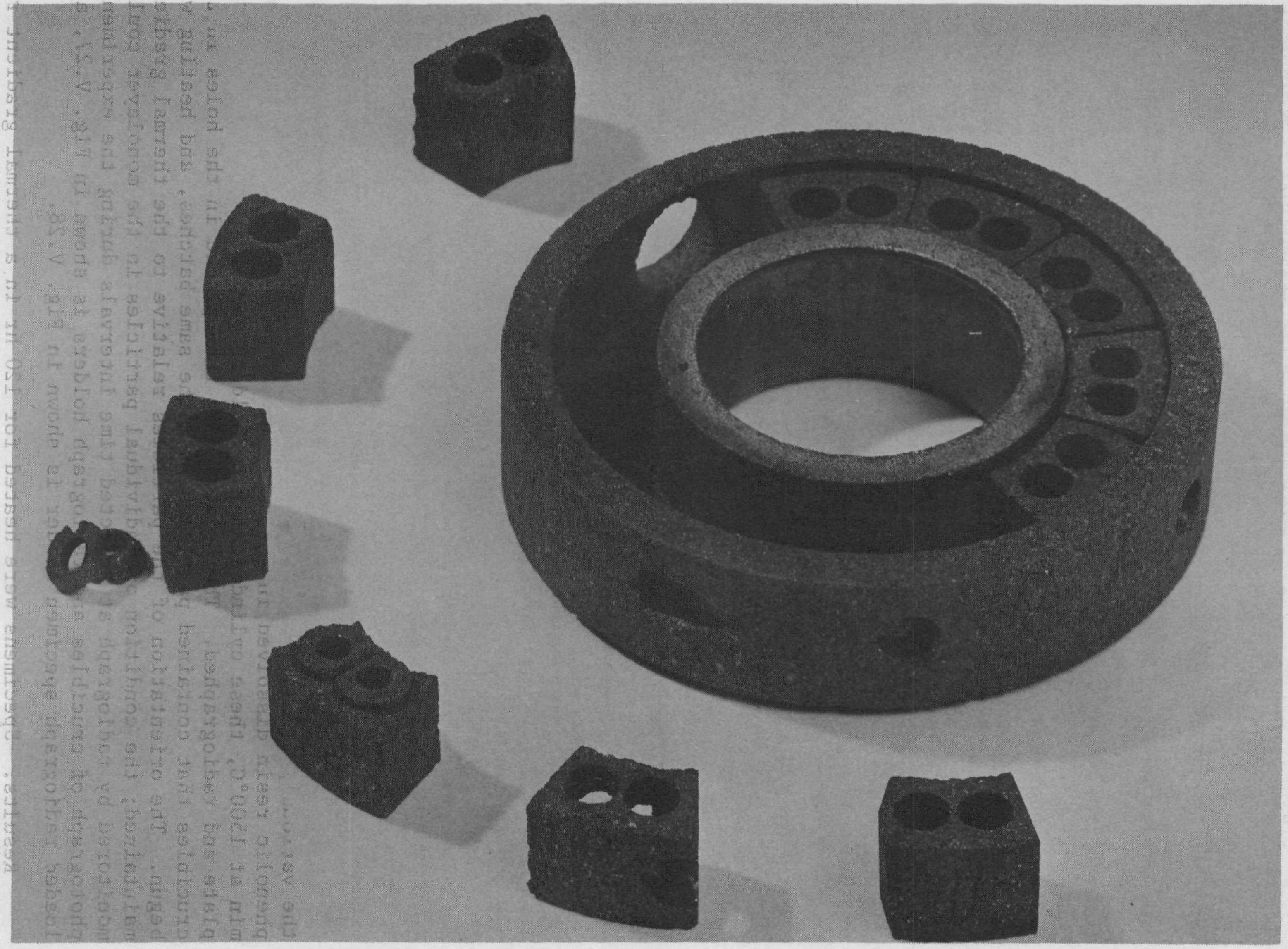

Fig. V.27--Thermal gradient crucibles and radiograph specimen holders (~3X)

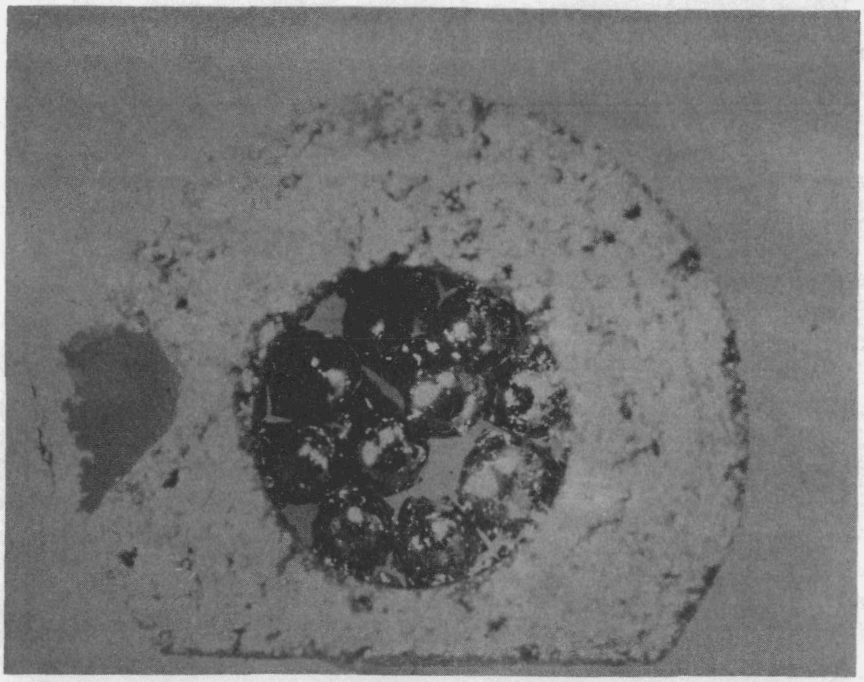

Fig. V.28--Radiograph specimen holder loaded with particles cemented in place with carbonized resin. The notch in the rim was positioned on the hot side during heating (20X) to 45° depending on particle size. In Experiment 4283-17, they were heated 58 hr in a similar thermal gradient with a maximum temperature of 1825°C. There were problems in temperature control, so that 16 hr were spent at temperatures from 1625° to 1825°C and 42 hr from 1525° to 1725°C. In both experiments there was catastrophic failure of some coatings on particles on the cool side of the particle bed. An example of the kind of failure observed is shown in Figs. V.29 and V.30. No failure or chemical attack was evident on the hot side of the crucible.

Some particles showed evidence that Fe had penetrated the outer PyC and then diffused around the particle at the PyC-SiC interface. Figure V.30a shows this effect in a TRISO-II particle.

Examination of a TRISO-I failed particle with a microprobe revealed that the core reaction zone constituents were highly variable in composition, but typical values were estimated at 40 to 50 wt-% thorium, 20 wt-% uranium, 20 to 30 wt-% iron, 10 wt-% silicon, and 10 wt-% carbon. Significant amounts of thorium, uranium, and iron were dispersed around the particle at the interface of the buffer-SiC and the PyC-SiC. Figure V.31 shows electron microprobe scanning micrographs of a failed particle similar to one shown in Fig. V.30b. The source of the iron was undoubtedly the carbon crucibles, since subsequent chemical analysis of unused crucibles revealed an iron content of 1.6 wt-%. Apparently, the iron was concentrated in the cooler portion of the particle bed where the outer PyC was penetrated, and rapid iron attack of the SiC took place. There was a trend for the coatings on particles with high uranium content in the core to show more iron attack than those with low uranium content. This may have resulted from coating contamination by the core during coating and the tendency of uranium to form lower-melting eutectics than thorium with iron and silicon.

On the hot side of the particle beds in the 120-hr test (4283-13), there was metallographic evidence that core movement toward the hot side of the particle had taken place in many particles. Some batches of particles showed no core movement. In the sample batches that did exhibit migration, about 10% or less of the particles in the bed showed the effect. A summary of the experimental results showing maximum detected core movement for each batch of particles is given in Table V.12. As pointed out in the section on microprobe analysis, core movement was considered important as a necessary step in the sequence of events leading to core-coating interaction.

One observation of, perhaps, incidental interest was that there was considerable deposition of PyC on the cool side of the particle beds. It was visually evident as a silver deposit on the particles and crucible walls. Some particles at the top of the beds were bonded together, presumably by the PyC deposit. A photograph of particles in the crucible shows the silver color on the cool side of the crucible and some debris (Fig. V.32). A photomicrograph of a PyC layer that developed on the bottom of an empty crucible is shown in Fig. V.33. The possible mechanism of carbon transport will not be discussed here, but it was probably dependent on the H_2O content of the helium, which ranged from 10 to 1000 ppm.

1925°C

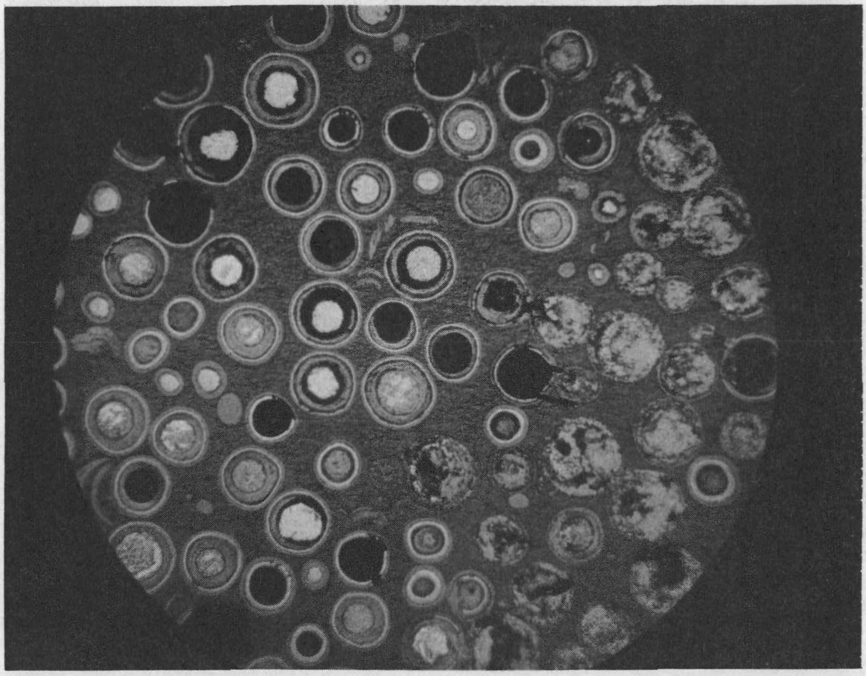

1725°C

Fig. V.29--Catastrophic failure of TRISO-I-coated particles (batch 3592-35E, Experiment 4283-13) on the cool side of a bed heated 120 hr at temperatures ranging from 1725° to 1925°C. Failure was caused by Fe penetration of outer PyC coating and attack of SiC layer. The Fe source was Fe contamination in the carbon crucible (~1.6 wt-% Fe) (30X)

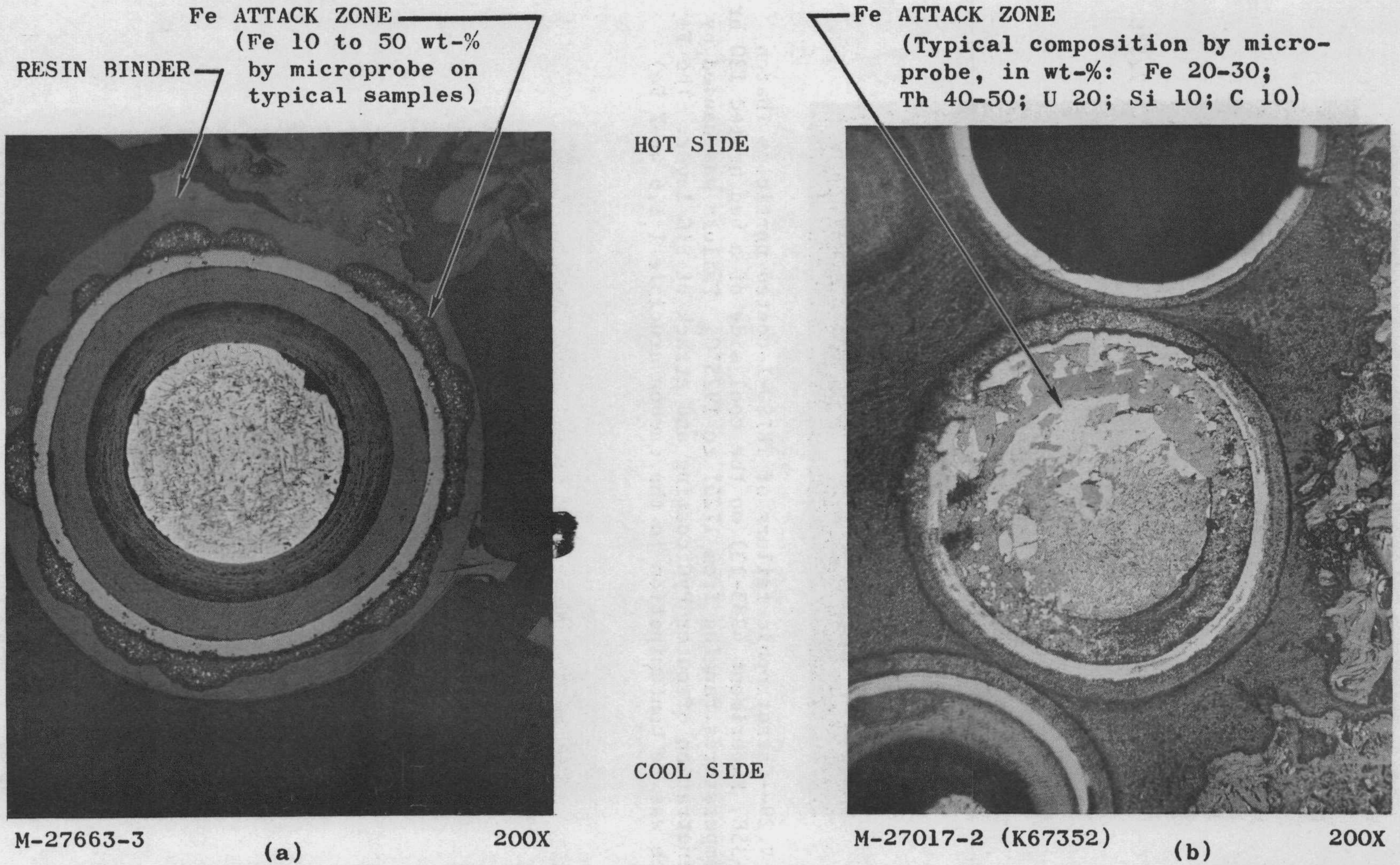

Fig. V.30--Iron attack of SiC-coated particles heated in a thermal gradient in Fe-contaminated carbon crucibles. (a) Particles from batch 4263-91E, Exp. 4283-31, 380 hr at 1350°C; the Fe had not penetrated the SiC but migrated along the SiC-PyC interface forming reaction products with SiC. The outer portion of the PyC was not attacked. (b) Particles from batch 3592-35E, Exp. 4283-17, 58 hr at 1600°C; the SiC coating was completely penetrated by Fe attack on hot side of particle. Reaction also took place in core. For comparison, typical unreacted core composition determined by microprobe, in wt-%, is Th 50, U 30, and C 12 (200X)

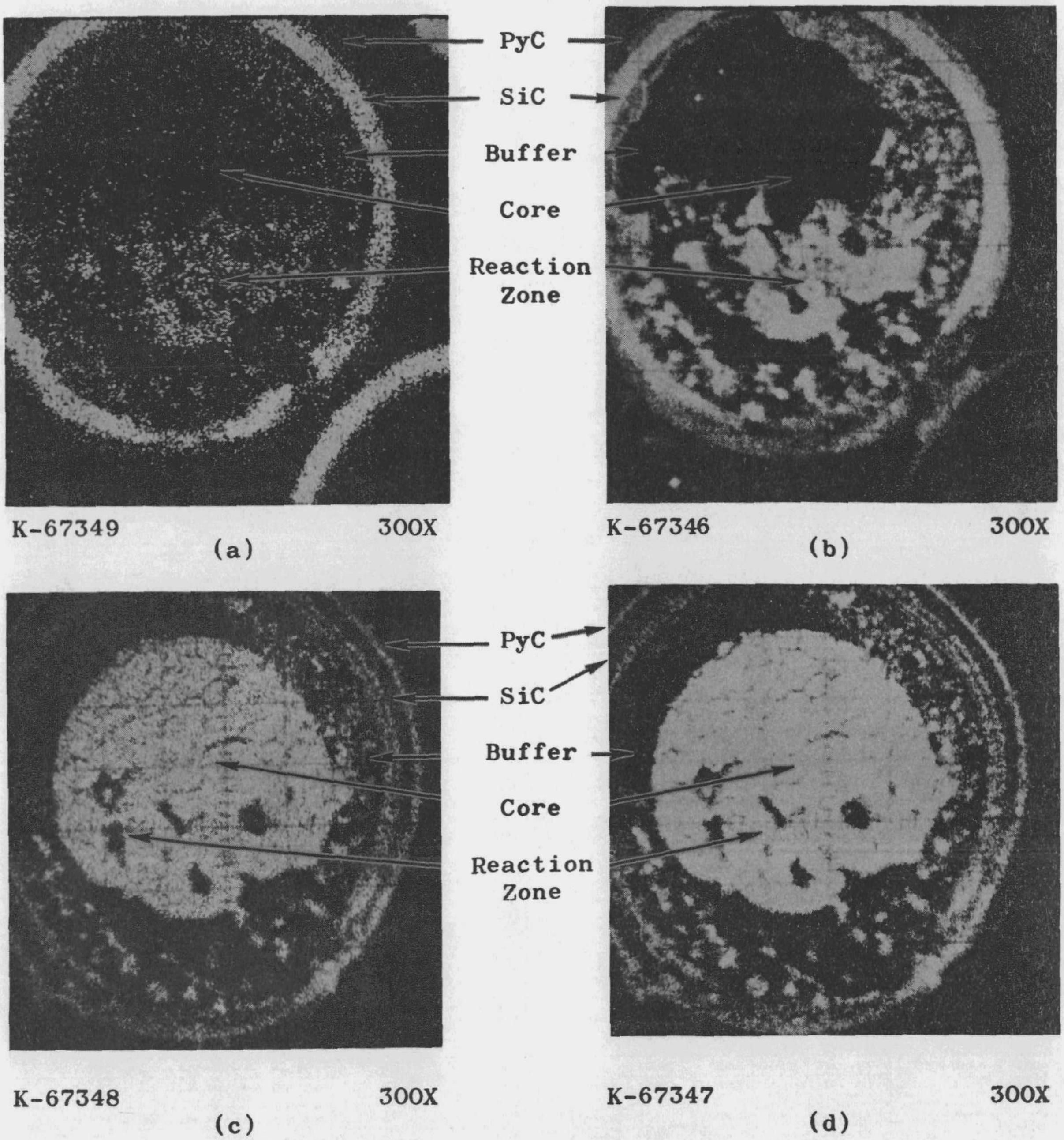

Fig. V.31--Electron microprobe scanning photographs: (a) Si (Kα), (b) Fe (Kα), (c) U (Mα), and (d) Th (Mα) of a TRISO-I-coated particle from batch 3592-35E similar to the one in Fig. V.30(b), showing Fe attack after heating 58 hr at a nominal temperature of 1600°C in an Fe-contaminated carbon crucible (1.6 wt-% Fe) with a temperature difference of about 200°C in the particle bed (Experiment 4283-17). Bright areas represent relative abundance of the respective element. Note that Th and U were apparently very mobile when combined with Si and Fe, and they penetrated the SiC interfaces completely around the particle. The reaction zone was on the hot side of the particle

Table V.12

SUMMARY TABLE OF THERMAL COMPATIBILITY EXPERIMENTS

Series Identification	Specimen No.	Th:U Ratio	Exper. No.	Estimated ΔT Across Particle (°C)	Time (hr)	Temperature Range (°C)		Amoeba Effect (Max. Core Movement)		Remarks
						Cool Side Min.	Hot Side Max.	Distance (μm)	Approx Temp (°C)	
Fission-product-doped cores. (TRISO-I, LTI) (Zr 2 wt-%, Mo 0.6 wt-%, Ce 0.6 wt-%, La 0.7 wt-%, Ru 0.4 wt-%)	4322-9D	7.5:1	4283-17	25-60	58	1525	1825	(a)		Failure cool side of crucible due to Fe attack, no failure hot side. Coating attacked by Fe cool side of crucible. No failure or core-coating attack hot side.
			4283-31	15-30	380	1400	1550			
			4283-31	15-30	500	1400	1550			
	4283-11D	7.5:1	4283-17	50-200	58	1525	1825	(a)		Hot side reaction core-coating interface. (These were large particles 1500 to 3000 μm diameter.)
Individual fission-product or contaminant addition. (TRISO-I, LTI)	4322-5D	3.5:1	4283-17	25-50	58	1525	1825	(a)		Failure cool side of crucible due to Fe attack. No core-coating attack. Radiographic evidence of Th:U diffusion to hot side of particle.
	(Ru doped)		4283-31	25-30	500	1400	1550			
	4322-7D	3.5:1	4283-17	25-50	58	1525	1825	(a)		Fe attack of coating cool side of crucible. No core-coating attack.
	(Fe doped)		4283-31	15-30	500	1400	1550			Slight Fe attack of coating cool side of crucible.
	4042-149D	3.5:1	4283-17	25-50	58	1525	1825	(a)		Fe attack of coating cool side of crucible. No core-coating attack.
	No fission products		4283-31	15-30	500	1400	1550			No coating failure, radiographic evidence.
Variable Th:U ratio series. (TRISO-I, LTI)	3592-35F	2:1	4283-17	15-25	58	1525	1825	0		Fe attack cool side crucible, no core-coating reaction on hot side.
			4283-13	15-25	120	1725	1925	20	1800	Fe attack cool side crucible, no core-coating reaction on hot side.
			4283-31	10-15	500	1350	1475	10	1475	No Fe attack.
				10-20	500	1400	1550	15	1500	Fe attack cool side crucible.
				10-20	380	1400	1550	15	1500	Fe attack cool side crucible.
Variable Th:U ratio series, no fission-product addition. (TRISO-I, LTI)	3325-121	7.8:1	4283-17	35-45	58	1525	1825	0		Fe attack cool side crucible.
			4283-13	35-45	120	1725	1925	10	1800	Fe attack cool side crucible.
			4283-31	25-35	500	1400	1550	0		No Fe attack.
TRISO-I, HTI	3332-137	12:1	4283-17	35-45	58	1525	1825	0		Very slight Fe attack.
			4283-13	35-45	120	1725	1925	0		No Fe attack.
	3332-139	12:1	4283-17	35-45	58	1525	1825	0		No Fe attack.
			4283-31	20-30	500	1400	1550	0		
$(Th,U)O_2$ (TRISO-I, HTI)	3332-141	3:1	4283-17	15-25	58	1525	1825	0		No Fe attack.
	$(Th,U)O_2$		4283-31	10-15	500	1400	1550	See remarks		No Fe attack. Migration of porosity to hot side ~5 μm porous layer in the core on hot side.
Variable Th:U ratio series. (TRISO-II, LTI)	4263-77E	2.25:1	4283-31	10-20	500	1350	1475	5	1425	No Fe attack.
					500	1400	1550	10	1500	No Fe attack.
					380	1400	1550	10	1550	Bonded bed (phenolic resin bonded), no Fe attack.
	T103A, T103C, T161B	ThC_2	4283-31	25-35	500	1400	1550	10	1550	No Fe attack, no sharp boundary between precipitate and core on cool side. Cracked buffer hot side.
	4042-129D	ThC_2	4283-17	35-40	58	1525	1825	0		No Fe attack.
Variable Th:U ratio series. (TRISO-II, HTI)	3325-117	1.6:1	4283-17	15-25	58	1525	1825	0		Fe attack cool side crucible.
			4283-31	10-20	500	1400	1550	0		Slight Fe attack cool side crucible.
	3332-149	3:1	4283-17	15-25	58	1525	1825	0		No Fe attack cool side.
	4263-91	2.2:1	4283-31	10-20	380	1400	1550	10	1500	Fe attack cool side crucible (phenolic resin bonded).
					500	1350	1475	0		No Fe attack.
					500	1400	1550	10	1550	Fe attack cool side crucible.
	3325-119	7.8:1	4283-17	35-45	58	1525	1825	0		Fe attack cool side crucible.
	T169 T105B	ThC_2	4283-31	25-35	500	1400	1550	10	1500	No Fe attack.
	4042-105D	ThC_2	4283-17	35-40	58	1525	1825	0		No Fe attack.
Variable Th:U ratio (BISO, LTI)	3592-141	2.2:1	4283-31	10-20	500	1400	1550	10	1500	No Fe attack, same core and buffer as 3542-137.
	3592-143	3.4:1	4283-31	10-20	500	1325	1450	0		No Fe attack, same core and buffer as 3592-151.
						1400	1550	5	1550	
Variable Th:U ratio (BISO, HTI)	3592-137	2.2:1	4283-31	10-20	500	1400	1550	0		No Fe attack, same core and buffer as 3592-141.
	3592-151	3.4:1	4283-31	10-20	500	1325	1450	0		No Fe attack, same core and buffer as 3592-143.
						1400	1550	0		
	3023-79	4:1	4283-31	10-20	500	1400	1550	0		No Fe attack.

[a] Any core movement or carbon deposit may have been masked because of difficult polishing conditions due to soft and thick buffer; however, radiography showed no movement.

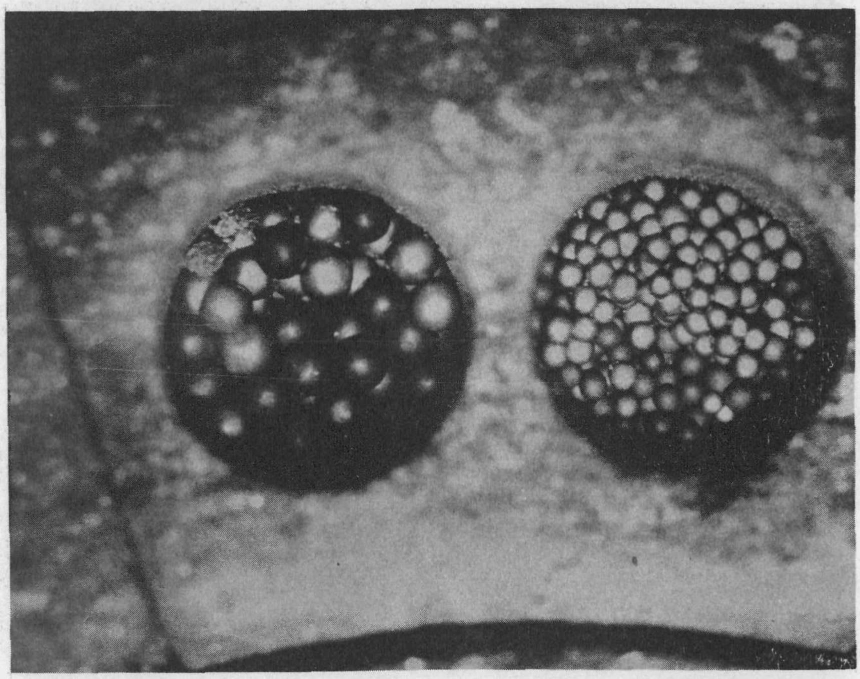

Fig. V.32--Beds of particles from batch 3325-121E (left) and batch 3542-35E (right) heated in helium for 58 hr in a temperature gradient with minimum temperature ranging from 1525° to 1625°C and maximum temperature 1725° to 1825°C. A silver-colored deposit and some debris, probably PyC, developed on the particles and crucible on the cool side of the holes, (Experiment 4283-17) (12X)

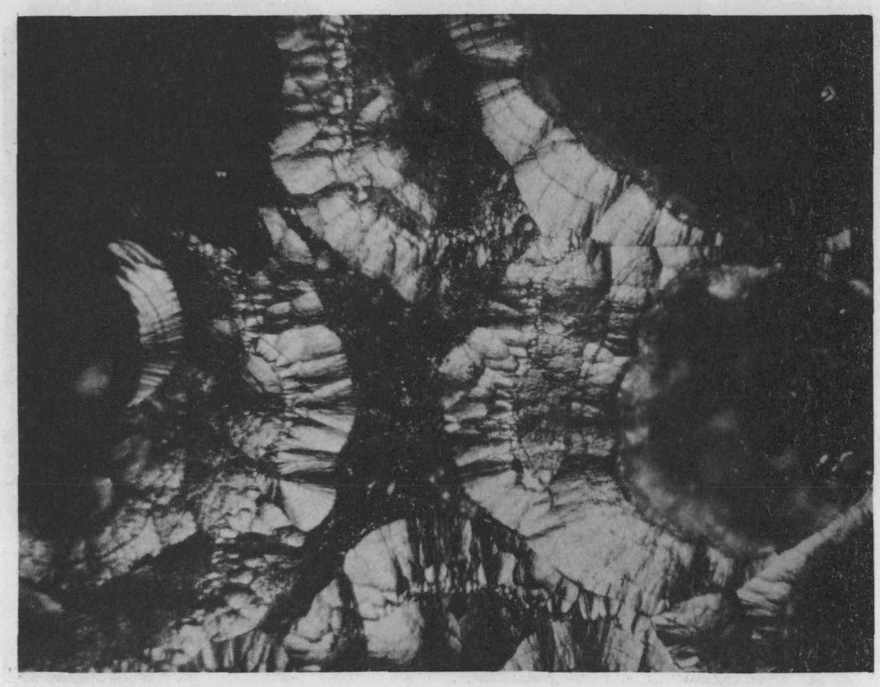

Fig. V.33--Pyrolytic carbon deposited on the bottom of an empty crucible during heating under conditions specified for the particles shown in Fig. V.32 (200X)

In Experiment 4283-31, particles were heated 500 hr in beds with a temperature gradient resulting from temperatures of either 1350° to 1475°C or 1400° to 1550°C. The temperature difference across the particles was estimated to vary from 10° to 35°C. Iron reaction with the SiC layer in some particle coatings was noted on the cool side of the beds, but the extent of reaction was much less than in previous tests at higher temperatures.

Metallographic examination revealed that seven of the 17 particle batches in the experiment showed evidence of core movement toward the hot side of the particle. The core movement was evident only in particles on the hot side of the crucible; however, not all particles on the hot side showed the effect. The results of this experiment are shown in Table V.12 along with the results for Experiments 4283-13 and 4283-17.

Core movement was observed in all three basic types of coatings examined, TRISO-I, TRISO-II, and BISO. Examples of the effect for the three types of coatings are shown in Figs. V.34, V.35, and V.36. Radiographic evidence of core migration is shown in Fig. V.37. In the lower-temperature beds, core movement was observed in only two particle batches (3592-35E and 4263-77E). The distance of core movement in these particles was less than that observed in samples at higher temperatures. The presence of a resin matrix (4263-77E and 4263-91) did not alter the amount of core movement observed. One of the most significant observations was that BISO LTI-coated particles showed core movement, while HTI coatings over the same buffer and core produced a particle that showed no core movement during the same heat treatment. This result indicates that the mechanism for core movement is sensitive to the temperature encountered by the particle during application of the BISO coating.

Metallographic examination of fission-product-doped cores after heating revealed no apparent change or reaction between core and coatings. There was some slight iron attack of SiC layers in the coatings on the cool side. Radiographic examination of 13 particles doped with Ru (4322-5D) revealed one example of heavy metal migration to the hot side and apparent depletion of heavy metal on the cool side of the core. Figure V.38 shows radiographic evidence of this effect.

The oxide cores did not exhibit core migration, but there was significant migration of porosity in the cores to the hot side of the core. Photomicrographs of typical oxide particles after heating are shown in Fig. V.39.

Discussion. The general features of a particle exhibiting core movement may be summarized as follows:

1. A deposit of dense, gray material resembling PyC at the core-buffer interface on the cool side of the core was observed. This deposit was not observed in unheated particles.
2. The core appeared to have moved relative to the rest of the particle in the direction of higher temperatures.
3. The portion of the buffer that was adjacent to the core on the hot side had been crushed or removed and the space taken by the core.
4. The buffer on the hot side sometimes appeared to be compressed and somewhat less porous than on the cool side.

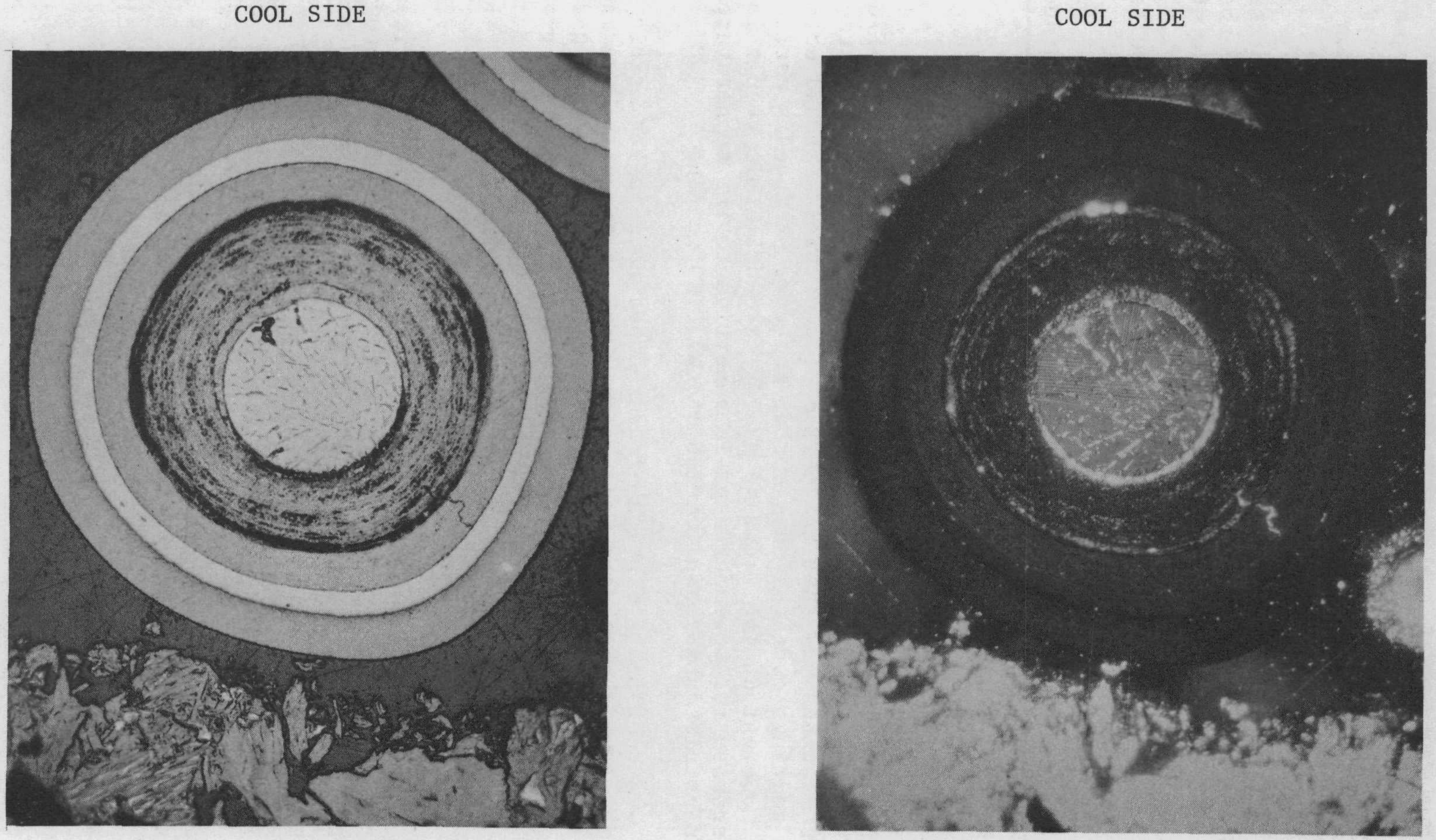

Fig. V.34--Core movement in TRISO-II-coated particle from batch 4263-91E heated for 500 hr at a nominal temperature of 1500°C with a temperature difference of 10° to 20°C along the diameter (Experiment 4283-31): (left) bright field and (right) polarized light. The core moved toward the hot side, and the region between the core and buffer on the cool side was filled with a deposit, probably carbon. The buffer on the hot side adjacent to the core was crushed or removed (200X)

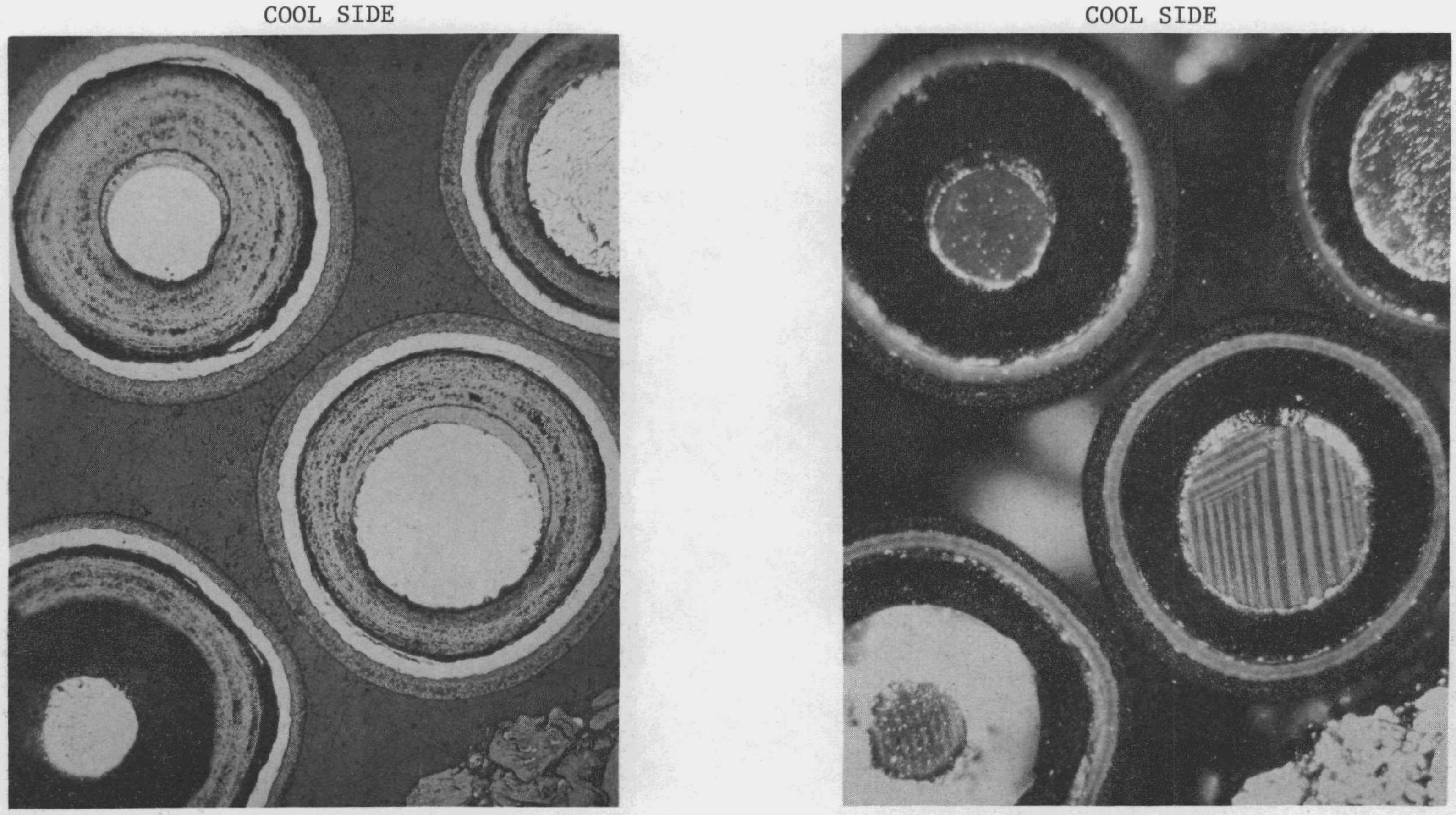

Fig. V.35--Core movement in TRISO-I-coated particles from batch 3592-35E heated for 500 hr at a nominal temperature of 1500°C with a temperature difference of 10° to 20°C along the diameter (Experiment 4283-31): (left) bright field and (right) polarized light. The cores moved toward the hot side. The deposit at the cool side of the core-buffer interface shows optical anisotropy in one particle, indicating it may be an oriented pyrocarbon deposit (200X)

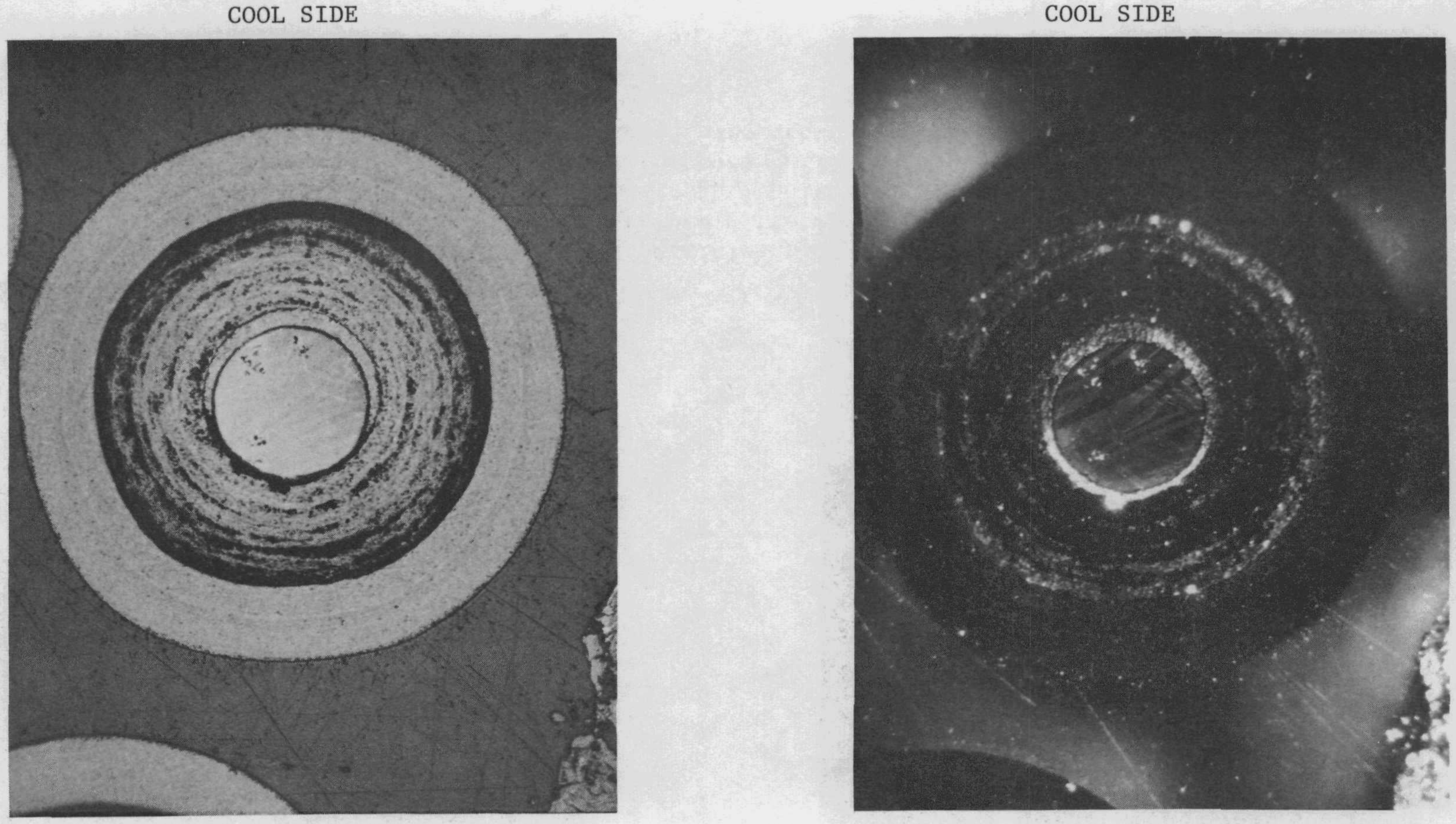

Fig. V.36--Core movement in an LTI BISO-coated particle from batch 3592-141E heated for 500 hr at a nominal temperature of 1500°C with a temperature difference of 10° to 20°C along the diameter (Experiment 4283-31): (left) bright field and (right) polarized light. The core moved toward the hot side. Particles with HTI coatings over particles from the same buffer coating run, i.e., similar core and buffer, did not show core movement when heated under the same conditions (200X)

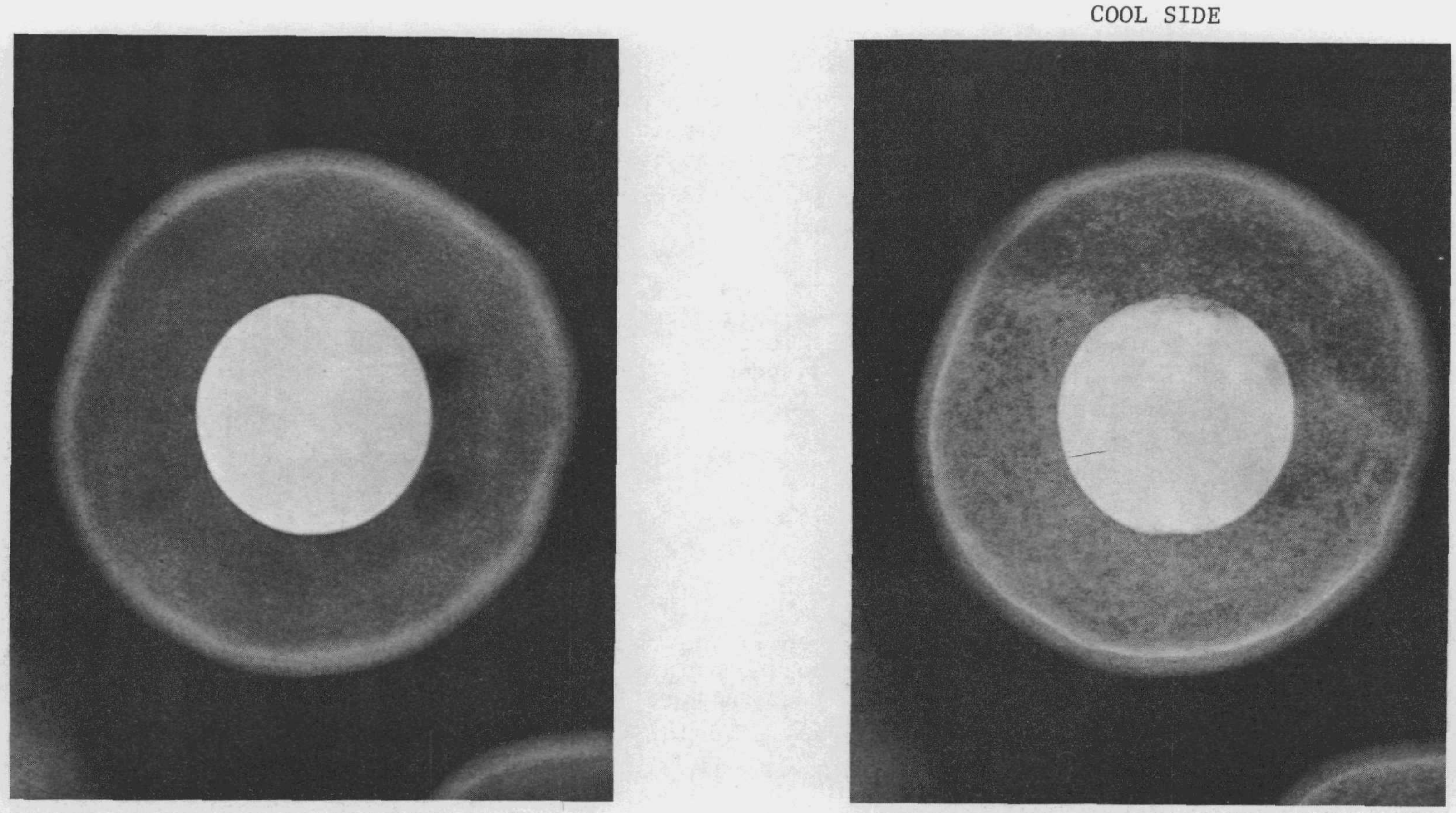

Fig. V.37--Radiographic evidence of core movement in TRISO-I-coated particles (batch 3592-35E) (left) before heating and (right) after heating for 500 hr at a nominal temperature of 1500°C with a temperature difference of 10° to 20°C along the diameter (Experiment 4283-31). A low-atomic-number material, presumably carbon, was deposited at the core-buffer interface on the cool side. High-atomic-number elements, Th,U, diffused out into the buffer on the hot side. These particles were taken from the same batch as the irradiated particles studied by microprobe (Figs. V.20 through V.26) and the metallographic specimen shown in Fig. V.35 (200X)

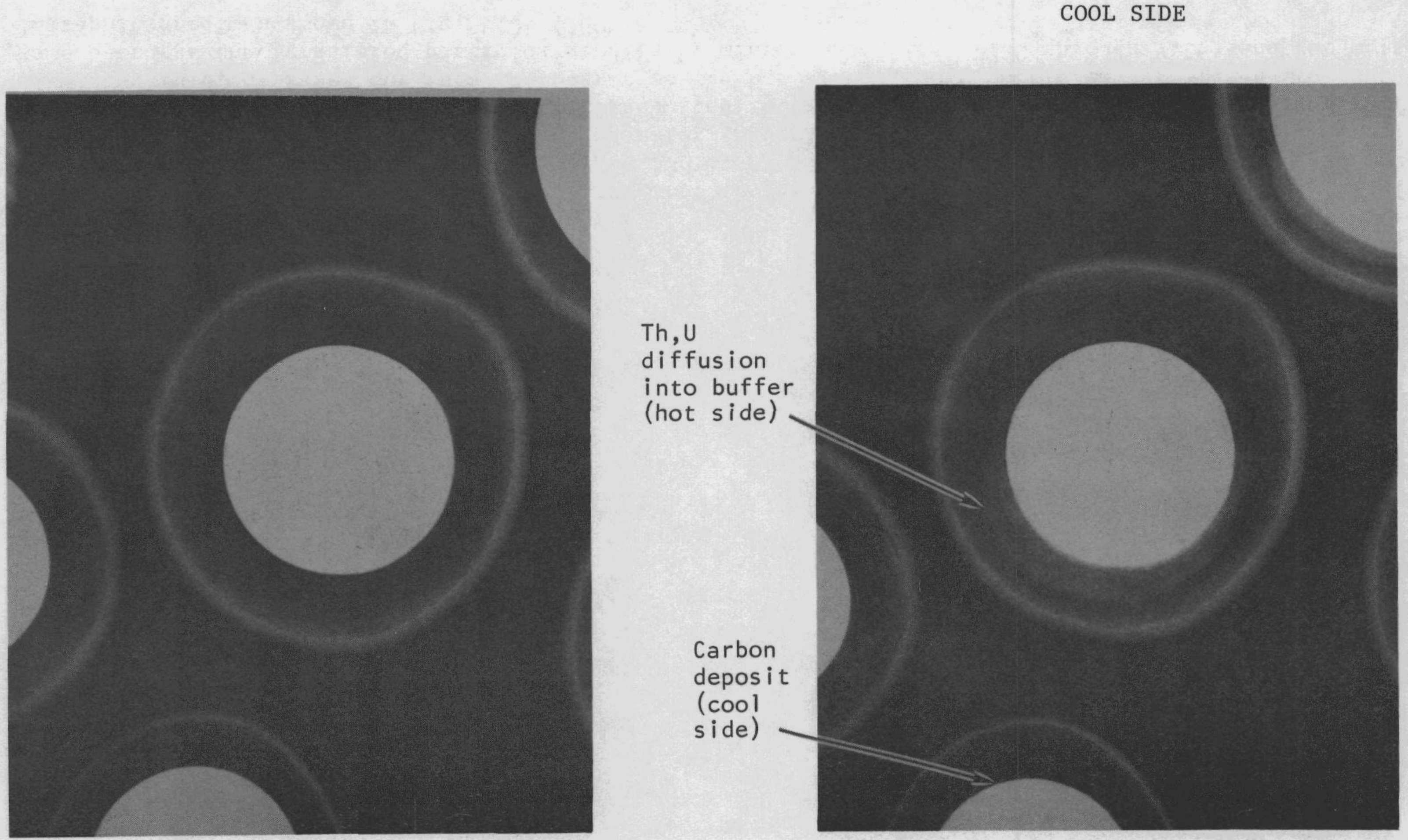

Fig. V.38--Radiographic evidence for heavy metal (Th,U) migration in a TRISO-I-coated particle doped with Ru (batch 4322-5D): (left) before heating and (right) after heating for 500 hr at a nominal temperature of 1500°C with a temperature difference across the diameter of 15° to 30°C (Experiment 4283-31). The diffuse region depleted in Th and U on the cool side was not observed in any other particles examined (200X)

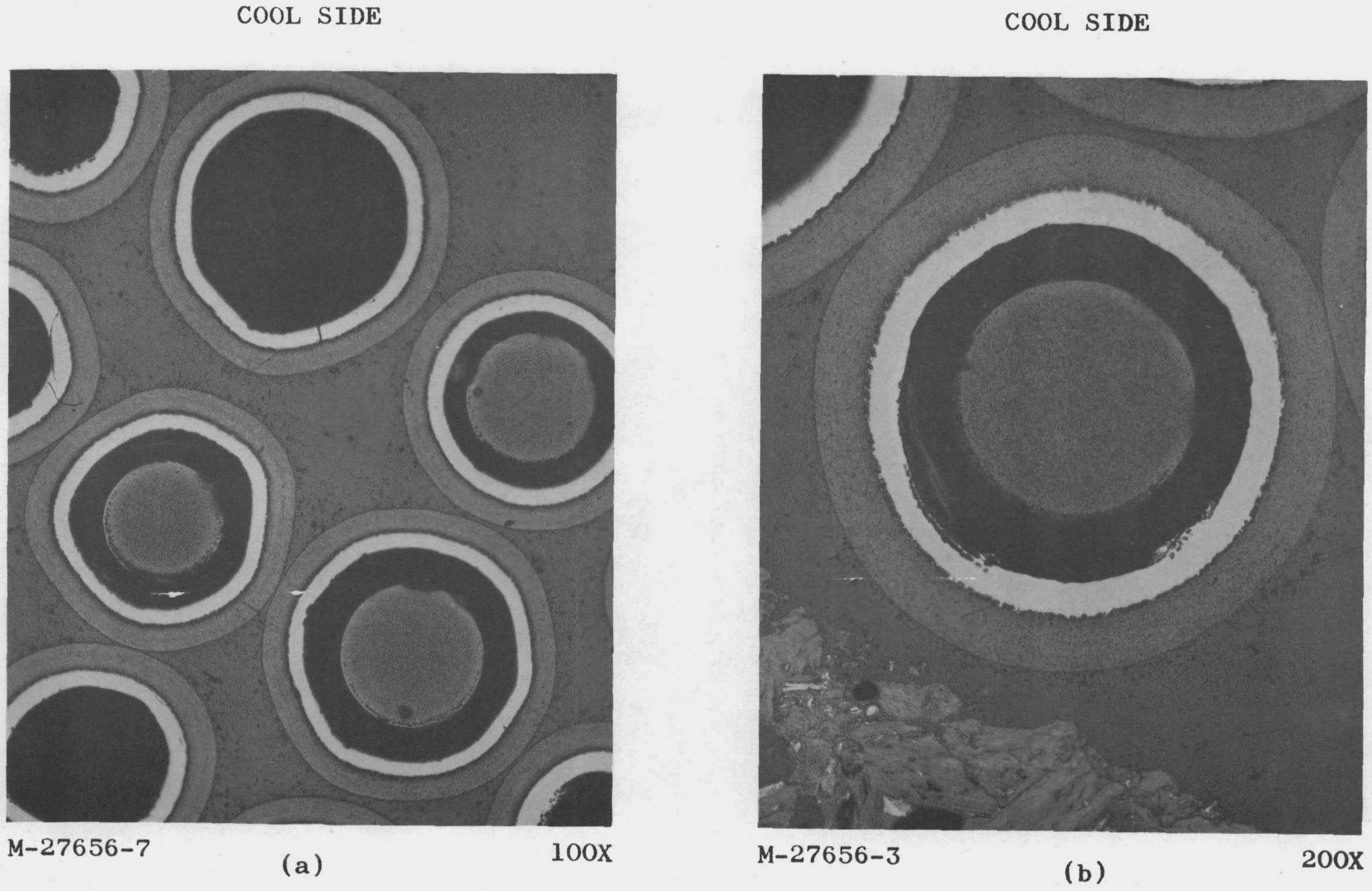

(a) (b)

Fig. V.39--TRISO-I HTI-coated particle (batch 3332-141E) heated 500 hr at a nominal temperature of 1350° to 1550°C with a temperature difference along the diameter of 10° to 15°C (Experiment 4283-31). Particles are shown at two different magnifications. Note migration of porosity toward the hot side in the $(Th,U)O_2$ core (Th:U = 3:1)

5. The buffer adjacent to the core on the hot side appeared darker in color than the remaining buffer.
6. As revealed by radiographic evidence, thorium and uranium diffused out from the core into the buffer on the hot side.

Prediction of time-temperature limits of chemical stability in TRISO-II coatings will depend upon a knowledge of the thermal dependence of the rate of this core movement through the buffer and inner isotropic PyC layer. Particles from batch 3592-35E irradiated in capsule P13J showed core movement resembling the type experimentally demonstrated in this work. In the irradiated particles, the core moved across a 40-μm buffer during irradiation at 1300°C for 2300 hr. With TRISO-II coatings heated in a gradient, the inner isotropic layer of PyC will provide a barrier between the SiC and a core that moves up the thermal gradient. However, the core may migrate through the PyC at an undetermined rate and eventually react with the SiC.

Knowledge of the mechanism for core movement in these particles would aid in estimating core movement rate, and minimizing movement or perhaps eliminating it. From the experimental results the following factors must be explained by any hypothesized mechanism:

1. Core movement is sensitive to coating temperature in BISO particles (LTI versus HTI).
2. Core movement is insensitive to Th:U ratio of the core.
3. A thermal gradient is required and movement is in the direction of higher temperature.
4. Core movement is enhanced at higher temperatures.
5. Core movement is not depdndent on neutron flux or fission-product inventory.
6. The presence of Cl or Si is not critical to the mechanism, since core movement was seen in BISO particles as well as TRISO-I and -II.
7. The deposit that develops on the cool surface of the core maintains a sharp interface between it and the thorium-uranium in the core. Interface diffusion of the deposit and the core was not detected in radiographs of out-of-pile specimens and microprobe examination of irradiated specimens (see GA-8879). The apparent depletion of thorium and uranium on the cool side of the core in the Ru-doped core (Fig. V.38) and the diffuse zone that developed was considered evidence that the mechanism for thorium and uranium migration in that case was not the same as the one discussed here.
8. Carbon is removed from the buffer on the hot side.
9. Particles from the same batch coated and heated under nominally identical conditions may or may not show core movement, at least under the experimental conditions described here. Longer test times or better characterization of test conditions might alter the criterion.

Experiments are planned or are in progress that will reveal more clearly the nature of the core movement mechanism. It seems evident at this time, however, that to explain the relatively rapid buildup of the deposit and the sharp interface between the deposit and the core, vapor transport of carbon from the hot side to the cool side of the particle must be present. Hydrogen is being considered as the most likely active element to react with carbon in the vapor-transport process.

Isothermal Experiments

Long-term Tests of BISO-coated Particles. The status of the long-term thermal stability test is shown in Table V.13. The six batches of particles currently under examination are being heated together in a six-hole crucible.

Table V.13

STATUS OF LONG-TERM ISOTHERMAL TEST OF BISO-COATED PARTICLES HEATED AT 1400°C IN 2-PSIG HELIUM

Coating Batch No.	Type of Coating	Accumulated Test Time (hr)	Remarks
3023-77E	HTI	18,000	Test terminated; analysis in progress. Previous test results (at 9300 hr) reported in GA-8420.
2814-149E	HTI	9,500	Analysis of results at 9000 hr in progress. Previous test results at 2400 hr reported in GA-8420.
3363-77E	LTI	9,500	Analysis of results at 9000 hr in progress. Previous test results at 2400 hr reported in GA-8420.
3592-141E	LTI	500	Analysis at 500 hr in progress. These particles were included in thermal gradient tests and capsule P18.
3592-143E	LTI	500	
3592-137E	HTI	500	
3592-151E	HTI	500	

Long-term Tests of TRISO-coated Particles. Heating of six batches of TRISO-coated particles continued, with the total accumulated exposure now 13,300 hr at 1400°C in 2-psig helium. Metallographic examination of these six batches at 10,000 hr and of two batches (2107-31 and 1485-77) heated for 18,000 hr at 1400°C was completed.

It was interesting to note that in some $(Th,U)_2$ cores (particle batch 3332-141E) porosity was concentrated uniformly around the periphery. In the thermal gradient experiments with these particles, the porosity migrated to the hot side of the core (see Fig. V.39).

Microprobe examination of four of the batches was also conducted to determine the extent of thorium and uranium migration into the coating from the core. Table V.14 summarizes the data and status for these particles.

There was some degree of penetration of both thorium and uranium to the ZrC or SiC barrier in all batches examined. The thorium content was always higher than uranium at the inner interface of the barrier carbide. Apparently, a compound of Th-Si or Th-Zr was formed at the interface, because the concentration of thorium and uranium always went through a minimum when traversing from the ZrC or SiC interface to the core. There was no significant penetration of thorium or uranium into the barrier layers. Iron was never found in significant amounts.

Postirradiation Isothermal Anneals of TRISO-coated Particles

Five separate batches of irradiated TRISO-coated fuel particles have been or are currently being given postirradiation anneals at high temperatures in order to obtain additional information about the time-temperature operational limitations of this type of particle. Previous attempts have been made to test fissium-doped particles; however, all the fission products could not be added to the particles, and the results obtained from these tests are therefore not thought to be completely representative of irradiated fuel particles. The high radiation levels of the irradiated particles have deterred the testing of this material in the past because only limited facilities are available outside the hot cell. The anneals are presently being conducted in a low-level facility in a high-temperature, graphite-tube King furnace. Approximately 15 to 20 particles from each batch of material are heated. To aid in the test analysis, the particles are radiographed before and after the heat treatment; for very long heat treatments, the particles are taken out of the furnace at selected time intervals and radiographed in order to progressively determine their condition.

Two fuel batches have been heat-treated at 1900°C for 30 hr and 1800°C for 250 hr, and currently three different batches of material are being annealed at 1600°C for a projected time of 2000 hr. This latter material has been examined after 20 hr and after 200 hr, and it will be checked again after 1000 hr.

Two batches of high-burnup, TRISO-I particles from the P13J capsule were tested initially; however, it was decided that more meaningful results would be obtained if the reference TRISO-II particles would be tested even though their burnups were not as high. The TRISO-II particles were from capsule P13F; along with this material, a TRISO-I batch from the same irradiation capsule was tested for comparison. Table V.15 describes the particles and gives the irradiation conditions.

The postirradiation (preanneal) radiography has proven to be a very useful tool in the evaluation of irradiated particles; the general integrity of the coatings is easily observed, and in particular, the degree of irradiation-induced fuel-kernel swelling can be determined.

Table V.14

LONG-TERM THERMAL STABILITY TESTS OF SILICON AND ZIRCONIUM CARBIDE BARRIER COATINGS AT 1400°C

Coating Batch No. and Core Type	Type Coating and Barrier	Cumulative Test Time at Examination (hr)	Migration of Th and U from Core by Radiographic Measurement (μm)	Metallographic Observations	Microprobe Observations	Status of Experiment and Remarks
2107-31E UC_2	Laminar PyC layer; SiC Laminar PyC layer (2 outer layers of PyC)	18,000	1 (same as at 8765 hr)	No change in core coating appearance except outer PyC layer separated from adjacent PyC layer due to apparent dimensional change.	No exam at 18,000 hr, as-received particles had some U contamination in buffer and SiC.	Terminated.
L1985-77N UC_2	Laminar PyC layer; SiC Laminar PyC layer	18,000	15 (same as at 8765 hr) 1/2 buffer thickness.	No change from as-coated appearance.	No exam at 18,000 hr, exam at 8765 hr showed high U (~25 wt-%) at buffer SiC interface.	Terminated.
3325-89E 8:1 $(Th,U)C_2$	TRISO-I ZrC	10,000	39	No change from as-coated appearance.	Exam at 10,000 hr, about 50% of particles had high Th (~50 wt-%) and U (~1 wt-%) at buffer ZrC interface. Less than 1 wt-% Th + U middle of buffer. Remaining 50% of particles had significantly less Th in buffer. Iron found rarely as tiny few-micron-sized regions in core and coating.	Test continued now at 13,300 hr.
3325-87E 1:6 $(Th,U)C_2$	TRISO-I ZrC	10,000	1	No examination.	No examination.	Test continued now at 13,300 hr.
3325-139E 1:6 $(Th,U)C_2$	TRISO-I SiC	10,000	4	No examination.	No examination.	Test continued now at 13,300 hr. These particles also heated in thermal gradient experiments.
3332-139E 12:1 $(Th,U)C_2$	TRISO-I SiC	10,000	14	No change from as-coated appearance.	Exam at 10,000 hr, about 10% of particles had 5 to 10 wt-% Th, ~1 wt-% U at buffer-SiC interface. Most particles had less than 1 wt-% Th + U at the interface of buffer and SiC. Th and U concentration was low <0.5 wt-% in middle of buffer. No Si in buffer or core. Iron found rarely as few-micron-sized regions in core and coating.	Test continued now at 13,300 hr. These particles also heated in thermal gradient experiments.
3332-141E 3:1 $(Th,U)O_2$	TRISO-I SiC	10,000	0	No change from as-coated appearance. Porosity in the core concentrated around the periphery in same particles.	Exam at 10,000 hr, a few particles had Th at the buffer SiC interface at a concentration of a few wt-% or less. In most particles the Th concentration at the interface was much less than 1%. U was low and barely detectable in buffer. No Si in buffer or core. Iron found rarely as few-micron-sized regions in core and coating.	Test continued now at 13,300 hr. These particles also heated in thermal gradient experiments.
3332-149E 3:1 $(Th,U)C_2$	TRISO-II SiC	10,000	1	No change from as-coated appearance except for some dimensional change causing gaps at the PyC-SiC interface.	Exam at 10,000 hr, a few wt-% Th + U at the SiC-PyC interface in less than 10% of the particles. The rest had less Th,U at the interface. Buffer contained very high Si concentrations. About 10% to 20% of the particles had significantly lower C content in core than remainder of particles. Iron was found rarely as few-micron-sized regions in core and coating.	Test continued now at 13,300 hr. These particles also heated in thermal gradient experiments.

Table V.15

DESCRIPTION OF IRRADIATED PARTICLES USED IN ANNEALS

Batch No.	Coating Thickness (μm)					Kernel			Irradiation Conditions			Capsule
	Buf	Iso	SiC	Iso	Total	Type	Size (μm)	Th:U	Avg. Temp (°C)	Burnup (% FIMA)	Fast Dose (10^{21} n/cm^2)	
3332-101E-1	51	7	13	40	111	$(Th,U)C_2$	150-250	3	1275	11	2.2	P13F
3332-101E-2	51	7	13	40	111	$(Th,U)C_2$	150-250	3	915	14	2.8	P13F
3332-147E-2	32	---	26	33	91	$(Th,U)C_2$	150-250	3	850	13	2.8	P13F
3592-37E-2	39	---	25	10	74	$(Th,U)C_2$	150-250	2	950	18	3.1	P13J
3592-37E-3	39	---	25	10	74	$(Th,U)C_2$	150-250	2	1300	18	3.6	P13J

Postirradiation radiographs of the two TRISO-I batches from capsule P13J, 3592-37E-2 and 3592-37E-3, indicate that there is a marked difference in the degree of fuel-kernel swelling of the particles that had been irradiated at 1300°C versus those irradiated at 1000°C (see Figs. V.40 and V.41). It is believed that core swelling of the degree shown in Fig. V.40 could influence the chemical as well as the mechanical integrity of the coated particles. Measurements indicate that for the particles irradiated at 1000°C negligible, if any, core expansion occurred.

The buffers of the 1300°C irradiated particles (3592-37E-3) are greatly compressed, and in many cases the core is indicated to be in contact with the SiC coating (Fig. V.42). Two cases were observed in which an apparent interaction took place between the core and the silicon carbide coating (Fig. V.42). An apparently similar but more pronounced reaction zone was observed metallographically in some of the other batches irradiated in the P13J capsule; however, it was not detected in this particular batch. It could be that only an incipient reaction occurred in the 3592-37E-3 sample. Other batches of particles from the P13J capsule which definitely have shown a reaction between the core and SiC are now scheduled to be radiographed.

The examination of the three particle batches from capsule P13F yield similar results since the 3332-101E-1 sample, irradiated at 1300°C, exhibited more fuel-kernel swelling than did the 3332-101E-2 and 3333-147E-2 samples, which were from lower-irradiation-temperature fuel batches (see Figs. V.43 through V.45). It also appears that with increased burnup, the amount of swelling increases. Although this phenomenon has been observed before, radiography of the samples now gives a relatively easy method for measuring the amount of core swelling as a function of both burnup and temperature.

It should be noted by comparing Figs. V.40 and V.42 with Fig. V.43 that the larger buffer (and inner isotropic) thickness appears to be very helpful in preventing the fuel from making contact with the silicon carbide layer. Since it is important to prevent any chemical interactions between the core and the SiC fission-product barrier, larger buffers and/or inner isotropic layers are indicated to be desirable.

Another interesting aspect of the postirradiation radiography is the observation of strong autoradiographs for some particles, whereas other particles from the same batch do not exhibit any autoradiographs under the same exposure conditions. This result is currently unexplained, although it is thought to be related to the fission-product inventory of the individual particles. Therefore, the degree of autoradiography is possibly related to the integrity of the coatings of the TRISO particles (assuming all particles have achieved the same degree of burnup).

The autoradiographs were more pronounced for the particles from the P13J capsule, but this would be expected, since the P13F material has been out of the reactor for approximately one year longer and more time has thus elapsed for a decay of many of the short-lived isotopes. The P13F material also had a lesser burnup than did the P13J particles.

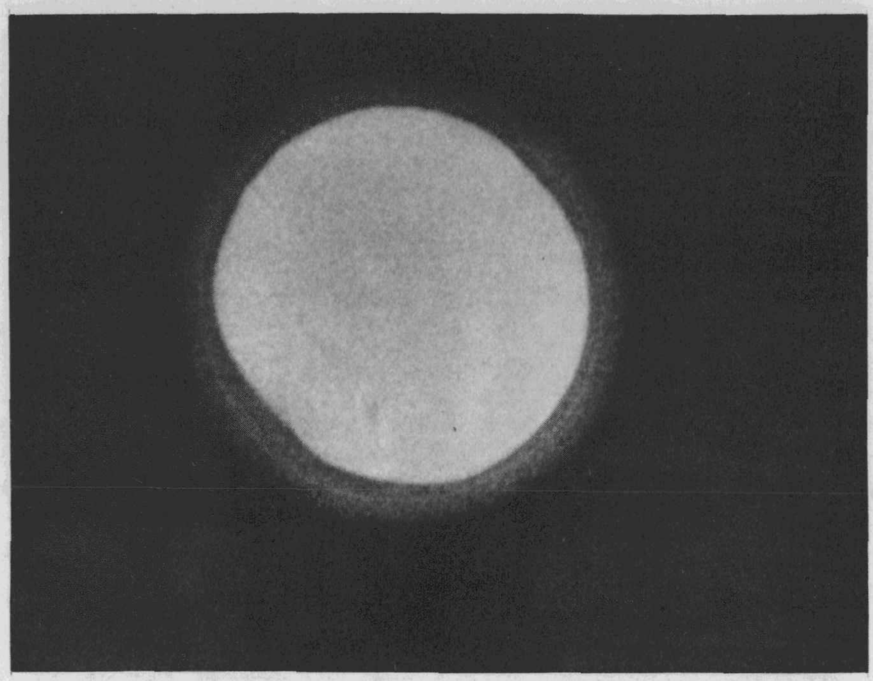

Fig. V.40--Radiomicrograph of a TRISO-I particle from batch 3592-37E-3 showing condition of particle after being irradiated at 1300°C; note swelling of the fuel kernel (white). The SiC layer is light gray (compare Fig. V.41) (200X)

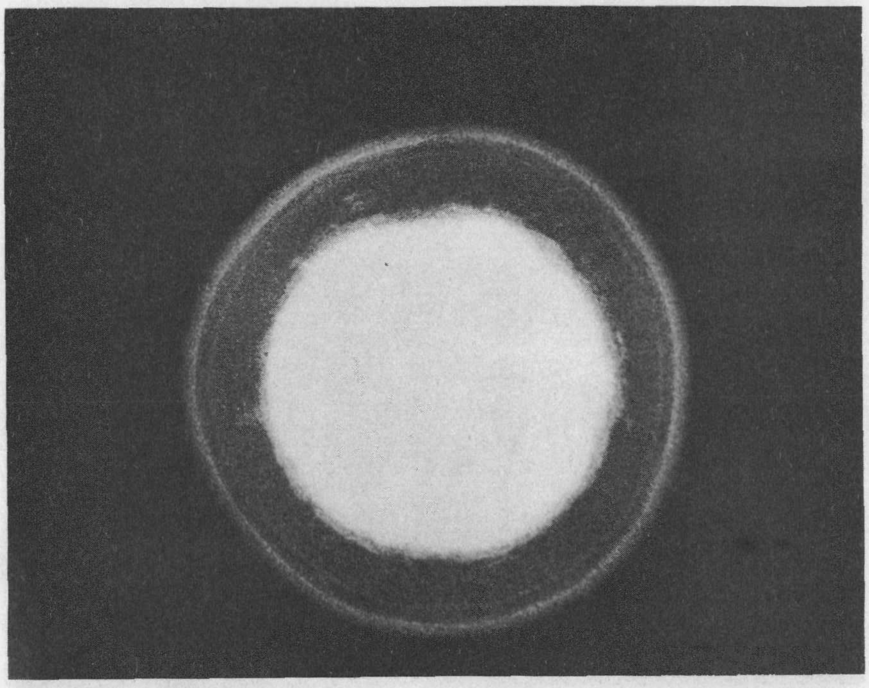

Fig. V.41--Radiomicrograph of a TRISO-I particle from batch 3592-37E-2 showing condition of particle after being irradiated at 950°C; swelling of fuel kernel is negligible. The white area is the fuel kernel, the gray is the buffer region, and the light gray is the silicon carbide coating (200X)

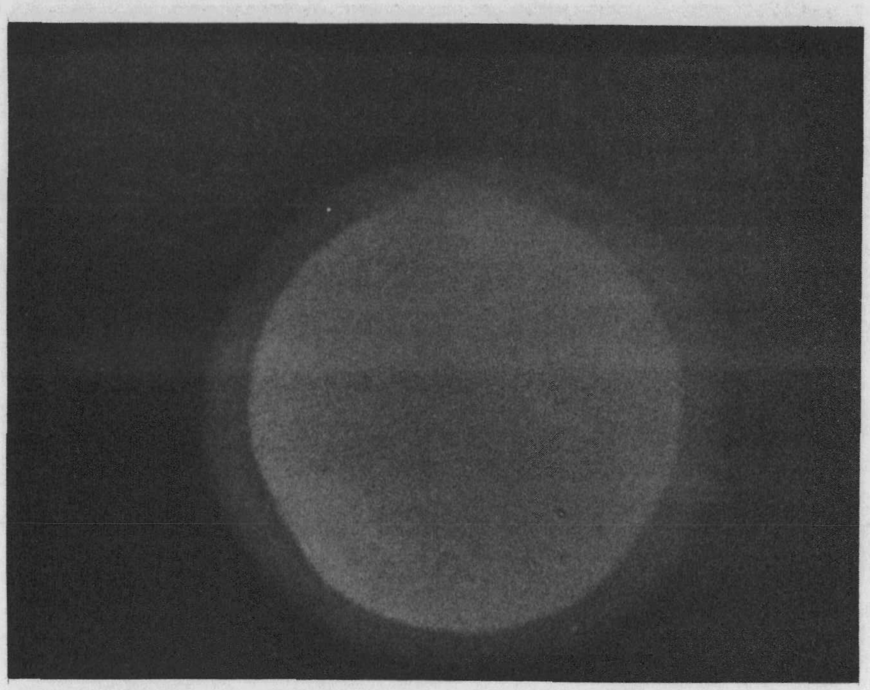

Fig. V.42--Radiomicrograph of an irradiated TRISO-I particle from batch 3592-37E-3 showing extensive core swelling. The core appears to be in contact with the silicon carbide layer; region of possible reaction between the fuel kernel and the SiC coating is at top of particle (200X)

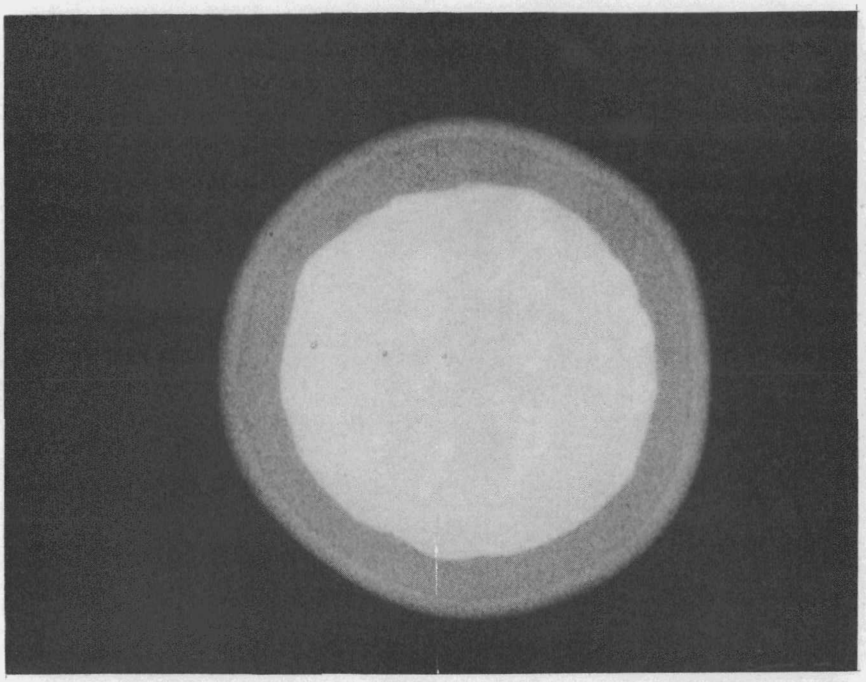

Fig. V.43--Radiomicrograph of an irradiated TRISO-II particle from batch 3332-101E-1 showing condition of particle after being irradiated at 1275°C (200X)

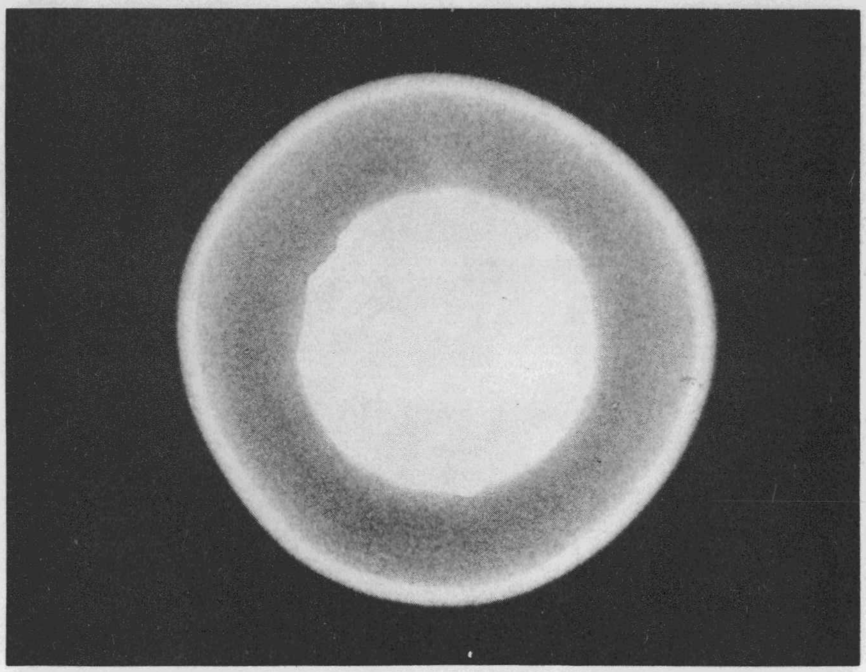

Fig. V.44--Radiomicrograph of an irradiated TRISO-II particle from batch 3332-101E-2 showing condition of particle after being irradiated at 915°C (200X)

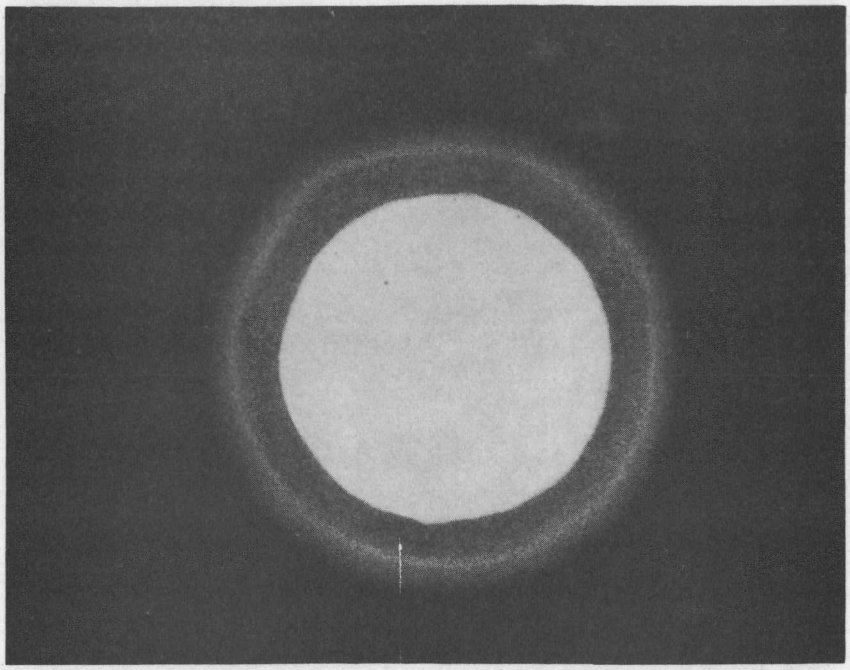

Fig. V.45--Radiomicrograph of irradiated TRISO-I particle from batch 3332-147E-2 showing condition of particle after being irradiated at 850°C (200X)

After the particles were heat-treated, it was noted that the intensity of the autoradiographs decreased in many cases. This effect was more pronounced for the capsule P13J particles. In instances where the particles had obviously failed, no autoradiographs were observed. From this result it is indicated that the presence of an autoradiograph signifies an intact particle; for particles without autoradiographs, it was inferred that a large fraction of the fission products had escaped.

The conditions of the postirradiation annealing as well as the results of these experiments are given in Table V.16. The time-temperature parameters were selected using the earlier results obtained from the unirradiated fission-doped carbide material.

Table V.16

ANNEALING OF IRRADIATED PARTICLES

Sample No.	P-capsule	Irradiation Conditions: Avg Temp (°C)	Irradiation Conditions: Burnup (% FIMA)	Postirradiation Annealing Conditions: Time (hr)	Postirradiation Annealing Conditions: Temp (°C)	Postirradiation Annealing Conditions: Atmosphere	Est Failure (%)
3332-101E-1	P13F	1275	11	200[a]	1600	Helium	0
3332-101E-2	P13F	915	14	200[b]	1600	Helium	(b)
3332-147E-3	P13F	850	13	200[a]	1600	Helium	0
3592-37E-2	P13J	950	18	30	1900	Vacuum	80
3592-37E-3	P13J	1300	18	30	1900	Helium	80
3592-37E-2	P13J	950	18	250	1800	Helium	60
3592-37E-3	P13J	1300	18	250	1800	Helium	100

[a] Test still in progress; scheduled anneal is ≥2000 hr at 1600°C.

[b] Anneal started after 200-hr shutdown.

A 1900°C anneal was conducted using TRISO-I material that was irradiated at both 1000°C and 1300°C; the burnups of these particles was 18% FIMA (see Table V.16). The 1000°C irradiated material (3592-37E-2) was heat-treated in a vacuum; however, this test does not reflect actual operating conditions, and as would be expected, the majority of the particles failed during this test. The 1900°C heating of the 1300°C irradiated particles (3592-37E-3) was conducted in a helium atmosphere; after 30 hr at this temperature, approximately 80% of the particles were believed to have failed. The failure of the particles was determined primarily from the radiographs, and was based on two observations. The first was the appearance of the particles from the radiograph, and the second was whether or not the particles produced autoradiographs comparable to the autoradiographs observed before annealing. Although the latter method has not been proven to be a valid method of evaluation, all observations were consistent with other results. Typical results obtained from the microradiographs are shown in Figs. V.46 through V.49. In several cases, considerable core diffusion was observed, and also the silicon carbide appeared to be no longer as uniform as it was before heating. Hot-cell metallography was performed, but because of some problems encountered during polishing and grinding, only two particles could be viewed. The results obtained by metallography were inconclusive and did not aid in the failure analysis. The appearance of the fuel core was observed to have changed from the postirradiation condition (preanneal condition), but the significance of this change could not be determined.

The same two particle batches, 3592-37E-2 and 3592-37E-3, were heated in helium for 250 hr at 1800°C. The results from the postanneal examination indicated that approximatdly 60% of the 1000°C irradiated particles and 100% of the 1300°C irradiated particles had failed. Typical microradiographs of these particles are shown in Figs. V.50 through V.53. The condition of the particles appeared somewhat better than the condition of the particles that were heat-treated at 1900°C. The autoradiographs, however, had completely disappeared from the 1300°C batch and only five of the twelve 1000°C irradiated particles retained their autographing tendencies. Core diffusion and degradation of the silicon carbide was again observed, and it appeared more severe in the case of the 1300°C irradiated particles.

Metallography was to be performed on both batches; however, all of the 3592-37E-3 particles hydrolyzed before they could be mounted. This hydrolyzation gives strong support to the radiographic observations that all of the particles had failed. The 3592-37E-2 particles remained intact and were examined metallographically; the results did not add any significant information to the above analyses. Photomicrographs of two particles are shown in Figs. V.54 and V.55.

For the 1600°C anneal, TRISO-II material was tested (see Table V.16), and for comparison purposes a TRISO-I batch was included in the test. The annealing of this material is still in progress; however, the particles were taken out of the furnace after annealing for 20 hr and 200 hr for radiographing. The particles were judged to be in good condition. Slight diffusion of the fuel kernel into the buffer zone was observed after 20 hr at temperature, indicating that this test is more severe than the irradiation at 1300°C for about 1500 hr. Typical microradiographs are shown in Figs. V.56 through V.58.

The limited results of the postirradiation annealings fall in the expected region of the failure as a function of the time and temperature plot that was obtained by the annealings of the fissium-doped particles (see Fig. V.59). Insufficient data are available at this time to construct a curve that could be used as a basis for projecting the operating life of fuel particles in the temperature range below 1500°C. It is hoped that the current tests will produce results that are consistent with past in-pile test and therefore will be of value for establishing the expected operating limits of TRISO fuel particles.

It has also been shown that radiography is a useful method for gathering additional information about the irradiated particles. The indication that

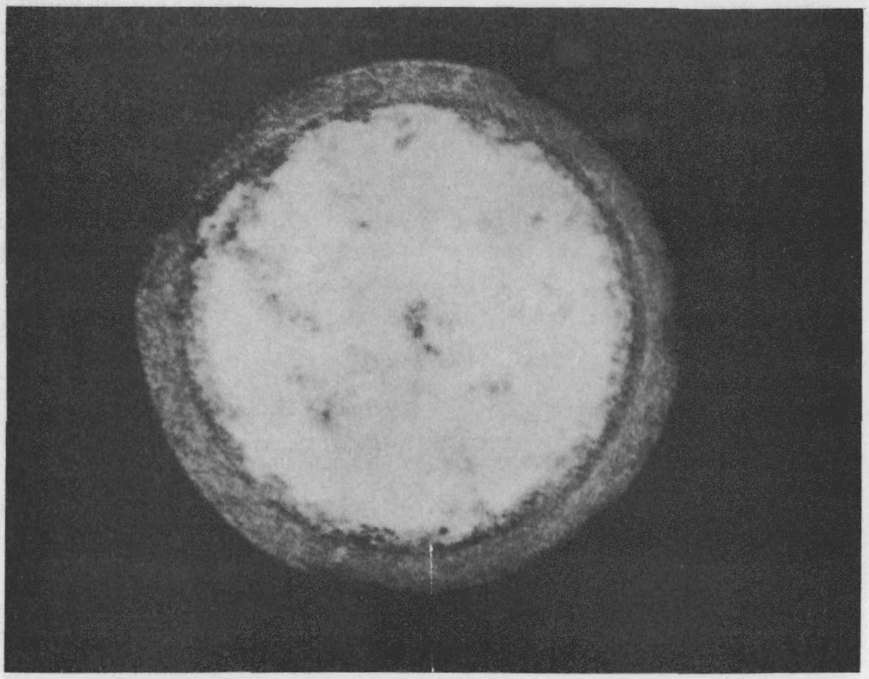

Fig. V.46--Radiomicrograph of TRISO-I particle from batch 3592-37E-2 irradiated at 950°C and subsequently annealed at 1900°C for 30 hr in vacuum; note core diffusion into the buffer coating, as well as apparent deterioration of the SiC layer (compare with Fig. V.41) (200X)

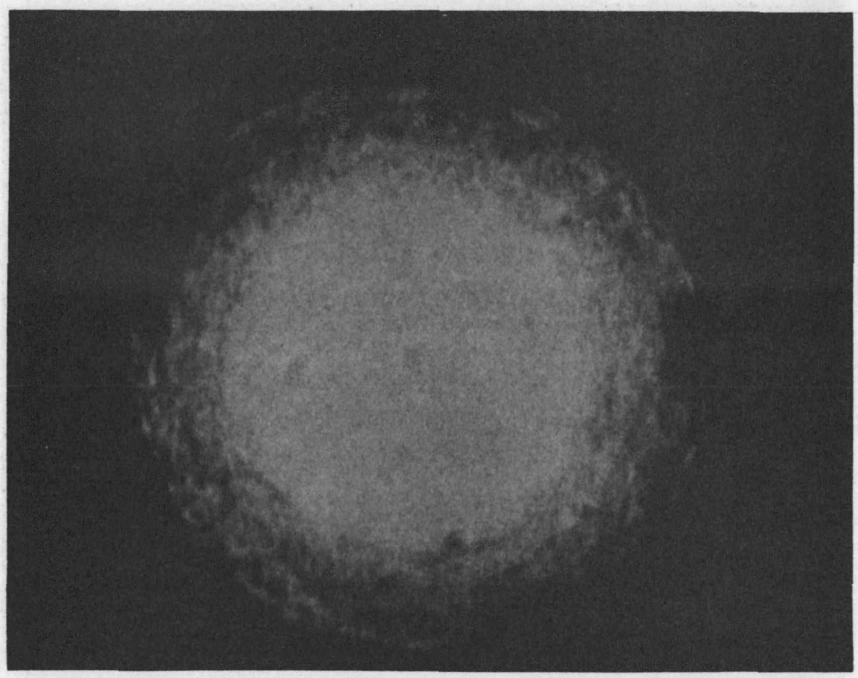

Fig. V.47--Radiomicrograph of TRISO-I particle from batch 3592-37E-2 irradiated at 950°C and subsequently annealed at 1900°C for 30 hr in vacuum; shows heavy core diffusion, as well as complete deterioration of SiC layer (200X)

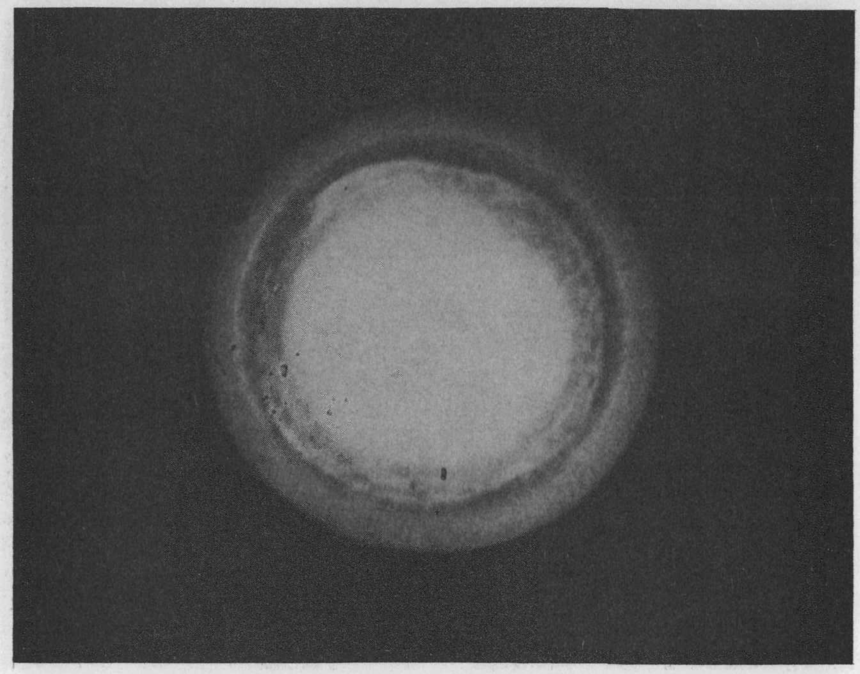

Fig. V.48--Radiomicrograph of TRISO-I particle from batch 3592-37E-3 irradiated at 1300°C and subsequently annealed at 1900°C for 30 hr in helium; shows moderate core diffusion into buffer coating (200X)

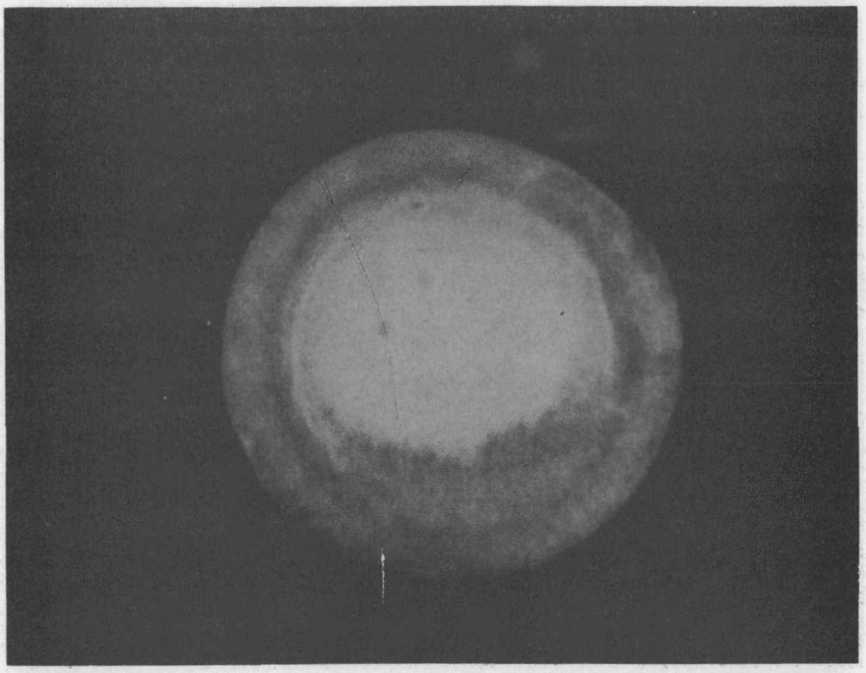

Fig. V.49--Radiomicrograph of TRISO-I particle from batch 3592-37E-3 irradiated at 1300°C and subsequently annealed at 1900°C for 30 hr in helium; shows heavy core diffusion, as well as deterioration of SiC coating (200X)

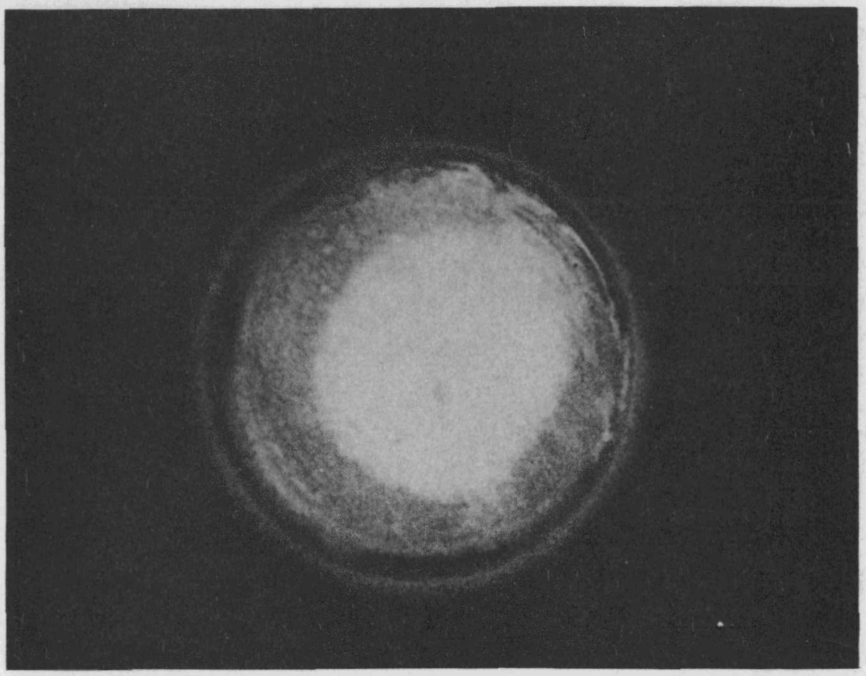

Fig. V.50--Radiomicrograph of TRISO-I particle from batch 3592-37E-2 irradiated at 950°C and subsequently annealed at 1800°C for 250 hr in helium; shows heavy core migration (200X)

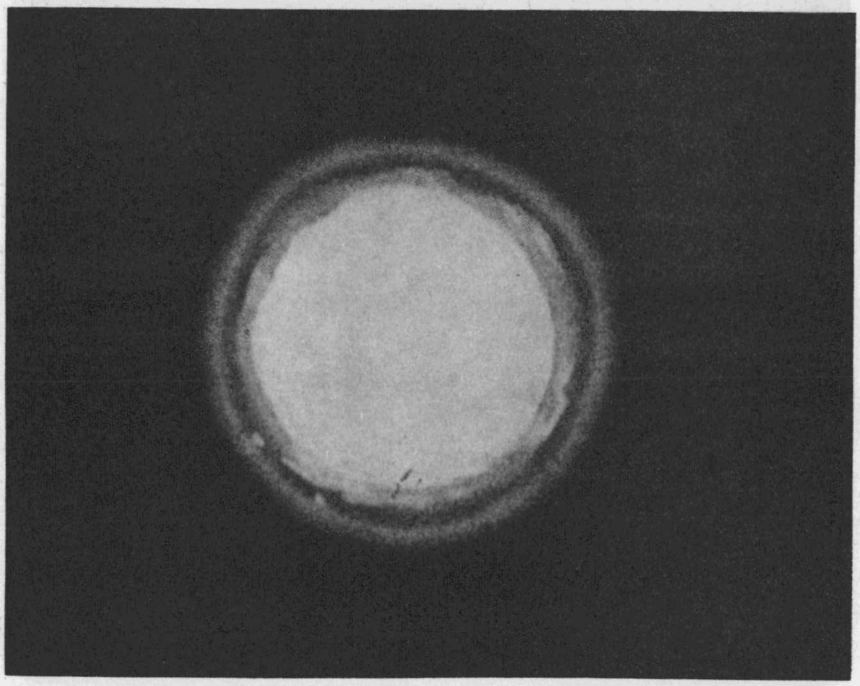

Fig. V.51--Radiomicrograph of TRISO-I particle from batch 3592-37E-2 irradiated at 950°C and subsequently annealed at 1800°C for 250 hr in helium; shows moderate core diffusion (200X)

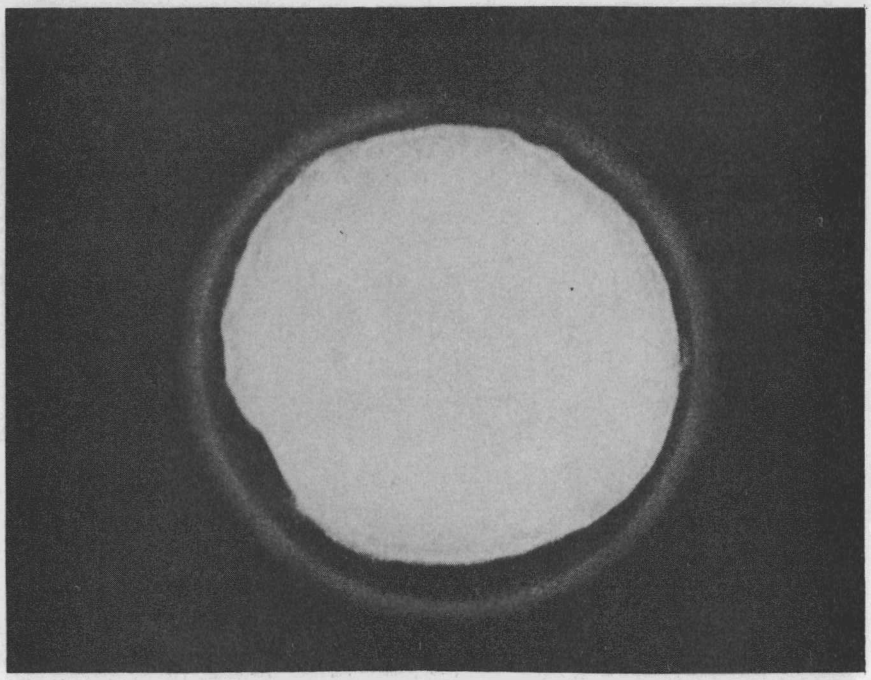

Fig. V.52--Radiomicrograph of TRISO-I particle from batch 3592-37E-3 irradiated at 1300°C and subsequently annealed at 1800°C for 250 hr in helium; slight core diffusion and possible deterioration of the SiC layer may be seen in area at top (200X)

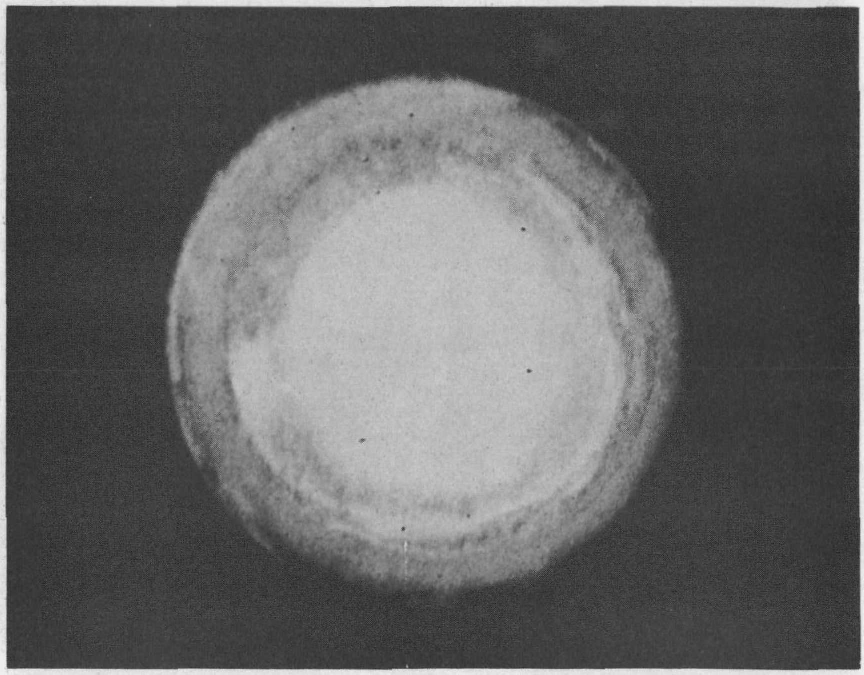

Fig. V.53--Radiomicrograph of TRISO-I particle from batch 3592-37E-3 irradiated at 1300°C and subsequently annealed at 1800°C for 250 hr in helium; shows gross core diffusion, as well as deterioration of SiC layer (200X)

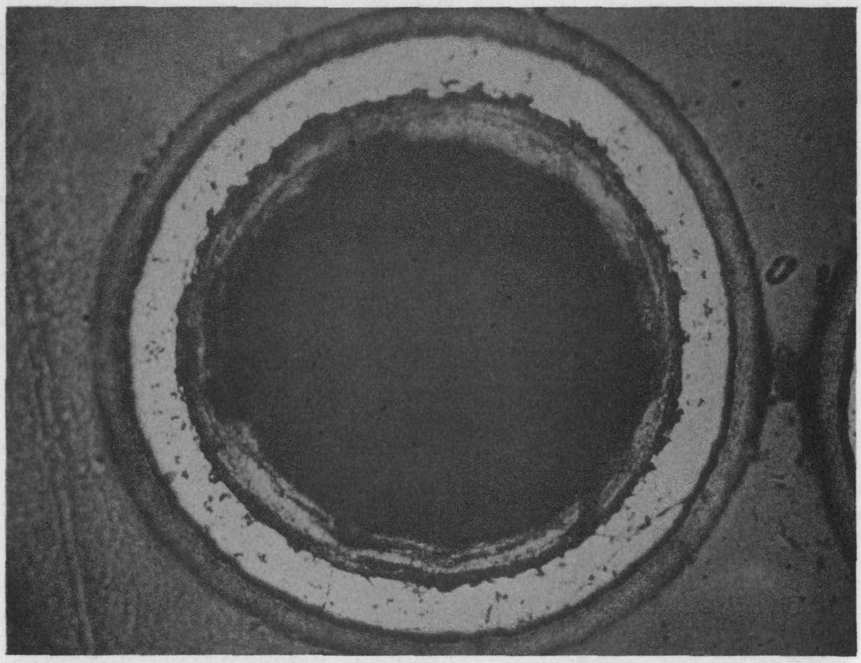

M-278-9 ~ 200X

Fig. V.54--Photomicrograph of a TRISO-I particle from batch 3592-37E-2 irradiated at 950°C and subsequently annealed at 1800°C for 250 hr in helium; shows general condition of particle after anneal; particle judged to have failed during the test (core fell out of particle during polishing

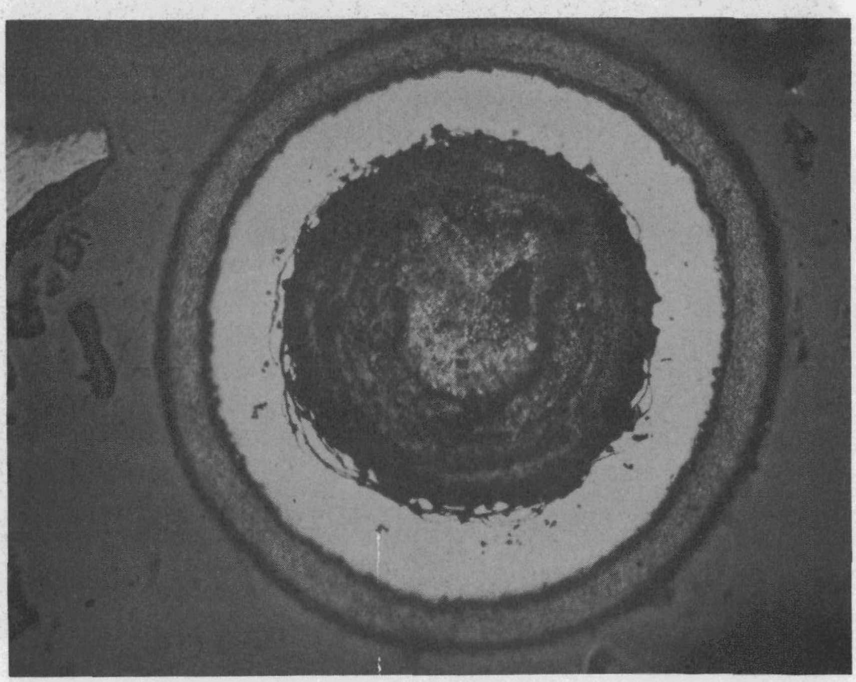

M-278-7 ~ 200X

Fig. V.55--Photomicrograph of a TRISO-I particle from batch 3592-37E-2 irradiated at 950°C and subsequently annealed at 1800°C for 250 hr in helium, shows general condition of particle after anneal, particle judged to have survived test

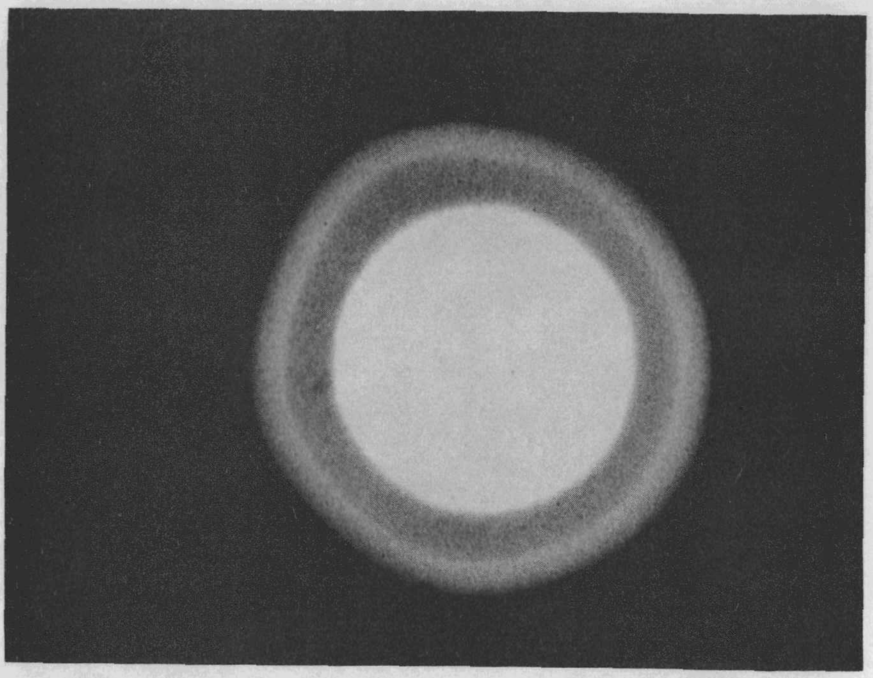

Fig. V.56--Radiomicrograph of TRISO-II particle from batch 3332-101E-1 irradiated at 1275°C and subsequently annealed at 1600°C for 20 hr in helium; shows slight diffusion of core material into buffer layer (200X)

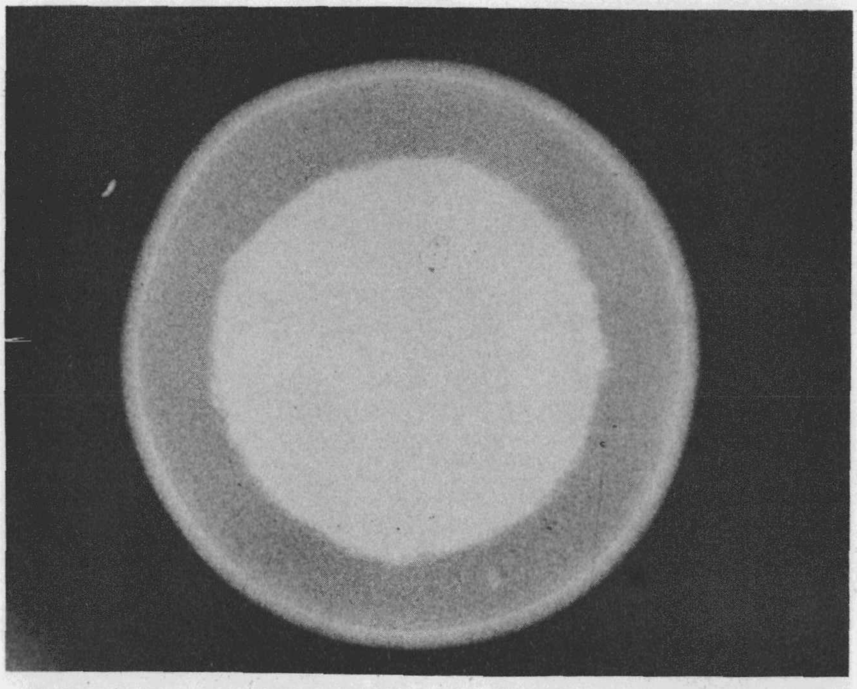

Fig. V.57--Radiomicrograph of a TRISO-II particle from batch 3332-101E-1 irradiated at 1275°C and subsequently annealed at 1600°C for 200 hr in helium; shows only slight core diffusion (200X)

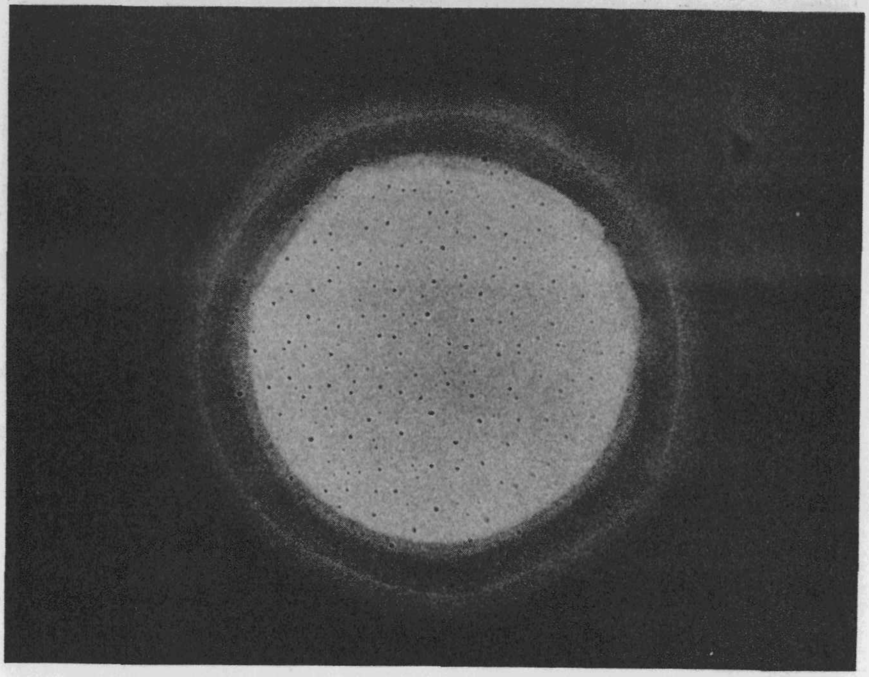

Fig. V.58--Radiomicrograph of TRISO-I particle from batch 3332-147E-2 irradiated at 850°C and subsequently annealed at 1000°C for 20 hr; shows evidence of core diffusion (200X)

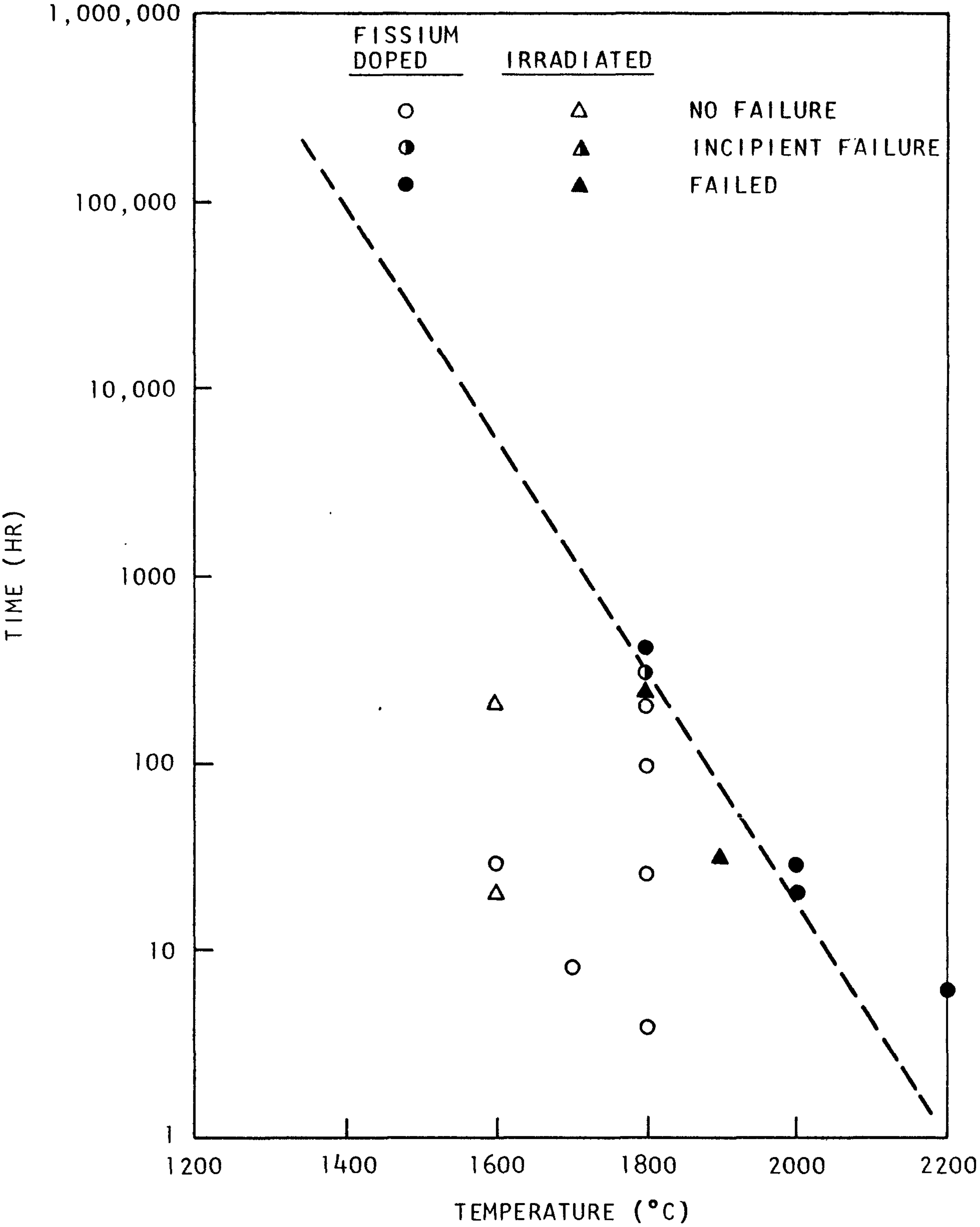

Fig. V.59--Heat-treating schedule curve for irradiated particles; curve based on fissium-doped data the fuel-kernel swelling poses a problem to the stability of the coated particles will be investigated in the near future using this technique.

ANALYTICAL STUDIES OF COATING DESIGN

Studies of the integrity of TRISO-coated fuel are being conducted using mathematical models. Schematic representations of spherical coated fuel particles are shown in Fig. V.60 for the TRISO-I and TRISO-II designs.

The mathematical model used in the TRISO-I studies is that of Kaae (Ref. 9). The Kaae model is an analysis of coating stresses induced by the buildup of fission-gas pressure, anisotropic radiation-induced dimensional changes in the outer pyrolytic carbon (PyC) layer, and differential thermal expansion of the SiC and PyC layers. The analysis also accounts for the influence of radiation-induced creep in the PyC layer.

The model was modified by Kaae to apply to the TRISO-II design (Ref. 10). The model is quite similar to the TRISO-I model, except that the three-layer stress-strain equations are solved (instead of two), and the occurrence of separation between the first two layers (inner PyC and SiC) is treated. The tensile strength of the inner PyC-SiC boundary was assumed to be very high in the present studies, and no interfacial separation occurred in any of the cases studied.

Irradiation-induced dimensional change and creep parameters for high-temperature isotropic (HTI) PyC were updated in accordance with the recent data reported by Bokros, et al. (Ref. 11). The remainder of the input parameters remained essentially the same as those reported last quarter. The models were then used to calculate stresses in samples irradiated in P-capsules. A correlation was obtained between calculated stresses and the observed fraction of the sample that failed.

The models were also used to conduct parametric studies. Coating stresses were calculated for various coating geometries, PyC densities, and irradiation temperatures. Acceptable ranges of design parameters were established by comparing the stresses with the limiting values indicated by P-capsule results.

P-capsule Calculations

Stresses were calculated for the TRISO-I and TRISO-II HTI coated particle samples irradiated in capsules P13F and P13H. In Table V.17, the results for TRISO-I samples are compared with the failure percentage; the comparison is shown in graphic form in Fig. V.61.

The results of TRISO-II HTI stress calculations are shown in Table V.18. The failure percentage was determined both by metallographic inspection and by the measurement of Sr release.

Samples P13H-1 and P13H-2 (Table V.17) indicate a calculated PyC tensile stress limit of about 20,000 psi. Sample P13H-3 gives some indication of a calculated SiC tensile stress limit of about 5000 psi.

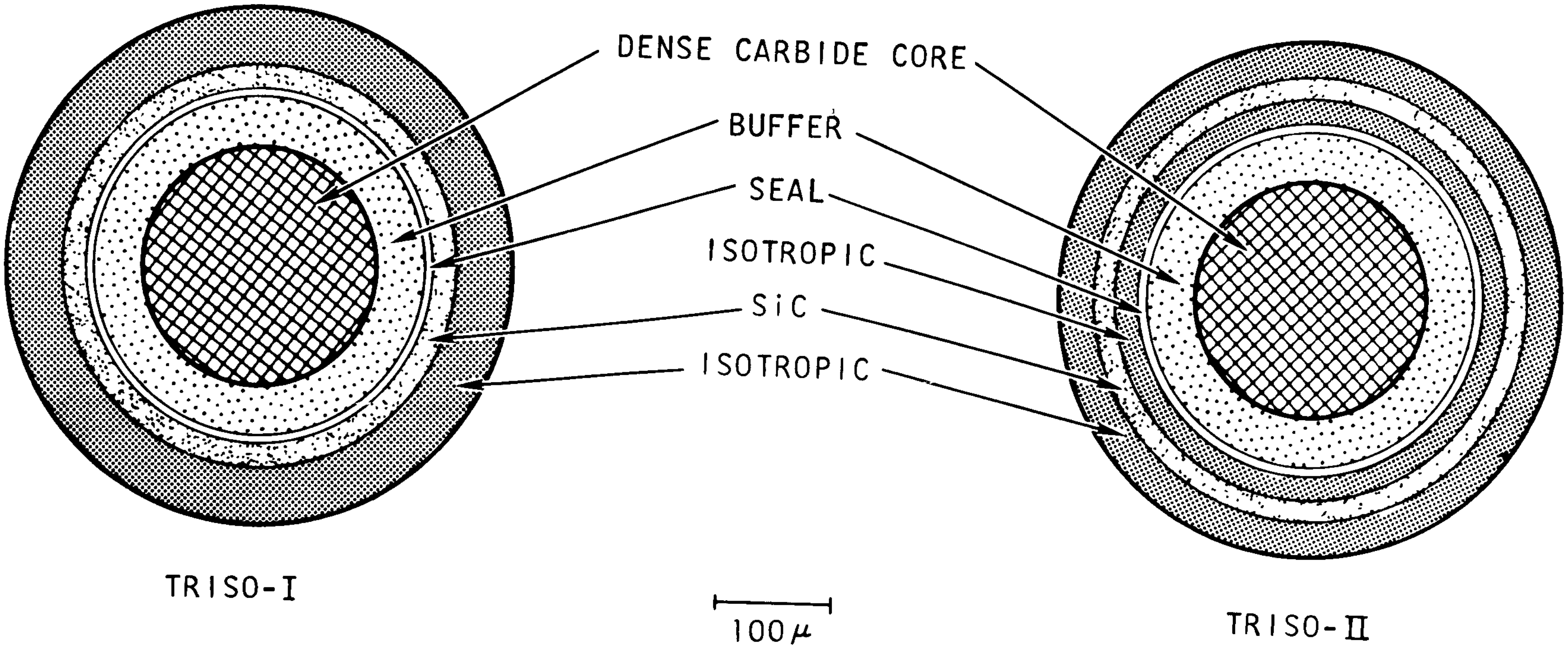

Fig. V.60--Schematic representation of TRISO-I and TRISO-II coated fuel particles

Table V.17

CALCULATED STRESSES FOR P13F AND P13H TRISO-I SAMPLES

Sample No.	Lot No.	Dimensions (μm)				HTI Density[a] (g/cm³)	HTI BAF	Burnup (% FIMA)	Fast-Neutron Dose (10^{21} n/cm²)	EOL Temp (°C)	Conditions for Selection of Dimensional Change Curve		PIE (% failed)		Calculated Stresses[b] (psi)		
		Core	Buf	SiC	PyC						Temp (°C)	Density (g/cm³)	Met.	Sr Release	Max. PyC Tensile Stress	Max. SiC Tensile Stress	Max. SiC Compressive Stress
P13F-1	3332-147E	200	32	26	33	2.00	1.01	11.9	2.2	1265	1200	1.97-2.00	0	12	13,860 (EOL)	1,170 (BOL)	8,200
P13F-2	3332-131E	200	34	30	10	1.95	1.00	11.5	2.2	1250[a]	1200	1.92-1.93	0	0.6	14,370	6,080	3,880
P13F-3	3332-145E	200	34	40	9	2.00	1.01	13.1	2.7	1300	1200	1.97-2.00	0	0.2	14,170 (EOL)	5,700 (EOL)	1,370
P13F-4	3332-101E	200	58	13	40	2.00	1.01	10.8	2.2	1290	1200	1.97-2.00	0	0.2	14,010 (EOL)	2,250 (BOL)	25,050 (EOL)
P13F-5	3332-137E	360	40	60	14	2.05	1.10	4.5	2.8	1310	1200	2.05	0	0	16,540 (EOL)	2,000	840
P13F-6	3332-139E	360	46	32	34	2.05	1.01	4.2	2.8	1305	1200	2.05	0	0	19,910 (EOL)	940 (BOL)	10,010 (EOL)
P13F-7	3332-141E	200	37	28	33	2.00	1.01	13.0	2.8	1245	1200	1.97-2.00	0	---	18,280 (EOL)	1,140 (BOL)	10,030 (EOL)
P13F-8	3332-147E	200	32	26	33	2.00	1.01	13.2	2.8	850[a]	900	1.97-2.00	0	0	9,770	1,840 (BOL)	11,940
P13F-9	3332-145E	200	34	40	9	2.00	1.01	13.7	2.8	910	900	1.97-2.00	0	0	12,200	3,940 (EOL)	1,850
P13F-10	3332-101E	200	58	13	40	2.00	1.01	13.7	2.8	910[a]	900	1.97-2.00	0	0	9,390	3,480 (BOL)	27,030
P13H-1	3325-111E	200	46	22	30	1.90	<1.1[a]	21.8	4.2	1225[a]	1200	1.92-1.93	30	32	25,270 (EOL)	1,300 (BOL)	16,220
P13H-2	3325-113E	200	36	27	11	1.99	<1.1[a]	21.8	4.2	1225[a]	1200	1.97-2.00	0.2	7	27,450 (EOL)	9,480 (EOL)	2,470
P13H-3	3325-123E	200	41	30	10	2.01	<1.1[a]	17.4	3.0	1260	1200	1.97-2.00	0.1	2	17,250 (EOL)	6,890 (EOL)	1,990
P13H-4	3325-121E	360	40	48	23	1.88	1.00	7.9	4.3	1225	1200	1.87	0	0.1	14,900	3,970 (EOL)	7,260
P13H-5	3325-113E	200	36	27	11	1.99	<1.1[a]	22.0	3.8	925[a]	900	1.98-2.00	0.2	---	11,900	12,580 (EOL)	3,030
P13H-6	3325-121E	360	40	48	23	1.88	1.0	7.8	3.8	1000[a]	1050	1.88	0.2	0	22,640	680 (BOL)	11,150

NOTE: All PyC is HTI. HTI dimensional change is current to GA-8700 (Ref. 11). A constant temperature equal to the EOL value is used. Median core diameter was used.

[a] Estimated.

[b] Stresses occurring at end of life are identified EOL. Stresses occurring at beginning of life (i.e., zero fast dose) are identified BOL.

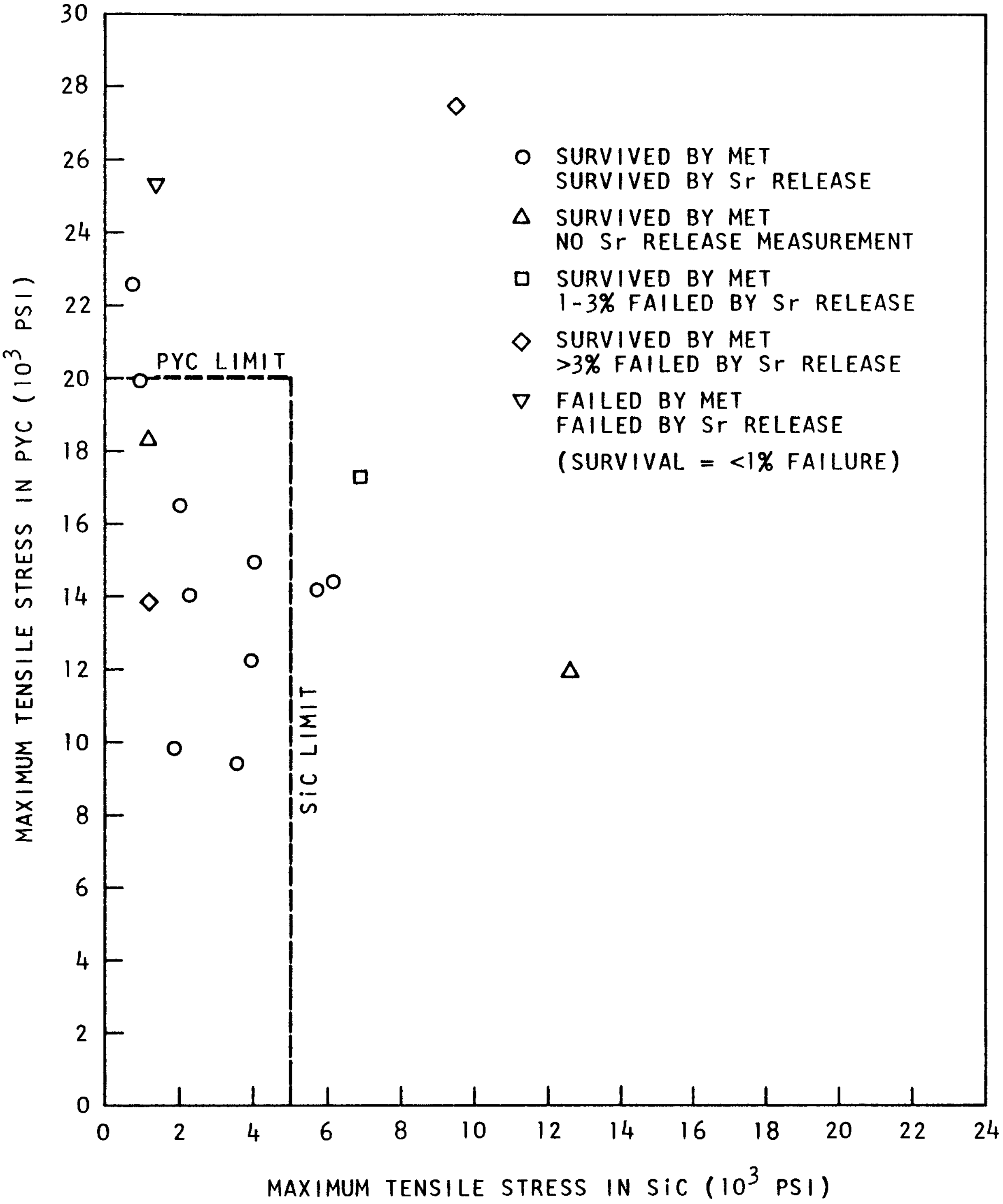

Fig. V.61--Stresses in irradiated TRISO-I-coated particles (HTI)

Table V.18

CALCULATED STRESSES FOR P13F AND P13H TRISO-II SAMPLES

Sample No.	Lot No.	Dimensions (μm)					HTI Density (g/cm³)	HTI BAF	Burnup (% FIMA)	Fast Dose (10^{21} n/cm²)	EOL Temp (°C)	Conditions for Selection of Dimensional Change Curve		PIE (% failed)		Stresses (psi)[a,b]					
																Max. PyC Tensile Stress		Max. SiC Tensile Stress		Max. SiC Compressive Stress	
		Core	Buf	Iso	SiC	Iso						Temp (°C)	Density (g/cm³)	Met.	Sr Release	Calculated	Extrapolated	Calculated	Extrapolated	Calculated	Extrapolated
P13F-11	3332-153E	200	29	25	6	38	2.00	1.01	12.7	2.7	1255	1200	1.97-2.00	0	3	17,700 (EOL)	47,930 (EOL)	3,840 (BOL)	3,840 (BOL)	89,980	297,760 (EOL)
P13F-12	3332-149E	200	23	40	22	6	2.00	1.01	12.5	2.7	1275[c]	1200	1.97-2.00	0	0.0	21,860	45,130 (EOL)	11,920 (EOL)	17,720	29,580	29,580
P13H-7	3325-117E	200	40	49	6	8	1.87	<1.1[c]	22.4	4.2	1225[c]	1200	1.87	0.2	18	33,550	33,550	1,950 (BOL)	35,870 (EOL)	216,700	216,700
P13H-8	3325-125E	200	30	38	9	11	1.93	<1.1[c]	22.3	4.3	1225[c]	1200	1.92-1.93	0	3	28,850	39,270 (EOL)	4,200 (EOL)	4,660	104,000	104,000
P13H-9	3325-119E	360	40	89	11	20	1.91	0.98	8.1	4.3	1200	1200	1.92-1.93	0	0.2	23,640	48,840 (EOL)	2,380 (BOL)	2,380 (BOL)	220,190	258,350 (EOL)
P13H-10	3325-117E	200	40	49	6	8	1.87	<1.1[c]	22.2	3.8	950[c]	900	1.87	0	0.05	35,830	35,830	4,120 (BOL)	17,820	230,010	230,010

NOTE: All PyC is HTI deposited from CH_4 at 2000°C. SiC is deposited at 1400°C (except P13F-11 - 1415°C). A constant temperature equal to the EOL temperature is used. Median core diameter was used.

[a] Calculated stress was done for experimentally observed burnup and dose using a linear path to this end point. The extrapolated stress was calculated assuming the linear relationship between burnup and dose was continued to design burnups (20% for fissile, 7% for fertile) at which point burnup was held constant while dose continued out to 8 x 10^{21} n/cm². When observed burnup exceeded design burnup, a linear path to observed burnup followed by constant burnup out to a dose of 8 x 10^{21} n/cm² was used.

[b] Stresses that occur at end of life are identified by EOL. Stresses that occur at beginning of life (i.e., zero fast dose) are identified by BOL.

[c] Estimated.

Calculated stress was obtained assuming a linear relationship between fast-neutron dose and burnup out to the final burnup and dose values, as shown in Tables V.17 and V.18. These conditions were extrapolated to establish whether maximum calculated stresses are sensitive to experimental errors in burnup and fast-neutron dose. The extrapolated stress was calculated assuming that the linear relationship between burnup and dose was continued to design burnups (20% FIMA for fissile and 7% FIMA for fertile), at which point, burnup was held constant while fast-neutron dose was continued out to 8 x 10^{21} n/cm^2. When observed burnup exceeded design burnup, a linear path to observed burnup, followed by constant burnup out to a fast dose of 8 x 10^{21} n/cm^2, was used. The extrapolated calculations indicated sensitivity to errors in dose and fast dose in some cases, particularly maximum SiC tensile stress in case P13H-7 (Table V.18). The results tend to substantiate the stress limits indicated by the TRISO-I results.

Parametric Studies

Stress calculations were done for the fissile- and fertile-coated particle types for various combinations of coating thicknesses, HTI density and irradiation temperature. The fuel core diameters were 525 and 225 μm for fertile and fissile particles, respectively; the buffer thickness was 50 μm and SiC thickness 20 μm in all cases. Calculations for TRISO-I particles were done for 70, 50, and 30 μm of HTI for the fertile particle and 60, 50, and 30 μm of HTI for the fissile particle. Each of these parameters was used for each of 21 combinations of irradiation temperature and HTI density. The TRISO-I calculations were performed because they accurately describe stress conditions in the outer PyC layer of both TRISO-I and TRISO-II coatings, and thereby the necessity for using the more time-consuming TRISO-II model to design the outer layer is eliminated.

Tangential stress at the radial position of maximum tensile stress both in the PyC and the SiC layers were plotted versus both PyC density and irradiation temperature at fast-neutron doses of "Dose I," 5 x 10^{21} and 8 x 10^{21} n/cm^2. Dose I is the fast dose at which the PyC stress reaches a maximum early in life (usually 1 x 10^{21} to 2 x 10^{21} n/cm^2).

The values of density and irradiation temperature at which PyC stress passed above 20,000 psi and at which SiC stress passed above 5,000 psi were plotted to form failure loci for each of the three PyC thicknesses and for the fissile and fertile types. These failure loci plots are shown in Figs. V.62 through V.67. The arrows indicate directions of increasing stress. The PyC failure locus at 1 to 2 x 10^{21} n/cm^2 is a lower limit in PyC density. A lower limit in PyC density occurs because low-density PyC densifies rapidly early in life. The rapid shrinkage onto the high-modulus SiC layer causes high-tensile stress in the PyC layer. The PyC failure locus at 8 x 10^{21} n/cm^2 is an upper limit in PyC density. An upper limit in PyC density occurs because high-density PyC behaves more anisotropically toward the end of life.

The SiC failure loci generally forms an upper limit to irradiation temperature because the rapid irradiation-induced creep at high temperatures allows shrinkage stresses in the PyC to be relieved, thereby requiring the SiC layer to restrain the fission-gas pressure unaided by the PyC layer. The

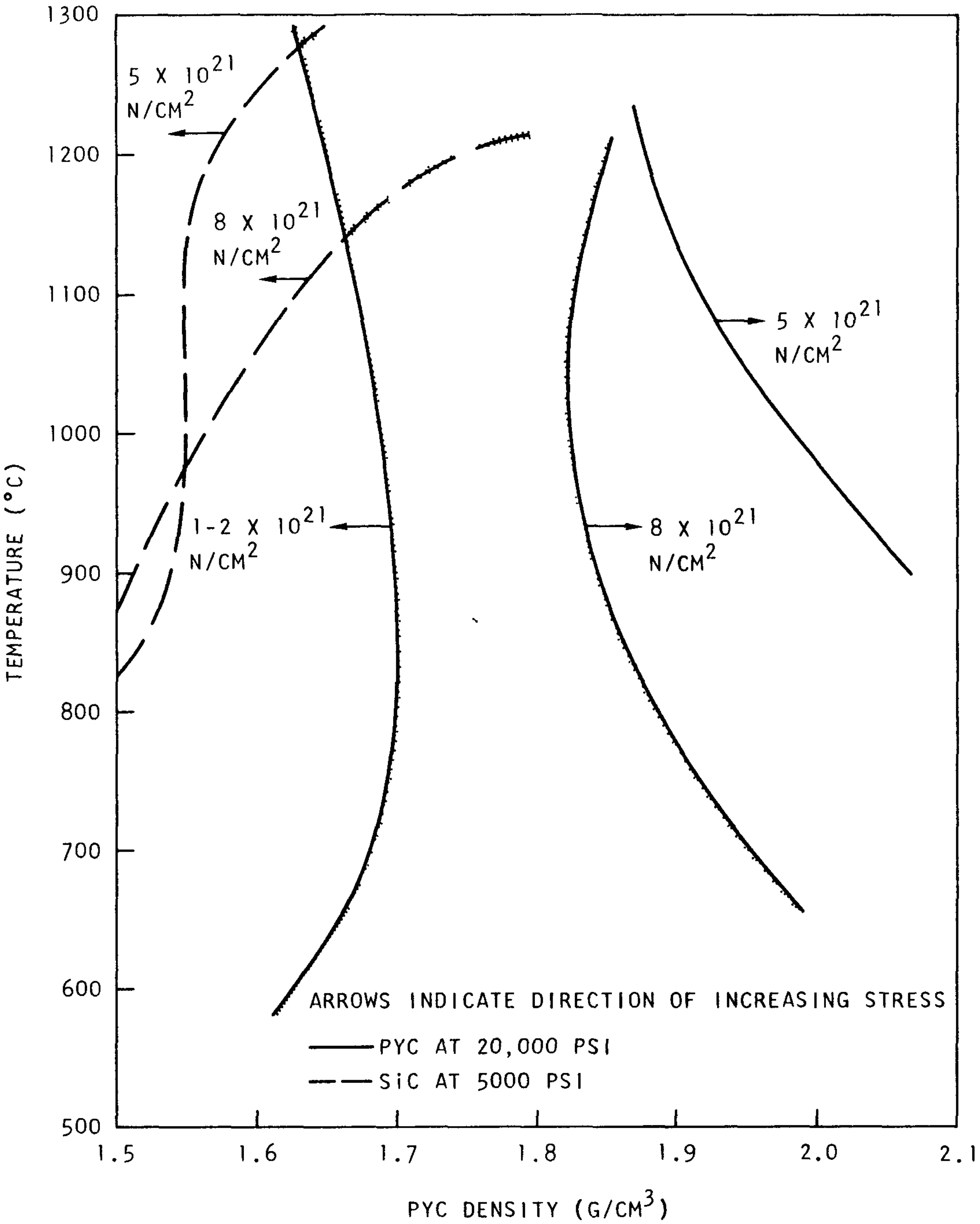

Fig. V.62--TRISO-I parametric study, loci of tensile stress limits (HTI fissile-B, 50-20-60 μm)

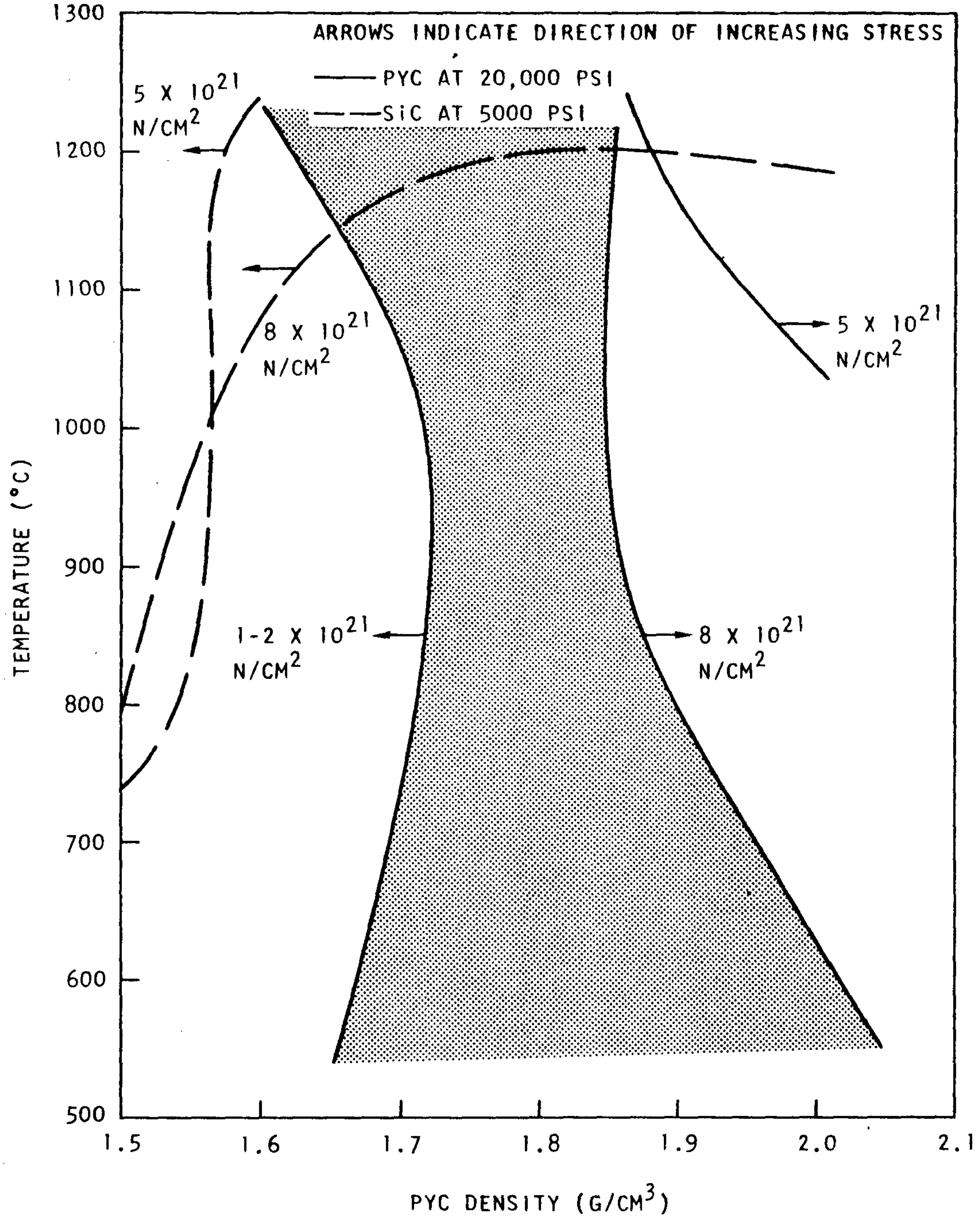

Fig. V.63--TRISO-I parametric study, loci of tensile stress limits (HTI fissile-B 50-20-50 µm)

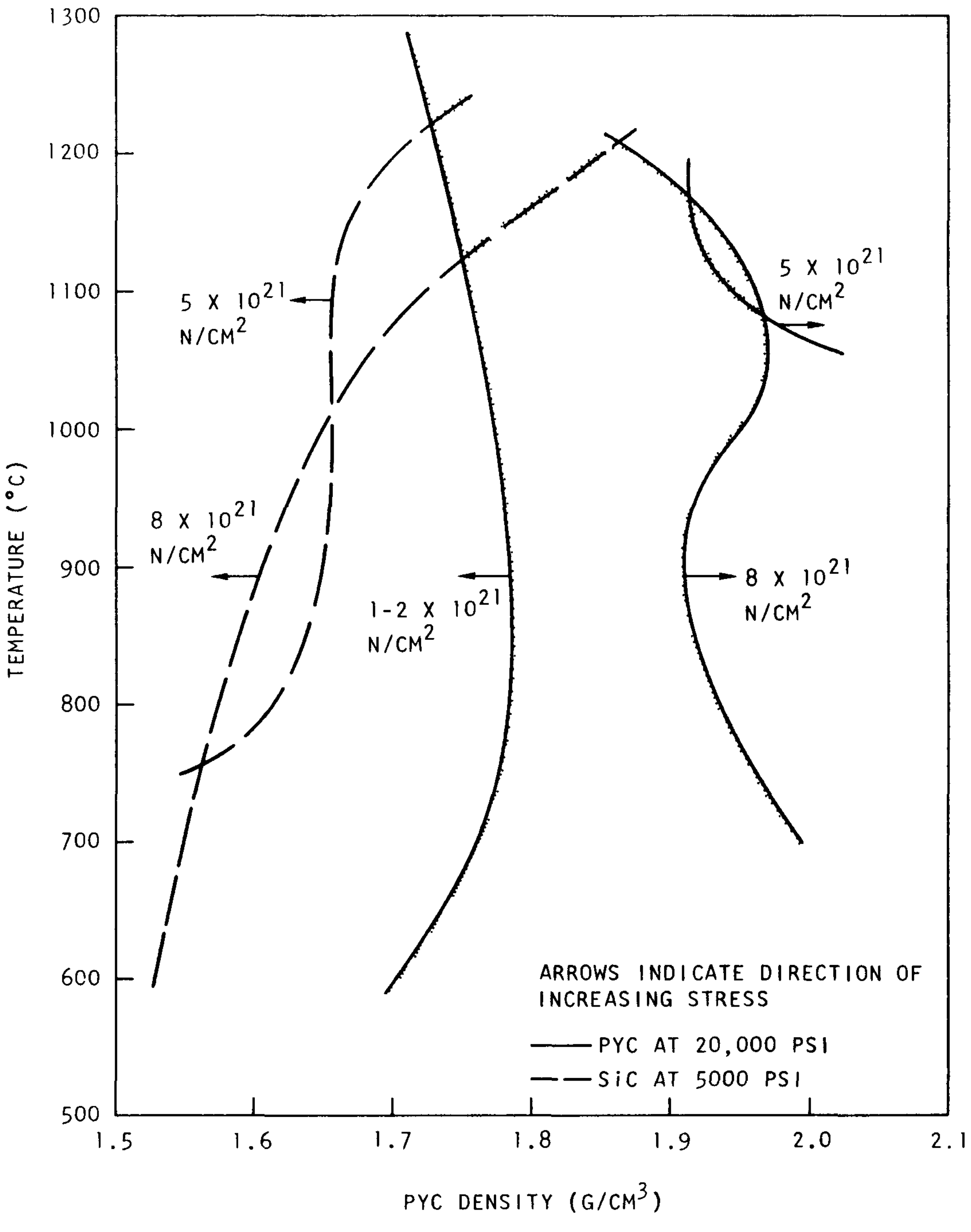

Fig. V.64--TRISO-I parametric study, loci of tensile stress limits (HTI fissile-B 50-20-30 μm)

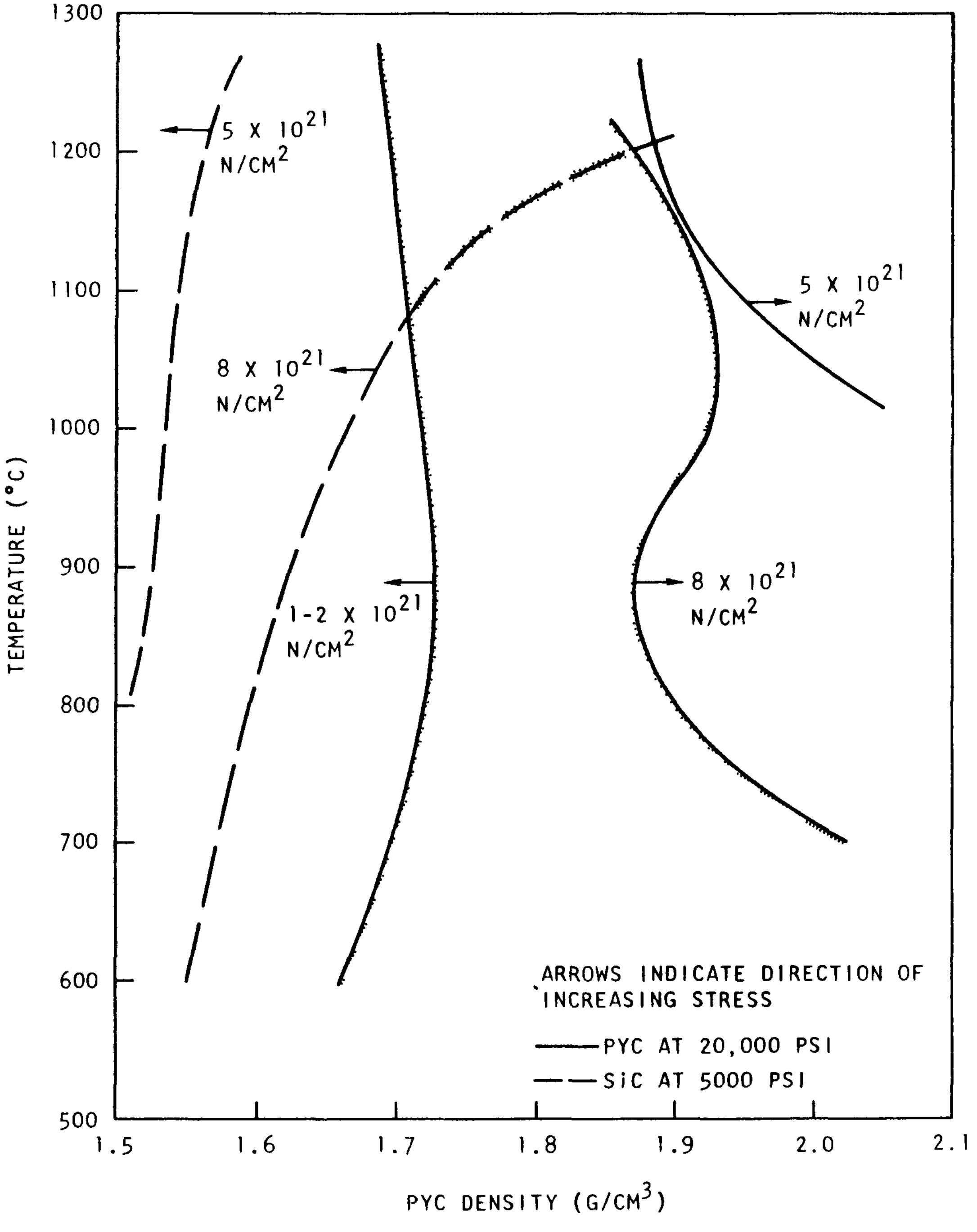

Fig. V.65--TRISO-I parametric study, loci of tensile stress limits (HTI fertile-B 50-20-70 μm)

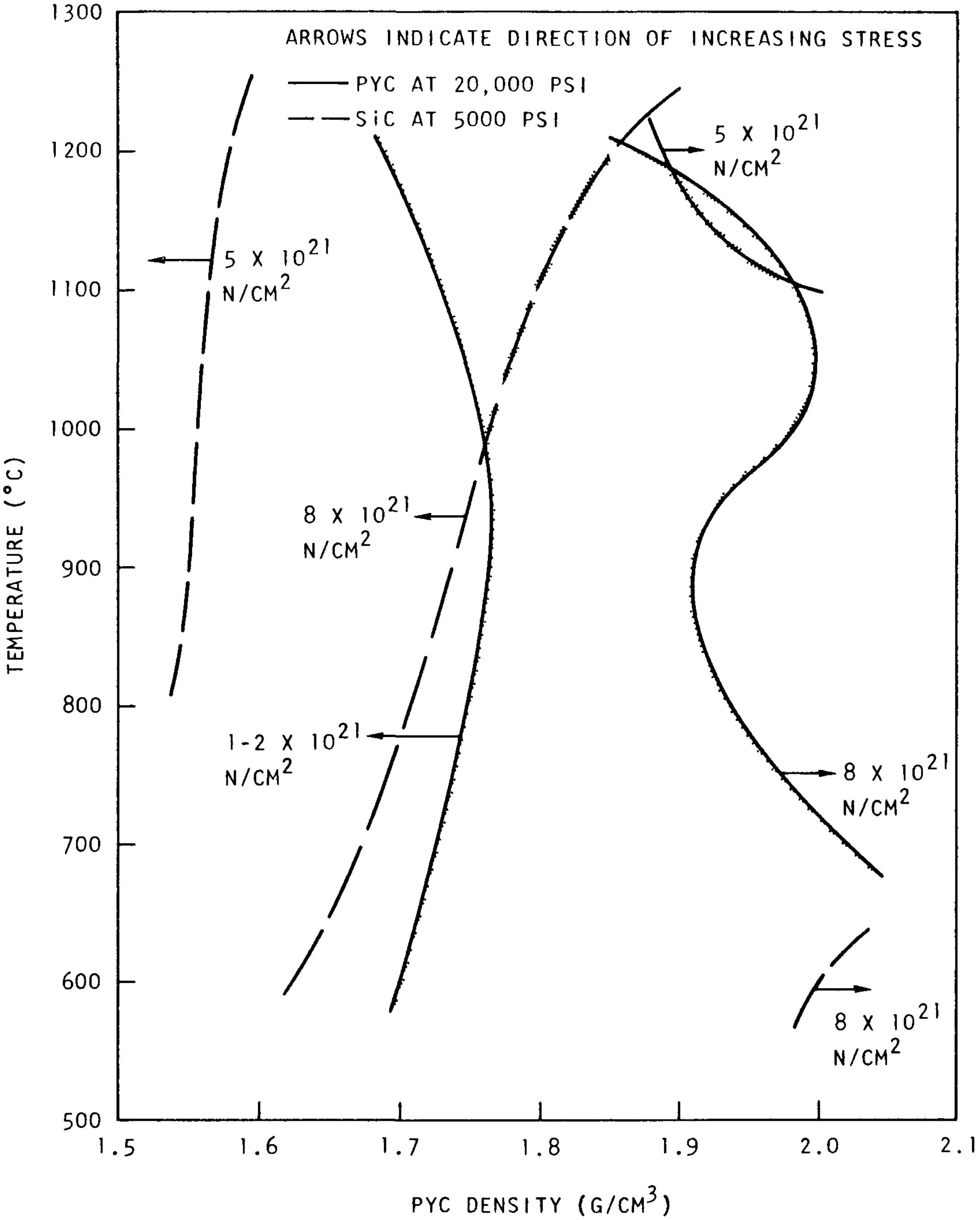

Fig. V.66--TRISO-I parametric study, loci of tensile stress limits (HTI fertile-B 50-20-50 μm)

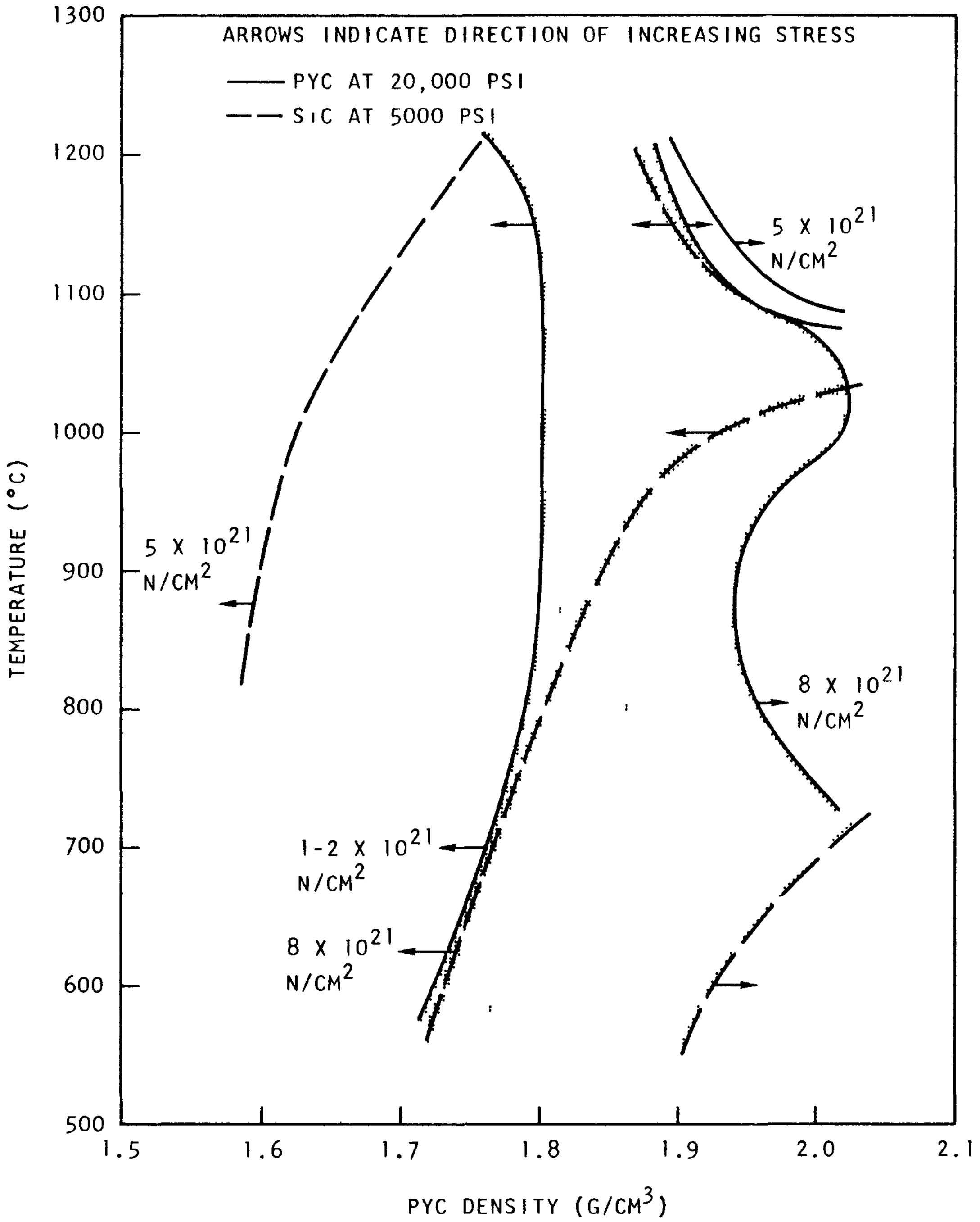

Fig. V.67--TRISO-I parametric study, loci of tensile stress limits (HTI fertile-B 50-20-30 μm)

SiC failure locus forms a design restriction in only one case (see Fig. V.67), where the fertile particle has only a 30-μm layer of HTI. The SiC failure locus is not restricting in the other cases, because the maximum fuel temperature at end of life is below 1000°C, and below 1050°C at the end of year three of the six-year equilibrium fuel cycle. The resulting restrictions on PyC density are summarized in Table V.19.

Table V.19

ACCEPTABLE HTI DENSITIES IN TRISO-I COATINGS AS INDICATED BY FAILURE LOCI

Coated Particle Type	HTI Thickness (μm)	Acceptable PyC Density Range[a] (g/cm^3)
Fissile	60	1.70-1.82
Fissile	50	1.72-1.85
Fissile	30	1.79-1.92
Fertile	70	1.73-1.87
Fertile	50	1.77-1.91
Fertile	30	1.80-1.94[b]

[a] Indicated from failure loci (see Figs. V.62 through V.67).

[b] Unacceptable range from the standpoint of SiC tensile stress (see Fig. V.67).

The TRISO-II parametric studies were made using only two HTI densities (1.79 and 1.87 g/cm^3) for the outer PyC layer. This was done to minimize calculations. Dimensional-change data were available for these densities, and the TRISO-I study indicated that these densities would be acceptable for the outer layer. In addition, only one value of outer PyC layer thickness was used, 50 μm for the fertile particle and 40 μm for the fissile particle. (It was felt that optimization of the outer layer would be quite similar to that of the TRISO-I coating because the outer coating is restrained and essentially isolated by the SiC layer, since the high-modulus SiC acts as a barrier to the transmission of strain.)

In addition to the two outer-layer densities, the TRISO-II variables included 15, 20, 25 μm inner-layer thicknesses and 21 combinations of inner-layer density and irradiation temperature. Each combination of variables was used for the fertile and the fissile particle types.

Maximum PyC and SiC tensile stresses were plotted versus inner PyC density and irradiation temperature at the same three fast-dose values, and failure loci were generated as in the TRISO-I study. The stress in the outer PyC layer did not exceed 20,000 psi in this study.

The SiC failure loci were not limiting. The restrictions on inner PyC density resulting from the inner PyC failure loci are summarized in Table V.20.

Table V.20

ACCEPTABLE INNER HTI DENSITIES IN TRISO-II COATINGS AS INDICATED BY FAILURE LOCI

Coated Particle Type	Outer HTI Density (g/cm^3)	Inner HTI Thickness (μm)	Acceptable Inner HTI Density Range[a] (g/cm^3)
Fertile	1.87	25	1.92-1.96
Fertile	1.79	25	1.93-1.98
Fertile	1.87	20	1.90-1.96
Fertile	1.79	20	1.91-1.98
Fertile	1.87	15	1.89-1.97
Fertile	1.79	15	1.91-1.98
Fissile	1.87	25	1.94[b]
Fissile	1.79	25	1.95-1.98
Fissile	1.87	20	1.940-1.945
Fissile	1.79	20	1.93-1.98
Fissile	1.87	15	1.91-1.97
Fissile	1.79	15	1.92-1.97

[a] Indicated from failure loci.

[b] PyC failure loci overlap at 1.94 g/cm^3 between 825° and 950°C. This fissile design appears to be unacceptable.

These results indicate that 20 and 25 μm inner HTI thicknesses restrict the acceptable inner HTI density range. The 1.87 g/cm^3 outer HTI density appears to be unacceptable for the fissile particle when inner layer thicknesses of 20 or 25 μm are used.

FISSION-PRODUCT RELEASE

Comparison of Calculated and Observed Fission-gas Release

The releases of gaseous fission products from TRISO-coated particles with intact SiC layers are governed largely by the fuel contamination in and on the surface of the outer pyrolytic carbon layers; therefore, fuel contamination data can be used to estimate levels of fission-gas release.

The release fractions of Kr^{88} expected from a sample of fissile particles, a sample of fertile particles, and a mixture composed of fertile and fissile particles were calculated and compared with release fractions of Kr^{88} measured in the TRIGA reactor. This work was done to demonstrate that the fission-gas release values currently being observed on samples irradiated in the TRIGA reactor are consistent with the contamination levels that have been measured.

Table V.21 gives the information used in calculating the Kr^{88} release fraction from fuel contamination data, outlines the calculation, and compares calculated and observed release values. Column 6 gives the calculated fraction of fissions in or on the coating. Columns 7 and 8 give the calculated fission-gas release assuming (1) all the U^{235} contamination is on the surface (assuming the release constant is 0.5) and (2) all the U^{235} contamination is in the outer pyrolytic carbon coating (assuming the release constant is 0.1).* The last column gives the observed Kr^{88} release values taken from the data for loose particles given in Table 3.7.

The Kr^{88} release data can be summarized as follows:

	Calculated	Measured
Fissile	$4.5\text{x}10^{-8}$ to $2.3\text{x}10^{-7}$	$6\text{x}10^{-8}$
Fertile	$8.3\text{x}10^{-4}$ to $4.2\text{x}10^{-3}$	$7\text{x}10^{-4}$
Mixture	$1.1\text{x}10^{-7}$ to $5.5\text{x}10^{-7}$	$2\text{x}10^{-7}$

The data from all three samples fall within or close to the expected range. Thus, the calculated and observed values are consistent and the increase in fission-gas release observed when fissile and fertile particles are mixed is readily explained by the presence of U^{235} contamination in the coatings of fertile particles. This contamination, of course, also accounts for the hitherto inexplicably high release of the fertile particles.

Steady-state Fission-gas Release Correction

In the past, fission-gas release measurements have been corrected to equilibrium R/B values† by application of correction factors to the measured releases of longer-lived isotopes to compensate for the nonattainment of steady-state conditions. These factors were calculated from equations discussed

---

*The fraction of recoils escaping from the coatings has been calculated to be 0.12 for fissile particles and 0.09 for fertile particles. Recoils occurring on the surface have a fractional release probability of 0.51. These calculations apply to isolated particles but are assumed to apply to an assembly of particles.

†R/B is the ratio of the instantaneous release rate to the instantaneous birth rate unually determined under steady-state conditions. The routine experiments in TRIGA measure a 1-hr average fractional release where steady-state conditions (the concentration of the radionuclides of interest in the particles does not change with time) have not been attained for the longer-lived isotopes.

Table V.21

COMPARISON OF CALCULATED AND OBSERVED Kr^{88} RELEASE FROM UNLEACHED TRISO-COATED PARTICLES[a]

Particle Type	Coating Contamination[b] (g U^{235}/g particles)	Particles in Sample (g)	Sample Kernels		Fraction of Fissions Associated with Coating[d]	Fractional Release Kr^{88}		
			U^{235} (g)	Th (g)		Assuming All U^{235} on Surface	Assuming All U^{235} in Coating	Observed[c] (Exp. Seq. 4-6)
Fissile	$1x10^{-7}$	5	1.1	--	$4.5x10^{-7}$	$2.3x10^{-7}$	$4.5x10^{-8}$	$6x10^{-8}$
Fertile	$1x10^{-7}$	1	--	0.53	$8.3x10^{-3}$	$4.2x10^{-3}$	$8.3x10^{-4}$	$7x10^{-4}$
Fissile	$1x10^{-7}$	2.0	0.44	--	$4.5x10^{-7}$	---	---	---
Fertile	$1x10^{-7}$	3.1	--	--	$6.8x10^{-7}$	---	---	---
Mixture	---	---	--	--	$1.1x10^{-6}$	$5.5x10^{-7}$	$1.1x10^{-7}$	$2x10^{-7}$

[a] In the calculation, (1) U^{235} fission-product cross section = 580 barns, (2) Th fission cross section (in TRIGA) = 0.013 barns, (3) release constant for fission gases produced from U^{235} contamination on surface is taken to be 0.50, and (4) release constant for fission gases produced from U^{235} contamination in coating is taken to be 0.10.

[b] Assumed fuel contamination values based on measured values given in Table V.7.

[c] See Table 3.7.

[d] Calculations: $\frac{(5)(10^{-7})}{1.1} = 4.5 \times 10^{-7}$,

$$\frac{(10^{-7})(580)(232)}{(0.53)(0.013)(235)} = 8.3 \times 10^{-3} \quad ,$$

$$\frac{(2.0 + 3.1)(10^{-7})}{(0.44)} = 1.1 \times 10^{-6} \quad .$$

in a paper by Zumwalt, Gethard, and Anderson (Ref. 12). Concern for the applicability of the steady-state correction under test conditions in the TRIGA reactor warranted conducting experiments designed to clarify the question. Accordingly, the fission-gas release of both BISO- and TRISO-II-coated fuel particles was measured during a continuous irradiation for 8 hr in the TRIGA King furnace. During the irradation, the fission gases released were collected every other hour and gamma-counted as described in the previous quarterly report (GA-8879). The BISO particles were irradiated at 1400°C for 7 hr, after which the temperature was reduced to 1000°C in an effort to determine the temperature dependence of the release. The TRISO-II particles were irradiated for the full 8 hr at 1000°C. The samples were leached before irradiation to remove any surface contamination that might enhance the krypton and xenon fission-gas release values.

The data obtained in these studies are given in Tables V.22 and V.23, and the release fractions are plotted versus time in Figs. V.68 through V.73. The fission-gas release values show little time dependence during the 8-hr irradiation. Figure V.74 is a plot of the uncorrected fractional release values versus half life of the gaseous nuclides for the BISO and TRISO-II fuel particles after irradiation for 1 hr. If the release of gaseous fission products from fuel particles were a diffusion-controlled process, Fig. V.74 would be expected to show a marked dependence on the half life of the nuclide. Such a dependence is not present. This indicates that, under the test conditions of the TRIGA King furnace experiment, the release of fission gases is primarily due to recoils from contamination in the PyC coating rather than being a diffusion-controlled process. A recoil-controlled phenomenon should not be half-life dependent. Accordingly, future release values at temperatures up to 1400°C will be reported without the application of a steady-state correction. This procedure was followed in reporting data for fuel rods manufactured for the second proof test element (see below).

Proof Test Element

Particles. Postactivation metallic fission-product release tests on candidate TRISO-coated particles for the second proof test element have been completed. The data for 25 samples tested this quarter showed a slight improvement in quality over fissile samples reported previously. Fertile particles showed about an order of magnitude improvement.

Fuel Rods. Thirty-one fuel rods made of TRISO-II particles were irradiated as part of a quality control program to evaluate fabrication techniques and to determine the acceptability of the fuel rods for use in the second proof test element. The rods were irradiated for 1 hr at 1000°C to approximately 10^{14} fissions, and the fission gases were collected and counted as described in the previous quarterly report (GA-8879). The data obtained are given in Table V.24. These data were not corrected to steady-state conditions, for reasons reported above.

During the fabrication of the second proof test element fuel rods, it was noted that breakage of fuel particles had occurred on the outer surface of a number of fuel rods. On the basis of this observed breakage, experimental work was initiated to determine what effect leaching of a fuel rod with known particle breakage would have on fission-gas release measurements.

Table V.22

FISSION-GAS RELEASE FROM BISO PARTICLES AT 1000° AND 1400°C[a]

Time (hr)	Release Fraction					
	Kr^{85m} (4.4 h)	Kr^{88} (2.8 h)	Kr^{87} (1.3 h)	Kr^{89} (0.053 h)	Xe^{138} (0.28 h)	Xe^{139} (0.011 h)
1	2x10^{-5}	2x10^{-5}	2x10^{-5}	2x10^{-5}	1x10^{-5}	5x10^{-6}
2	3x10^{-5}	4x10^{-5}	3x10^{-5}	9x10^{-6}	6x10^{-6}	1x10^{-6}
4	3x10^{-5}	4x10^{-5}	3x10^{-5}	1x10^{-5}	7x10^{-6}	1x10^{-6}
6	3x10^{-5}	3x10^{-5}	3x10^{-5}	1x10^{-5}	9x10^{-6}	4x10^{-6}
8[b]	4x10^{-6}	5x10^{-6}	4x10^{-6}	8x10^{-6}	4x10^{-6}	3x10^{-6}

[a] Blended sample XETK-HTI-LTI-COMP-2 (leached).

[b] During the last hour the irradiation temperature was 1000°C; all other data were at 1400°C.

Table V.23

FISSION-GAS RELEASE FROM TRISO-II PARTICLES AT 1000°C[a]

Time (hr)	Release Fraction					
	Kr^{85m} (4.4 h)	Kr^{88} (2.8 h)	Kr^{87} (1.3 h)	Kr^{89} (0.053 h)	Xe^{138} (0.28 h)	Xe^{139} (0.011 h)
1	2x10^{-6}	1x10^{-6}	4x10^{-7}	8x10^{-7}	3x10^{-7}	7x10^{-7}
2	2x10^{-6}	2x10^{-6}	3x10^{-7}	1x10^{-6}	7x10^{-7}	1x10^{-6}
4	2x10^{-6}	1x10^{-6}	3x10^{-7}	1x10^{-6}	5x10^{-7}	8x10^{-7}
6	1x10^{-6}	8x10^{-7}	2x10^{-7}	9x10^{-7}	3x10^{-7}	8x10^{-7}
8	1x10^{-6}	2x10^{-6}	2x10^{-7}	1x10^{-6}	2x10^{-7}	6x10^{-7}

[a] Lot ET109A (leached).

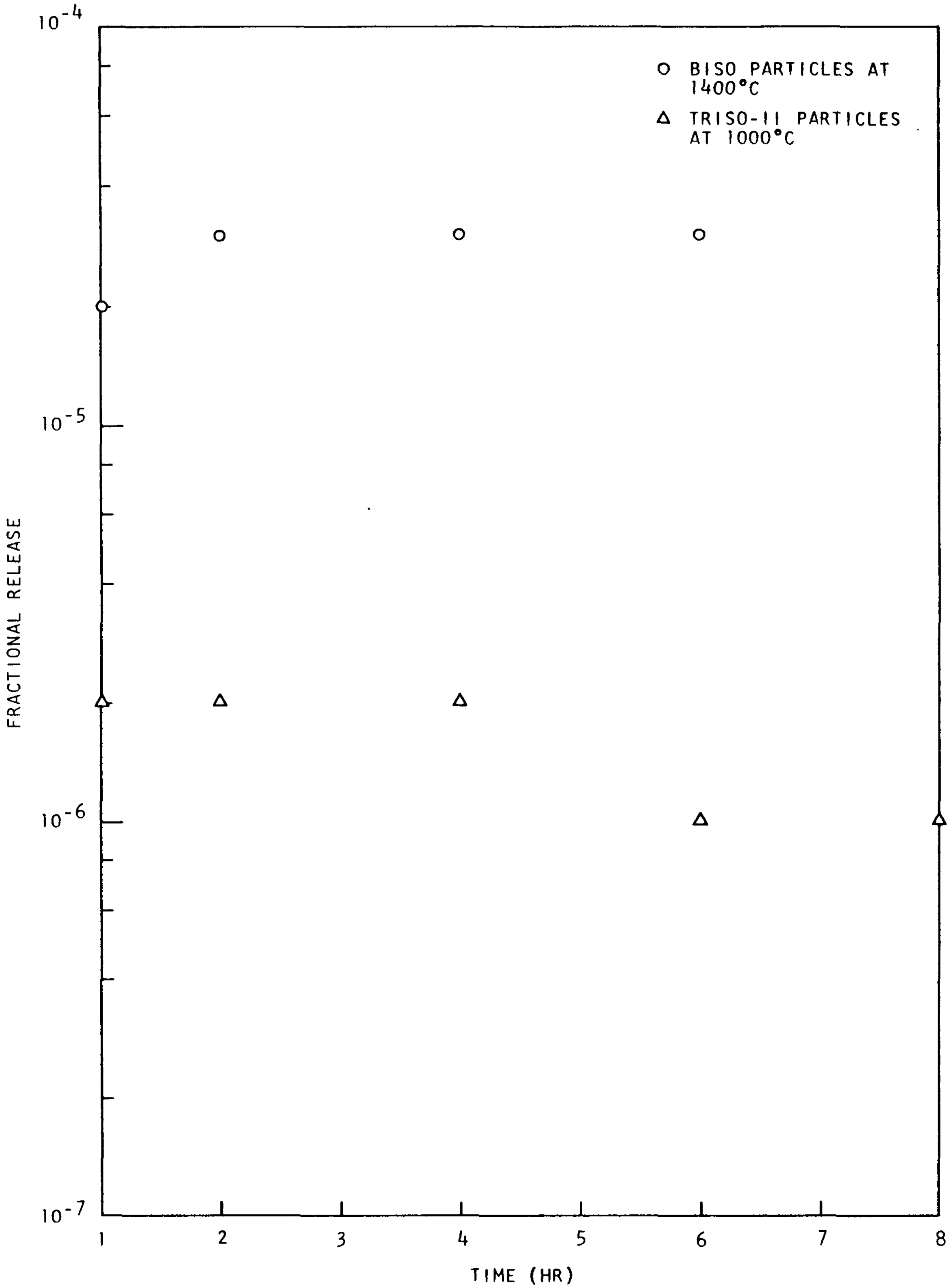

Fig. V.68--Kr^{85m} fractional release for 8-hr irradiation

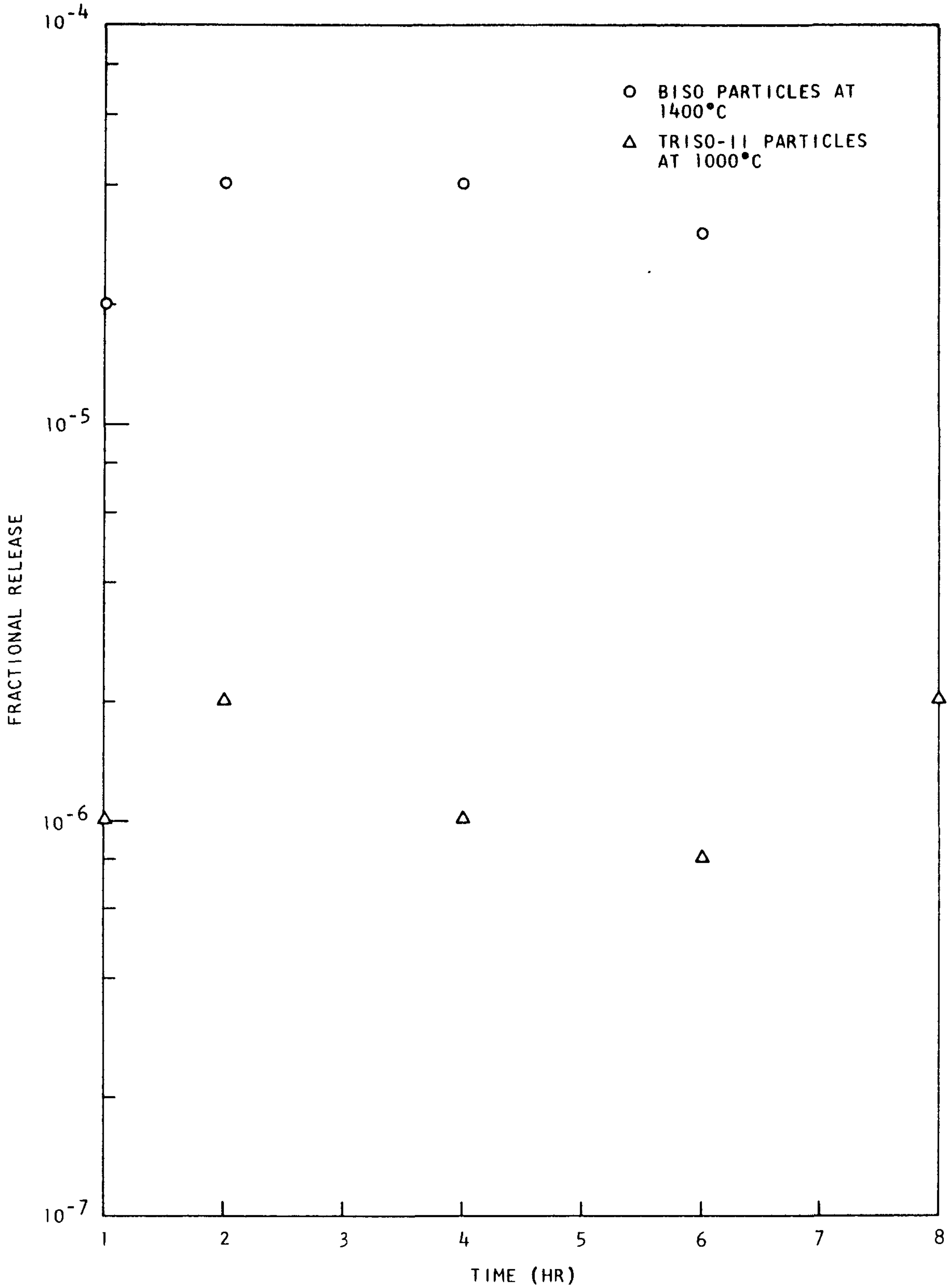

Fig. V.69--Kr^{88} fractional release for 8-hr irradiation

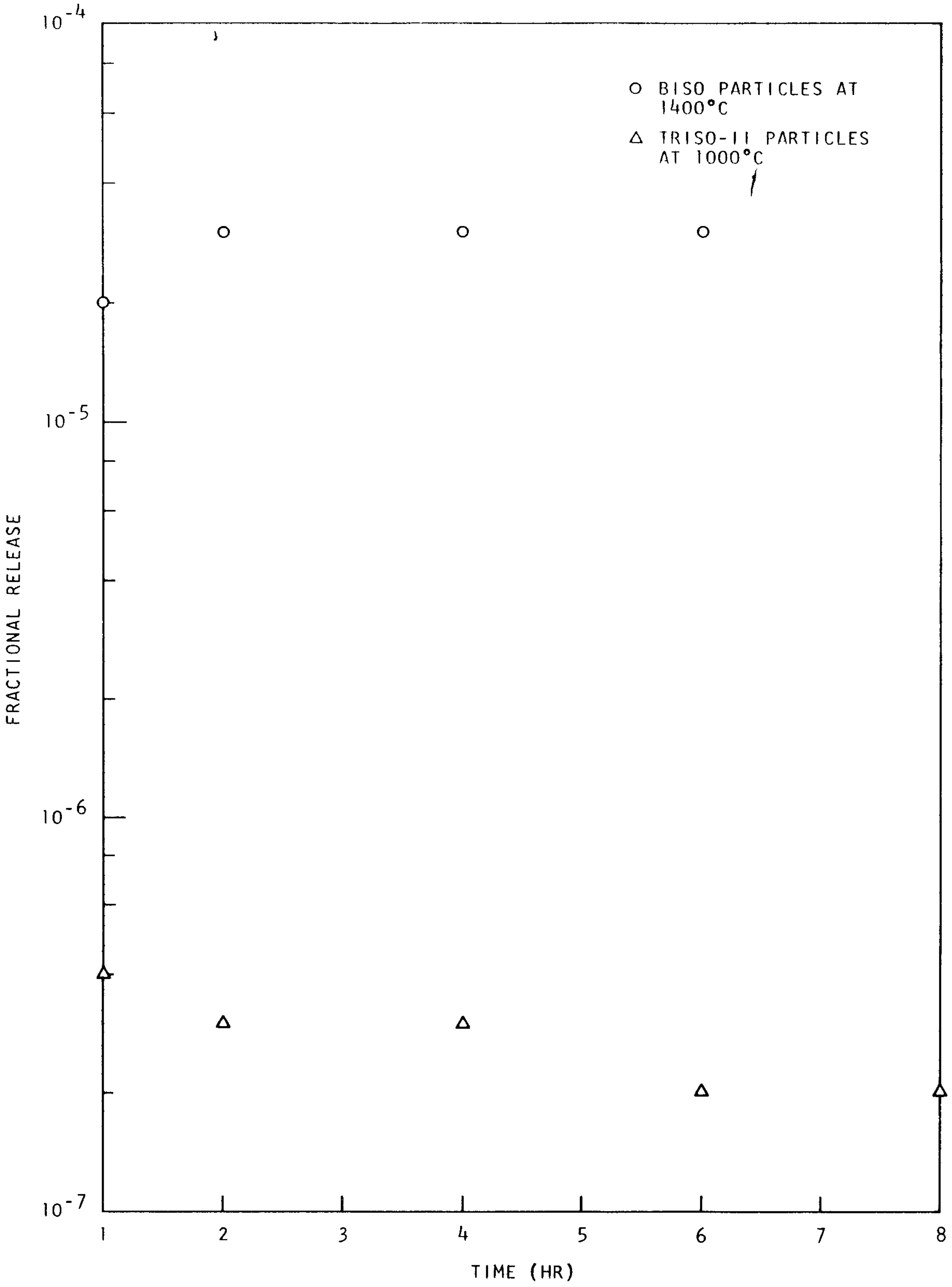

Fig. V.70--Kr^{87} fractional release for 8-hr irradiation

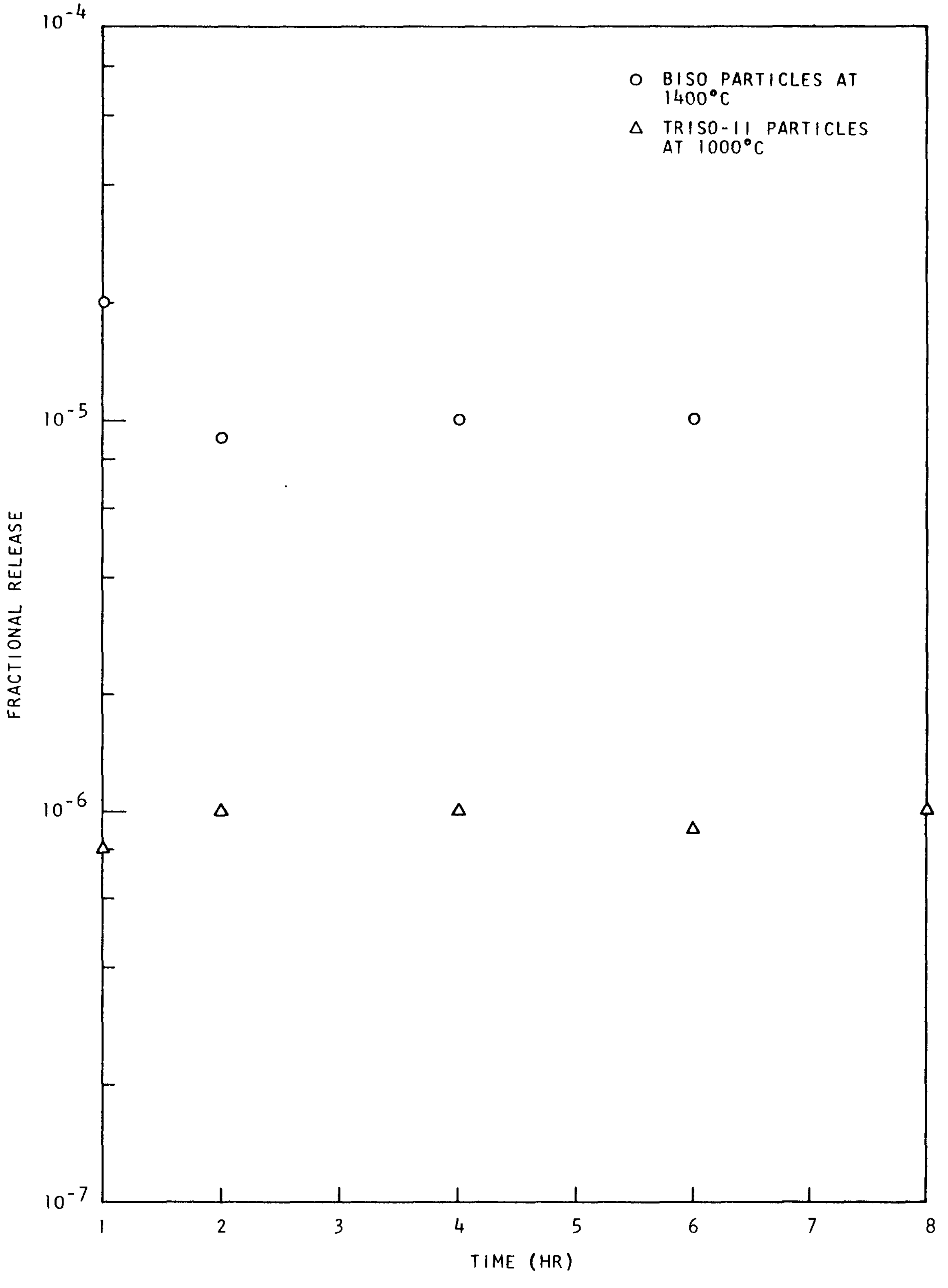

Fig. V.71--Kr^{89} fractional release for 8-hr irradiation

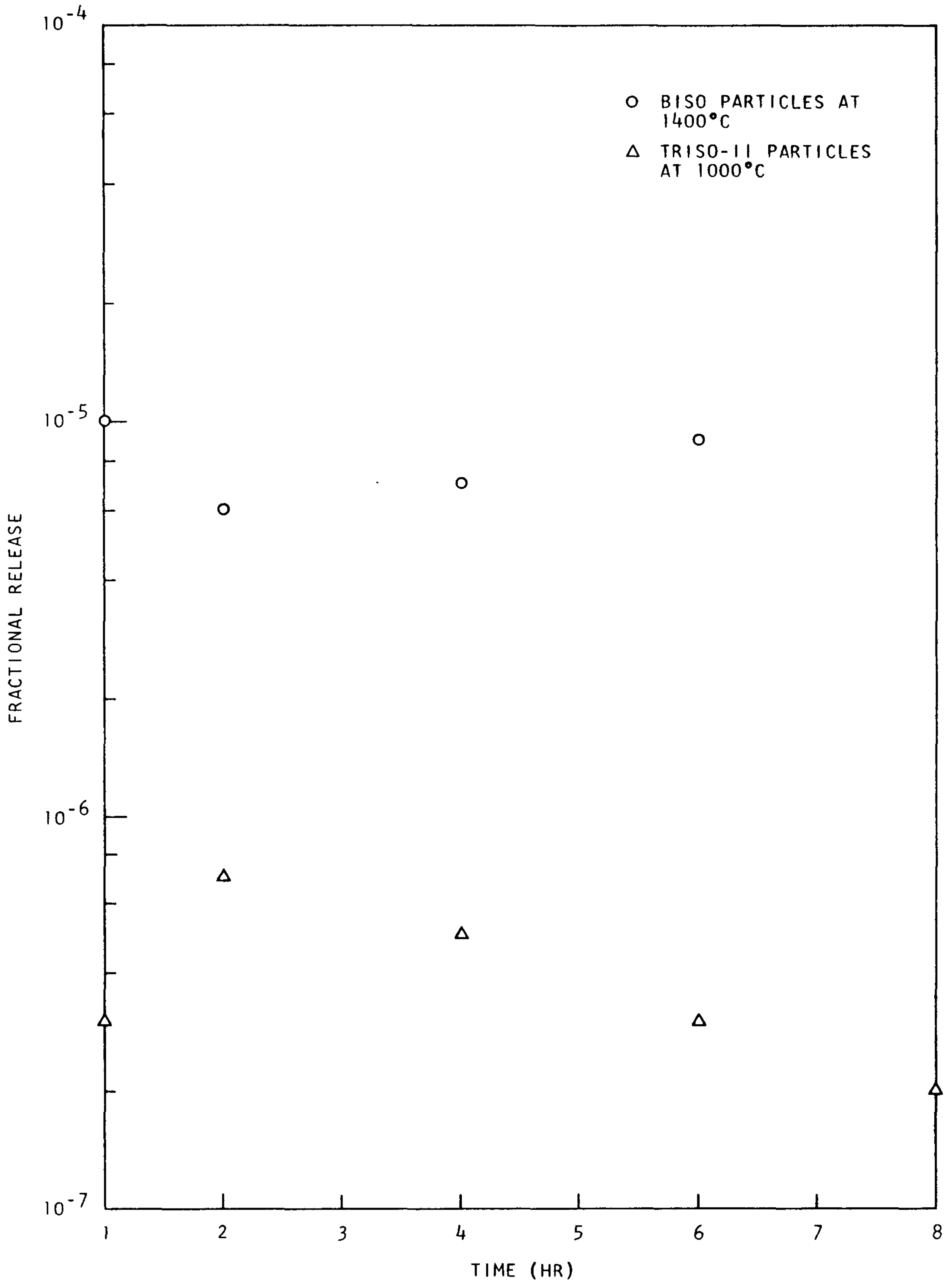

Fig. V.72--Xe^{138} fractional release for 8-hr irradiation

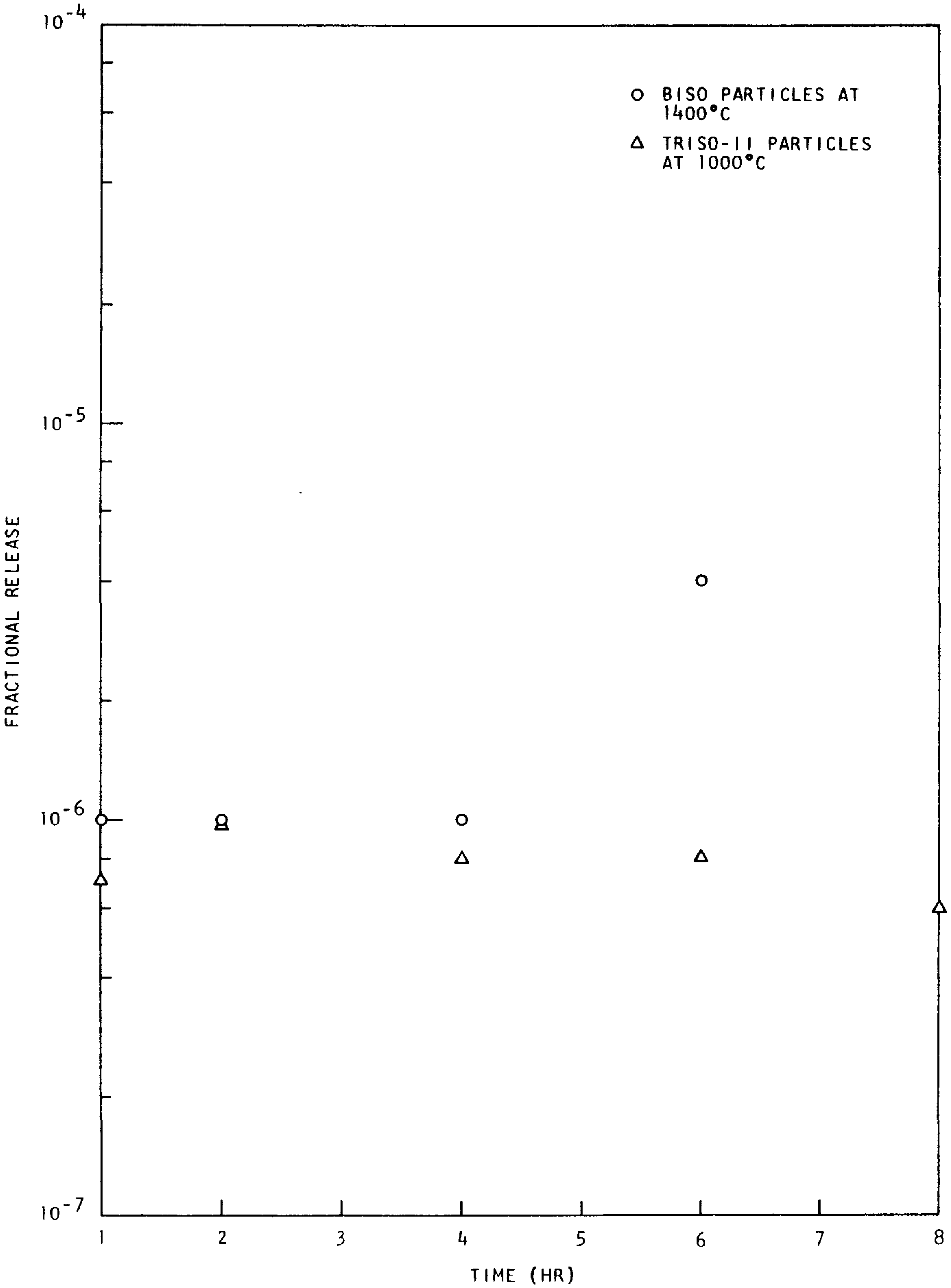

Fig. V.73--Xe^{139} fractional release for 8-hr irradiation

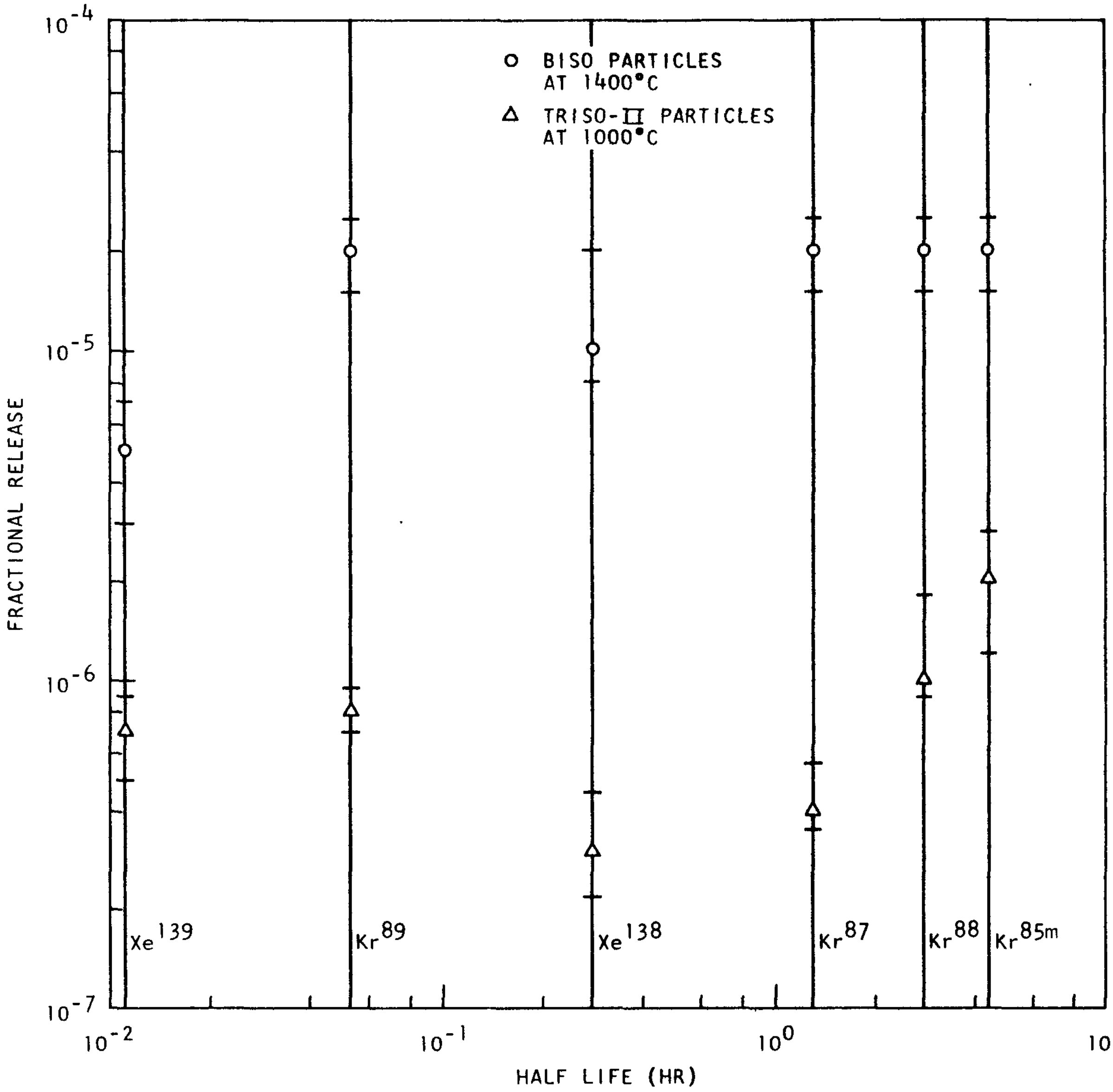

Fig. V.74--Fission-gas release from BISO and TRISO-II fuel particles

Table V.24

FISSION-GAS RELEASE FROM PROOF TEST FUEL RODS

Sample No.	Release Fraction					
	Kr^{85m}	Kr^{88}	Kr^{87}	Kr^{89}	Xe^{138}	Xe^{139}
LTI High Density						
Samp. 1, Load. 1	$3x10^{-6}$	$4x10^{-6}$	$4x10^{-6}$	$1x10^{-5*}$	$1x10^{-5*}$	$7x10^{-6*}$
456 Loading 2	$2x10^{-6}$	$3x10^{-6}$	$3x10^{-6}$	$3x10^{-6}$	$3x10^{-6}$	$9x10^{-7}$
569 Loading 3	$3x10^{-6}$	$4x10^{-6}$	$4x10^{-6}$	$3x10^{-6}$	$5x10^{-6*}$	$3x10^{-6*}$
559 Loading 4	$3x10^{-6}$	$3x10^{-6}$	$1x10^{-6}$	$3x10^{-6}$	$2x10^{-6}$	$3x10^{-6*}$
Samp. 5, Load. 5	$2x10^{-6}$	$3x10^{-6}$	$2x10^{-6}$	$3x10^{-6}$	$3x10^{-6}$	$2x10^{-6*}$
570 Loading 6	$4x10^{-6}$	$7x10^{-6}$	$3x10^{-6}$	$5x10^{-6}$	$5x10^{-6*}$	$2x10^{-6*}$
963 Loading 15	$2x10^{-5}$	$3x10^{-5}$	$2x10^{-5}$	$3x10^{-5*}$	$3x10^{-5*}$	$1x10^{-5*}$
958 Loading 16	$2x10^{-6}$	$4x10^{-6}$	$2x10^{-6}$	$7x10^{-6}$	$6x10^{-6*}$	$3x10^{-6*}$
877	$1x10^{-5}$	$1x10^{-5}$	$1x10^{-5}$	$7x10^{-6*}$	$7x10^{-6*}$	$4x10^{-6*}$
889	$2x10^{-6}$	$2x10^{-6}$	$8x10^{-7}$	$1x10^{-6}$	$2x10^{-7}$	$3x10^{-7}$
901	$2x10^{-6}$	$3x10^{-6}$	$1x10^{-6}$	$1x10^{-6}$	$6x10^{-7}$	$9x10^{-7}$
918	$2x10^{-6}$	$1x10^{-6}$	$3x10^{-7}$	$3x10^{-7}$	$2x10^{-7}$	$2x10^{-7}$
953	$2x10^{-6}$	$2x10^{-6}$	$1x10^{-6}$	$2x10^{-6}$	$2x10^{-6}$	$1x10^{-6}$
24A	$5x10^{-7}$	$6x10^{-7}$	$3x10^{-7}$	$3x10^{-7}$	$3x10^{-7}$	$3x10^{-7}$
LTI Low Density						
924	$1x10^{-6}$	$2x10^{-6}$	$1x10^{-6}$	$2x10^{-6}$	$9x10^{-7}$	$8x10^{-7}$
936	$6x10^{-6}$	$6x10^{-6}$	$6x10^{-6}$	$3x10^{-6}$	$3x10^{-6}$	$2x10^{-6*}$
947	$2x10^{-6}$	$2x10^{-6}$	$3x10^{-7}$	$2x10^{-7}$	$3x10^{-7}$	$5x10^{-7}$
13A	$2x10^{-5}$	$2x10^{-5}$	$2x10^{-5}$	$2x10^{-5*}$	$2x10^{-5*}$	$1x10^{-5*}$
580 Loading 7	$2x10^{-6}$	$1x10^{-6}$	$7x10^{-7}$	$1x10^{-6}$	$1x10^{-6}$	$1x10^{-6}$
589 Loading 8	$3x10^{-6}$	$3x10^{-6}$	$2x10^{-6}$	$3x10^{-6}$	$2x10^{-6}$	$1x10^{-6}$
979 Loading 9	$3x10^{-5}$	$3x10^{-5}$	$2x10^{-5}$	$9x10^{-6*}$	$1x10^{-5*}$	$4x10^{-6*}$
977 Loading 10	$5x10^{-6}$	$6x10^{-6}$	$3x10^{-6}$	$3x10^{-6}$	$3x10^{-6}$	$4x10^{-7}$
994 Loading 11	$3x10^{-6}$	$3x10^{-6}$	$1x10^{-6}$	$2x10^{-6}$	$2x10^{-6}$	$6x10^{-7}$
976 Loading 12	$3x10^{-5}$	$3x10^{-5}$	$3x10^{-5*}$	$2x10^{-5*}$	$2x10^{-5*}$	$5x10^{-6*}$
993 Loading 13	$2x10^{-5}$	$2x10^{-5}$	$2x10^{-5}$	$2x10^{-5*}$	$2x10^{-5*}$	$5x10^{-6*}$
972 Loading 14	$9x10^{-5*}$	$7x10^{-5*}$	$7x10^{-5*}$	$6x10^{-5*}$	$6x10^{-5*}$	$2x10^{-5*}$
HTI						
834	$2x10^{-6}$	$3x10^{-6}$	$1x10^{-6}$	$3x10^{-6}$	$3x10^{-6}$	$1x10^{-6}$
849	$2x10^{-6}$	$3x10^{-6}$	$1x10^{-6}$	$3x10^{-6}$	$3x10^{-6}$	$4x10^{-7}$
870	$9x10^{-6}$	$7x10^{-6}$	$8x10^{-6}$	$6x10^{-6*}$	$5x10^{-6*}$	$2x10^{-6*}$
3A	$3x10^{-6}$	$3x10^{-6}$	$2x10^{-6}$	$5x10^{-6*}$	$4x10^{-6*}$	$2x10^{-6*}$
51A	$4x10^{-6}$	$6x10^{-6}$	$3x10^{-6}$	$4x10^{-6}$	$3x10^{-6}$	$2x10^{-6*}$
Fuel Rod Leaching Experiment						
25A	$4x10^{-6}$	$4x10^{-6}$	$3x10^{-6}$	$5x10^{-6}$	$6x10^{-6}$	$5x10^{-6}$
33A	$3x10^{-6}$	$4x10^{-6}$	$3x10^{-6}$	$3x10^{-6}$	$3x10^{-6}$	$4x10^{-6}$

NOTE: Asterisk (*) denotes value exceeds specification.

Two fuel rods, 25A and 33A (see Table V.24), were fabricated under identical conditions. Fuel rod 25A was irradiated as fabricated; rod 33A was leached before irradiation to remove contamination caused by a single deliberately broken fuel particle on the outer surface of the rod. (The extent of the particle breakage is unknown. The crack in the fuel particle may not have extended to the fuel core, thus preventing hydrolysis.) The data in Table V.24 indicate that the fractional release values are the same within the experimental error. While one experiment is hardly conclusive, it may be possible to salvage fuel rods damaged during fabrication by leaching to remove surface contamination from one or two broken fuel particles. Since it is also known that the matrix material and the outer surface of coated fuel particles are slightly contaminated with uranium, the leaching step might aid in removing this contamination as well. This experiment should be repeated.

PHASE BEHAVIOR OF THE Th-Si-C SYSTEM AT HIGH TEMPERATURES

Diffusion-couple experiments between ThC_2 and SiC have continued during the quarter. An anneal was completed at 1800°C for 1000 hr. The annealed specimen consisted of a vertical stack of two ThC_2 pellets, a SiC-coated graphite disk, and a thin disk of buffer carbon pressed together inside a graphite crucible. The SiC-coated disk and buffer carbon disk were sandwiched between the two ThC_2 pellets.

The diffusion couple was subjected to a 200°C thermal gradient between the top and bottom ThC_2 pellets. A 50°C gradient was also maintained across the SiC and ThC_2 interface. Visual inspection indicates that only a very slight reaction between the buffer and SiC and between the SiC and ThC_2 may have occurred. The specimen has been submitted for metallographic examination.

Thermal and X-ray analysis of the ternary Th-Si-C system is under way using thorium silicide and carbon as starting materials to confirm earlier results using mixtures of ThC_2 and SiC. In the earlier studies, the absence of a reaction indicated that these were the stable species in the system. Also, rapid vaporization of SiC at temperatures in excess of 2000°C led to losses of phases suitable for X-ray analysis. The lower-melting thorium silicide should react at temperatures below 2000°C and form the stable species, thereby minimizing the vaporization of SiC.

References

1. Grisdale, R. O., "The Formation of Carbon Block," J. Appl. Phys., Vol. 24, 1953, p. 1082.

2. Bokros, J. C., "Variations in the Crystallinity of Carbons Deposited in Fluidized Beds," Carbon, Vol. 3, 1965, p. 201.

3. Egloff, G., The Reactions of Pure Hydrocarbons, Reinhold Publishing Company, 1935.

4. Bokros, J. C., et al., The Influence of Crystallite Size on the Dimensional Changes Induced in Carbonaceous Materials by High-temperature Irradiation, USAEC report GA-8001, General Dynamics, General Atomic Division, July 28, 1967.

5. Steward, K. P., The Mica Foil Technique for Determining Fuel Particle Coating Contaminations, USAEC report GAMD-9015, Gulf General Atomic, to be published.

6. Price, P. B., and R. M. Walker, "A Simple Method of Measuring Low Uranium Concentrations in Natural Crystals," Appl. Phys. Letters, Vol. 2, 1963, p. 23.

7. Steward, K. P., Types of Defective Particles, Their Orgins, and Frequencies of Occurrence, USAEC report GAMD-8742, Gulf General Atomic, to be published.

8. Goeddel, W. V., Pyrolytic-Carbon-Coated Carbide Fuel Particles and Their Use in Graphite-Matrix Fuel Compacts, USAEC report GA-3588, General Dynamics, General Atomic Division, October 30, 1962.

9. Kaae, J. L., "A Mathematical Model for Calculating Stresses in a Pyrocarbon- and Silicon Carbide-Coated Fuel Particle," submitted for publication in J. Nucl. Mater.; also Gulf General Atomic report GA-8563, July 1, 1968.

10. Kaae, J. L., "A Mathematical Model for Calculating Stresses in a Four-layer Carbon-Silicon-Carbide-Coated Fuel Particle," submitted for publication in J. Nucl. Mater.; also Gulf General Atomic report GA-9031, October 14, 1968.

11. Bokros, J. C., et al., "Radiation-Induced Dimensional Changes and Creep in Carbonaceous Materials," to be published in J. Nucl. Mater.; also USAEC report GA-8700, Gulf General Atomic, to be published.

12. Zumwalt, L. R., P. E. Gethard, and E. E. Anderson, "Fission-product Release from Monogranular UC_2 Particles," Nucl. Sci. Eng., Vol. 21, 1965, p. 1.